

Neutral Radicals as Strongly Correlated Materials: Insights from Theory and Experiment

by

Stephen Michael Winter

A thesis
presented to the University of Waterloo
in fulfillment of the
thesis requirement for the degree of
Doctor of Philosophy
in
Chemistry

Waterloo, Ontario, Canada, 2014

© Stephen Michael Winter 2014

Author's Declaration

I hereby declare that I am the sole author of this thesis. This is a true copy of the thesis, including any required final revisions, as accepted by my examiners.

I understand that my thesis may be made electronically available to the public.

Abstract

Neutral organic radicals have been pursued for conductive and magnetic solid state properties associated with their unpaired electron. Historically, synthetic challenges and design limitations restricted these materials into Mott insulating states as a result of a strong Coulomb repulsion preventing the mobility of electrons. As a result, electrons were localized to their parent radicals, and exhibit only weak magnetic interactions. Recent synthetic advances by the Oakley group have allowed access more strongly interacting regimes in neutral radicals, where the kinetic and potential energies are in competition, and the electrons are on the verge of delocalization. This regime is characterized by a variety of strong magnetic interactions, and, under pressure, metallic states have been accessed for the first time. For this reason, it is important to consider the placement of these radicals with respect to other “strongly correlated” materials at the border between metals and magnets, which has proved a fruitful region, hosting unconventional high T_c superconductors, colossal magnetoresistive oxides, and other materials of technological interest. The purpose of this thesis is to consider radicals within this context, as well as introduce theoretical and experimental methods for probing this emerging class of correlated solids.

We consider, in particular, the role of orbital degrees of freedom on the electronic and magnetic properties. To this end, we present a general framework for computing magnetic exchange interactions incorporating Hund’s rule coupling and multiple orbitals in the vicinity of the Fermi level. We extend this framework to include spin-orbit coupling, which directly mixes the spin and orbital degrees of freedom over wide energy scales. This effect leads to anisotropic exchange interactions, which are responsible for a wide variety of magnetic phenomena in heavy selenium-based radicals. A new ab-initio method for constructing effective Hubbard models is presented, which allows us for the first time to directly compute the magnitude and character of anisotropic interactions for organic materials. In order to directly probe the effects of spin-orbit coupling, we have performed magnetic resonance experiments on an isostructural series of heavy selenium-based radicals. We demonstrate conclusively that the observed effects are the result of anisotropic exchange interactions, and find excellent agreement between the experimental and theoretical results, both at ambient, and high pressures.

The modes of magnetic order are investigated over a range of pyridine-bridged bis-dithiazolyl radicals. On the basis of symmetry analysis, such materials may be grouped according to the sign of magnetic exchange along their π -stacks, with ferromagnetic interactions required for the appearance of a net moment, either due to bulk ferromagnetic order or spin-canting in antiferromagnets. We find evidence for a strong multi-orbital ferromagnetic contribution to the interactions between stacks in a selection of Se-based radicals. However, the empty orbitals responsible for this effect are not sufficiently low in energy to contribute to the states in the vicinity of the Fermi level in the solid state. This observation has implications for the response of these materials to pressure, which enhances solid state bandwidth, and prompts a transition from an insulating magnetic state to one exhibiting metallic properties above 6–8 GPa. We compare the properties of this metallic state to those predicted using the Dynamical Mean Field approach.

We further consider how the modification of the orbital manifold may stabilize metallic states at lower pressures, and without need for synthetically challenging Se incorporation. The first materials considered are hybrid dithiazolyl/thiadiazinyl radicals for which additional orbitals may be introduced near the Fermi level through judicious choice of exocyclic groups. However, despite demonstrating a new and general synthetic pathway to these radicals, we find that the introduced orbitals do not satisfy the requirements for hybridization with the SOMO band appearing at the Fermi energy. Instead, we investigate the properties of sulphur based oxobenzene bridged radicals. These materials are found to have an exceedingly low-lying empty LUMO that is strongly coupled to the SOMO through Hund exchange. The interaction of the LUMO and SOMO allows metallic states to be accessed as low as 3 GPa, and generates strong ferromagnetic interactions. We investigate this Mott transition through infrared measurements, and introduce a phenomenological model for the evolution of the electronic structure, which is confirmed through Dynamical Mean Field calculations. On the basis of this model, we consider chemical modifications to further tune the properties of these radicals, which leads to a nearly metallic material already at ambient pressure, and a spin-orbit coupled system that can only be understood outside the context of Moriya’s standard treatment of anisotropic exchange.

Viewing neutral radicals within the context of other strongly correlated materials not only provides insights into their properties, but also suggests routes to future functional

materials. The most dramatic and exotic properties are often found where different energy scales compete, as in the kinetic and potential energy in the vicinity of the Mott transition. The results of this thesis suggest neutral organic radicals may additionally be influenced by spin-orbit effects and Hund's rule coupling of similar magnitude, the full exploration of which will no doubt lead to novel properties.

Acknowledgements

First and foremost, I'd like to thank my supervisor Prof. Richard Oakley, who has taught me, by example, more lessons in life and academics than I can fully appreciate. Your dedication to your students is felt more than you may know. I'd also like to thank the various members of the Oakley group who has not only contributed scientifically, but also made work very enjoyable. In particular, this work would not have been possible without the efforts of Dr. Aaron Mailman, Dr. Alicea Leitch, Dr. Kristina Lakin, Aidin Balo, Ryan Roberts, Karinna Yu, and Joanne Wong.

Thank you to my supervisory committee, which has included (at various times) Prof. Holger Kleinke, Prof. Robert Hill, Prof. Kathryn Preuss, and Prof. Marcel Nooijen. Your patience and guidance has been greatly appreciated.

I'd like to thank our collaborators at Florida State University. I must particularly acknowledge Prof. Stephen Hill, with whom I have enjoyed not only a strong and successful scientific collaboration, but also a great personal relationship. I would not be where I am today without his timely advice and the career opportunities he has given me. I would also like to thank those (past and present) members of his group who have been instrumental in our collaboration: Dr. Saiti Datta, Dr. Alexey Kovalev, Dr. Chris Beedle, and especially Dr. Komalavalli Thirunavukkuarasu. I'd also like to thank Prof. Vladimir Dobrosavljević, who was always willing to challenge me and put up with my ignorance. The members of his group, Yohanes Pramudya, Hossein Mard, and especially Samiyeh Mahmoudian made my stay at the National High Magnetic Field Lab both comfortable and enjoyable. Finally, I'd like to thank Prof. Michael Shatruk, and his student Hoa Phan for their unlimited energy and tireless efforts toward our collaboration.

Finally, I'd like to acknowledge the remainder of our collaborators for their contributions: Dr. Paul Dube (Brockhouse), Richard Secco (Western Ontario), Dr. Masaki Mito (Kyushu), Dr. David Graf, Dr. Eden Steven (NHMFL), Dr. Craig Robertson (Liverpool), and Prof. Stephen Julian (Toronto). I would like to particularly acknowledge Prof. John Tse, whose ability to secure beam time seems unlimited, and who taught me many lessons, both scientific, and otherwise.

*Neither from itself nor from another,
Nor from both,
Nor without a cause,
Does anything whatever, anywhere arise.*

Nāgārjuna, Mūlamadhyamakakārikā

Table of Contents

List of Tables	xiii
List of Figures	xv
List of Symbols and Abbreviations	xxi
1 Introduction	1
1.1 Radicals as Strongly Correlated Materials	1
1.2 Introduction to the Hubbard Model	3
1.2.1 Definitions	3
1.2.2 Phases of the Hubbard Model	5
1.3 Historical Perspective on Radical Design	9
1.3.1 Carbon-Centered Radicals	9
1.3.2 Light Heteroatom Radicals	10
1.3.3 Heavy Heteroatom Radicals	12
1.3.4 Radical Ion and Charge Transfer Salts	19
1.4 Thesis Organization	24

2	Theoretical Aspects of Magnetism	26
2.1	Derivation of Effective Spin Hamiltonians	26
2.1.1	Adiabatic Concept and Low-Energy Theories	26
2.1.2	Diagrammatic Representation in the $U \gg t$ Limit	30
2.1.3	Single Orbital Hubbard Model in the $U \gg t$ limit	33
2.1.4	Ferromagnetism in Multi-Orbital Models	35
2.1.5	Importance of Multi-orbital Exchange in Organics	37
2.2	Role of Spin-Orbit Effects in Magnetism	40
2.2.1	Introduction	40
2.2.2	Qualitative Aspects of Atomic Spin-Orbit Coupling	41
2.2.3	Derivation of Anisotropic Exchange Hamiltonians	47
2.2.4	Multi-Orbital Anisotropic Exchange	57
2.3	Ab-Initio Methods for Exchange Interactions in Organics	62
2.3.1	Broken-Symmetry Density Functional Theory	62
2.3.2	Failure of Existing SOC Calculations for Organics	65
2.4	Constructing Effective Hubbard Models	67
2.4.1	Introduction	67
2.4.2	Calculation of Hopping Parameters	67
2.5	Chapter Summary	76
3	Theoretical Aspects of Electrical Transport	77
3.1	Conventional Theory of Metals	77
3.2	Dynamical Mean Field Approach	81
3.3	Phenomenology of the Mott Transition	85
3.4	Chapter Summary	87

4	Magnetic Properties of Pyridine-Bridged bis-Dithiazolyls and Their Selenium Analogues	89
4.1	Synthetic Review	89
4.2	Magnetostructural Phase Diagram	93
4.2.1	Structural Organization	93
4.2.2	Symmetry Considerations	96
4.2.3	Organization of Magnetic Phases by $\mathcal{J}_{ij}^{(\pi)}$	104
4.3	Low Dimensional Radical Systems: Ladders	109
4.3.1	Theoretical Introduction	109
4.3.2	Studies of Radical Spin Ladders	112
4.4	Chapter Summary	118
5	Isostructural Tetragonal Radical Family $R_1 = Et, R_2 = Cl$	119
5.1	Introduction	119
5.2	Magnetic Structures	121
5.2.1	Molecular Electronic Structure	123
5.2.2	Solid State Electronic Structure	126
5.2.3	Summary / Conclusions	130
5.3	Response to Physical Pressure	131
5.3.1	Magnetic Response	132
5.3.2	Transport Properties and Metallization	135
5.3.3	Evolution of Electronic Structure	136
5.3.4	Summary / Conclusions	141

6	Spin-Orbit Effects in Heavy Atom Radicals	142
6.1	Introduction	142
6.2	FMR Studies of Tetragonal Ferromagnets	143
6.2.1	Experimental	143
6.2.2	Sources of Magnetic Anisotropy	148
6.2.3	Analysis of Anisotropic Exchange	151
6.3	FMR Under Pressure	156
6.4	AFMR in Mixed S/Se Antiferromagnet	158
6.5	Discussion of Magnitudes	161
6.6	Chapter Summary	162
7	Multi-Orbital Radicals	163
7.1	Introduction	163
7.2	Hybrid Dithiazolyl/Thiadiazinyl Radicals	164
7.2.1	Synthesis and Structure	164
7.2.2	Electronic Structure	168
7.3	oxobenzene Bridged Radicals	171
7.3.1	Introduction	171
7.3.2	Fluorine Substituted Radical FBBO	174
7.3.3	Nitro Substituted Radical NO ₂ BBO	199
7.3.4	Iodine Substituted Radical IBBO	206
7.4	Chapter Summary	214
	APPENDICES	216

A	Mathematical Details	217
A.1	Details for BW Perturbation Section	217
A.1.1	Operator Perturbation Theory	217
A.1.2	Representations of Spin Operators	219
A.1.3	Properties of Pauli Matrices	219
A.1.4	Expansion of Operator Products	220
A.1.5	Commutation Relations in Spinor Form	220
B	Green Functions Review	221
B.1	Zero Temperature Correlation Functions	221
B.2	Two-Point Green Functions and Spectral Theory	223
B.3	Finite Temperature Formalism	228
C	Letters of Copyright Permission	230
	References	236

List of Tables

1.1	Properties of selected pyridine bridged radicals 1-19	15
1.2	Properties of selected mixed S/Se pyridine bridged radicals 1-21	16
1.3	Properties of selected mixed S/Se pyridine bridged radicals 1-22	17
1.4	Properties of selected all-Se pyridine bridged radicals 1-23	18
4.1	Symmetry classification of basis functions for describing the magnetic structure of 4-4 ($R_1 = \text{Et}$, $R_2 = \text{H}$)	101
4.2	Symmetry classification of basis functions for describing the magnetic structure of 4-3 ($R_1 = \text{Me}$, $R_2 = \text{Cl}$)	104
4.3	Representative slippage coordinates for the various crystallographic phases of pyridine-bridged radicals.	108
4.4	Magnetic exchange parameters for spin-ladder compounds 4-1 $R_2 = \text{F}$. . .	115
5.1	Symmetry classification of collinear basis functions for describing the magnetic structure of 5-1-5-4	122
5.2	Symmetry classification of noncollinear basis functions for describing the magnetic structure of 5-1-5-4	123
5.3	Single-site Hamiltonian parameters for 5-4 ($R_1 = \text{Et}$, $R_2 = \text{Cl}$)	125
5.4	Computed one-electron Hamiltonian parameters for 5-4 using the MOMO method	128

5.5	Hopping integrals computed by the MOMO method for 5-1–5-4	129
5.6	Computed one-electron Hamiltonian parameters for 5-4 using the MLWO method	131
7.1	Properties of selected oxobenzene bridged radicals 7-2	171
7.2	Symmetry classification of basis functions for describing the magnetic structure of FBBO (7-2 , R = F)	176
7.3	Tight-binding parameters for FBBO for maximally localized orbitals	180
7.4	Tight-binding parameters for FBBO obtained from a rotation of maximally localized orbitals	183
7.5	Ambient pressure magnetic exchange parameters for FBBO up to second order in hopping	184
7.6	Computed hopping integrals for NO ₂ BBO	204
7.7	Tight-binding parameters for IBBO	209

List of Figures

1.1	(a) Cartoon of the density of states $D_0(\epsilon)$ in the metallic Fermi liquid state FS>. (b) Comparison of mean-field energies of the metallic and Mott insulating state MI> as a function of Coulomb repulsion U . (c) Cartoon of the finite temperature phase diagram. MO = Magnetic Order, SC = Semiconducting, BM = Bad Metal. $\Delta_c \sim U - W$ is the charge gap. Such phases will be described in greater detail in Chapter 3.	6
1.2	Nodal properties of the π -type Singly Occupied Molecular Orbital (SOMO) of verdazyl and nitronyl-nitroxide radicals.	12
1.3	Nodal properties of the π -type SOMO of thiazyl radicals.	13
1.4	Electronic structure of (a) spiro-phenalenyl 1-30 and (b) ET ₂ dimer based materials in the absence of Coulomb repulsion.	21
1.5	Cartoon of the integrated one-electron spectral density for spiro-phenalenyl materials 1-30	23
2.1	Cartoon of the evolution of state energies for the generic Hamiltonian $\mathcal{H} = \mathcal{H}_0 + \lambda\mathcal{H}_1$	28
2.2	Electronic structure of (a) C ₆₀ ⁻ , (b) BBDTA ⁺ and (c) neutral BBDTA.	39
2.3	Evolution of the one-electron state energies as a function of crystal field splitting $\Delta\epsilon$ for single atom model.	43
2.4	Anatomy of the $ (+)\rangle$ state as a function of γ	44
2.5	Anatomy of the $ (R)\rangle$ state as a function of γ	45
2.6	MOMOs for 1-23 (R ₁ = Et, R ₂ = Cl) for a particular pair of radicals showing over localization of the $\alpha = +1, +2$ orbitals at site i	74

3.1	Schematic representation of the Dynamical Mean Field Approach.	82
3.2	Evolution of spectral density $A(\omega)$ and self-energy $\Sigma(\omega)$ as a function of U/W (horizontal axis) and temperature (vertical axis).	86
3.3	Schematic temperature dependence of the DC resistivity and frequency dependence of $\text{Re}\sigma(\omega)$ in the vicinity of the Mott transition.	87
4.1	Evolution of solution EPR spectrum of 4-1 ($R_1 = \text{Me}$, $R_2 = \text{OMe}$) showing percent conversion to the N -Me radical 4-6	92
4.2	Examples of slipped π -stacks.	94
4.3	A selection of magnetic properties of pyridine-bridged bis-dithiazolyl radicals 5-1 and Se analogues 5-2–5-4	95
4.4	Comparing the relative slippage of adjacent radicals in the same π -stack, viewed perpendicular to the molecular planes.	96
4.5	Positions of the symmetry elements in the unit cell of 4-4 ($R_1 = \text{Et}$, $R_2 = \text{H}$), as viewed down the π -stacking a -axis. The material orders as a spin-canted antiferromagnet. . . .	100
4.6	Positions of the symmetry elements in the unit cell of 4-3 ($R_1 = \text{Me}$, $R_2 = \text{Cl}$), as viewed down the π -stacking a -axis.	103
4.7	Variation of magnetic exchange interactions $\mathcal{J}_{ij}^{(\pi)}$ along the π -stacks as a function of slippage estimated by broken symmetry density functional theory calculations.	106
4.8	Variation of 1D dispersion energy $\Delta E_k = 4t_{ij}^{00,(\pi)}$ with slippage, calculated using Extend Huckel theory.	107
4.9	Unit cells of spin ladders 4-1 ($R_2 = \text{F}$) viewed parallel to the π -stacking axis.	112
4.10	Comparison of π -stack slippage of spin ladders 4-1 ($R_2 = \text{F}$), which occurs in both the molecular x - and y -directions consistent with strong antiferromagnetic interactions. . .	113
4.11	Definitions of unique magnetic interactions $\mathcal{J}_{(\pi)}$ and $\mathcal{J}_{(1)-(4)}$	114
4.12	Experimental magnetic susceptibility $\chi = M/H$ and inset χT for ladder compounds 4-1 ($R_1 = \text{Bu}$, Pn , Hx).	116

4.13	Evolution of EPR spectra of dilute solution of 4-1 ($R_1 = \text{Hx}$, $R_2 = \text{F}$) showing conversion to an asymmetric radical consistent with 4-8	117
5.1	Crystal structure of 5-4 . All four S/Se variants 5-1–5-4 are isostructural.	120
5.2	Relevant orbitals in three orbital model of the electronic structure of 5-1–5-4 . Plots were generated from B3LYP/6-311G(d,p) calculations on 5-4	124
5.3	MOMOs for 5-4 for interaction (2) showing over localization of the $\alpha = +1, +2$ orbitals at site i	126
5.4	(a) Band structure of 5-4 computed with PW-SCF as described in the text. (b) Cartoon of the electronic structure in the absence of correlation.	130
5.5	AC-susceptibility χ' as a function of pressure for (a) 5-5 and (b) 5-4	132
5.6	Pressure dependence of ferromagnetic ordering temperature and slippage coordinates for 5-4 and 5-5	133
5.7	Theoretical pressure dependence of magnetic exchange constants and hopping integrals for 5-4 (Cl).	134
5.8	(a) Resistivity data measured on pressed pellet samples of 5-4 . (b) Resistivity data measured on pressed pellet samples of 5-5 . (c) Putative phase diagram.	136
5.9	Evolution of momentum-resolved spectral density $A(\mathbf{k}, \omega)$ for 5-4 with pressure.	137
5.10	Comparison of the momentum-integrated spectral function at $k_B T = 0.1$ eV with correlation (i.e. density of states) obtained from IPT (<i>top</i>), and integration of $A(\alpha, \mathbf{k}, \omega)$ obtained from the DFT band structure and analytic continuation of the HF-QMC DMFT self-energy using Padé approximants.	138
5.11	Evolution of spectral density $A(\omega)$ predicted from IPT-DMFT calculations with decreasing temperature for 5-4	139
6.1	(a) Dependence of resonance frequency on magnitude of external field H_{ext} for 5-4 . (b) Angular dependence of the resonant field for 5-2 and 5-4 . (c) Temperature dependence of H_A for 5-2 and 5-4	147

6.2	Value of the spin-orbit weighting function defined in eq'n (6.23) as a function of energy window ϵ	150
6.3	(a) Highest occupied orbital (SOMO, $\alpha = 0$) at each radical site i for 5-4 . (b) Pseudo-orbital functions to describe SOC hopping parameters \mathbf{C}_{ij}	153
6.4	Orientations of the local \mathbf{C}_{ij}^{00} for 5-4 for interactions (π), (1), and (2), respectively.	154
6.5	Field dependence of $f_{res} = \omega_{res}/2\pi$ for 5-4 as a function of pressure for $\theta_H = 0^\circ$	156
6.6	Comparison of experimental and calculated values of H_A for 5-4 as a function of pressure, with contributions from interactions (1) and (2) indicated by the heights of the bars.	157
6.7	Powder AFMR derivative line shape for 5-3 at $T = 5$ K and a frequency of 329 GHz, along with semiclassical simulations for (b) easy-plane anisotropy, and (c) easy-axis anisotropy.	159
7.1	Frontier molecular orbitals of hybrid radicals 7-1 ($R_1 = \text{Me}$, $R_2 = \text{H}$, $R_3 = 2\text{-thiophene}$) showing π -character of orbitals in the energetic vicinity of the SOMO.	165
7.2	Selected properties of 7-1 ($R_1 = \text{Me}$, $R_2 = \text{H}$, $R_3 = \text{Ph}$) and 7-1 ($R_1 = \text{Me}$, $R_2 = \text{H}$, $R_3 = 2\text{-Th}$).	167
7.3	Cartoon representation of the electronic states obtained by either removal (left) or addition (right) of an electron to 7-1 $R_1 = \text{Me}$, $R_2 = \text{H}$, $R_3 = 2\text{-Th}$	169
7.4	Arrhenius plots of conductivity $\sigma = 1/\rho$ in order to compare the response of pyridine 4-1 ($R_1 = \text{Me}$, $R_2 = \text{Cl}$) and oxobenzene bridged 7-2 ($R = \text{F}$, Cl , H , Ph) radicals.	172
7.5	(a) Evolution of room temperature electrical conductivity of HBBO and FBBO under pressure. (b) Activation energy obtained from Arrhenius fits.	173
7.6	Crystal packing of FBBO.	174
7.7	(a) Field-Cooled (FC) and Zero-Field-Cooled (ZFC) susceptibility for FBBO. (b) The spontaneous magnetization.	175
7.8	Unique nearest neighbour magnetic interactions $\mathcal{J}_1 - \mathcal{J}_4$ for FBBO.	177
7.9	(a) Field-Cooled (FC) susceptibility of FBBO under pressure showing possible magnetic transition. (b) High pressure resistivity.	178

7.10	Cartoon representation of the states of the anion of FBBO. Comparison of calculated state energies allows estimation of various molecular parameters.	179
7.11	Computed DFT band structure of FBBO with Wannier interpolation are shown with solid lines, the colour of which indicated the contribution of MLWOs.	181
7.12	Comparison of the Maximally Localized Wannier Orbital (MLWO) basis, and rotated SOMO/LUMO basis orbitals from solid state calculations.	182
7.13	Possible magnetic structure of FBBO for pressures above 0.2 GPa.	186
7.14	(a) Ambient pressure single crystal optical conductivity of FBBO. (b) Optical conductivity under pressure. (c) Pressure dependence of the scattering rate.	189
7.15	Preliminary high pressure resistivity measurements on FBBO showing a region of metallic conductivity at 2.7 GPa and below 20 K.	191
7.16	Cartoon of the electronic structure of FBBO in the insulating and metallic states. . . .	192
7.17	Evolution of (a) quasiparticle weight, (b) orbital occupancy, and (c) double occupancy for FBBO as a function of U	195
7.18	Evolution of the integrated spectral weight (i.e. density of states) for FBBO with increasing correlation computed using HF-QMC DFT.	196
7.19	(a) Computed real part of the optical conductivity $\sigma_1(\omega)$ within the DMFT approximation for FBBO. (b) Extrapolated experimental optical conductivity based on KK-analysis of normal incidence reflectivity.	197
7.20	Frontier molecular orbitals relevant to the electronic structure of NO ₂ BBO obtained from DFT calculations at the B3LYP/6-31G(d,p) level.	200
7.21	Crystal structure of MeCN solvate of NO ₂ BBO	201
7.22	Electronic structure of NO ₂ BBO at the DFT level.	202
7.23	Site diagonal orbitals for NO ₂ BBO. The mixing of the SOMO and LUMO to produce $ \phi_i^+\rangle$ and $ \phi_i^-\rangle$ is reflective of the near degeneracy of the orbitals at this level of theory. .	203
7.24	(a) Polarized single crystal reflectivity of NO ₂ BBO at ambient pressure and room temperature. (b) Comparison of the optical conductivity $\sigma_1(\omega)$ obtained by Kramers-Kronig analysis for NO ₂ BBO and FBBO.	205

7.25	Ambient pressure magnetic susceptibility of NO ₂ BBO showing linear χT , i.e. a temperature independent susceptibility.	206
7.26	Crystal structure of EtCN solvate of IBBO showing definition of nearest neighbour interactions (π) and (1).	207
7.27	Magnetic data on IBBO. (a) Field cooled magnetic susceptibility as a function of temperature. (b) Magnetization as a function of field. (c) Spontaneous magnetization as a function of temperature.	208
7.28	SOMO ($\alpha = 0$), LUMO ($\alpha = +1$) and pseudo-orbital functions at each radical site i for IBBO computed at the B3LYP/6-311G(d,p) level.	212
7.29	Magnetic structure predicted for IBBO·EtCN, emphasizing canting of spins to produce a net moment along the c -direction.	213
7.30	dM/dH curves over one hysteresis loop for IBBO showing evidence for a spin-flop transition near 2.1 Tesla.	214

List of Symbols and Abbreviations

α, β	Orbital indices
χ	Magnetic susceptibility
ΔH_{disp}	Disproportionation Enthalpy
Δ_c	Charge gap
ϵ	Single particle energy
ϵ_F	Fermi energy
γ	Gyromagnetic ratio
\hbar	Plank's constant
λ	(Atomic) spin-orbit constant
\mathbb{P}	Projection operator
\mathbb{D}	Zero-field splitting tensor
η	Order paramater
$\mathbf{\Gamma}$	Pseudo-dipolar anisotropic exchange tensor
\mathbf{C}	Orbital basis matrix
\mathbf{C}	Spin-orbit mediated hopping paramater

c^\dagger, c	Electron creation and annihilation operators
D	Dzyaloshinskii-Moriya anisotropic exchange (pseudo)vector
E	Kohn-Sham orbital energy matrix
F	Kohn-Sham-Fock matrix
f	Ferromagnetic basis function for symmetry classification
L	Angular momentum operator
l	Antiferromagnetic basis function for symmetry classification
M	Magnetization (typically of the entire sample)
m	Magnetization (typically of a single site)
n	Magnetic basis function for symmetry classification
r	Particle position
S	Overlap matrix
S	Spin operator
U	Unitary transformation matrix
H	Magnetic field
H_c	Coercive magnetic field
k	Wavevector
\mathcal{G}	Green operator
\mathcal{J}	Magnetic exchange parameter
\mathcal{K}	Hund's coupling operator

\mathcal{L}	Effective molecular orbital angular momentum operator
\mathcal{Q}	Hund's coupling operator
\mathcal{T}	Kinetic energy operator
\mathcal{U}	(On-site) coulomb repulsion operator
\mathcal{P}	Spin-orbit coupling weighting function
μ_B	Bohr magneton
Ω	Orbital spread function (for constructing MLWOs)
Φ	Many particle state
ϕ	Singe particle state
ρ	Electrical resistivity
Σ	Self-energy
σ_μ	Pauli matrix, for $\mu = \{x, y, z\}$
σ	Electrical conductivity
τ	Imaginary time = it
Θ	Weiss constant
$\tilde{\mathbf{S}}$	pseudospin operator
A	Single particle spectral function
$a^\dagger, a, b^\dagger, b$	Bosonic creation and annihilation operators
C	Curie constant
c	Speed of light

D_0	One electron density of states
E	Energy
E_A	Thermal activation energy
E_{cell}	Electrochemical cell potential
EA	Electron affinity
F	Free energy density
G	Impurity Green function (DMFT)
H	Magnetic field magnitude
H_A	Anisotropy field
i, j	Site label (typically)
$i\omega_n$	Matsubara frequency
IP	Ionization potential
K	(Magnetic) anisotropic constant
k	Boltzmann constant
m	Magnetic quantum number
m	Mass
p -NPNN	para-nitrophenyl nitronyl nitroxide radical
Q, K	Hund's rule coupling
T	Temperature
t	Hopping integral

T_C Curie temperature (ferromagnetic ordering temperature)

T_N Néel temperature (antiferromagnetic ordering temperature)

U, V On-site Coulomb repulsion

W One electron bandwidth

Z Atomic number

1D One-dimensional

2-Th 2-Thiophene, -C₄H₃S

4-Pyr 4-Pyridine, -C₅H₄N

AC Alternating current; finite frequency measurement

AFM Antiferromagnet(ic)

AFMR Antiferromagnetic resonance

AI Anderson Insulator

ALPS Algorithms and Libraries for Physics Simulations (quantum simulation package)

B3LYP DFT function combining 3 parameter Becke exchange with correlation functional of Lee Yang and Parr

BM Bad metal

BS-DFT Broken symmetry density functional theory

BSS Broken-symmetry singlet (state)

Bu Butyl, -CH₂CH₂CH₃

CSS Closed shell singlet (state)

DDCI Difference dedicated configuration interaction method

DDPH 2,2-diphenyl-1-picrylhydrazyl radical

DFT Density functional theory

DM Dzyaloshinskii-Moriya

DMFT Dynamical mean field theory

EPR Electron paramagnetic resonance

ESR Electron spin resonance

Et Ethyl, $-\text{CH}_2\text{CH}_3$

ET, BEDT-TTF Bis(ethylenedithio)tetrathiafulvalene

FC Field cooled (magnetic susceptibility)

FM Ferromagnet(ic)

FMR Ferromagnetic resonance

FS Fermi sea

HOMO Highest (fully) occupied molecular orbital

Hx Hexyl, $-\text{CH}_2\text{CH}_2\text{CH}_2\text{CH}_2\text{CH}_3$

J-W Jordan-Wigner

LHB Lower Hubbard band

LIESST Light Induced Excited State Trapping

LUMO Lowest unoccupied molecular orbital

MaxEnt Maximum Entropy method (for analytic continuation)

MCT Mercury cadmium telluride

Me Methyl, $-\text{CH}_3$

MI Mott insulator

MLWO Maximally localized Wannier orbital)

MOMO Maximally overlapping Wannier orbital

NHMFL National High Magnetic Field Laboratory

NMR Nuclear Magnetic Resonance

OMFc Octamethylferrocene

ORCA Quantum chemistry program.

OTf Triflate, trifluoromethanesulfonate

PBE PerdewBurkeErnzerhof exchange correlation functional

Ph Phenyl, $-\text{C}_6\text{H}_5$

PM Paramagnet(ic)

Pn Pentyl, $-\text{CH}_2\text{CH}_2\text{CH}_2\text{CH}_3$

PW-SCF Plane Wave Self Consistent Field = Quantum Espresso (ab-initio program)

QMC Quantum Monte Carlo

R, R_n Variable chemical position

SC-AFM Spin-canted antiferromagnet(ic)

SCF Self-consistent field

SG Spin glass

SO Spin-Orbit

SOC Spin-Orbit Coupling

SOI Spin-Orbit Interactions

SOMO Singly occupied molecular orbital

SORCI Spectroscopy oriented configuration interaction method

SQUID Superconducting Quantum Interference Device

SS Singlet state

TCNQ 7,7,8,8-Tetracyanoquinodimethane

TDAE Tetra-kis-diethylaminoethylene

TEMPO (2,2,6,6-tetramethylpiperidin-1-yl)oxidanyl radical

TLL Tomonaga-Luttinger liquid

TMTSF Tetramethyltetraselenafulvalene

TMTTF Tetramethyltetrathiafulvalene

TS Triplet state

TTF Tetrathiafulvalene

UHB Upper Hubbard band

Vac Vacuum (state)

ZFC Zero Field cooled (magnetic susceptibility)

ZFS Zero-field splitting

p-CDTV 3-(4-chlorophenyl)-1,5-dimethyl-6-thioxoverdazyl radical

Chapter 1

Introduction

1.1 Radicals as Strongly Correlated Materials

The notion that radicals, molecules with unpaired electrons, could display electronic or magnetic properties associated with metallic elements was first advanced in 1911 when McCoy and Moore¹ wrote:

“If the electron theory of the metallic state is as fundamental as it seems to be, there would be little reason to doubt that an aggregate of free radicals would be a body having metallic properties; for such a hypothetical body would be made up of radicals which, analogous to metallic atoms, could easily lose electrons.”

The realization of the envisioned aggregates displaying metallic conduction is faced with two main challenges. The first is that typical radical species are highly reactive and short lived owing to the significant energetic drive to couple the unpaired electrons in covalent bonds.² This fact implies that radicals will tend to be unstable, either to reactions with other species in the environment, or with each other to form covalently bonded dimers. The achievement of stable *free* radicals therefore requires special synthetic strategies. The historical development of such strategies is briefly reviewed in the second section of this chapter. The second challenge for the development of metallic radicals is to design species

that can “*easily lose electrons*”, that is, radicals for which the electrons are sufficiently mobile in the solid state to allow for conduction over large distances. From a chemical perspective, this condition is satisfied when there is i) a large electronic communication between orbitals hosting the unpaired electrons on adjacent radicals, as well as ii) various accessible oxidation states in a narrow energy window, so that the energetic cost of transferring electrons between radicals is low. These ideas were originally given a physical basis particularly through the seminal work of Mott³⁻⁶ and Hubbard,⁷⁻¹⁰ who noted that the competition between the kinetic energy and potential Coulomb repulsion of the unpaired electrons would give rise to various electronic states. The kinetic energy is minimized by delocalization of electrons across many (radical) sites, while the Coulomb interaction is minimized by localization of electrons to their parent sites in order maximize the distance between any two electrons. In the naive model of one orbital and one electron per site, the energy barrier for electron motion can be approximated by the local Coulomb repulsion U between electrons forced to occupy the same (radical) site. This is, essentially, the disproportionation enthalpy:

$$U \sim \Delta H_{\text{disp}} = E(+)+E(-)-2E(\cdot) \quad (1.1)$$

where $E(+)$, $E(-)$, and $E(\cdot)$ are the energies of the +1, -1, and neutral oxidation states of the radical. If this Coulomb term significantly exceeds the kinetic energy, parameterized by the solid state one-electron bandwidth $U \gg W$, then a Mott-Hubbard insulating state is expected. In such a state, residual interactions between localized unpaired electrons results in the broad range of magnetic properties. In the case where $W \gg U$, a metallic state should instead prevail, in which the magnetic response is largely quenched, and electrons are instead freely conducting. Of particular physical interest are materials at the border of these two regimes, in the vicinity of the metal to insulator transition $U \sim W$, which has been shown to play host to various exotic phenomena including superconductivity, and still evades a complete physical description. Due to significant synthetic progress in recent years, this strongly-correlated border region is beginning to be accessible by current generations of neutral radical materials especially through the application of physical pressure. It is for this reason that understanding the properties of such materials, as well as the design of future synthetic targets, requires insights from both experiment and theory. The most recent developments by the Oakley group in the design of radical materials has focussed on

the role of multiple orbitals in determining the magnetic and electronic properties, either when such orbitals are all in close proximity to the Fermi level, or through spin-orbit coupling. This thesis will seek to discuss these advances.

1.2 Introduction to the Hubbard Model

1.2.1 Definitions

The origin of the Hubbard model is attributed to a series of papers by Hubbard appearing from 1963 to 1965,⁷⁻¹⁰ although similar models were studied by Gutzwiller¹¹ and Kanamori¹² around the same time. Since that time, the model has become ubiquitous in solid state physics, and has been reviewed extensively.¹³⁻¹⁶ The early work focussed on the properties of a single electronic band with narrow bandwidth comparable to the strength of electron-electron repulsion. The model may be easily extended to include multiple orbitals, as is required for discussion of organic radical materials. The generic Hamiltonian of a solid is given by:

$$\mathcal{H} = \mathcal{F} + \mathcal{V} \quad (1.2)$$

$$\mathcal{F} = \sum_{i,j} \sum_{\alpha,\beta} f_{ij}^{\alpha\beta} \mathbf{c}_{i,\alpha}^\dagger \mathbf{c}_{j,\beta} \quad (1.3)$$

$$\mathcal{V} = \frac{1}{2} \sum_{i,j,k,l} \sum_{\alpha,\beta,\gamma,\delta} W_{ijkl}^{\alpha\beta\gamma\delta} \mathbf{c}_{i,\alpha}^\dagger \mathbf{c}_{j,\beta}^\dagger \mathbf{c}_{k,\gamma} \mathbf{c}_{l,\delta} \quad (1.4)$$

where $c_{i,\alpha,s}^\dagger$ creates an electron at site i , in the orbital labelled α , and with spin s . For convenience of notation, we will often write these local creation and annihilation operators in vector (spinor) form:

$$\mathbf{c}_{i,\alpha}^\dagger = \begin{pmatrix} c_{i,\alpha,\uparrow}^\dagger & c_{i,\alpha,\downarrow}^\dagger \end{pmatrix}, \quad \mathbf{c}_{i,\alpha} = \begin{pmatrix} c_{i,\alpha,\uparrow} \\ c_{i,\alpha,\downarrow} \end{pmatrix} \quad (1.5)$$

so that summations over spin indices become matrix operations:

$$\mathbf{c}_{i,\alpha}^\dagger \mathbf{c}_{j,\beta} = \sum_s c_{i,\alpha,s}^\dagger c_{j,\beta,s} \quad (1.6)$$

The parameters of the Hamiltonian are given by the integrals:

$$f_{ij}^{\alpha\beta} = \int_{\mathbf{x}} \phi_i^{\alpha}(\mathbf{x})^* \left[-\frac{\hbar^2}{2m} \nabla_{\mathbf{x}}^2 + u(\mathbf{x}) \right] \phi_j^{\beta}(\mathbf{x}) \quad (1.7)$$

$$W_{ijkl}^{\alpha\beta\gamma\delta} = \int_{\mathbf{x}} \int_{\mathbf{x}'} v(\mathbf{x} - \mathbf{x}') \phi_i^{\alpha}(\mathbf{x})^* \phi_j^{\beta}(\mathbf{x}')^* \phi_k^{\gamma}(\mathbf{x}') \phi_l^{\delta}(\mathbf{x}) \quad (1.8)$$

In order to simplify these expressions, Hubbard suggested some practical approximations for $f_{ij}^{\alpha\beta}$ and $W_{ijkl}^{\alpha\beta\gamma\delta}$. He noted that the magnitude of the Fock integrals falls off rapidly with distance between sites, and may be ignored in all cases where sites are farther than nearest neighbours. This approximation is particularly valid for radical crystals, due to the relatively large volume of each molecular site. In this “tight-binding” approximation:

$$f_{ij}^{\alpha\beta} = \begin{cases} \epsilon_i^{\alpha} & i = j, \alpha = \beta \\ t_{ij}^{\alpha\beta} & i, j \text{ are nearest neighbours} \\ 0 & \text{otherwise} \end{cases} \quad (1.9)$$

where ϵ_i^{α} is the energy of the α orbital at site i , and $t_{ij}^{\alpha\beta}$ is the “tunnelling”, “transfer” or “hopping” integral between orbitals α at site i and β at site j . Hubbard also suggested that the two-electron integrals may be similarly truncated to on-site terms due to near complete screening of the long-range Coulomb interaction. The two-electron integrals are thus approximated:

$$W_{ijkl}^{\alpha\beta\gamma\delta} = \begin{cases} U_i^{\alpha\beta} & i = j = k = l \text{ and } \alpha = \delta, \beta = \gamma \\ Q_i^{\alpha\beta} & i = j = k = l \text{ and } \alpha = \gamma, \beta = \delta \\ K_{ij}^{\alpha\beta} & i = k, j = l, \alpha = \gamma, \beta = \delta \text{ and } i, j \text{ are nearest neighbours} \\ 0 & \text{otherwise} \end{cases} \quad (1.10)$$

Here $U_i^{\alpha\beta}$ is the on-site Coulomb repulsion, $Q_i^{\alpha\beta}$ is the on-site ferromagnetic exchange, and $K_{ij}^{\alpha\beta}$ is the nearest neighbour ferromagnetic exchange. For historical reasons, the ferromagnetic exchange terms are often called Hund’s rule coupling terms, as the $Q_i^{\alpha\beta}$ term is the origin of the Hund’s rule of maximum multiplicity. With these approximations,

the full Hamiltonian is:

$$\begin{aligned}
\mathcal{H}_{EH} = & \sum_{i,\alpha} \epsilon_i^\alpha \mathbf{c}_{i,\alpha}^\dagger \mathbf{c}_{i,\alpha} + \sum_{\substack{\langle i,j \rangle \\ \alpha,\beta}} t_{ij}^{\alpha\beta} \mathbf{c}_{i,\alpha}^\dagger \mathbf{c}_{j,\beta} + \sum_{\substack{i,s,s' \\ \alpha,\beta}} U_i^{\alpha\beta} n_{i,s}^\alpha n_{i,s'}^\beta \\
& + \sum_{i,\alpha \neq \beta} Q_i^{\alpha\beta} \mathbf{c}_{i,\alpha}^\dagger \mathbf{c}_{i,\beta}^\dagger \mathbf{c}_{i,\alpha} \mathbf{c}_{i,\beta} + \sum_{\substack{\langle i,j \rangle \\ \alpha,\beta}} K_{ij}^{\alpha\beta} \mathbf{c}_{i,\alpha}^\dagger \mathbf{c}_{j,\beta}^\dagger \mathbf{c}_{i,\alpha} \mathbf{c}_{j,\beta}
\end{aligned} \tag{1.11}$$

where the notation $\langle i, j \rangle$ denotes a sum over nearest neighbours. The competition between the non-commuting Coulomb and kinetic terms is responsible for the electronic and magnetic phases that emerge in different parameter regimes of the Hubbard model. Such phases may be anticipated on the basis of a mean-field decoupling of the interaction terms, as discussed in the next section.

1.2.2 Phases of the Hubbard Model

In the absence of Coulomb terms ($U, Q, K = 0$), the Hamiltonian may be diagonalized in terms of the Bloch states:

$$\phi_{\mathbf{k}}^\beta(\mathbf{x}) = \sum_{i,\alpha} b_{\mathbf{k}}^{\alpha,\beta} \phi_i^\alpha(\mathbf{x}) e^{i\mathbf{k}\cdot\mathbf{r}_i} \tag{1.12}$$

$$\mathbf{c}_{\mathbf{k},\beta}^\dagger = \sum_{i,\alpha} b_{\mathbf{k}}^{\alpha,\beta} \mathbf{c}_{i,\alpha}^\dagger e^{i\mathbf{k}\cdot\mathbf{r}_i} \tag{1.13}$$

$$\mathcal{H}|_{U,Q,K=0} = \sum_{\mathbf{k},\beta} \epsilon_{\mathbf{k}}^\beta \mathbf{c}_{\mathbf{k},\beta}^\dagger \mathbf{c}_{\mathbf{k},\beta} \tag{1.14}$$

where \mathbf{k} is the crystal momentum, and the coefficients $b_{\mathbf{k}}^{\alpha\beta}$ describe the possible \mathbf{k} -dependent mixing of local orbital functions to form the solid state energy bands. The energy of a particular Bloch state is given by $\epsilon_{\mathbf{k}}^\beta$. The ground state ‘‘Fermi sea’’ $|\text{FS}\rangle$ is obtained by filling all such one-electron Bloch states up to the Fermi energy ϵ_F :

$$|\text{FS}\rangle = \prod_{\epsilon_{\mathbf{k}}^\beta < \epsilon_F} \left(c_{\mathbf{k},\beta,\uparrow}^\dagger c_{\mathbf{k},\beta,\downarrow}^\dagger \right) |\text{Vac}\rangle \tag{1.15}$$

where $|\text{Vac}\rangle$ represents the vacuum state, containing no electrons. Provided ϵ_F lies within

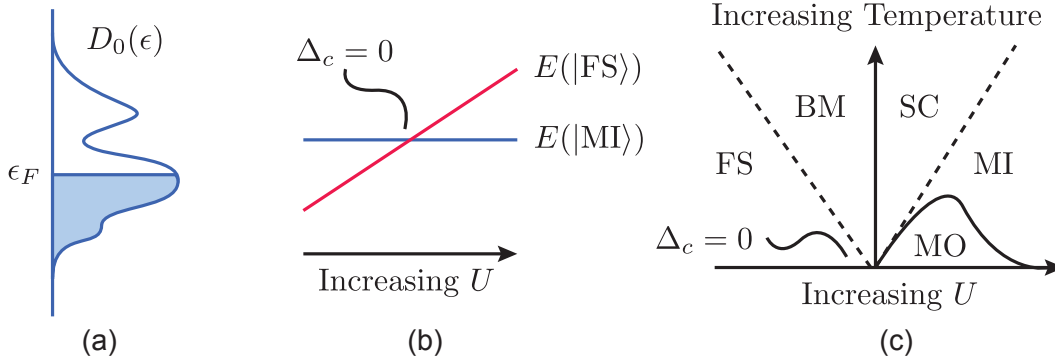


Figure 1.1: (a) Cartoon of the density of states $D_0(\epsilon)$ in the metallic Fermi liquid state $|FS\rangle$. (b) Comparison of mean-field energies of the metallic and Mott insulating state $|MI\rangle$ as a function of Coulomb repulsion U . (c) Cartoon of the finite temperature phase diagram. MO = Magnetic Order, SC = Semi-conducting, BM = Bad Metal. $\Delta_c \sim U - W$ is the charge gap. Such phases will be described in greater detail in Chapter 3.

an energy band, this state is a conventional metal, whose high electrical conductivity arises due to the fact that an infinitesimally small electric field is required to shift the occupancy of Bloch states to produce a net current. However, $|FS\rangle$ is severely penalized at finite U , due to the fact that it contains component states of nonuniform electron density, e.g. where a surplus of electrons occupy the same local site. The opposite limit where hopping t is set to zero describes the case of isolated molecules with uniform electron density whose Mott insulating ground state $|MI\rangle$ is described best in terms of the localized $\phi_i^\alpha(\mathbf{x})$ orbitals. Such a state can be written:

$$|MI\rangle = \prod_{i,\{\sigma\}} c_{i,0,\sigma}^\dagger \prod_{i,\alpha<0} \left(c_{i,\alpha,\uparrow}^\dagger c_{i,\alpha,\downarrow}^\dagger \right) |\text{Vac}\rangle \quad (1.16)$$

for a particular arrangement of unpaired spins, given by $\{\sigma\}$. Consider the case in which the SOMO band ($\alpha = 0$) is energetically isolated from the remaining bands, and is half-filled, having one electron on average per site. In this case, the energy of the Mott insulator is independent of the hopping t_{ij}^{00} and Coulomb repulsion U_i^{00} ; ignoring the Coulomb exchange

terms, the energy of the above states can be approximated:

$$E(|\text{MI}\rangle) \sim \text{const.} + \sum_i^N \epsilon_i^0 \quad (1.17)$$

$$E(|\text{FS}\rangle) \sim \text{const.} + \sum_{\mathbf{k}} \epsilon_{\mathbf{k}}^0 \mathbf{c}_{\mathbf{k},0}^\dagger \mathbf{c}_{\mathbf{k},0} + U_i^{00} \sum_{\mathbf{k},\mathbf{k}'} \langle n_{\mathbf{k},0,\uparrow} \rangle \langle n_{\mathbf{k}',0,\downarrow} \rangle \quad (1.18)$$

$$= \text{const.} + \frac{N}{4} U_i^{00} + \int_{-\infty}^{\epsilon_F} \epsilon D_0(\epsilon) d\epsilon \quad (1.19)$$

where the constant terms reflecting the contribution to the energy by all electrons in other bands or orbitals. The density of states of the SOMO band is given by $D_0(\epsilon)$. Here, we have taken advantage of the fact that $\sum_{\mathbf{k}} \langle n_{\mathbf{k},0,\sigma} \rangle = 1/2$ for the half-filled band assuming no net spin-polarization. On the basis of this discussion, we define the single electron charge gap as:

$$\Delta_c \equiv U_i^{00} - \frac{4}{N} \int_{-\infty}^{\epsilon_F} (\epsilon_i^0 - \epsilon) D_0(\epsilon) d\epsilon \sim U - W \quad (1.20)$$

where the final integral representing the reduction in kinetic energy through delocalization of the electron into Bloch states is of the order of the width of the isolated SOMO band W , but not precisely equal. For example, in the one-dimensional case, $\epsilon_k^0 = \epsilon_i^0 - 2t_{ij}^{00} \cos(ka)$, $\epsilon_F = \epsilon_i^0$, $W = 4t_{ij}^{00}$, and $\Delta_c = U - (4/\pi)W$. It is easy to see that a Mott insulating state will tend to prevail for cases where $\Delta_c > 0$, while a Fermi liquid metal will be preferred for $\Delta_c < 0$, offering a rough estimate of the location of the Mott transition (Fig 1.1(b)). It is worth noting, however, that the crossover between the metallic and insulating states is only expected to be sharp at low temperature. At high temperature, a smooth crossover is typically observed between semiconducting-like states¹ at $U > W$ for which the electrical resistivity ρ obeys $d\rho/dT < 0$ and bad metal states at $U < W$ for which $d\rho/dT > 0$ (Fig 1.1(c)).¹⁷⁻¹⁹ The properties of such states will be discussed further in chapter 3 with

¹Semiconducting-like states refer to those with sufficiently small thermal activation energies that a significant carrier density and thus conductivity is possible at reasonable temperatures. Conductivity is expected to be activated $\sigma \sim e^{-E_A/kT}$ with small activation energy E_A due to correlation effects, although this specific temperature dependence is not strictly required. Such states should be contrasted with conventional semiconductors where the the activation energy corresponds to a band gap of kinetic origin, and is not correlation induced.

reference to the Dynamical Mean Field approach to treat strong correlations in the solid state. There are three general strategies employed for the development of organic materials capable of accessing the metallic state:

1. The design of molecular building blocks to have low on-site Coulomb repulsion U , and favourable crystal packing to allow for large hopping integrals t_{ij} and therefore bandwidth W . This approach, applied to neutral radicals, has been pursued strongly by the Oakley group.
2. Altering the filling of the SOMO band typically through doping by cocrystallization of different organic or inorganic components. It is easy to see from the above that reduction of $\sum_{\mathbf{k}} \langle n_{\mathbf{k},0,\sigma} \rangle$ rapidly suppresses the effects of Coulomb repulsion. For example, in the case of a quarter-filled band, with one electron on average per two sites, the charge gap as defined above would be reduced to $\Delta_c \sim U/4 - W$, clearly favouring a metallic state. In fact, this naive approach greatly underestimates the stability of the metallic state as the doped holes are almost immediately mobile, as evidenced by several orders of magnitude changes in conductivity with very little hole doping.^{20,21} This approach has been used with great success in the so-called radical-ion and charge transfer salts.
3. Designing molecular radicals with multiple orbitals in close proximity to the Fermi energy. This design tends to enhance $\int_{-\infty}^{\epsilon_F} (\epsilon_i^0 - \epsilon) D_0(\epsilon) d\epsilon$ by pushing filled Bloch states down in energy through band hybridization, as well as reduce the average Coulomb repulsion between electrons at a given site. The latter result follows from the fact that the Coulomb repulsion between electrons in different orbitals $U_i^{\alpha\beta}$ will tend to be lower than that in the same orbital $U_i^{\alpha\alpha}$, and that local orbitals may always hybridize to minimize the repulsion. As will be discussed below, this effect is critical to the properties of certain classes of radical-ion salts. It's understanding and exploitation of multi-orbital effects in neutral radical materials represents a major topic of this thesis.

As a final point, we note that at the level of approximation described above, the energy of the Mott insulator was assumed to be independent of spin configuration, which does not

generally hold in the presence of finite K_{ij} or t_{ij} . These terms give rise to residual magnetic interactions that will be discussed in great detail in chapter 2, particularly in multi-orbital models with inclusion of relativistic spin-orbit coupling. In organic materials based on light atoms, the magnetic interactions are predominantly isotropic, being described in terms of the Heisenberg Hamiltonian:

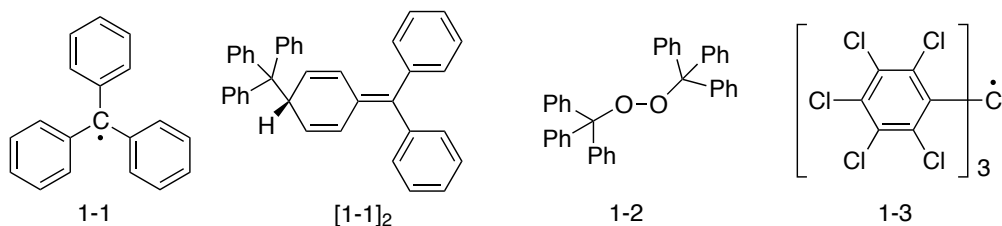
$$\mathcal{H}_{\text{spin}} = - \sum_{\langle i,j \rangle} \mathcal{J}_{ij} \mathbf{S}_i \cdot \mathbf{S}_j \quad , \quad \mathcal{J}_{ij} \sim \mathcal{O}(K, t^2/U) \quad (1.21)$$

The scale of \mathcal{J} is indicative of the strength of electronic communication between radicals in the insulating state, with strong interactions $\mathcal{J}/k_B \sim 10^2 - 10^3$ K suggesting proximity to the Mott transition. Exploration of the resultant magnetic properties represents a major theme in this thesis.

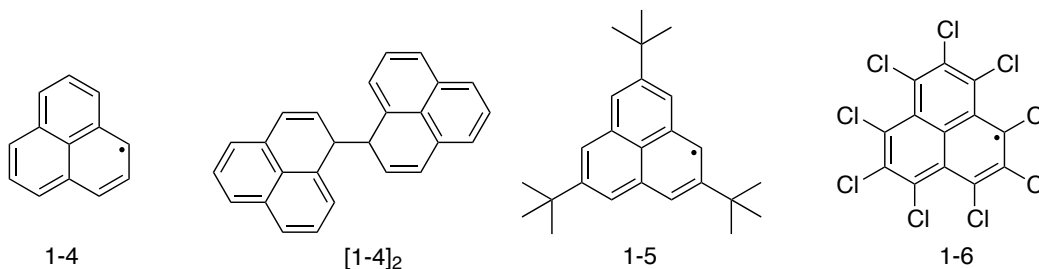
1.3 Historical Perspective on Radical Design

1.3.1 Carbon-Centered Radicals

The first radicals to be isolated were stabilized largely by virtue of bulky groups sterically blocking reaction at spin-bearing sites. A classic example is Gomberg's triphenylmethyl radical **1-1**, reported in 1900.²² However, despite protection of the central carbon centre, an equilibrium exists in solution between the radical and its sigma-bonded dimer **[1-1]₂** formed by covalent bonding through the spin-bearing para position of one phenyl ring.²³ Moreover, exposure to oxygen results in rapid oxidation to form the peroxide **1-2**. Further protection, through perchlorination of the phenyl rings to afford **1-3**, is necessary to produce a stable species that is monomeric in both the solid state, and in solution.^{24,25}



The most significant disadvantage to the use of steric protection to stabilize radical materials in the solid state is that *all* electronic communication between adjacent radicals is compromised by such bulky groups. Not only is dimerization avoided, but also all magnetic interactions and solid state bandwidth is quenched producing trivial paramagnetic insulators. A complementary strategy for avoiding dimerization without steric protection involves delocalization of the unpaired electron across many sites in the molecule, which reduces the energy of any local covalent bonding mode. In carbon-based radicals, a well-studied example of such a delocalized radical is the phenylenyl **1-4**, although this radical also forms σ -bonded dimers $[\mathbf{1-4}]_2$.²⁶ Steric protection through addition of bulky *t*-butyl groups at the β -carbon position prevents σ -dimerization in **1-5**, but such radicals associate instead via multicenter π -interactions in the solid state.²⁷ Perchlorination of the phenylenyl rings is again required in order to produce stable, monomeric species **1-6**.²⁸

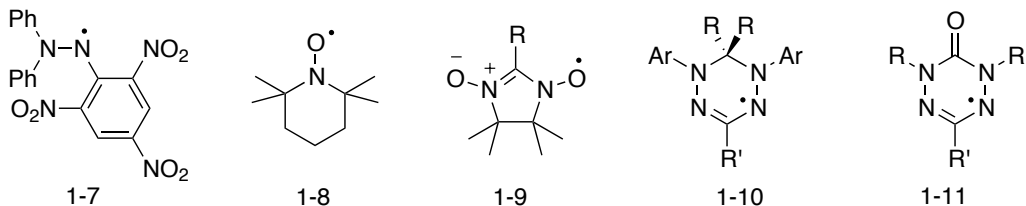


The propensity for dimerization through σ -bond formation in carbon centred radicals can be anticipated on the basis of the strong C-C single bond, which has a bond dissociation energy of ~ 370 kJ/mol compared with 150 – 250 kJ/mol for O-O and N-N single bonds.²⁹ The instability of the latter bonds may be attributed to repulsion between stereochemically active lone pairs on the atomic centres: what Coulson called the “alpha-effect”.³⁰ This effect may be exploited to achieve stable π -radicals in the absence of steric protection by ensuring that spin-bearing sites are predominantly heteroatoms.

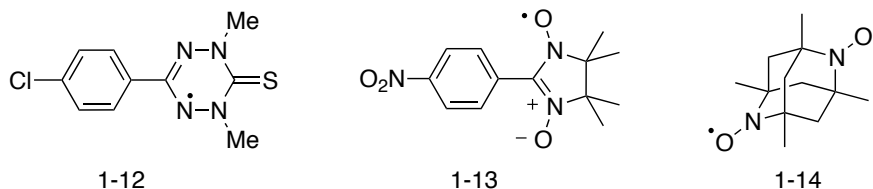
1.3.2 Light Heteroatom Radicals

Over the years, many varieties of oxygen and nitrogen centred radicals have been studied, with various properties and chemical stabilities. Particularly notable examples include the

very stable hydroxyl radical DPPH **1-7** and nitroxide radical TEMPO **1-8**, both of which have seen applications in EPR (electron paramagnetic resonance) spectroscopy, and radical polymerization reactions.²



In both cases, stability arises through both steric protection and heteroatom radical centres due to the alpha effect.³¹ The need for steric protection may be partially alleviated by delocalization of the unpaired electron across multiple heteroatoms as in the nitronyl-nitroxide **1-9**, verdazyl **1-10**, and oxoverdazyl **1-11** type radicals. These classes are sufficiently unhindered to allow communication between unpaired spins in the solid state giving rise to weak magnetic interactions. For example, the magnetic response of the thioverdazyl *p*-CDTV **1-12** has been interpreted in terms of a one dimensional (1D) ferromagnetic chain with interchain $\mathcal{J}/k_B = 12$ K and intrachain $z\mathcal{J}'/k_B = 0.4$ K,² where z denotes the number of nearest neighbours.³² The weakness of the intrachain interactions ultimately suppresses magnetic order, although evidence suggest bulk ferromagnetic order below 0.68 K.³³ A ferromagnetic ordering temperature of similar magnitude ($T_C = 0.6$ K) is also seen for the β -phase of the *p*-nitrophenyl substituted nitronyl nitroxide *p*-NPNN **1-13** the report of which in 1991 represented the first ordered purely organic ferromagnet.^{34,35} The γ -phase of the same material displays antiferromagnetic order at $T_N = 0.65$ K.³⁶ Shortly after the report of such materials, Chiarelli showed ferromagnetic order at $T_C = 1.48$ K in the adamantane biradical **1-14**.³⁷ Since then, the magnetic response of many nitroxyl^{38,39} and verdazyl⁴⁰ radicals has been studied.



²with reference to the Hamiltonian $\mathcal{H}_{ij} = -\mathcal{J}_{ij} \mathbf{S}_i \cdot \mathbf{S}_j$

The most significant limitation of the above N,O-based radicals is that the combination of bulky nonmagnetic R -groups and the small spatial extent of the singly occupied molecular orbital (SOMO, Fig. 1.2) results in weak, low-dimensional interactions in the solid state. These materials are thus strongly one-dimensional Mott insulators, with magnetic ordering temperatures ~ 1 K determined essentially by weak interchain interactions.

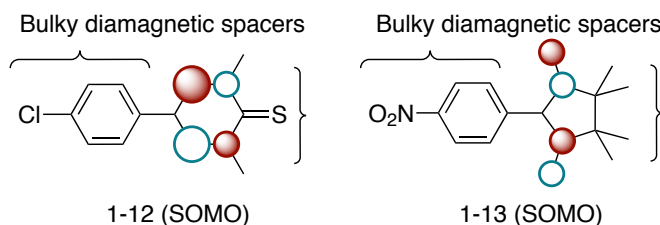
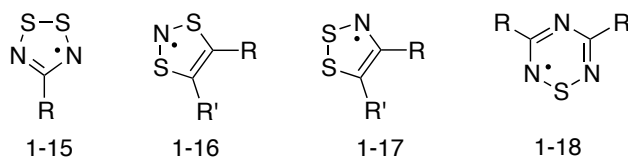


Figure 1.2: Nodal properties of the π -type Singly Occupied Molecular Orbital (SOMO) of verdazyl and nitronyl-nitroxide radicals. The SOMO density is largely confined to one part of the molecule, with strong interactions in the solid state being mitigated by the presence of bulky groups.

1.3.3 Heavy Heteroatom Radicals

Interactions may be enhanced by further reduction of steric bulk, and incorporation of heavier elements into the radical framework, in order to take advantage of more diffuse $3p$ or $4p$ orbitals.⁴¹ These conditions may be satisfied, in principle, in the several known classes of stable thiazyl (S-N) and related selenazyl (Se-N) radicals based on the 1,2,3,5-dithiadiazolyl⁴²⁻⁴⁸ **1-15**, 1,3,2-dithiazolyl⁴⁹⁻⁵³ **1-16**, 1,2,3-dithiazolyl⁵⁴⁻⁵⁷ **1-17**, and 1,2,4,6-thiatriazinyl⁵⁸⁻⁶⁰ **1-18** frameworks.



The SOMO of such radicals is largely exposed, having significant density along the outer periphery of the molecule, which allows for strong intermolecular interactions (Fig. 1.3). As a consequence, however, such thiazyl (and related selenazyl) radicals tend to dimerize

both in solution and in the solid state, through a variety of π -dimerization modes.⁶¹ In the solid state, this dimerization quenches the unpaired spins and results in the opening of a large one-electron energy gap at the Fermi level, analogous to the well-known phenomenon of Peierls distortions or charge-density waves. Such dimers are thus diamagnetic insulators even in the absence of correlation effects. As a result, dimerization was historically considered to be undesirable. However, in some cases, the coupling is sufficiently weak to allow the dimers to be ruptured in the solid by heating, resulting in magnetostructural phase transitions between the $S = 0$ dimer and $S = \frac{1}{2}$ radical forms.⁶²⁻⁶⁴

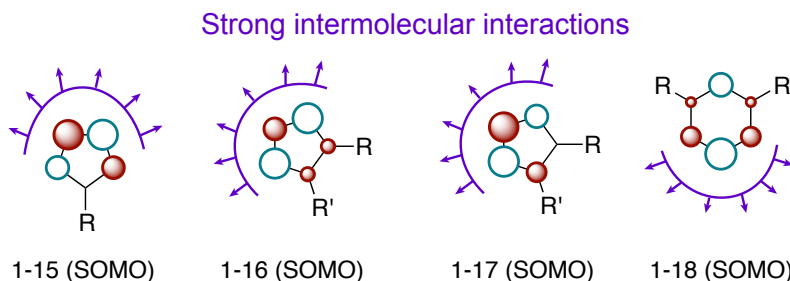
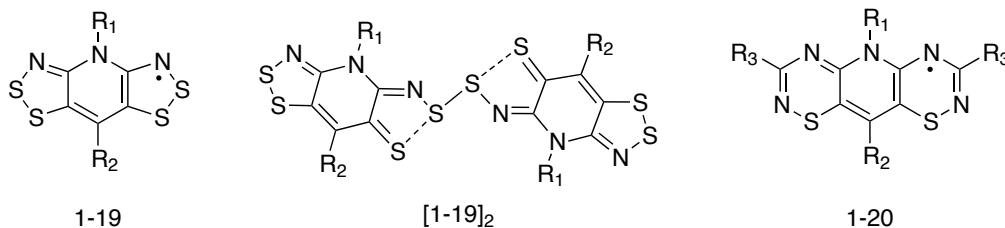


Figure 1.3: Nodal properties of the π -type SOMO of thiazyl radicals. The SOMO density is largely located around the periphery of the molecule, allowing strong solid state intermolecular interactions in the directions indicated.

In order to suppress dimerization, the Oakley group developed the resonance delocalized pyridine bridged *bis*-dithiazolyl⁶⁵⁻⁶⁷ **1-19** and *bis*-thiadiazinyl^{68,69} **1-20** radicals in which the unpaired electron is shared amongst multiple organic rings. This design ensures that the majority of such radicals are monomeric in the solid state due to the weakness of any local dimerization mode. Nonetheless, for some choices of R-groups, the former crystallize as dimers [**1-19**]₂ linked through hypervalent chalcogen–chalcogen σ -bonds rather than π -interactions.⁷⁰⁻⁷⁴ The unique nature of such bonds allows them to be opened photochemically in the solid state through excitation to higher orbital states.^{75,76} We have shown that the photo-generated $S = \frac{1}{2}$ radicals may be trapped at low temperatures, analogous

to the LIESST³ effect observed in transition metal spin-crossover (SCO) materials.^{77,78}



Those examples of **1-19** that are monomeric in the solid state crystallize in one-dimensional slipped π -stacks, with the specific packing arrangement determined by the nature of the exocyclic R-groups. The absence of bulky groups allows relatively strong interactions between stacks, producing a quasi-3D network of magnetic interactions. The average character of these magnetic interactions can be probed by measurement of the magnetic susceptibility, χ , which far above the ordering temperatures typically follows a Curie-Weiss law:

$$\chi = \frac{C}{T - \Theta} \quad (1.22)$$

for “Curie constant” $C \sim 0.375$ for $S = \frac{1}{2}$ spins, and Weiss constant Θ indicating roughly the sign and strength of magnetic interactions. For **1-19**, the Weiss constants range between $\Theta = -15$ to $+7$ K indicating significant interactions. However, the presence of magnetic order has not been thoroughly investigated in the majority of derivatives. Perhaps the most well-studied example is the case of $R_1 = \text{Me}$, $R_2 = \text{H}$, which orders antiferromagnetically at $T_N = 5$ K, and shows metamagnetic behaviour at low temperatures.⁷⁹ In contrast to the properties of **1-19**, the two currently reported variants of **1-20** ($R_1 = \text{Me}$, Et , $R_2 = \text{Cl}$) are sterically protected by bulky $R_3 = \text{Ph}$ groups and thus form strongly interacting but essentially electronically isolated 1D radical stacks in the solid state. The magnetic response of the $R_1 = \text{Et}$ material, for example, is consistent with a one-dimensional antiferromagnetic chain with $\mathcal{J}/k_B = -141$ K, and interchain interactions $z\mathcal{J}/k_B = -9$ K.

In addition to avoiding dimerization, a significant advantage of the resonance stabilized **1-19** and **1-20** from the perspective of charge transport is that delocalization of electron

³LIESST = “Light Induced Excited Spin State Trapping”

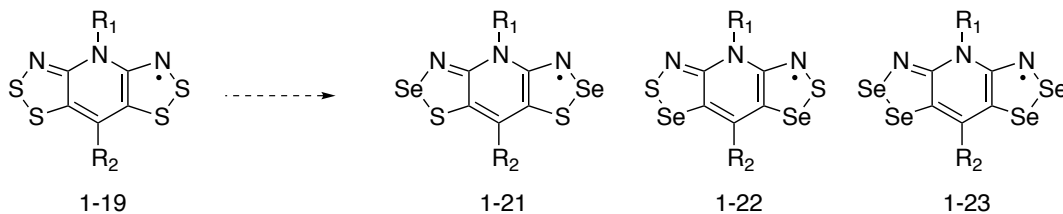
Table 1.1: Properties of selected pyridine bridged radicals **1-19** as a function of exocyclic groups R_1 and R_2 . MM = Metamagnet, SC-AFM = Spin Canted Antiferromagnet. $E_{cell} \sim U$ is the electrochemical cell potential, and $E_A \sim U - W$ is the thermal activation energy for conductivity.

R_1	R_2	Space Group	Θ	E_{cell}	E_A	Notes	Ref
Me	H	$P2_12_12_1$	~ 0 K	0.79 V	0.41 eV	MM, $T_N = 5$ K	65, 67
Me	Cl	$P2_12_12_1$	-13 K	0.83 V	0.40 eV		66
Et	H	$P2_1/c$	-4.5 K	0.76 V	0.41 eV		67
Et	Cl	$P\bar{4}2_1m$	+7 K	0.83 V	0.43 eV	Maybe SC-AFM	67
Et	Br	$P\bar{4}2_1m$	+7.6 K			SC-AFM, $T_N \sim 10$ K	Unpublished
Et	I	$P\bar{4}2_1m$	-9.6 K			Maybe SC-AFM	Unpublished
Pr	Cl	$P\bar{4}2_1m$	-11.5 K		0.48 eV		67

density results in significant reduction of on-site Coulomb repulsion, U .⁸⁰ This may be seen from comparison of the experimental electrochemical cell potential $E_{cell} = E_{1/2}^{(0/+1)} - E_{1/2}^{(-1/0)}$, which measures the potential difference in solution between oxidation and reduction of the neutral radical. This value is analogous to the gas-phase disproportionation enthalpy, but the screening effects of the solvent in the experiment more closely approximate the crystalline environment. While the mono-dithiazolyl radicals **1-17** have $U \sim E_{cell} \sim 1.4$ eV, the resonance delocalized **1-19** has $U \sim E_{cell} \sim 0.8$ eV representing a lowering of U by nearly a factor of two. Nonetheless, solid state bandwidth in **1-19** is not sufficient to overcome this repulsion barrier, and all such radicals are Mott insulators displaying activated conductivity $\sigma = \sigma_0 e^{-E_A/kT}$. The activation energy $E_A \sim U - W$ remains large, and ranges from 0.40 eV to 0.48 eV depending on solid-state packing. For this reason, Se-incorporation into the **1-19** framework to produce **1-21**, **1-22** and **1-23** was pursued by the Oakley group as a means of enhancing intermolecular interactions and thus bandwidth.⁸¹⁻⁸⁸

Table 1.2: Properties of selected mixed S/Se pyridine bridged radicals **1-21** as a function of exocyclic groups R₁ and R₂. FM = Ferromagnetic Order, PM = Paramagnet. “Strong AFM” refers to materials with strong antiferromagnetic coupling that may order but do not display a canted moment. $E_{cell} \sim U$ is the electrochemical cell potential, and $E_A \sim U - W$ is the thermal activation energy for conductivity.

R ₁	R ₂	Space Group	Θ	E_{cell}	E_A	Notes	Ref
Me	Cl	$P2_1/c$	< -100 K		0.20 eV	Strong AFM	88
Et	F	$P\bar{4}2_1m$	+17.6 K			FM, $T_C = 12$ K	Unpublished
Et	Cl	$P\bar{4}2_1m$	+20.3 K	0.74 V	0.27 eV	FM, $T_C = 12.8$ K	85, 86
Et	Br	$P\bar{4}2_1m$	+21.0 K	0.70 V	0.29 eV	FM, $T_C = 14.1$ K	87
Et	I	$P\bar{4}2_1m$	+4.4 K			FM, $T_C = 10.0$ K	Unpublished
Et	Me	$P\bar{4}2_1m$	+18.4 K	0.73 V	0.27 eV	FM, $T_C = 13.6$ K	87
Pr	Cl	$P\bar{4}2_1m$	-3.5 K	0.69 V	0.31 eV	Essentially PM	87
CH ₂ CF ₃	Cl	$P\bar{4}2_1m$	-0.4 K	0.69 V	0.31 eV	Essentially PM	87



This approach results in the lowering of E_A to 0.20 - 0.30 eV for the mixed S/Se radicals **1-21** and **1-22**, and $E_A \sim 0.18$ eV for the all-Se radicals **1-23**. Concomitant with the enhancement of intermolecular hopping integrals is a significant enhancement of the strength and dimensionality of magnetic interactions, resulting in a variety of magnetically ordered phases. Such phases range from bulk ferromagnets to spin-canted antiferromagnets, as summarized in Tables 1.2 – 1.4. In some cases such as **1-21** (R₁ = Me, R₂ = Cl), strong antiferromagnetic interactions are observed ($\Theta < -100$ K), but ordering has not been conclusively demonstrated due to the absence of a canted moment. The correlations between the various magnetic phases and structural packing motifs is addressed in chapter

Table 1.3: Properties of selected mixed S/Se pyridine bridged radicals **1-22** as a function of exocyclic groups R_1 and R_2 . SC-AFM = Spin canted antiferromagnetic order. $E_{cell} \sim U$ is the electrochemical cell potential, and $E_A \sim U - W$ is the thermal activation energy for conductivity.

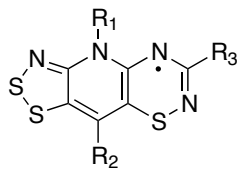
R_1	R_2	Space Group	Θ	E_{cell}	E_A	Notes	Ref
Me	H	$P2_12_12_1$	-78.3 K		0.24 eV		83
Me	Cl	$P2_12_12_1$	-28 K		0.30 eV		88
Et	H	$P2_1/c$	+6.3 K		0.22 eV	SC-AFM, $T_N = 18$ K	84
Et	Cl	$P\bar{4}2_1m$	-2.3 K	0.84 V	0.31 eV	SC-AFM, $T_N = 14$ K	86

4. The incorporation of Se also enhances the strength of spin-orbit coupling resulting in a large anisotropic component to the magnetic exchange. This effect is responsible for both large coercive fields in the Se-based ferromagnets, and spin-canting in the antiferromagnets. Such anisotropic interactions represent a major topic of this thesis, and will be addressed in great detail in chapter 6, through both ab-initio calculations and electron spin resonance (ESR) measurements. The response of **1-23** ($R_1 = \text{Et}$, $R_2 = \text{Cl}$ and Br) to pressure has also been investigated; in both cases the further enhancement of $t_{ij}^{\alpha\beta}$ with pressure results in an apparent breakdown of ferromagnetic order in the vicinity of ~ 3 GPa,^{90,91} and metallic transport ($d\rho/dT > 0$) is observed above ~ 6 GPa.⁸⁹ This observation likely represents the first example of a metallic state in a neutral radical material, although its properties are not consistent with a true Fermi liquid, but rather a “bad metal” state, as discussed in chapter 4.

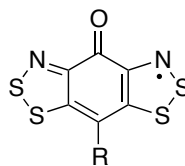
Further development of radical materials by the Oakley group has focussed on the question whether a metallic state could be achieved at lower pressure in order to facilitate study. This work has followed two approaches. The first is to manipulate the energies of various filled or empty orbitals in the vicinity of the SOMO so that U may be further reduced through electronic push-pull effects in asymmetric radicals. In order to test the effectiveness of this approach, synthetic techniques were developed for obtaining the hybrid dithiazolyl/thiadiazinyl radical **1-24**⁹² with an expanded range of R_3 groups compared with previous **1-20** radicals. These will be addressed in chapter 7.

Table 1.4: Properties of selected all-Se pyridine bridged radicals **1-23** as a function of exocyclic groups R_1 and R_2 . FM = Ferromagnet, SC-AFM = Spin canted antiferromagnetic order. “Strong AFM” refers to materials with strong antiferromagnetic coupling that may order but do not display a canted moment. $E_{cell} \sim U$ is the electrochemical cell potential, and $E_A \sim U - W$ is the thermal activation energy for conductivity.

R_1	R_2	Space Group	Θ	E_A	Notes	Ref
Me	H	$P2_12_12_1$	-44.3 K	0.17 eV		83
Me	Cl	$P2_1/c$	< -100 K	0.17 eV	Strong AFM	88
Et	H	$P2_1/c$	-8.0 K	0.19 eV	SC-AFM, $T_N = 27$ K	84
Et	Cl	$P\bar{4}2_1m$	+22.9 K	0.19 eV	FM, $T_C = 17$ K	86
Et	Br	$P\bar{4}2_1m$	+23.2 K	0.23 eV	FM, $T_C = 17.5$ K	89



1-24



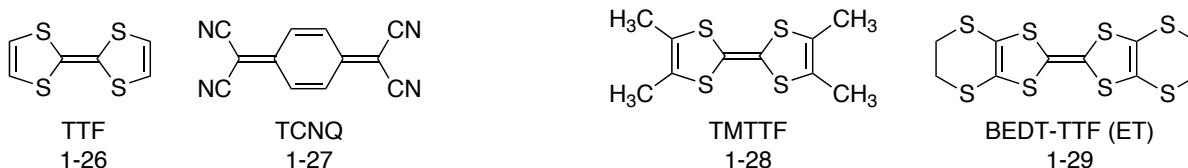
1-25

The second approach recently pursued by the Oakley group was initially intended to enhance bandwidth through further reduction of steric bulk by replacement of the N- R_1 in **1-19** with the isoelectronic C=O to form **1-25**. These materials indeed show very small activation energies $E_A = 0.05 - 0.20$ eV, lower even than the pyridine bridged Se variants **1-23**.⁹³⁻⁹⁷ Moreover these oxo-benzo bridged radicals display a strong propensity for magnetic order, particularly as spin-canted antiferromagnets often with large positive Weiss constants indicating strong ferromagnetic interactions. We will discuss in chapter 7 that these two observations are related not to favourable solid-state packing, but rather the presence of a low-lying LUMO afforded by the C=O group that hybridizes with the SOMO to significantly lower the one-electron charge gap. The influence of the low-lying LUMO on spin-orbit anisotropic exchange will also be considered in chapter 7. The importance of the

LUMO for the charge transport properties can be appreciated from discussion of related radical-ion and charge transfer salt materials, addressed in the next section.

1.3.4 Radical Ion and Charge Transfer Salts

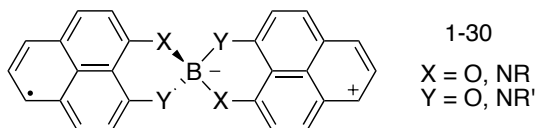
Although this thesis is devoted to the study of neutral radical materials, we introduce for completeness an alternate design strategy that involves producing charged radicals in-situ through co-crystallization of multiple components of differing electron affinity. The utility of this approach is that band-filling can be controlled essentially by the stoichiometry of the various components, so that metallic states can be promoted by ensuring non-half-filled bands as discussed in section 1.2.2. The first purely organic material to display metallic conductivity was formed by cocrystallization of the strong electron donor TCNQ **1-27** and strong electron acceptor TTF **1-26** in a 1:1 ratio.^{98,99} In the solid state, the two components form segregated π -stacks, providing well dispersing 1D bands along the stacking axis. Charge transfer, estimated to be on the order of 0.6 electrons per molecule,^{100,101} from the HOMO band of TCNQ to the overlapping LUMO band of TTF then results in two partially filled bands of hole and electron character, respectively. The solid remains metallic above $T = 60$ K, but below this temperature an incommensurate charge density wave state emerges as a result of the relative one-dimensionality of the Fermi surface.¹⁰² From a chemical perspective, the charge transfer between components can be considered as a partial redox reaction to generate some density of organic radical ions in the solid.



Viewed in this way, it is natural to consider alternate materials where the oxidation state of the organic donor is well defined by crystallization with strong inorganic acceptors so that charge transfer is essentially complete. The most well-studied examples of such radical ion materials are based on the TTF-like donors TMTTF **1-28** and ET **1-29** (and Se analogues) in 2:1 salts with inorganic components, i.e. $[\text{TMTTF}]_2[\text{X}]$, where $\text{X} = (\text{PF}_6)^-, (\text{AsF}_6)^-$,

(ClO₄)⁻, etc.¹⁰³⁻¹⁰⁷ This 2:1 stoichiometry ensures $\frac{3}{4}$ -filled bands, which are significantly less susceptible to a Mott insulating state than 1:1 salts with $\frac{1}{2}$ -filled bands. These salts crystallize in a variety of structural motifs, depending on the specific combination of organic and inorganic components, and thus display a wide variety of properties from charge and spin density wave insulators to metals to superconductors.¹⁰⁸⁻¹¹¹

A related class of materials are the spiro-phenalenyls **1-30** first studied by the Haddon group.¹¹²⁻¹¹⁶ In such systems, charge transfer from two phenalenyl radicals to a coordinated boron atom results in a neutral complex with one unpaired electron on average, shared between two phenalenyl components.



Of particular note is the case where X = O, Y = NR, R = cyclohexyl, which simultaneously displays a large but activated conductivity ($E_A = 0.05$ eV) and a weak temperature independent paramagnetic susceptibility. These results were interpreted by the authors in terms of an intermolecular resonating valence bond state.^{117,118} In such spiro-phenalenyl complexes, the overlap of the two phenalenyl SOMOs denoted ϕ_A and ϕ_B provides two orbitals in the vicinity of the Fermi energy:

$$|\psi_+\rangle = \frac{1}{\sqrt{2}} (|\phi_A\rangle + |\phi_B\rangle) \quad (1.23)$$

$$|\psi_-\rangle = \frac{1}{\sqrt{2}} (|\phi_A\rangle - |\phi_B\rangle) \quad (1.24)$$

The unpaired electron associated with each complex occupies the orbital denoted ψ_+ formed by the in-phase combination of the individual phenalenyl SOMOs, while an empty LUMO representing the out-of-phase combination appears at higher energy (Fig. 1.4(a)). The energetic splitting of the two orbitals is twice the hopping integral between the two phenalenyl SOMOs, denoted $2 t_{AB}$. In the solid state, each of these orbitals broadens into a band, where the lower in-phase band is nominally half-filled, similar to the neutral radical materials described in previous sections. However, the presence of the low-lying LUMO band has significant consequences for the charge transport properties.

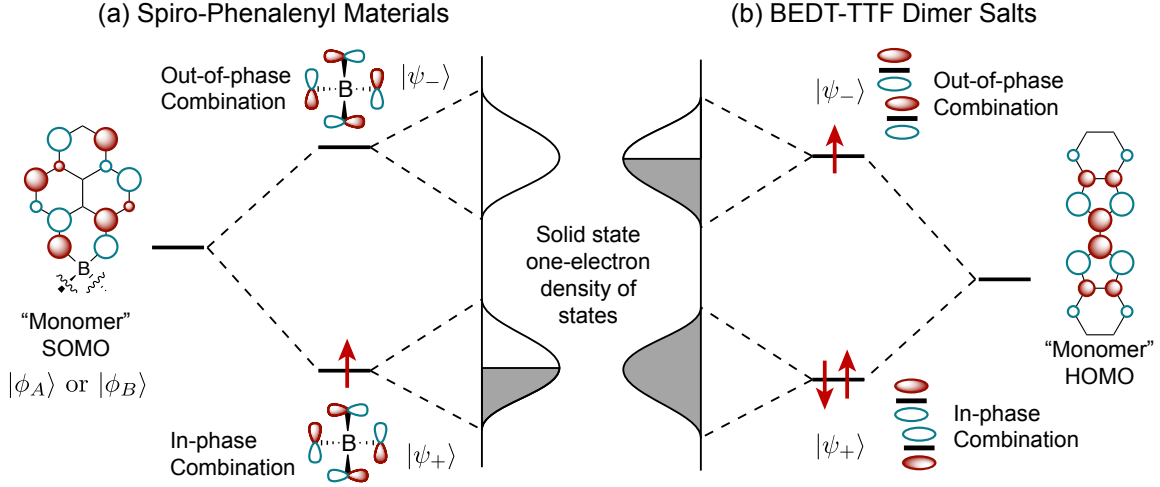


Figure 1.4: Electronic structure of (a) spiro-phenalenyl **1-30** and (b) $[\text{ET}]_2$ dimer based materials in the absence of Coulomb repulsion. In the former, there is one unpaired electron per **1-30** complex, occupying an in-phase combination of phenalenyl monomer SOMOs. In the latter, there is one unpaired electron per dimer, occupying the out-of-phase combination of ET monomer HOMOs.

Before discussing this point in detail, we remark that a very similar situation applies to the well-studied κ -phase of $[\text{ET}]_2[\text{X}]$ salts, in which ET molecules are dimerized with one unpaired electron on average per $[\text{ET}]_2^{+\bullet}$ dimer. The dimerization results in a similar splitting of the HOMO band into bonding (in-phase) ψ_+ and anti bonding (out-of-phase) ψ_- bands with respect to the local dimers (Fig. 1.4(b)). In this case, it is the higher lying anti-bonding band that is half-filled. It has become customary in the literature to treat each whole dimer as a single Hubbard site, so that such ET dimers are discussed in the context of an effective single band, half-filled Hubbard model.¹¹⁹ However, in analogy with spiro-phenalenyl materials, the effective parameters of this model are significantly influenced by the additional degrees of freedom associated with the filled HOMO bonding band. To see this, note that the charge gap $\Delta_c \sim U_{eff} - W$ is related to the disproportionation enthalpy, which is given for each of these systems by:

$$(a) \text{ Spiro-Phenalenyls: } U_{eff} \sim \Delta H_{disp} = E([\mathbf{1-30}]^+) + E([\mathbf{1-30}]^-) - 2 E([\mathbf{1-30}]^{\bullet}) \quad (1.25)$$

$$(b) \text{ ET Dimers: } U_{eff} \sim \Delta H_{disp} = E([\text{ET}]_2) + E([\text{ET}]_2^{2+}) - 2 E([\text{ET}]_2^{+\bullet}) \quad (1.26)$$

In both cases, it is useful to consider the energy of the state in which two electrons or

holes occupy the same site, either $E([\mathbf{1-30}]^-)$ or $E([\text{ET}]_2^{2+})$. In the latter case, because the on-site Coulomb repulsion between two electrons occupying the same ET monomer U_{mono} is very large, the $[\text{ET}]_2^{2+}$ ground state is essentially non-bonding, being best described by having two holes completely localized to the HOMO of the different monomers within the dimer site, i.e. $[\text{ET}^{+\bullet}]_2$. This state is thus open-shell, and is neither stabilized by delocalization of the electrons across the dimer nor destabilized by Coulomb repulsion between the holes since they are far apart. This situation is in contrast with state with one unpaired electron per dimer, $[\text{ET}_2]^{+\bullet}$, which is kinetically stabilized by sharing the electron between monomers to form a weak dimer bond. In accordance with this discussion, it is straightforward to show that in the limit where $U_{mono} \gg t_{AB}$ the effective energy cost for transferring electrons between dimer sites is given by:

$$U_{eff} \sim E([\text{ET}]_2) + E([\text{ET}^{+\bullet}]_2) - 2 E([\text{ET}]_2^{+\bullet}) \quad (1.27)$$

$$\sim (2U_{mono}) + (0) - 2(U_{mono} - t_{AB}) \quad (1.28)$$

$$= 2 t_{AB} < U_{mono} \quad (1.29)$$

This value is precisely the binding energy of the dimer. More generally, ignoring repulsion between electrons on different monomers,

$$U_{eff} = 2 t_{AB} + \frac{U_{mono}}{2} - \sqrt{(2 t_{AB})^2 + \left(\frac{U_{mono}}{2}\right)^2} \quad (1.30)$$

which is shown in Fig. 1.5 as a function of t_{AB} ; $U_{eff} < 0.5 U_{mono}$ for all values of t_{AB} . The same condition applies for spiro-phenalenyl materials, for which:

$$U_{eff} \sim E([\mathbf{1-30}]^+) + E([\mathbf{1-30}]^-) - 2 E([\mathbf{1-30}]^\bullet) \quad (1.31)$$

$$\sim (0) + (0) - 2(-t_{AB}) \quad (1.32)$$

$$= 2 t_{AB} < U_{mono} \quad (1.33)$$

A cartoon of the integrated one-electron spectral density (see Appendix B) for this latter material in the presence of interactions is shown in Fig. 1.5. The important lesson for neutral radical design that emerges from this discussion is that although the above materials may be considered in the context of single, half-filled bands, the additional degrees of freedom inherited from multiple bands in the vicinity of the Fermi level provides a significant

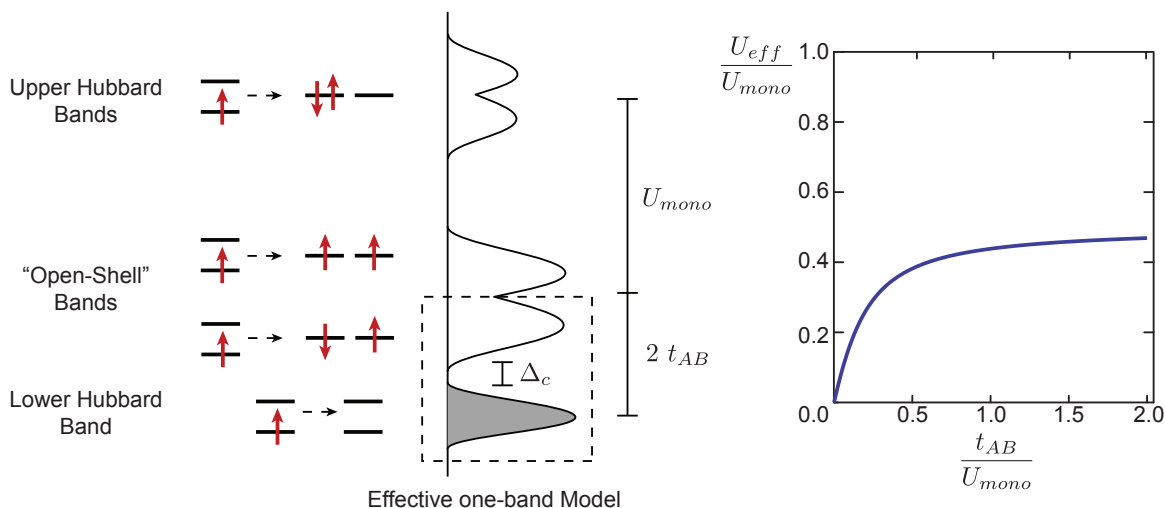
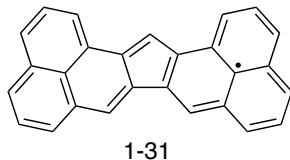


Figure 1.5: Cartoon of the integrated one-electron spectral density for spiro-phenalenyl materials **1-30**. Despite being considered an effective half-filled system, the presence of a low-lying LUMO results in additional open-shell states appearing at low energy. Access to such states significantly lowers the charge gap denoted Δ_c .

reduction in the effective Coulomb barrier. This energy barrier, in the context of a single-band Hubbard model, is a measure of the energy cost of forcing two electrons (or holes) to occupy the same site. When there are multiple orbital degrees of freedom available to such electrons, this energy cost will always tend to be lower, because the electrons are free to arrange themselves in whatever state minimizes such energy.

This discussion can be made concrete by noting that electrochemical measurements suggest that the on-site Coulomb repulsion of a single phenalenyl radical is $U_{mono} \sim 1.0-1.6$ eV,¹²⁰⁻¹²² while $t_{AB} \sim 0.2-0.4$ eV has been computed by extended Huckel methods. This provides the theoretical estimate $U_{eff} \sim 0.26-0.44$ eV for the spiro-phenalenyl complex **1-30**, in agreement with the measured cell potential $0.29-0.37$ V,^{113,114} and optical gaps e.g. $\Delta E \sim 0.34$ eV,¹¹⁷ both of which are significantly lower than the bare Coulomb repulsion. In contrast, the stronger conjugation of the phenalenyl moieties afforded by a cyclopentadiene

bridge, as in **1-31**, results in a much larger cell potential of $U_{eff} \sim \Delta E_{cell} = 1.03$ V.¹²³



In this case, the energetic splitting of the SOMO and LUMO is much greater, so that there is no substantial stabilization due to low-lying orbital degrees of freedom. From this discussion, it should be clear that the reduction of U_{eff} is crucial to the realization of highly conducting states in both κ -phase $[\text{ET}]_2[\text{X}]$ salts and spiro-phenalenyl materials. Investigating how to take advantage of such effects in Oakley-type radicals represents a major topic of this thesis.

1.4 Thesis Organization

In order to motivate the discussion of the electronic and magnetic properties of neutral radicals presented in this thesis, we present, in chapters 2 and 3, an introduction to the theoretical concepts and methods employed in later chapters. In particular:

- Chapter 2: We focus on the theoretical aspects of magnetic properties. We present a systematic method for the derivation of effective spin Hamiltonians, and employ this method to consider the effects of multiple orbitals, Hund's rule coupling, and spin-orbit effects in combination. We discuss theoretical methods for determining the parameters in such effective Hamiltonians from first principles, and introduce a new method for computing hopping integrals that allows us to treat spin-orbit anisotropic exchange interactions.
- Chapter 3: This brief chapter discusses theoretical aspects of charge transport. We introduce Dynamical Mean Field Theory calculations, and describe the phenomenology of the Mott transition in terms of measured resistivity and optical conductivity. Importantly, we introduce the concept of Mott's minimum metallic conductivity, and define bad metal states, which appear in radicals in the vicinity of the Mott transition.

On first reading, one may wish to skip these chapters, as they are referred to in the remainder of the thesis when necessary. In the remaining four chapters, we employ the introduced methods to understand the properties of several classes of organic radicals. Specifically:

- Chapter 4: We address the correlations between structure and magnetic response in pyridine-bridged radicals **1-19**, **1-20** – **1-22**. Through the classification of the symmetries of various magnetic order parameters, we derive restrictions on magnetic structures that may exhibit a net canted moment, such as bulk ferromagnets and spin-canted antiferromagnets. This provides a natural division of materials by the sign of magnetic exchange along the π -stacks. We then go on to discuss a series of low-dimensional radical spin-ladders where magnetic order is avoided by strong quantum fluctuations.
- Chapter 5: We focus on the magnetic and electronic properties of the isostructural tetragonal radicals **1-19**, **1-20** – **1-22** ($R_1 = \text{Et}$, $R_2 = \text{Cl}$) both at ambient and high pressure. We suggest that the dichotomy in the magnetic response between the ferromagnets **1-20**, **1-22** and spin-canted antiferromagnets **1-19**, **1-21** arises to due relative importance of ferromagnetic exchange through weak multi-orbital effects. Under pressure, these magnetic phases are suppressed, and a bad metallic state appears.
- Chapter 6: In this chapter, we further address the magnetic anisotropy in the tetragonal family **1-19**, **1-20** – **1-22** ($R_1 = \text{Et}$, $R_2 = \text{Cl}$) through electron spin resonance measurements and spin-orbit calculations.
- Chapter 7: In this final chapter, we focus on the design and study of radicals incorporating multiple orbitals in the vicinity of the Fermi level. We discuss unsuccessful efforts to tune hybrid radicals **1-24** to this condition, but find a low-lying empty LUMO in oxobenzene bridged radicals **1-25**. By studying three such radicals, we discuss the effect of this low-lying LUMO on the magnetic, electronic, and spin-orbit physics of these materials.

Chapter 2

Theoretical Aspects of Magnetism

2.1 Derivation of Effective Spin Hamiltonians

In this section, the systematic derivation of low-energy magnetic Hamiltonians starting from the extended Hubbard model is reviewed. The formal method of choice is to formulate a perturbation theory directly in terms of electron creation and annihilation operators, allowing for direct calculation of effective spin Hamiltonians. We introduce a diagrammatic method for keeping track of the terms emerging from $1/U$ expansion that allows for rapid evaluation of such magnetic Hamiltonians. As some derivations of this section are formal and somewhat lengthy, the main physical consequences of each calculation are summarized at the end of each subsection. It is worth emphasizing that while the results of Chapters 4–7 rely heavily on the discussion in this chapter, the mathematical details may be skipped without loss of understanding.

2.1.1 Adiabatic Concept and Low-Energy Theories

When experimentally probing physical systems, there is typically an energy scale associated with each measurement, as determined by the temperature of the sample, or the nature of the experiment. Microstates of the system that exist at far higher excitation energies than

either the experimental temperature $k_B T$, or the excitation frequency $\hbar\omega$, are not accessed, and remain experimentally irrelevant. For example, when probing the response of a Mott insulator for $k_B T, \hbar\omega \ll \Delta_c$, only the magnetic degrees of freedom are typically relevant. In order to describe the properties of a material at a specific energy scale, it is therefore advantageous to develop an effective model that includes only the (much smaller) subspace of states accessible by the experiment. For strongly interacting systems, determining these low-energy states exactly is often impossible, as it amounts to solving the fully interacting problem. For conceptual simplicity therefore, low-energy models are often formulated in terms of an unphysical Hilbert space of states that becomes exact only in some limit, but is adiabatically connected to the true low energy subspace.¹ The relevant example to this section is the use of spin Hamiltonians in quantum magnetism. Such Hamiltonians act on pure spin states with exactly one electron confined to each magnetic orbital, which are the true low energy eigenstates only in the limit $t/U \rightarrow 0$. As we will discuss below, magnetic interactions arise expressly because these pure spin states are mixed with higher energy charge separated states at finite hopping. The effective spin Hamiltonians are constructed with parameters designed to obtain correct state energies for fictitious pure spin wavefunctions.

In order to make this discussion more concrete, consider a system described by the Hamiltonian $\mathcal{H} = \mathcal{H}_0 + \lambda\mathcal{H}_1$, where λ is a parameter that varies the strength of \mathcal{H}_1 . For $\lambda = 0$, the eigenstates of the system are those of \mathcal{H}_0 , which we label by some quantum number n , with associated energy $\mathcal{H}_0|\Phi_n^0\rangle = E_n^0|\Phi_n^0\rangle$. Usually \mathcal{H}_0 is chosen so that these eigenstates are well understood, and there is considerable conceptual advantage to working with such states. Suppose we divide the Hilbert space into two sections by introducing a high energy cut-off Λ so that all states $n \geq \Lambda$, denoted $\{|\Phi_{n \geq \Lambda}^0\rangle\}$, are essentially inaccessible to the experiment. An effective theory incorporating only the low energy subspace $\{|\Phi_{n < \Lambda}^0\rangle\}$ may therefore be developed and remains valid below the energy scale E_Λ^0 . The Hamiltonian for this theory at $\lambda = 0$ is given simply by:

$$\mathcal{H}_{\text{eff}}^0 = \mathbb{P}_L^0 \mathcal{H}_0 \mathbb{P}_L^0 \tag{2.1}$$

¹In the sense of the Quantum Adiabatic Theorem.

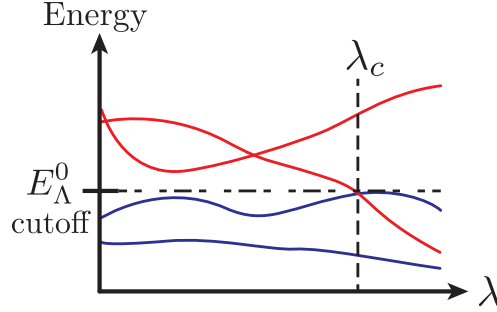


Figure 2.1: Cartoon of the evolution of state energies for the generic Hamiltonian $\mathcal{H} = \mathcal{H}_0 + \lambda\mathcal{H}_1$. As λ is increased, all states below the energy cutoff E_Λ , are adiabatically connected to corresponding $\lambda = 0$ states. A low-energy effective theory may therefore be written in terms of such states, and remains valid until $\lambda = \lambda_c$.

where \mathbb{P}_L is a projection operator into the lower energy subspace, and is given by:

$$\begin{aligned} \mathbb{P}_L^0 &= \sum_{n < \Lambda} |\Phi_n^0\rangle\langle\Phi_n^0| \\ &= \begin{cases} 1 & \text{if state is in lower Hilbert space } \{|\Phi_{n < \Lambda}^0\rangle\} \text{ for } \lambda = 0 \\ 0 & \text{otherwise} \end{cases} \end{aligned} \quad (2.2)$$

so that:

$$\mathcal{H}_{\text{eff}}^0|\Phi_n^0\rangle = \begin{cases} E_n^0|\Phi_n^0\rangle & \text{if state is in lower Hilbert space } \{|\Phi_{n < \Lambda}^0\rangle\} \text{ for } \lambda = 0 \\ 0 & \text{otherwise} \end{cases} \quad (2.3)$$

As λ is increased from zero, the effect of “turning on” \mathcal{H}_1 will be to alter the energies and composition of the eigenstates appearing at low energy. The new eigenstates of \mathcal{H} may be generally written in terms of the eigenstates at $\lambda = 0$ since both form a complete basis:

$$|\Phi_{m < \Lambda}^\lambda\rangle = \sum_{n < \Lambda} A_{mn}^\lambda |\Phi_{n < \Lambda}^0\rangle + \sum_{n \geq \Lambda} B_{mn}^\lambda |\Phi_{n \geq \Lambda}^0\rangle \quad (2.4)$$

The associated energies of such states are given by $\mathcal{H}|\Phi_m^\lambda\rangle = E_m^\lambda|\Phi_m^\lambda\rangle$. For the case where $B_{mn}^\lambda \neq 0$ it is clear that the zeroth order lower Hilbert space $\{|\Phi_{n < \Lambda}^0\rangle\}$ does not represent a complete subspace for the \mathcal{H}_1 operator, which appears to invalidate the choice of Hilbert space. That is, because \mathcal{H}_1 may mix states above and below the cutoff Λ , it

seems impossible to ignore the high energy states $\{|\Phi_{n \geq \Lambda}^0\rangle\}$. However, it is important to observe that all low energy states appearing at finite $\lambda < \lambda_c$ are adiabatically connected to those appearing at $\lambda = 0$, so that they may be labelled by identical quantum numbers. That is, we can slowly turn on the interactions λ and find that the states in the lower Hilbert space remain in 1:1 correspondence with those at $\lambda = 0$. This makes it possible to define a Hamiltonian that acts on the unphysical zeroth order lower Hilbert space $\{|\Phi_{n < \Lambda}^0\rangle\}$ but yields the correct energies:

$$\mathcal{H}_{\text{eff}}^\lambda |\Phi_m^0\rangle = \begin{cases} E_m^\lambda |\Phi_m^0\rangle & \text{if state is in lower Hilbert space } \{|\Phi_{m < \Lambda}^0\rangle\} \text{ for } \lambda = 0 \\ 0 & \text{otherwise} \end{cases} \quad (2.5)$$

where $|\Phi_m^0\rangle$ is defined essentially as the state appearing in $\{|\Phi_{n < \Lambda}^0\rangle\}$ that is adiabatically connected to the state $|\Phi_m^\lambda\rangle$. For small λ , this often implies $|A_{mn}^\lambda|$ is maximal. In this way, the high energy states $\{|\Phi_{n \geq \Lambda}^0\rangle\}$ may be safely neglected so long as the Hamiltonian is appropriately modified to preserve the exact spectrum. Colloquially, this process is known as “renormalization”, and the new parameters of the Hamiltonian are said to be “renormalized” in the process of projecting out the high energy states. It is very important to note that virtually all models in materials science are effective low energy theories and one must be careful not to apply such theories outside their range of applicability, that is $E < E_\Lambda, \lambda < \lambda_c$. In order to avoid certain interpretation problems, one must also always remember that the states described in these models are not identical to the true states of the system. As discussed further in the Appendix section A.1.1, low-energy effective Hamiltonians may often be calculated reliably using perturbation theory, via:

$$\boxed{\mathcal{H}_{\text{eff}}(\omega) = \mathbb{P}_L^0 \mathcal{H}_0 \mathbb{P}_L^0 + \sum_{n=0}^{\infty} \lambda^{n+1} \mathbb{P}_L^0 \mathcal{H}_1 [\mathbb{P}_U^0 (\omega - \mathcal{H}_0)^{-1} \mathbb{P}_U^0 \mathcal{H}_1]^n \mathbb{P}_L^0} \quad (2.6)$$

where \mathbb{P}_U^0 is the projection operator into the upper Hilbert space:

$$\mathbb{P}_U^0 = 1 - \mathbb{P}_L^0 = \begin{cases} 0 & \text{if state is in lower Hilbert space} \\ 1 & \text{otherwise} \end{cases} \quad (2.7)$$

The most significant disadvantage of this perturbative formulation is that the effective Hamiltonian depends explicitly on the exact energy of the state it acts upon, through

the appearance of ω in the denominator! However, provided there is a significant energy gap between the low and high energy subspaces, ω may be replaced approximately by the zeroth order energy, that is $\omega \sim E_n^0$, which for all cases considered below is a constant.

2.1.2 Diagrammatic Representation in the $U \gg t$ Limit

Of particular interest in this chapter is the case of the large U limit of the Hubbard model, in which one seeks to project out all high energy states in which the occupancy of the SOMO ($\alpha = 0$) differs from one, which costs at least an energy U , and/or the occupancy of the $\alpha = +(-)n$ orbitals differs from zero (two), which costs at least $|\epsilon_n - \epsilon_0|$. The resulting renormalized Hamiltonian is written in terms of spin operators, and describes the varied magnetic properties of the Mott insulating state. A formalism for accomplishing this systematically is presented below, with useful expressions given in Appendix A. We identify:

$$\mathcal{H}_0 = \mathcal{E} + \mathcal{U} \quad (2.8)$$

$$\mathcal{H}_1 = \mathcal{T} + \mathcal{K} + \mathcal{Q} \quad (2.9)$$

where:

$$\mathcal{E} = \sum_{i,\alpha} \epsilon_i^\alpha \mathbf{c}_{i,\alpha}^\dagger \mathbf{c}_{i,\alpha} \quad , \quad \mathcal{U} = \sum_{\substack{i,s,s' \\ \alpha,\beta}} U_i^{\alpha\beta} n_{i,s}^\alpha n_{i,s'}^\beta \quad , \quad \mathcal{T} = \sum_{\substack{\langle i,j \rangle \\ \alpha,\beta}} t_{ij}^{\alpha\beta} \mathbf{c}_{i,\alpha}^\dagger \mathbf{c}_{j,\beta} \quad (2.10)$$

$$\mathcal{K} = \sum_{\substack{\langle i,j \rangle \\ \alpha,\beta}} K_{ij}^{\alpha\beta} \mathbf{c}_{i,\alpha}^\dagger \mathbf{c}_{j,\beta}^\dagger \mathbf{c}_{i,\alpha} \mathbf{c}_{j,\beta} \quad , \quad \mathcal{Q} = \sum_{i,\alpha,\beta} Q_i^{\alpha\beta} \mathbf{c}_{i,\alpha}^\dagger \mathbf{c}_{i,\beta}^\dagger \mathbf{c}_{i,\alpha} \mathbf{c}_{i,\beta} \quad (2.11)$$

Inserting these expressions for \mathcal{H}_0 and \mathcal{H}_1 into eq'n (2.6) allows for the evaluation of \mathcal{H}_{eff} in terms of products of electron creation and annihilation operators. A particular feature of the effective theory is that only products of operators that connect states within the lower Hilbert space survive projection by \mathbb{P}_L^0 . This means, typically, that the vast majority of operator products appearing at a particular order n are irrelevant. It is therefore advantageous to introduce a diagrammatic method for quickly identifying those combinations that survive projection. The diagrammatic convention used throughout this thesis will be

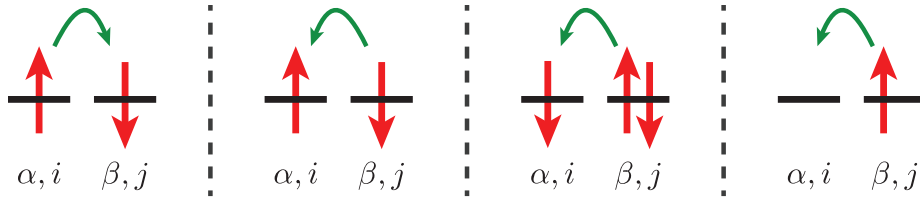
as follows. Singly occupied local orbitals are represented by a single line, doubly occupied orbitals by a double line, and empty orbitals by a dashed line. Each line carries a set of indices (i, α) identifying the orbital, and an arrow indicating its connectivity with vertices:

$$\begin{aligned}
 \text{Empty Orbital: } & \text{---} \blacktriangleleft \text{---} \quad i, \alpha \\
 \text{Singly Occupied: } & \text{---} \blacktriangleleft \text{---} \quad i, \alpha \\
 \text{Doubly Occupied: } & \text{=} \blacktriangleleft \text{=} \quad i, \alpha
 \end{aligned} \tag{2.12}$$

Operators in \mathcal{H}_1 are represented by vertices. The hopping vertex, associated with \mathcal{T} is represented by an empty circle. In order to conserve particle number, the number of electrons contained in incoming lines must match those in outgoing lines. This restricts the vertex to take the following form:

$$\mathcal{T} = \sum_{\substack{\langle i,j \rangle \\ \alpha,\beta}} t_{ij}^{\alpha\beta} \left(\begin{array}{cccc}
 \begin{array}{c} \alpha, i \\ \beta, j \end{array} & \begin{array}{c} \alpha, i \\ \beta, j \end{array} & \begin{array}{c} \alpha, i \\ \beta, j \end{array} & \begin{array}{c} \alpha, i \\ \beta, j \end{array} \\
 \begin{array}{c} \alpha, i \\ \beta, j \end{array} & \begin{array}{c} \alpha, i \\ \beta, j \end{array} & \begin{array}{c} \alpha, i \\ \beta, j \end{array} & \begin{array}{c} \alpha, i \\ \beta, j \end{array} \\
 \begin{array}{c} \alpha, i \\ \beta, j \end{array} & \begin{array}{c} \alpha, i \\ \beta, j \end{array} & \begin{array}{c} \alpha, i \\ \beta, j \end{array} & \begin{array}{c} \alpha, i \\ \beta, j \end{array} \\
 \begin{array}{c} \alpha, i \\ \beta, j \end{array} & \begin{array}{c} \alpha, i \\ \beta, j \end{array} & \begin{array}{c} \alpha, i \\ \beta, j \end{array} & \begin{array}{c} \alpha, i \\ \beta, j \end{array}
 \end{array} \right) + \text{h.c.} \tag{2.13}$$

where the Hermitian conjugate of a diagram, denoted (h.c.) is obtained by reversing the direction of all arrows. These four diagrams refer, respectively, to the following types of hops:



The Coulomb exchange vertices are indicated by a square box:

$$\mathcal{K} = \sum_{\substack{\langle i,j \rangle \\ \alpha,\beta}} K_{ij}^{\alpha\beta} \left(\begin{array}{c} \alpha, i \quad \alpha, i \\ \beta, j \quad \beta, j \end{array} \right) \quad (2.14)$$

$$\mathcal{Q} = \sum_{i,\alpha,\beta} Q_i^{\alpha\beta} \left(\begin{array}{c} \alpha, i \quad \alpha, i \\ \beta, i \quad \beta, i \end{array} \right) \quad (2.15)$$

Diagrams representing terms that survive projection are obtained by linking lines so that the directions of arrows match, and all lines external to the diagram are consistent with the lower Hilbert space. All internal combinations of lines must correspond to states in the upper Hilbert space, so that only so-called “irreducible” diagrams contribute. In the true physical system, these states are mixed with those in the lower Hilbert space, but in the renormalized effective model they enter only as corrections to the Hamiltonian. Interactions between spins at sites i, j must include external single lines for the SOMOs $|0_i\rangle, |0_j\rangle$ at both sites. Diagrams may be translated to mathematical expressions by the following rules:

1. All permutations of internal indices are summed.
2. The matrix elements associated with each vertex are multiplied together. Diagrams contain $n + 1$ vertices.
3. A value for $\langle(\omega - \mathcal{H}_0)^{-1}\rangle$ is assigned to each set of internal lines between each vertex. Diagrams contain n such Green operators. These values are also multiplied.
4. Appropriate products of creation and annihilation operators are assigned to each vertex, and combined in the order the vertices appear in the diagram; the opposite direction of the arrows.

For example, the simplest irreducible linked diagram for hopping vertices is:

$$= - \sum_{i,j} t_{ij}^{00} t_{ji}^{00} \frac{1}{U_j^{00}} \mathbf{c}_{i,0}^\dagger \mathbf{c}_{j,0} \mathbf{c}_{j,0}^\dagger \mathbf{c}_{i,0} \quad (2.16)$$

The two hopping vertices contribute t_{ij}^{00} and t_{ji}^{00} , while the single set of internal lines contributes $\langle (\omega - \mathcal{H}_0)^{-1} \rangle = -1/U_j^{00}$. The conversion of such terms into spin Hamiltonians may be affected using the relations in Appendix A. In the next sections, we finally show how such diagrams aid in the calculation of effective spin Hamiltonians.

2.1.3 Spin Hamiltonian from the One-Orbital Hubbard Model

In this section, we demonstrate the formalism outlined above and in Appendix A to derive the well known spin interactions arising in single band Hubbard model. In this case, we consider only the electrons occupying each radical SOMO, so that the orbital energy and on-site Hund's coupling may both be ignored. The electron Hamiltonian may be written:

$$\mathcal{H}_0 = \mathcal{U} = U \sum_i n_{i,0,\uparrow} n_{i,0,\downarrow} \quad (2.17)$$

$$\mathcal{H}_1 = \mathcal{T} + \mathcal{K} = \sum_{\langle i,j \rangle} t_{ij}^{00} \mathbf{c}_{i,0}^\dagger \mathbf{c}_{j,0} + \sum_{\langle i,j \rangle} K_{ij}^{00} \mathbf{c}_{i,0}^\dagger \mathbf{c}_{j,0}^\dagger \mathbf{c}_{i,0} \mathbf{c}_{j,0} \quad (2.18)$$

with the projection operator into the lower Hilbert space given by:

$$\mathbb{P}_L^0 = \prod_i \delta(\mathbf{c}_{i,0}^\dagger \mathbf{c}_{i,0} - 1) \quad (2.19)$$

which ensures there is exactly one electron per site for all states in the lower Hilbert space. It is useful to note in this case that:

$$\mathbb{P}_L^0 \mathcal{U} \mathbb{P}_L^0 = 0 \quad , \quad \mathbb{P}_U^0 \mathcal{U} \mathbb{P}_U^0 = U \quad , \quad \mathbb{P}_L^0 \mathcal{T} \mathbb{P}_L^0 = 0 \quad (2.20)$$

$$\mathbb{P}_U^0 \mathcal{K} \mathbb{P}_L^0 = \mathbb{P}_L^0 \mathcal{K} \mathbb{P}_U^0 = \mathbb{P}_U^0 \mathcal{K} \mathbb{P}_U^0 = 0 \quad (2.21)$$

so that the effective spin Hamiltonian may be derived from:

$$\mathcal{H}_{\text{eff}} = \mathbb{P}_L^0 \mathcal{K} \mathbb{P}_L^0 + \sum_{n=0}^{\infty} \mathbb{P}_L^0 \mathcal{T} [(\omega - \mathcal{H}_0)^{-1} \mathbb{P}_U^0 \mathcal{T}]^n \mathbb{P}_L^0 \quad (2.22)$$

Coulomb Exchange, $n = 0$:

The zeroth order contribution arises from Hund's rule coupling between electrons occupying the SOMO of different radicals, described by the diagram:

$$\mathcal{H}_{\text{eff}}^{(n=0)} = \begin{array}{c} \begin{array}{ccc} & 0, i & \\ & \swarrow \quad \searrow & \\ & \square & \\ & \swarrow \quad \searrow & \\ 0, j & & 0, j \end{array} & = \mathbb{P}_L^0 \sum_{\langle i, j \rangle} K_{ij}^{00} \mathbf{c}_{i,0}^\dagger \mathbf{c}_{j,0}^\dagger \mathbf{c}_{i,0} \mathbf{c}_{j,0} \mathbb{P}_L^0 \end{array} \quad (2.23)$$

Using eq'n (A.20), this is:

$$\mathcal{H}_{\text{eff}}^{(n=0)} = \mathbb{P}_L^0 \sum_{\langle i, j \rangle} K_{ij}^{00} \left(\mathbf{c}_{i,0}^\dagger \mathbf{c}_{j,0} \mathbf{c}_{j,0}^\dagger \mathbf{c}_{i,0} - \mathbf{c}_{i,0}^\dagger \mathbf{c}_{i,0} \right) \mathbb{P}_L^0 \quad (2.24)$$

But $\mathbb{P}_L^0 \mathbf{c}_{i,0}^\dagger \mathbf{c}_{i,0} \mathbb{P}_L^0 = 1$ is a constant, and may be subtracted from the Hamiltonian. Using eq'n (A.18), this is:

$$\mathcal{H}_{\text{eff}}^{(n=0)} = \mathbb{P}_L^0 \sum_{\langle i, j \rangle} K_{ij}^{00} \mathbf{c}_{i,0}^\dagger \left(\frac{1}{2} \mathbb{I} - \mathbf{S}_j \cdot \vec{\sigma} \right) \mathbf{c}_{i,0} \mathbb{P}_L^0 \quad (2.25)$$

$$= \mathbb{P}_L^0 \sum_{\langle i, j \rangle} K_{ij}^{00} \left(\frac{1}{2} \mathbf{c}_{i,0}^\dagger \mathbf{c}_{i,0} - \mathbf{S}_j \cdot \mathbf{c}_{i,0}^\dagger \vec{\sigma} \mathbf{c}_{i,0} \right) \mathbb{P}_L^0 \quad (2.26)$$

which, using eq'n (A.10) gives:

$$\mathcal{H}_{\text{eff}}^{(n=0)} = \mathbb{P}_L^0 \sum_{\langle i, j \rangle} K_{ij}^{00} \left(\frac{1}{2} \mathbf{c}_{i,0}^\dagger \mathbf{c}_{i,0} - 2 \mathbf{S}_j \cdot \mathbf{S}_i \right) \mathbb{P}_L^0 \quad (2.27)$$

Finally, applying the projection operators, and subtracting constant terms gives:

$$\mathcal{H}_{\text{eff}}^{(n=0)} = - \sum_{\langle i, j \rangle} 2K_{ij}^{00} \mathbf{S}_i \cdot \mathbf{S}_j \quad \rightarrow \quad \mathcal{J}_{ij}^{\text{FM}} = -2K_{ij}^{00} \quad (2.28)$$

As is well known, the so-called Coulomb contribution to the magnetic exchange provides a ferromagnetic interaction, with $\mathcal{H}_{\text{eff}}^{(n=0)}$ minimized for adjacent spins aligned in parallel. This effect arises due to the physics of the Pauli exclusion principle, which requires the many-body wavefunction to vanish whenever two electrons occupy the same state. Electrons with the same spin thus tend to avoid one another in space, reducing the average Coulomb repulsion between such electrons, and lowering the energy of such a configuration.¹²⁴ This effect is opposed by antiferromagnetic kinetic exchange:

Kinetic Exchange, $n = 1$:

As discussed above, the lowest order irreducible diagram from the hopping term is:

$$\mathcal{H}_{\text{eff}}^{(n=1)} = \sum_{i,j} t_{ij}^{00} t_{ji}^{00} \frac{1}{U} \mathbf{c}_{i,0}^\dagger \mathbf{c}_{j,0} \mathbf{c}_{j,0}^\dagger \mathbf{c}_{i,0} \quad (2.29)$$

Using the expressions in the previous section, and dropping constant terms, this becomes:

$$\mathcal{H}_{\text{eff}}^{(n=1)} = + \sum_{i,j} \frac{2(t_{ij}^{00})^2}{U} \mathbf{S}_i \cdot \mathbf{S}_j \quad (2.30)$$

Finally, summing over internal lines gives the two combinations (i, j) and (j, i) , both of which give identical terms. Therefore, the total summation is:

$$\mathcal{H}_{\text{eff}}^{(n=1)} = + \sum_{\langle i,j \rangle} \frac{4(t_{ij}^{00})^2}{U} \mathbf{S}_i \cdot \mathbf{S}_j \quad \rightarrow \quad \mathcal{J}_{ij}^{\text{AFM}} = \frac{4(t_{ij}^{00})^2}{U} \quad (2.31)$$

This term arises due to the effect of local (quantum) charge fluctuations, which reduce the kinetic energy of electrons through partial delocalization to neighbouring radical sites. Due to the Pauli exclusion principle, this delocalization may only occur in single orbital models if the electron spins on neighbouring sites are aligned oppositely, leading to a net antiferromagnetic interaction. Combining this term with the $n = 0$ Coulomb exchange gives the familiar result:

$$\mathcal{H}_{\text{eff}} = \sum_{\langle i,j \rangle} \mathcal{J}_{ij} \mathbf{S}_i \cdot \mathbf{S}_j \quad (2.32)$$

$$\mathcal{J}_{ij} = \frac{4(t_{ij}^{00})^2}{U} - 2K_{ij} \quad (2.33)$$

2.1.4 Ferromagnetism in Multi-Orbital Models

Diagrammatic Approach

In the previous section, all magnetic interactions were considered to arise from direct interactions between partially filled SOMO orbitals. An alternate mechanism for magnetic

exchange through filled and empty orbitals on the magnetic centers was originally proposed by Anderson,¹²⁵ and later described by Goodenough.¹²⁶ Their result may be recovered, in spirit, from the following diagrams, appearing at order $n = 2$:

$$\mathcal{H}_{\text{eff}}^{(n=2)} = \text{Diagram 1} + \text{Diagram 2} \quad (2.34)$$

$$= \mathbb{P}_L^0 \left\{ \begin{aligned} & \sum_{i,j,\alpha>0} \frac{Q_j^{0\alpha} (t_{ij}^{0\alpha})^2}{(U_j^{0\alpha} + \epsilon_\alpha - \epsilon_0)^2} \left(\mathbf{c}_{i,0}^\dagger \mathbf{c}_{j,\alpha} \mathbf{c}_{j,\alpha}^\dagger \mathbf{c}_{j,0} \mathbf{c}_{j,\alpha} \mathbf{c}_{j,0}^\dagger \mathbf{c}_{i,0} \right) \\ & + \sum_{i,j,\alpha<0} \frac{Q_j^{0\alpha} (t_{ij}^{0\alpha})^2}{(U_j^{0\alpha} + \epsilon_0 - \epsilon_\alpha)^2} \left(\mathbf{c}_{j,\alpha}^\dagger \mathbf{c}_{i,0} \mathbf{c}_{j,\alpha}^\dagger \mathbf{c}_{j,0} \mathbf{c}_{j,\alpha} \mathbf{c}_{j,0}^\dagger \mathbf{c}_{i,0} \mathbf{c}_{j,\alpha} \right) \end{aligned} \right\} \mathbb{P}_L^0 \quad (2.35)$$

which after some manipulations, and neglecting constant terms gives:

$$\mathcal{H}_{\text{eff}}^{(n=2)} = \mathbb{P}_L^0 \left\{ \sum_{\substack{i,j \\ \alpha \neq 0}} \frac{Q_j^{0\alpha} (t_{ij}^{0\alpha})^2}{(U_j^{0\alpha} + \Delta\epsilon_j^\alpha)^2} \left(\mathbf{c}_{i,0}^\dagger \mathbf{c}_{j,0} \mathbf{c}_{j,0}^\dagger \mathbf{c}_{i,0} \right) \right\} \mathbb{P}_L^0 \quad (2.36)$$

$$= - \sum_{\substack{\langle i,j \rangle \\ \alpha \neq 0}} \left\{ \frac{2Q_j^{0\alpha} (t_{ij}^{0\alpha})^2}{(U_j^{0\alpha} + \Delta\epsilon_j^\alpha)^2} + \frac{2Q_i^{0\alpha} (t_{ji}^{0\alpha})^2}{(U_i^{0\alpha} + \Delta\epsilon_i^\alpha)^2} \right\} \mathbf{S}_i \cdot \mathbf{S}_j \quad (2.37)$$

where $\Delta\epsilon_j^\alpha = |\epsilon_j^\alpha - \epsilon_j^0|$. This expression agrees with Anderson's result, apart from fixing the denominator to include the energy difference between the orbitals. However, it is very straightforward to improve on this result. For this specific case, the Coulomb vertex can in fact be summed to infinite order; we introduce the resummed vertex:

$$\star = \text{Diagram 1} + \text{Diagram 2} + \text{Diagram 3} + \text{Diagram 4} + \dots \quad (2.38)$$

which is given by:

$$\star = \mathcal{G}_U^{-1} \sum_{n=0}^{\infty} (Q_i^{\alpha\beta} \mathcal{G}_U \mathbf{c}_{i,\alpha}^\dagger \mathbf{c}_{i,0}^\dagger \mathbf{c}_{i,\alpha} \mathbf{c}_{i,0})^n \quad (2.39)$$

$$= \frac{\mathcal{G}_U^{-3}}{\mathcal{G}_U^{-2} - (Q_i^{\alpha\beta})^2} (1 + Q_i^{\alpha\beta} \mathcal{G}_U \mathbf{c}_{i,\alpha}^\dagger \mathbf{c}_{i,0}^\dagger \mathbf{c}_{i,\alpha} \mathbf{c}_{i,0}) \quad (2.40)$$

Inserting this expression into \mathcal{H}_{eff} gives, up to second order in t , but infinite order in Q :

$$\mathcal{H}_{\text{eff}} = - \sum_{\substack{\langle i,j \rangle \\ \alpha \neq 0}} \left\{ \frac{2Q_j^{0\alpha}(t_{ij}^{0\alpha})^2}{(U_j^{0\alpha} + \Delta\epsilon_j^\alpha)^2 - (Q_j^{0\alpha})^2} + \frac{2Q_i^{0\alpha}(t_{ji}^{0\alpha})^2}{(U_i^{0\alpha} + \Delta\epsilon_i^\alpha)^2 - (Q_i^{0\alpha})^2} \right\} \mathbf{S}_i \cdot \mathbf{S}_j \quad (2.41)$$

which is similar to the expression found by Kahn by comparison of state energies of centrosymmetric magnetic centres.¹²⁷ As interacting radicals rarely possess such symmetry, the general expression in eq'n (2.41) is of greater utility. From the sign of the exchange constant, it is clear that this interaction is ferromagnetic, and as such it is colloquially known as ‘‘ferromagnetic exchange through empty and filled orbitals’’.¹²⁷ The effect arises due to a lowering of the kinetic energy of electrons (holes) through delocalization onto empty (filled) orbitals on neighbouring sites in the crystal. The zeroth order ground state is mixed with configurations that have multiple unpaired electrons in different orbitals on the same site, for which on-site Hund’s coupling is active. The Hund interaction stabilizes high spin configurations through the reduction of Coulomb repulsion between like spins, so that delocalization is enhanced for ferromagnetic alignment of spins.

2.1.5 Importance of Multi-orbital Exchange in Organics

Combining the previous expressions for ferromagnetic multi-orbital exchange with the direct SOMO-SOMO coupling gives:

$$\mathcal{J}_{ij} = \mathcal{J}_{ij}^{AFM} + \mathcal{J}_{ij}^{FM} \quad , \quad \mathcal{J}_{ij}^{AFM} = \frac{4(t_{ij}^{00})^2}{U} \quad , \quad \mathcal{J}_{ij}^{FM} = -2\tilde{K}_{ij} \quad (2.42)$$

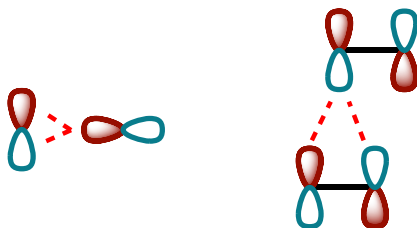
where \tilde{K}_{ij} represents the renormalized Hund’s coupling:

$$\tilde{K}_{ij} = K_{ij}^{00} + \sum_{\alpha \neq 0} \left\{ \frac{Q_j^{0\alpha}(t_{ij}^{0\alpha})^2}{(U_j^{0\alpha} + \Delta\epsilon_j^\alpha)^2 - (Q_j^{0\alpha})^2} + \frac{Q_i^{0\alpha}(t_{ji}^{0\alpha})^2}{(U_i^{0\alpha} + \Delta\epsilon_i^\alpha)^2 - (Q_i^{0\alpha})^2} \right\} \quad (2.43)$$

For metal ions, Anderson suggested that both contributions to \tilde{K}_{ij} would be small and of similar magnitude, and therefore one should expect $|\mathcal{J}_{ij}^{AFM}| > |\mathcal{J}_{ij}^{FM}|$, leading to a significant preference for antiferromagnetic interactions between localized spins.¹²⁵ For this reason, organic Mott insulators with an integral number of unpaired electrons per site tend

to be dominated by antiferromagnetic interactions. The generation of strong ferromagnetic interactions, in contrast, requires satisfying a combination of the following conditions:

- Small hopping t_{ij}^{00} directly between SOMOs in order to suppress the antiferromagnetic exchange. This condition is known as “orthogonal overlap”,¹²⁸ for historical reasons, arising from an alternate descriptions of magnetic coupling based on nonorthogonal local orbitals. Examples of orthogonal overlap of p -orbitals are shown below:



These geometric conditions for small t_{ij}^{00} are the same even when the local orbitals are chosen to be explicitly orthogonal.

- The presence of a very low-lying empty orbital ($\Delta\epsilon_i^1 \sim Q_i^{01}$) or high lying filled orbital ($\Delta\epsilon_i^{-1} \sim Q_i^{0-1}$). This condition ensures that the multi-orbital component of \tilde{K}_{ij} is large, and competitive with the usual antiferromagnetic exchange. In this case, provided that $t_{ij}^{01}, t_{ij}^{10} > t_{ij}^{00}$, ferromagnetism is expected.

In prominent examples of “high- T_C ” (i.e. $T_C > 5$ K) organic ferromagnets, it is likely that both these conditions are satisfied. Consider, for example, the fullerene salt TDAE·C₆₀ ($T_C \sim 15$ K), for which the role of multi-orbital exchange in generating strong ferromagnetic interactions is already well recognized.^{129,130} The electronic structure at each [C₆₀]^{•-} molecule consists of a single unpaired electron, donated by the TDAE, occupying a set of triply degenerate orbitals (Fig. 2.2(a)). With reference to the above model, this can be considered the extreme limit where $\Delta\epsilon^{01}, \Delta\epsilon^{02} \rightarrow 0$, providing for strong multi-orbital ferromagnetic interactions in combination with Hund’s coupling.

A second example of interest is γ -BBDTA·GaCl₄ ($T_C \sim 7$ K).^{131–133} Each [BBDTA]^{•+} site contains one unpaired electron occupying a non degenerate SOMO (Fig. 2.2(b)). In addition to the SOMOs on adjacent molecules being nearly orthogonal, there is strong

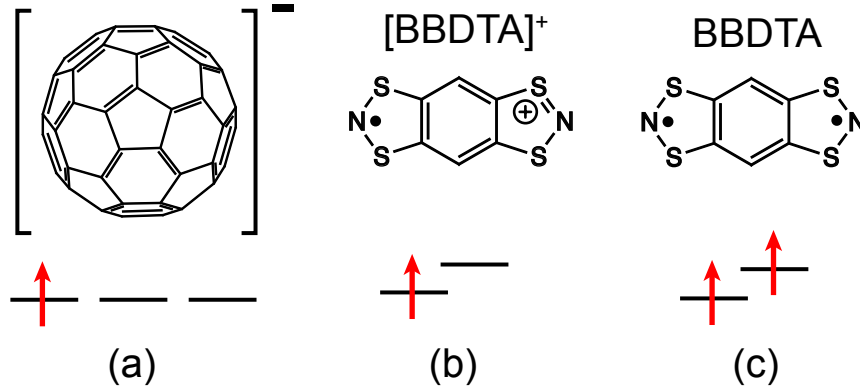


Figure 2.2: Electronic structure of (a) $[C_{60}]^-$, (b) $[BBDTA]^+$ and (c) neutral BBDTA. Ferromagnetism in TDAE· C_{60} originates from multi-orbital interactions occasioned by the triply degenerate SOMO. Multi-orbital exchange may also play a role in BBDTA· $GaCl_4$ for which the presence of a low lying SOMO+1 orbital is evidenced by the low-lying triplet state of the neutral BBDTA molecule.

evidence for the presence of a low-lying empty LUMO. This may be seen in the fact that the neutral molecule, containing one additional electron, is a ground state singlet with significant biradical character, and with a low-lying excited triplet state shown in Fig. 2.2(c).^{134,135} That is, $Q^{01} \sim \Delta\epsilon^{01}$. For this reason, multi-orbital exchange may be expected to play a prominent role in this material as well,¹³⁶ provided a sufficient discrepancy between hopping integrals t_{ij}^{00} and t_{ij}^{01} .

In contrast, despite having multiple relevant orbitals, and low-lying open shell states when two electrons (holes) occupy the same site, the spiro-phenalenyl **1-30** and κ -phase $[ET]_2X$ salts introduced in section 1.3.4 do not satisfy the above conditions for ferromagnetic coupling. Due to geometrical packing constraints, $t_{ij}^{00} \approx t_{ij}^{01}, t_{ij}^{10}, t_{ij}^{11}$ for the spiro-phenalenyl or $t_{ij}^{00} \approx t_{ij}^{0-1}, t_{ij}^{-10}, t_{ij}^{-1-1}$ for the ET salts. This follows from the fact that the SOMO and HOMO/LUMO in such dimeric materials are simply in-phase and out-of-phase combinations of local monomer orbitals $|0_i\rangle, |1_i\rangle = \frac{1}{\sqrt{2}} (|a_i\rangle \pm |b_i\rangle)$. This implies, for **1-30**,

the hopping integrals follow:

$$t_{ij}^{00} = \frac{1}{2} (t_{ij}^{aa} + t_{ij}^{ab} + t_{ij}^{ba} + t_{ij}^{bb}) \quad (2.44)$$

$$t_{ij}^{01} = \frac{1}{2} (t_{ij}^{aa} - t_{ij}^{ab} + t_{ij}^{ba} - t_{ij}^{bb}) \quad (2.45)$$

$$t_{ij}^{10} = \frac{1}{2} (t_{ij}^{aa} + t_{ij}^{ab} - t_{ij}^{ba} - t_{ij}^{bb}) \quad (2.46)$$

$$t_{ij}^{11} = \frac{1}{2} (t_{ij}^{aa} - t_{ij}^{ab} - t_{ij}^{ba} + t_{ij}^{bb}) \quad (2.47)$$

However, by geometrical considerations, only one monomer from each dimer site is expected to interact strongly, so that $t_{ij}^{aa} \gg t_{ij}^{ab}, t_{ij}^{ba}, t_{ij}^{bb}$, for example. Therefore all hopping integrals in the dimer basis are nearly equal, and antiferromagnetic interactions are expected to dominate. It is thus not surprising that such materials do not display ferromagnetism.

2.2 Role of Spin-Orbit Effects in Magnetism

2.2.1 Introduction

In a semiclassical picture, spin-orbit coupling (SOC) is a relativistic effect that involves the interaction of the electronic spins with the magnetic field generated by their own orbital motion.^{137–139} The Hamiltonian associated with this effect is often written with respect to field operators:

$$\mathcal{H}_{SO} = \sum_{s,s'} \int_{\mathbf{x}} \int_{\mathbf{r}} \psi_s^\dagger(\mathbf{x}) \left[\frac{-i\hbar\mu_B}{mc^2} \frac{1}{r} \frac{\partial u(\mathbf{r})}{\partial r} (\mathbf{r} \times \nabla_{\mathbf{x}}) \cdot \mathbf{S} \right] \psi_{s'}(\mathbf{x}) \quad (2.48)$$

where $u(\mathbf{r})$ is an effective one-electron potential. Chemists usually first meet this interaction in the context of hyperfine splitting of single atomic energy levels.^{140,141} In this case, $u(\mathbf{r})$ is a central potential, and $-i\hbar(\mathbf{r} \times \nabla_{\mathbf{x}}) = \mathbf{L}$ is the angular momentum about the atomic center. The Hamiltonian can be rewritten in the more familiar form:

$$\mathcal{H}_{SOC}^{\text{hyd}} = \lambda \mathbf{L} \cdot \mathbf{S} \quad (2.49)$$

where λ is the spin-orbit constant is the expectation value:

$$\lambda = \left\langle \frac{e^2}{2m_e^2 c^2} \frac{Z_{eff}}{r^3} \right\rangle \quad (2.50)$$

where Z_{eff} is the screened effective charge of the atomic nucleus. For atoms with only one electron, $Z_{eff} = Z$ and $\langle r^3 \rangle \propto (n/Z)^3$, where n is the principle quantum number. From this discussion one can see that the strength of spin-orbit coupling will tend to increase significantly in heavier elements, naively as $\lambda \sim Z^4/n^3$. For example, in isolated neutral chalcogen atoms:¹⁴²

$$\lambda_S = 0.06 \text{ eV} \quad \lambda_{Se} = 0.22 \text{ eV} \quad \lambda_{Te} = 0.49 \text{ eV}$$

For this reason, spin-orbit coupling becomes most prominent in heavy atom materials. In the solid state, the mixing of spin and orbital angular momentum produces anisotropic exchange interactions between the resulting local moments. In heavy element radicals incorporating S and especially Se , such interactions can play a prominent role in the magnetic response, as discussed in chapter 6.

2.2.2 Qualitative Aspects of Atomic Spin-Orbit Coupling

In this section, we consider an artificial example that allows for understanding of the salient aspects of spin-orbit coupling in p -block materials. Consider the case of a single atom, with a single electron confined to occupy a particular p -orbital manifold. For the isolated atom, the Hamiltonian commutes with the total spin \mathbf{S}^2 , orbital angular momentum \mathbf{L}^2 and total angular momentum \mathbf{J}^2 operators; it is thus conventional to label states by the term symbol $(^{2S+1})L_J$. In the absence of spin-orbit coupling, all term symbols are degenerate. When spin-orbit coupling is turned on, the states are split such that the ground state is the Kramers' doublet $^2P_{1/2}$. The two components of this doublet with $m_J^z = \pm 1/2$ may be represented in terms of pure spin and orbital states as:

$$|^2P_{1/2}, +1/2\rangle_J = \sqrt{\frac{1}{3}}|p_0, \uparrow\rangle_S - \sqrt{\frac{2}{3}}|p_+, \downarrow\rangle_S \quad (2.51)$$

$$|^2P_{1/2}, -1/2\rangle_J = \sqrt{\frac{1}{3}}|p_0, \downarrow\rangle_S - \sqrt{\frac{2}{3}}|p_-, \uparrow\rangle_S \quad (2.52)$$

where the states on the left are pure J -states, indicated by a subscript J , while those on the right are pure S -states for which \uparrow (\downarrow) indicates $m_S^z = +1/2$ ($-1/2$). Here, we have also introduced the pure angular momentum orbitals with $m_L^z = 0, +1, -1$, respectively:

$$|p_0\rangle = |p_z\rangle \quad , \quad |p_+\rangle = \sqrt{\frac{1}{2}}(|p_x\rangle - i|p_y\rangle) \quad , \quad |p_-\rangle = \sqrt{\frac{1}{2}}(|p_x\rangle + i|p_y\rangle) \quad (2.53)$$

In terms of these orbitals, quartet- J manifold appearing at higher energy is given by:

$$|^2P_{3/2}, +3/2\rangle_J = |p_+, \uparrow\rangle_S \quad (2.54)$$

$$|^2P_{3/2}, +1/2\rangle_J = \sqrt{\frac{2}{3}}|p_0, \uparrow\rangle_S + \sqrt{\frac{1}{3}}|p_+, \downarrow\rangle_S \quad (2.55)$$

$$|^2P_{3/2}, -1/2\rangle_J = \sqrt{\frac{2}{3}}|p_0, \downarrow\rangle_S + \sqrt{\frac{1}{3}}|p_-, \uparrow\rangle_S \quad (2.56)$$

$$|^2P_{3/2}, -3/2\rangle_J = |p_-, \downarrow\rangle_S \quad (2.57)$$

Taken together, these states form an appropriate one-electron basis even for describing multi-electron states at strong spin-orbit coupling, as in the so-called $j-j$ coupling scheme. The ground state of atomic Pb, for example, is well described as a J -singlet with one electron occupying the $j = 1/2, m_j^z = +1/2$ state of eq'n (2.51), and one electron occupying the $j = 1/2, m_j^z = -1/2$ state of eq'n (2.52).¹⁴³ It is important to note, however, that while these one-electron states are eigenstates of J_z , they are clearly not eigenstates of either L_z or S_z . Indeed, the effect of spin-orbit coupling is to mix states of different m_S and m_L values. In the presence of a crystal field, the effects of spin-orbit coupling may be mitigated. Returning to the one-electron example, consider an equatorial crystal field such that $\epsilon_{p_+} = \epsilon_{p_-} = \epsilon_{p_0} + \Delta\epsilon$. As $\Delta\epsilon$ is increased, the increasing cost of occupying the $|p_-\rangle$ and $|p_+\rangle$ orbitals modifies the composition of the eigenstates (Fig. 2.3). For example, as $\Delta\epsilon/\lambda \rightarrow \infty$, the ground state becomes a pure spin doublet $\{|p_0, \uparrow\rangle, |p_0, \downarrow\rangle\}$, in which only the p_0 orbitals are occupied and all orbital momentum has been quenched. For arbitrary coupling, the two-fold degeneracy of the ground state is ensured by Kramers' theorem, and time-reversed pairs can be written:

$$|(+)\rangle = \gamma|p_0, \uparrow\rangle_S - \sqrt{1 - \gamma^2}|p_+, \downarrow\rangle_S \quad (2.58)$$

$$|(-)\rangle = \gamma|p_0, \downarrow\rangle_S - \sqrt{1 - \gamma^2}|p_-, \uparrow\rangle_S \quad (2.59)$$

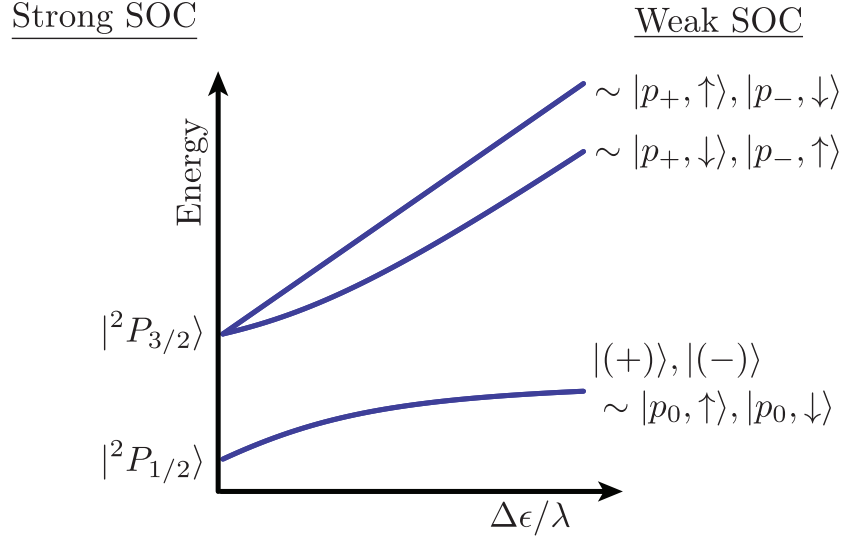


Figure 2.3: Evolution of the one-electron state energies as a function of crystal field splitting $\Delta\epsilon$ for single atom model. The ground state remains a Kramers' doublet at all relative strengths of spin-orbit coupling, but the admixture of pure spin and orbital functions changes.

where $\gamma \rightarrow 1$ as $\lambda/\Delta\epsilon \rightarrow 0$, and $\gamma \rightarrow \sqrt{1/3}$ as $\lambda/\Delta\epsilon \rightarrow \infty$. Similarly, the second quantized operators associated with these one-electron states are:

$$\tilde{c}_{(+)}^\dagger = \gamma c_{p0,\uparrow}^\dagger - \sqrt{1-\gamma^2} c_{p+,\downarrow}^\dagger, \quad \tilde{c}_{(-)}^\dagger = \gamma c_{p0,\downarrow}^\dagger - \sqrt{1-\gamma^2} c_{p+,\uparrow}^\dagger \quad (2.60)$$

$$\tilde{\mathbf{c}}^\dagger(\gamma) = \begin{pmatrix} \tilde{c}_{(+)}^\dagger & \tilde{c}_{(-)}^\dagger \end{pmatrix}, \quad \tilde{\mathbf{c}}(\gamma) = \begin{pmatrix} \tilde{c}_{(+)} \\ \tilde{c}_{(-)} \end{pmatrix} \quad (2.61)$$

Suppose we embed our atom into a crystal, find that electrons are localized to these states, and wish to describe the magnetic properties of such electrons. This description is hampered by the fact that at intermediate coupling, $|(+)\rangle$ and $|(-)\rangle$ are neither eigenstates of spin nor total angular momentum invalidating use of either \mathbf{S} or \mathbf{J} operators to construct our effective magnetic Hamiltonian. However, one may define analogous pseudospin operators:

$$\tilde{\mathbf{S}} = \tilde{\mathbf{c}}^\dagger(\gamma) \vec{\sigma} \tilde{\mathbf{c}}(\gamma) \quad (2.62)$$

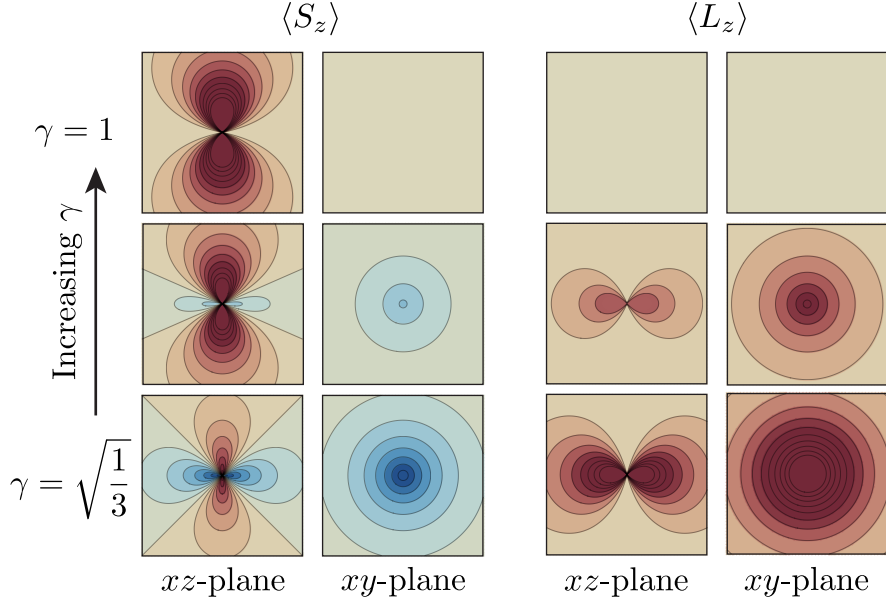


Figure 2.4: Anatomy of the $|(+)\rangle$ state as a function of γ . At all values of γ , this state is an eigenstate \tilde{S}_z , and therefore has well defined pseudospin along the z -direction. The expectation values of the pure spin and pure angular momentum density along the same direction are shown. Positive values are shown in red, and negative values in blue. For $\gamma = 0$, $|(+)\rangle = |p_z, \uparrow\rangle_S$; the spin density is confined entirely to the p_z orbital, and the expectation value of the angular momentum is zero everywhere. For $\gamma = \sqrt{1/3}$, $|(+)\rangle = |^2P_{1/2}, +1/2\rangle$ and has significant angular momentum component to the total moment.

that have the usual properties of angular momentum operators, but act in the intermediate basis. For example:

$$\tilde{S}_z|(+)\rangle = +\frac{1}{2}|(+)\rangle \quad , \quad \tilde{S}_z|(-)\rangle = -\frac{1}{2}|(-)\rangle \quad (2.63)$$

While these operators may appear to be purely mathematical constructions, they represent approximately the true physically observable magnetic moment at intermediate coupling. In the appropriate limits, $\tilde{\mathbf{S}}$ becomes equal to either \mathbf{S} or \mathbf{J} . At intermediate coupling, the total pseudospin moment is composed, very roughly speaking, of different parts real spin and real orbital components. In order to visualize such components, it is useful to consider expectation values of spin and orbital angular momentum density $\langle S_z \delta(\mathbf{r}) \rangle$ and $\langle L_z \delta(\mathbf{r}) \rangle$, along the pseudospin quantization axis (z -axis), as shown in Fig. 2.4 for $|(+)\rangle$. For $\lambda = 0$,

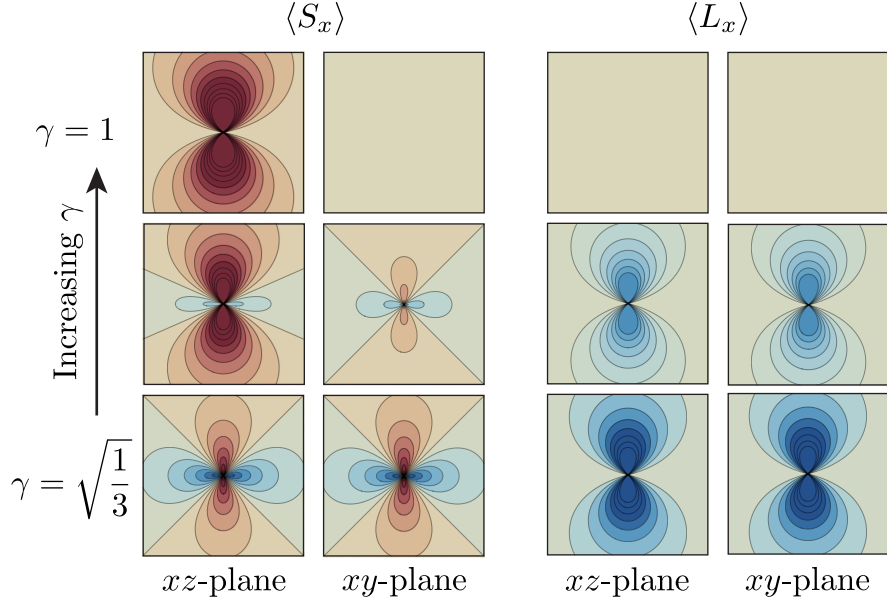


Figure 2.5: Anatomy of the $|R\rangle$ state as a function of γ . The expectation values of the pure spin and pure angular momentum density along the x -direction are shown. The pattern of spin density can be compared with that of $|+\rangle$ shown in Fig. 2.4.

or $\gamma = 1$, the state is a pure spin state, with positive spin density localized to the p_z orbital. As may already be seen from eq'n (2.58), increasing $\lambda/\Delta\epsilon$ introduces an orbital component to the magnetic moment, which is offset by negative spin-density through mixing with the $|p_{+,\downarrow}\rangle_S$ state. The key observation is that this pattern of orbital and spin density depends on the orientation of the overall pseudospin moment with respect to the crystal field. For example we may equally define pseudospin states that are eigenstates of \tilde{S}_x ; these are given by:

$$|R\rangle = \sqrt{\frac{1}{2}} (|+\rangle + |-\rangle) \quad (2.64)$$

$$|L\rangle = \sqrt{\frac{1}{2}} (|+\rangle - |-\rangle) \quad (2.65)$$

$$\tilde{S}_x|R\rangle = +\frac{1}{2}|R\rangle \quad , \quad \tilde{S}_x|L\rangle = -\frac{1}{2}|L\rangle \quad (2.66)$$

where $|(R)\rangle$ has a well defined pseudospin moment along the right direction, and $|(L)\rangle$ has a pseudospin moment along the left direction. The spin and angular momentum densities $\langle S_x \delta(\mathbf{r}) \rangle$ and $\langle L_x \delta(\mathbf{r}) \rangle$ of this state are shown in Fig. 2.5. In this case, the induced orbital moment actually opposes the majority spin moment, and the pattern of induced spin density in the xy -plane is altered with respect to $|(+)\rangle$. These observations highlight two important characteristics of the pseudospin moments:

- The pseudospin states are generally composed of linear combinations of pure spin and angular momentum functions. The specific contributions to the pseudospin moment by such functions depend on the orientation of the moment with respect to the crystal field. This has an important consequence on the Zeeman splitting of pseudospin states when placed in an external magnetic field, for which the Hamiltonian is generally written:

$$\mathcal{H} = \sum_i \tilde{\mathbf{S}}_i \cdot \mathbf{g} \cdot \mathbf{H}_{ext} \quad (2.67)$$

Specifically, because g -values of pure spin and orbital moments differ by a factor of two, the Zeeman splitting of pseudospin moments are generally anisotropic; this is roughly speaking the origin of the so-called Orbital-Zeeman contribution to anisotropy of the \mathbf{g} -tensor.¹⁴⁴

- When considering the interactions between such pseudospin moments, it is important to note that the magnetic interactions typically depend *only* on the spin components of the pseudospin state. Since this component is orientation dependent, such interactions may be energetically minimized only for specific orientations of the pseudospin moments both with respect to one another, and the crystal field. Thus the interactions between pseudospin moments are typically anisotropic, with interactions reduced to the symmetry of the local crystalline environment.

Finally, we note that while this section considered only single electrons in atomic p -orbitals, many of the salient aspects apply equally to many-electron organic radicals in which the unpaired electron is contained in a π -SOMO. This molecular orbital can be considered a

linear combination of p_z orbitals centred on different atoms. The action of spin-orbit coupling is to mix the SOMO with orbitals of p_x and p_y character making up the σ -bonding framework. In this way, the crystal field splitting the atomic orbitals in the above example represents the energetic splitting of such molecular orbitals due to covalent bonding interactions in molecules. This analogy will be useful in sections 6.2.3 and 7.3.4; next we describe how to construct anisotropic exchange Hamiltonians for molecular systems.

2.2.3 Derivation of Anisotropic Exchange Hamiltonians

Mean Field Molecular One-Electron SOC Operators

In this section, we review the construction of spin-orbit coupling operators appropriate for molecular systems with many electrons. The mean-field decoupling scheme is attributed originally to Hess,^{145,146} and has since been implemented by Neese and coworkers¹⁴⁷ in the ab-initio program ORCA.¹⁴⁸ The discussion in this section follows closely Ref. 147. In the semi-classical picture, spin-orbit coupling arises because in the rest frame of an electron orbiting a charged body, the relative motion of the charged body appears as a magnetic field which couples to the electron spin.¹³⁸ The treatment of spin-orbit coupling in molecules begins from the Breit-Pauli Hamiltonian, which is comprised of three components:

$$\mathcal{H}_{SO}^{BP} = \mathcal{H}_{SOC}^{(1)} + \mathcal{H}_{SOC}^{(2)} + \mathcal{H}_{SOO}^{(2)} \quad (2.68)$$

The first term in eq'n (2.68) is a one-electron term that describes the interaction between the electron labelled $\{k\}$ and its own orbit about the positively charged nuclei $\{A\}$:

$$\mathcal{H}_{SOC}^{(1)} = \frac{e^2}{2m_e^2 c^2} \sum_{A,k} \frac{Z_A}{r_{A,k}^3} \mathbf{L}_{A,k} \cdot \mathbf{S}_k \quad (2.69)$$

$$\equiv \frac{1}{2} \sum_{\alpha,\beta,\mu} \langle \alpha | g_1^\mu | \beta \rangle \mathbf{c}_{i,\alpha}^\dagger \sigma_\mu \mathbf{c}_{i,\beta} \quad (2.70)$$

where Z_A is the atomic number of nucleus A , $r_{a,b}$ is the absolute distance between a and b and $\mathbf{L}_{a,b} = \mathbf{r}_{a,b} \times \mathbf{p}_b$ is the angular momentum of b about a . The second term in eq'n (2.68) is a two-electron term that describes the coupling between an electron spin its and

own orbit around other negatively charged electrons labelled $\{l\}$ which screen the nuclear charges:

$$\mathcal{H}_{SOC}^{(2)} = -\frac{e^2}{2m_e^2c^2} \sum_{k \neq l} \frac{1}{r_{k,l}^3} \mathbf{L}_{l,k} \cdot \mathbf{S}_k \quad (2.71)$$

$$\equiv -\frac{1}{2} \sum_{\alpha, \beta, \delta, \gamma, \mu} \langle \delta \alpha | g_2^\mu | \beta \gamma \rangle \mathbf{c}_{i,\delta}^\dagger \left(\mathbf{c}_{i,\alpha}^\dagger \sigma_\mu \mathbf{c}_{i,\beta} \right) \mathbf{c}_{i,\gamma} \quad (2.72)$$

The final term is the so-called spin-other-orbit term which accounts for the coupling between the spin of electron l to the real orbit, in the laboratory frame, of electron k :

$$\mathcal{H}_{SOO}^{(2)} = -2 \frac{e^2}{2m_e^2c^2} \sum_{k \neq l} \frac{1}{r_{k,l}^3} \mathbf{L}_{l,k} \cdot \mathbf{S}_l \quad (2.73)$$

$$\equiv - \sum_{\alpha, \beta, \delta, \gamma, \mu} \langle \delta \alpha | g_2^\mu | \beta \gamma \rangle \mathbf{c}_{i,\alpha}^\dagger \left(\mathbf{c}_{i,\delta}^\dagger \sigma_\mu \mathbf{c}_{i,\gamma} \right) \mathbf{c}_{i,\beta} \quad (2.74)$$

The presence of the two-electron terms makes full evaluation of the spin-orbit operator computationally expensive. However, accurate results can be obtained from an effective one-electron operator obtained by making a mean-field decomposition of the two-electron terms similar to the Hartree-Fock approximation for Coulomb repulsion. After some further approximations one arrives at:

$$\mathcal{H}_{SOC}^{MF} = \frac{1}{2} \sum_{\alpha, \beta, \mu} \langle \alpha | \mathcal{L}_i^\mu | \beta \rangle \mathbf{c}_{i,\alpha}^\dagger \sigma_\mu \mathbf{c}_{i,\beta} \quad (2.75)$$

with the matrix elements of the pseudo-angular momentum operator \mathcal{L}_i^μ given by:

$$\begin{aligned} \langle \alpha | \mathcal{L}_i^\mu | \beta \rangle = & \langle \alpha | g_1^\mu | \beta \rangle - \frac{1}{2} \sum_{\delta} n_{i,\delta} [2 \langle \delta \alpha | g_2^\mu | \beta \delta \rangle \\ & - 3 \langle \delta \alpha | g_2^\mu | \delta \beta \rangle - 3 \langle \alpha \delta | g_2^\mu | \beta \delta \rangle] \end{aligned} \quad (2.76)$$

It is worth noting that \mathcal{H}_{SOC}^{MF} does not explicitly contain the spin-orbit constant λ , which follows from that fact that the strength of spin-orbit coupling of any two molecular orbitals cannot be related to a single energy scale as it can for atomic orbitals.

Moriya's Approach to Anisotropic Exchange

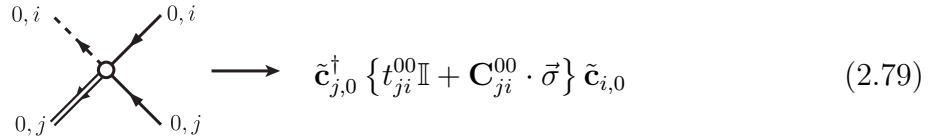
The first major development in the theory of anisotropic exchange was due to Dzyaloshinskii, who observed that weak ferromagnet moments in compounds such as $\alpha\text{-Fe}_2\text{O}_3$ (resulting from spin-canting) could arise due to symmetry-allowed terms in the magnetic free energy like $\mathbf{S}_i \times \mathbf{S}_j$.¹⁴⁹ The origin of such terms was explained by Moriya, who extended Anderson's super exchange theory to include local spin-orbit coupling.¹⁵⁰ Moriya's approach was to assume that spin-orbit effects could be described entirely in terms of a rotation of the local single particle operators into the pseudospin basis described in section 2.2.2:

$$\tilde{\mathbf{c}}_{i,\alpha}^\dagger = \mathbf{c}_{i,\alpha}^\dagger + \frac{1}{2} \sum_{\beta} \frac{\vec{\mathcal{L}}_i^{\beta\alpha} \cdot \vec{\sigma}}{\epsilon_{\beta} - \epsilon_{\alpha}} \mathbf{c}_{i,\beta}^\dagger + \mathcal{O}(\mathcal{L}^2) \quad (2.77)$$

where $\vec{\mathcal{L}}_i^{\alpha\beta}$ is given by:

$$\vec{\mathcal{L}}_i^{\alpha\beta} = \langle \alpha_i | \mathcal{L}_i^x | \beta_i \rangle \hat{i} + \langle \alpha_i | \mathcal{L}_i^y | \beta_i \rangle \hat{j} + \langle \alpha_i | \mathcal{L}_i^z | \beta_i \rangle \hat{k} \quad (2.78)$$

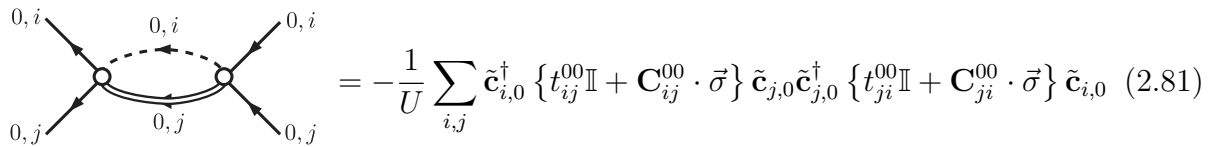
The key observation is that, while hopping preserves the electron spin, it generally does not preserve the pseudospin. Therefore, after rotation into this basis, the hopping vertex must be replaced by a 2×2 matrix quantity:



where \mathbf{C}_{ij} is Moriya's spin-orbit mediated hopping parameter given by:

$$\mathbf{C}_{ij}^{00} = \frac{1}{2} \sum_{\alpha} \left\{ \frac{\vec{\mathcal{L}}_i^{0\alpha}}{\Delta\epsilon_i^{\alpha}} t_{ij}^{\alpha 0} + t_{ij}^{0\alpha} \frac{\vec{\mathcal{L}}_j^{\alpha 0}}{\Delta\epsilon_j^{\alpha}} \right\} + \mathcal{O}(\mathcal{L}^2) \quad (2.80)$$

It is worth noting that, in the case where the SOMO is non degenerate, then the orbital functions $|0_i\rangle$ and $|\alpha_i\rangle$ can always be chosen to be completely real without loss of generality. This implies that \mathbf{C}_{ij}^{00} is completely imaginary, and has the property $\mathbf{C}_{ij}^{00} = (\mathbf{C}_{ji}^{00})^* = -\mathbf{C}_{ji}^{00}$. In terms of this modified hopping operator, the lowest order hopping diagram is:



This term represents the modified antiferromagnetic component of the exchange when rotated into the pseudospin basis. Ignoring constant terms, and using eq'n (A.18), this can be written:

$$+\frac{1}{U} \sum_{i,j} \tilde{\mathbf{c}}_{i,0}^\dagger \{t_{ij}^{00}\mathbb{I} + \mathbf{C}_{ij}^{00} \cdot \vec{\sigma}\} \tilde{\mathbf{S}}_j \cdot \vec{\sigma} \{t_{ji}^{00}\mathbb{I} + \mathbf{C}_{ji}^{00} \cdot \vec{\sigma}\} \tilde{\mathbf{c}}_{i,0} \quad (2.82)$$

This may be evaluated using identities (A.15) and (A.16). After summation over internal indices, the effective Hamiltonian is:

$$\mathcal{H}_{\text{eff}} = \sum_{\langle i,j \rangle} \mathcal{J}_{ij} \tilde{\mathbf{S}}_i \cdot \tilde{\mathbf{S}}_j + \mathbf{D}_{ij} \cdot \tilde{\mathbf{S}}_i \times \tilde{\mathbf{S}}_j + \tilde{\mathbf{S}}_i \cdot \mathbf{\Gamma}_{ij} \cdot \tilde{\mathbf{S}}_j \quad (2.83)$$

$$\mathcal{J}_{ij} = \frac{4}{U} \{ (t_{ij}^{00})^2 - |\mathbf{C}_{ij}^{00} \cdot \mathbf{C}_{ji}^{00}| \} \quad (2.84)$$

$$\mathbf{D}_{ij} = \frac{4i}{U} \{ t_{ij}^{00} \mathbf{C}_{ji}^{00} - \mathbf{C}_{ij}^{00} t_{ji}^{00} \} \quad (2.85)$$

$$\mathbf{\Gamma}_{ij} = \frac{4}{U} \{ \mathbf{C}_{ij}^{00} \otimes \mathbf{C}_{ji}^{00} + \mathbf{C}_{ji}^{00} \otimes \mathbf{C}_{ij}^{00} \} \quad (2.86)$$

The first of these terms, parameterized by \mathcal{J}_{ij} , is the isotropic (antiferromagnetic) exchange between pseudospin moments. There is a small ferromagnetic spin-orbit correction that arises due to relaxation of the Pauli exclusion blockage for hopping of pseudospin electrons onto the same site. The second term is the celebrated Dzyaloshinskii-Moriya antisymmetric interaction, which is minimized when local spins are orthogonal to one another, and thus is often responsible for spin-canting in the solid state. The third pseudo-dipolar term provides an energetic preference for collinear orientation of pseudospins along specific crystallographic directions. In chapter 6, we discuss the role of this latter term in the magnetic anisotropy of Se-based radical ferromagnets.

The next significant advance in the understanding of anisotropic exchange was not made until 35 years after the publication of Moriya's work, when Yildirim et. al. pointed out that the single-particle pseudospin transformation was generally inappropriate for studying more complicated models.^{151,152} In particular, they noted an anomalous symmetry of Moriya's expressions $\mathbf{\Gamma}_{ij} \propto \mathbf{D}_{ij} \otimes \mathbf{D}_{ij}$, which does not follow from any fundamental symmetry of the lattice.^{153,154} In fact, this symmetry is only preserved if one neglects all Hund's coupling between excited states, and assumes that Coulomb repulsion is orbital independent. When either of these conditions are violated, the excited charged states (in the upper

pseudospin Hilbert space) are not obtained simply in terms of the defined $\tilde{\mathbf{c}}_{i,\alpha}^\dagger$ operators.² To see this, note that for non constant U , the pair of creation operators describing a state with two electrons at the same site transform as:

$$\mathbf{c}_{i,\alpha}^\dagger \mathbf{c}_{i,\beta}^\dagger \rightarrow \frac{\lambda}{2} \sum_{\gamma} \frac{(\langle \gamma_i | \mathbf{L} | \alpha_i \rangle \cdot \vec{\sigma}_{i,\gamma}^\dagger) \mathbf{c}_{i,\beta}^\dagger}{\epsilon_{\gamma} - \epsilon_{\alpha} + U_i^{\gamma\beta} - U_i^{\alpha\beta}} + \frac{\mathbf{c}_{i,\alpha}^\dagger (\langle \gamma_i | \mathbf{L} | \beta_i \rangle \cdot \vec{\sigma}_{i,\gamma}^\dagger)}{\epsilon_{\gamma} - \epsilon_{\alpha} + U_i^{\gamma\alpha} - U_i^{\alpha\beta}} + \mathcal{O}(\lambda^2) \quad (2.87)$$

which can generally not be decomposed into the pseudospin operators $\tilde{\mathbf{c}}_{i,\alpha}^\dagger \tilde{\mathbf{c}}_{i,\beta}^\dagger$ due to the discrepancies in the energy denominator. Yildirim et. al. showed how Hund's coupling and the deviation from uniform U could be accounted for perturbatively, within the pseudospin basis.¹⁵² The major advantage of their approach is that the pseudospin basis may be defined arbitrarily, so the form of the resulting effective Hamiltonian is valid to any order in spin-orbit coupling. The disadvantage is that spin-orbit corrections enter into the effective Hamiltonian through modifications to both the $\mathcal{H}_1 = \mathcal{T} + \mathcal{Q}$ vertices and state energies (i.e \mathcal{G}_U^0), which becomes particularly inconvenient to actually evaluate at finite order.

In this light, it is useful to note that the pseudospin operators $\tilde{\mathbf{S}}_i$ are adiabatically connected to the real spin operators \mathbf{S}_i as spin-orbit coupling $\lambda \rightarrow 0$. For this reason, we can choose to label the true pseudospin states in terms of the zeroth order pure spin quantum numbers. It is possible therefore to derive identical effective anisotropic exchange Hamiltonians directly in terms of the unphysical pure spin basis, provided that spin-orbit coupling is added to the perturbing Hamiltonian \mathcal{H}_1 . This approach, while mathematically less elegant, facilitates calculation of exact Hund's coupling corrections, and admits a simple diagrammatic expansion. In the following sections, we show how Moriya's results may be reproduced in this approach, and go on to investigate the effect of multi-orbital exchange on the anisotropic terms.

²This observation should not be surprising to chemists because it is precisely the reason why different spin-orbit coupling schemes are necessary to predict energetic ordering of atomic term symbols in either the $K \gg \lambda$ limit (Russell-Saunders) or $K \ll \lambda$ limit ($j - j$ coupling). The Hund's and spin-orbit coupling don't commute, and so do not have simultaneous eigenstates.

Diagrammatic Derivation of Anisotropic Hopping Exchange Terms

The mean-field form of the spin-orbit Hamiltonian derived in the previous section appears as an on-site hopping term that is spin-dependent. In this way, it may be represented diagrammatically in an analogous fashion to the hopping operator \mathcal{T} :

$$\mathcal{H}_{SOC}^{MF} = \sum_{i,\alpha,\beta} \left(\begin{array}{cccc} \begin{array}{c} \alpha, i \\ \beta, i \end{array} \begin{array}{c} \alpha, i \\ \beta, i \end{array} & + & \begin{array}{c} \alpha, i \\ \beta, i \end{array} \begin{array}{c} \alpha, i \\ \beta, i \end{array} & + & \begin{array}{c} \alpha, i \\ \beta, i \end{array} \begin{array}{c} \alpha, i \\ \beta, i \end{array} & + & \begin{array}{c} \alpha, i \\ \beta, i \end{array} \begin{array}{c} \alpha, i \\ \beta, i \end{array} & + \text{h.c.} \end{array} \right) \quad (2.88)$$

where the SOC vertex is represented by a filled circle, and is translated for all the above diagrams as the compact form $\frac{1}{2}\mathbf{c}_{i,\alpha}^\dagger(\vec{\mathcal{L}}_i^{\alpha\beta} \cdot \vec{\sigma})\mathbf{c}_{i,\beta}$. With the inclusion of spin-orbit coupling, we divide the Hamiltonian as:

$$\mathcal{H}_0 = \mathcal{E} + \mathcal{U} \quad (2.89)$$

$$\mathcal{H}_1 = \mathcal{T} + \mathcal{K} + \mathcal{Q} + \mathcal{H}_{SOC}^{MF} \quad (2.90)$$

The lowest order diagrams incorporating \mathcal{H}_{SOC}^{MF} appear at order $t^2\mathcal{L}$:

$$\begin{array}{c} \begin{array}{c} 0, j \\ 0, i \end{array} \begin{array}{c} 0, i \\ \alpha, i \end{array} \\ \begin{array}{c} \alpha, i \\ 0, j \end{array} \end{array} = \mathbb{P}_L^0 \sum_{i,j,\alpha} \frac{t_{ij}^{00} t_{ji}^{0\alpha}}{2U_i^\alpha \Delta\epsilon_i^\alpha} \mathbf{c}_{i,0}^\dagger \mathbf{c}_{j,0} \mathbf{c}_{j,0}^\dagger \mathbf{c}_{i,\alpha} \mathbf{c}_{i,\alpha}^\dagger (\vec{\mathcal{L}}_i^{\alpha 0} \cdot \vec{\sigma}) \mathbf{c}_{i,0} \mathbb{P}_L^0 \quad (2.91)$$

$$\begin{array}{c} \begin{array}{c} \alpha, i \\ 0, i \end{array} \begin{array}{c} 0, i \\ 0, j \end{array} \\ \begin{array}{c} 0, i \\ 0, j \end{array} \end{array} = \mathbb{P}_L^0 \sum_{i,j,\alpha} \frac{t_{ij}^{\alpha 0} t_{ji}^{00}}{2\Delta\epsilon_i^\alpha U} \mathbf{c}_{i,0}^\dagger (\vec{\mathcal{L}}_i^{0\alpha} \cdot \vec{\sigma}) \mathbf{c}_{i,\alpha} \mathbf{c}_{i,\alpha}^\dagger \mathbf{c}_{j,0} \mathbf{c}_{j,0}^\dagger \mathbf{c}_{i,0} \mathbb{P}_L^0 \quad (2.92)$$

$$= \mathbb{P}_L^0 \sum_{i,j,\alpha} \frac{t_{ij}^{00} t_{ji}^{\alpha 0}}{2U(\Delta\epsilon_j^\alpha + U)} \mathbf{c}_{i,0}^\dagger \mathbf{c}_{j,0} \mathbf{c}_{j,0}^\dagger (\vec{\mathcal{L}}_j^{0\alpha} \cdot \vec{\sigma}) \mathbf{c}_{j,\alpha} \mathbf{c}_{j,\alpha}^\dagger \mathbf{c}_{i,0} \mathbb{P}_L^0 \quad (2.93)$$

$$= \mathbb{P}_L^0 \sum_{i,j,\alpha} \frac{t_{ij}^{0\alpha} t_{ji}^{00}}{2(\Delta\epsilon_j^\alpha + U)U} \mathbf{c}_{i,0}^\dagger \mathbf{c}_{j,\alpha} \mathbf{c}_{j,\alpha}^\dagger (\vec{\mathcal{L}}_j^{\alpha 0} \cdot \vec{\sigma}) \mathbf{c}_{j,0} \mathbf{c}_{j,0}^\dagger \mathbf{c}_{i,0} \mathbb{P}_L^0 \quad (2.94)$$

$$= \mathbb{P}_L^0 \sum_{i,j,\alpha} \frac{t_{ij}^{0\alpha} t_{ij}^{00}}{2(\Delta\epsilon_i^\alpha + U)\Delta\epsilon_i^\alpha} \mathbf{c}_{j,0}^\dagger \mathbf{c}_{i,\alpha} \mathbf{c}_{i,0}^\dagger \mathbf{c}_{j,0} \mathbf{c}_{i,\alpha}^\dagger (\vec{\mathcal{L}}_i^{\alpha 0} \cdot \vec{\sigma}) \mathbf{c}_{i,0} \mathbb{P}_L^0 \quad (2.95)$$

$$= \mathbb{P}_L^0 \sum_{i,j,\alpha} \frac{t_{ij}^{00} t_{ji}^{\alpha 0}}{2\Delta\epsilon_j^\alpha (\Delta\epsilon_j^\alpha + U)} \mathbf{c}_{j,0}^\dagger (\vec{\mathcal{L}}_j^{0\alpha} \cdot \vec{\sigma}) \mathbf{c}_{j,\alpha} \mathbf{c}_{i,0}^\dagger \mathbf{c}_{j,0} \mathbf{c}_{j,\alpha}^\dagger \mathbf{c}_{i,0} \mathbb{P}_L^0 \quad (2.96)$$

All of the above diagrams represent the mixing of the SOMO with empty orbitals through spin-orbit coupling. Analogous diagrams may be drawn with all double and dashed lines reversed representing the mixing with filled orbitals. However, as these diagrams evaluate to precisely the same expressions, they are omitted for brevity. Using identity (A.15), and the fact that:

$$\frac{1}{\Delta\epsilon_\alpha(\Delta\epsilon_\alpha + U)} + \frac{1}{U(\Delta\epsilon_\alpha + U)} + \frac{1}{\Delta\epsilon_\alpha U} = \frac{2}{U\Delta\epsilon_\alpha} \quad (2.97)$$

it is easy to show that the full summation over third order diagrams (2.91)-(2.96) gives the expected expression for the Dzyaloshinskii-Moriya (DM) antisymmetric exchange interac-

The second two sets of diagrams involve interchange of electrons at sites i, j without double occupation of any orbital:

$$\begin{aligned}
& \left(\begin{array}{c} \text{Diagram 1: } \alpha, j \text{ and } \beta, i \text{ electrons at site } i, \text{ with } 0, i \text{ and } 0, j \text{ orbitals.} \\ \text{Diagram 2: } \beta, i \text{ and } \alpha, j \text{ electrons at site } j, \text{ with } 0, i \text{ and } 0, j \text{ orbitals.} \end{array} \right) \\
& = \mathbb{P}_L^0 \sum_{i,j,\alpha,\beta} \frac{-t_{ji}^{0\beta} t_{ij}^{0\alpha}}{4(\Delta\epsilon_j^\alpha + \Delta\epsilon_i^\beta)(\Delta\epsilon_i^\beta + U)} \left\{ \mathbf{c}_{j,0}^\dagger \mathbf{c}_{i,\beta} \mathbf{c}_{i,0}^\dagger \mathbf{c}_{j,\alpha} \right\} \times \\
& \times \left\{ \frac{1}{\Delta\epsilon_j^\alpha} \mathbf{c}_{i,\beta}^\dagger (\vec{\mathcal{L}}_i^{\beta 0} \cdot \vec{\sigma}) \mathbf{c}_{i,0} \mathbf{c}_{j,\alpha}^\dagger (\vec{\mathcal{L}}_j^{\alpha 0} \cdot \vec{\sigma}) \mathbf{c}_{j,0} + \frac{1}{\Delta\epsilon_i^\beta} \mathbf{c}_{j,\alpha}^\dagger (\vec{\mathcal{L}}_j^{\alpha 0} \cdot \vec{\sigma}) \mathbf{c}_{j,0} \mathbf{c}_{i,\beta}^\dagger (\vec{\mathcal{L}}_i^{\beta 0} \cdot \vec{\sigma}) \mathbf{c}_{i,0} \right\} \mathbb{P}_L^0 \quad (2.101)
\end{aligned}$$

$$\begin{aligned}
& \left(\begin{array}{c} \text{Diagram 1: } \beta, i \text{ and } \alpha, j \text{ electrons at site } i, \text{ with } 0, i \text{ and } 0, j \text{ orbitals.} \\ \text{Diagram 2: } \alpha, j \text{ and } \beta, i \text{ electrons at site } j, \text{ with } 0, i \text{ and } 0, j \text{ orbitals.} \end{array} \right) \\
& = \mathbb{P}_L^0 \sum_{i,j,\alpha,\beta} \frac{-t_{ji}^{0\beta} t_{ij}^{0\alpha}}{4(\Delta\epsilon_j^\alpha + \Delta\epsilon_i^\beta) \Delta\epsilon_j^\alpha} \left\{ \mathbf{c}_{j,0}^\dagger (\vec{\mathcal{L}}_j^{0\alpha} \cdot \vec{\sigma}) \mathbf{c}_{j,\alpha} \mathbf{c}_{i,0}^\dagger (\vec{\mathcal{L}}_i^{0\beta} \cdot \vec{\sigma}) \mathbf{c}_{i,\beta} \right\} \times \\
& \times \left\{ \frac{1}{\Delta\epsilon_i^\beta + U} \mathbf{c}_{j,\alpha}^\dagger \mathbf{c}_{i,0} \mathbf{c}_{i,\beta}^\dagger \mathbf{c}_{j,0} + \frac{1}{\Delta\epsilon_j^\alpha + U} \mathbf{c}_{i,\beta}^\dagger \mathbf{c}_{j,0} \mathbf{c}_{j,\alpha}^\dagger \mathbf{c}_{i,0} \right\} \mathbb{P}_L^0 \quad (2.102)
\end{aligned}$$

The final set of diagrams involves an intermediate state where both electrons occupy the same site in excited orbitals. Although not explicitly shown, for $\alpha = \beta$, the electrons will

both occupy the same orbital.

$$\begin{aligned}
& \left(\begin{array}{c} \text{Diagram 1} \\ \text{Diagram 2} \end{array} \right) + \left(\begin{array}{c} \text{Diagram 3} \\ \text{Diagram 4} \end{array} \right) \\
&= \mathbb{P}_L^0 \sum_{i,j,\alpha,\beta} \frac{-t_{ji}^{0\alpha} t_{ij}^{\beta 0}}{4(\Delta\epsilon_i^\alpha + \Delta\epsilon_i^\beta + U)} \left\{ \frac{1}{\Delta\epsilon_i^\alpha + U} \mathbf{c}_{j,0}^\dagger \mathbf{c}_{i,\alpha} \mathbf{c}_{i,0}^\dagger \left(\vec{\mathcal{L}}_i^{0\beta} \cdot \vec{\sigma} \right) \mathbf{c}_{i,\beta} + \right. \\
&\quad \left. + \frac{1}{\Delta\epsilon_i^\beta} \mathbf{c}_{i,0}^\dagger \left(\vec{\mathcal{L}}_i^{0\beta} \cdot \vec{\sigma} \right) \mathbf{c}_{i,\beta} \mathbf{c}_{j,0}^\dagger \mathbf{c}_{i,\alpha} \right\} \left\{ \frac{1}{\Delta\epsilon_i^\beta + U} \mathbf{c}_{i,\alpha}^\dagger \left(\vec{\mathcal{L}}_i^{\alpha 0} \cdot \vec{\sigma} \right) \mathbf{c}_{i,0} \mathbf{c}_{i,\beta}^\dagger \mathbf{c}_{j,0} + \right. \\
&\quad \left. + \frac{1}{\Delta\epsilon_i^\alpha} \mathbf{c}_{i,\beta}^\dagger \mathbf{c}_{j,0} \mathbf{c}_{i,\alpha}^\dagger \left(\vec{\mathcal{L}}_i^{\alpha 0} \cdot \vec{\sigma} \right) \mathbf{c}_{i,0} \right\} \mathbb{P}_L^0
\end{aligned} \tag{2.103}$$

These diagrams may be easily evaluated using identity (A.16) and the fact that:

$$\left(\begin{array}{c} \frac{1}{(\Delta\epsilon_i^\beta + U)U\Delta\epsilon_j^\alpha} + \frac{1}{\Delta\epsilon_i^\beta U(\epsilon_j^\alpha + U)} + \frac{1}{(\Delta\epsilon_i^\beta + U)(\Delta\epsilon_i^\beta + \Delta\epsilon_j^\alpha)\Delta\epsilon_j^\alpha} \\ \frac{1}{\Delta\epsilon_i^\beta(\Delta\epsilon_i^\beta + \Delta\epsilon_j^\alpha)(\Delta\epsilon_i^\beta + U)} + \frac{1}{\epsilon_j^\alpha(\Delta\epsilon_i^\beta + \Delta\epsilon_j^\alpha)(\Delta\epsilon_i^\beta + U)} + \frac{1}{(\epsilon_j^\alpha + U)(\Delta\epsilon_i^\beta + \Delta\epsilon_j^\alpha)\epsilon_i^\alpha} \end{array} \right) = \frac{2}{U\Delta\epsilon_j^\alpha\Delta\epsilon_i^\beta} \tag{2.104}$$

$$\left(\begin{array}{c} \frac{1}{(\Delta\epsilon_j^\beta + U)U(\Delta\epsilon_j^\alpha + U)} + \frac{1}{\Delta\epsilon_j^\beta(\Delta\epsilon_j^\beta + \Delta\epsilon_j^\alpha + U)\Delta\epsilon_j^\alpha} + \frac{1}{(\Delta\epsilon_j^\beta + U)(\Delta\epsilon_j^\beta + \Delta\epsilon_j^\alpha + U)(\Delta\epsilon_j^\alpha + U)} \\ \frac{1}{\Delta\epsilon_j^\beta U\Delta\epsilon_j^\alpha} + \frac{1}{\Delta\epsilon_j^\alpha(\Delta\epsilon_j^\beta + \Delta\epsilon_j^\alpha + U)(\Delta\epsilon_j^\alpha + U)} + \frac{1}{(\Delta\epsilon_j^\beta + U)(\Delta\epsilon_j^\beta + \Delta\epsilon_j^\alpha + U)\Delta\epsilon_j^\beta} \end{array} \right) = \frac{2}{U\Delta\epsilon_j^\alpha\Delta\epsilon_j^\beta} \tag{2.105}$$

giving both the pseudodipolar part and ferromagnetic correction to the isotropic exchange in terms of the ordinary spin operators:

$$\mathcal{H}_{\text{eff}} = \sum_{\langle i,j \rangle} \mathcal{J}_{ij} \mathbf{S}_i \cdot \mathbf{S}_j + \mathbf{S}_i \cdot \mathbf{\Gamma}_{ij} \cdot \mathbf{S}_j \tag{2.106}$$

$$\mathcal{J}_{ij} = -\frac{4}{U} \{ |\mathbf{C}_{ij}^{00} \cdot \mathbf{C}_{ji}^{00}| \} \tag{2.107}$$

$$\mathbf{\Gamma}_{ij} = \frac{4}{U} \{ \mathbf{C}_{ij}^{00} \otimes \mathbf{C}_{ji}^{00} + \mathbf{C}_{ji}^{00} \otimes \mathbf{C}_{ij}^{00} \} \tag{2.108}$$

It is interesting to note from eq'ns (2.97), (2.104) and (2.105) that Moriya's expressions for the anisotropic exchange emerge from the more general simultaneous perturbation expansion in both \mathcal{T} and \mathcal{H}_{SO} due to fortunate cancellation of many terms. As noted above, this cancellation is not exact when U is not constant, or Hund's coupling is included. We consider the latter case in the next section.

2.2.4 Multi-Orbital Anisotropic Exchange

In the same vein as section 2.1.4 we consider the influence of Hund's rule coupling and empty and filled orbitals on the anisotropic exchange terms. As suggested by Ref. 152, and discussed in section 2.2.3, the incorporation of Hund's coupling invalidates the single-particle pseudospin basis of Moriya, which can be expected to lead to very complicated expressions for the anisotropic exchange terms. In order to simplify this problem, we consider only the case of strong Hund coupling between the SOMO and a single low-lying empty orbital, which is relevant to materials discussed in chapter 7. In this case, there are two sources of corrections to the theory of the previous section. The first involves direct modification of the diagrams already presented by addition of the renormalized Hund vertex of eq'n (2.38) wherever two electron lines exist on the same site in the SOMO and SOMO+1 orbitals. As this represents a very small fraction of diagrams, we expect these corrections to be small, but nonetheless have computed them approximately under the assumption $(U + \Delta\epsilon^1) \gg Q^{01}$. The second modification involves wholly new diagrams, which we have computed exactly.

Corrections to the antisymmetric exchange appear first at order $\sim t^2 Q \mathcal{L}$. In total, the Dzyaloshinskii-Moriya vector can be written:

$$\mathbf{D}_{ij}^{\text{tot}} = \mathbf{D}_{ij}^{\text{AFM}} + \Delta \mathbf{D}_{ij} + \mathbf{D}_{ij}^{\text{FM}} \quad (2.109)$$

where $\mathbf{D}_{ij}^{\text{AFM}}$ is the component given in eq'n (2.85), which originates from predominantly antiferromagnetic interactions between the spin-orbit mixed states. The correction to such interactions by Hund's coupling is denoted $\Delta \mathbf{D}_{ij}$, which is given approximately:

$$\Delta \mathbf{D}_{ij} = 2i \frac{t_{ij}^{00}}{U} \left\{ \frac{t_{ij}^{01} Q_j^{01} \vec{\mathcal{L}}_j^{10}}{(U + \Delta\epsilon_j^1)^2 - (Q_j^{01})^2} - \frac{t_{ji}^{01} Q_i^{01} \vec{\mathcal{L}}_i^{10}}{(U + \Delta\epsilon_i^1)^2 - (Q_i^{01})^2} \right\} \quad (2.110)$$

This correction slightly enhances the magnitude of the DM-interaction by lowering the energy of the excited high spin states mixed into the ground state. The $\mathbf{D}_{ij}^{\text{FM}}$ component originates from primarily ferromagnetic interactions within the spin-orbit mixed states, as described by the four diagrams obtained by linking the combinations of the following:

$$\left(\begin{array}{c} \text{Diagram 1} \\ \text{Diagram 2} \end{array} \right) + \left(\begin{array}{c} \text{Diagram 3} \\ \text{Diagram 4} \end{array} \right) \left(\begin{array}{c} \text{Diagram 5} \end{array} \right) \quad (2.111)$$

$$\left(\begin{array}{c} \text{Diagram 6} \end{array} \right) \left(\begin{array}{c} \text{Diagram 7} \\ \text{Diagram 8} \end{array} \right) \quad (2.112)$$

Summing over the above diagrams yields:

$$\mathbf{D}_{ij}^{\text{FM}} = -2i \left\{ \mathbf{C}_{ij}^{01} t_{ji}^{10} \frac{Q_j^{01}}{(U + \Delta\epsilon_j^1)^2 - (Q_j^{01})^2} - t_{ij}^{10} \mathbf{C}_{ji}^{01} \frac{Q_i^{01}}{(U + \Delta\epsilon_i^1)^2 - (Q_i^{01})^2} \right\} \quad (2.113)$$

where we have introduced the spin-orbit mediated hopping parameter between the SOMO and SOMO+1, given by:

$$\mathbf{C}_{ij}^{01} = \frac{1}{2} \sum_{\alpha} \left\{ \frac{\vec{\mathcal{L}}_i^{0\alpha}}{\Delta\epsilon_i^{\alpha}} t_{ij}^{\alpha 1} + t_{ij}^{0\alpha} \frac{\vec{\mathcal{L}}_j^{\alpha 1}}{\Delta\epsilon_j^{\alpha} + U} \right\} + \mathcal{O}(\mathcal{L}^2) \quad (2.114)$$

The corrections to the pseudo-dipolar part of the anisotropic exchange appearing at order $\sim t^2 \mathcal{L}^2 Q$ may be divided in a similar fashion:

$$\mathbf{\Gamma}_{ij}^{\text{tot}} = \mathbf{\Gamma}_{ij}^{\text{AFM}} + \Delta\mathbf{\Gamma}_{ij} + \mathbf{\Gamma}_{ij}^{\text{FM}} \quad (2.115)$$

where Γ_{ij}^{AFM} is given by eq'n (2.86). The correction term to the hopping diagrams evaluates approximately to:

$$\Delta\Gamma_{ij} = \frac{4}{U} \left\{ \frac{t_{ij}^{01} Q_j^{01} \mathbf{C}_{ij}^{01} \otimes \vec{\mathcal{L}}_j^{10}}{(U + \Delta\epsilon_j^1)^2 - (Q_j^{01})^2} + \frac{t_{ji}^{01} Q_i^{01} \mathbf{C}_{ji}^{01} \otimes \vec{\mathcal{L}}_i^{10}}{(U + \Delta\epsilon_i^1)^2 - (Q_i^{01})^2} \right\} \quad (2.116)$$

The Γ_{ij}^{FM} contribution may be computed from the following four additional diagrams:

$$\left(\begin{array}{c} \text{Diagram 1} \\ \text{Diagram 2} \end{array} \right) \left(\begin{array}{c} \text{Diagram 3} \end{array} \right) \times \left(\begin{array}{c} \text{Diagram 4} \\ \text{Diagram 5} \end{array} \right) \quad (2.117)$$

which evaluate to give:

$$\Gamma_{ij}^{\text{FM}} = -2 \left\{ \mathbf{C}_{ij}^{01} \otimes \mathbf{C}_{ji}^{10} \frac{Q_j^{01}}{(U + \Delta\epsilon_j^1)^2 - (Q_j^{01})^2} + \mathbf{C}_{ji}^{01} \otimes \mathbf{C}_{ij}^{10} \frac{Q_i^{01}}{(U + \Delta\epsilon_i^1)^2 - (Q_i^{01})^2} \right\} \quad (2.118)$$

Some important observations are in order regarding these modifications to the total pseudo-dipolar exchange Γ_{ij}^{tot} . In Moriya's original expressions, which included only antiferromagnetic exchange between pseudospin moments, the pseudo-dipolar tensor can be written as the outer product of the single (pseudo)-vector quantity $\Gamma_{ij}^{\text{AFM}} \propto \mathbf{C}_{ij}^{00} \otimes \mathbf{C}_{ij}^{00}$. One can always rotate the coordinate system so that one axis lies along the direction of \mathbf{C}_{ij}^{00} , and in terms of such coordinates it is easy to see that Γ_{ij}^{AFM} has only one nonzero eigenvalue, and that it must be positive. In terms of such coordinate, the pseudo-dipolar part of the

Hamiltonian is for example:

$$\mathcal{H} = \mathbf{S}_i \cdot \begin{pmatrix} |\Gamma| & 0 & 0 \\ 0 & 0 & 0 \\ 0 & 0 & 0 \end{pmatrix} \cdot \mathbf{S}_j \quad (2.119)$$

If \mathbf{S}_i and \mathbf{S}_j are ordered antiferromagnetically with respect to one another, then this interaction is minimized when both spins are oriented parallel to \mathbf{C}_{ij}^{00} , so that $\langle \mathcal{H} \rangle = -|\Gamma|/4$. This direction therefore represents an easy-axis for AFM coupled spins. In contrast, for ferromagnetically ordered spins, the same direction represents a hard axis of magnetization, and the interaction is minimized for spins oriented anywhere in the plane normal to \mathbf{C}_{ij}^{00} , for which $\langle \mathcal{H} \rangle = 0$. There are two important modifications to this picture that occur with the addition of Hund's rule coupling:

- With the addition of $\Delta\mathbf{\Gamma}_{ij}$ and $\mathbf{\Gamma}_{ij}^{\text{FM}}$, the pseudo-dipolar tensor may have multiple nonzero eigenvalues, leading to local easy, intermediate, and hard directions of magnetization, regardless of the ordering of spins \mathbf{S}_i and \mathbf{S}_j . This result can be anticipated already from the fact that these latter terms depend not on a single (pseudo)-vector quantity, but rather two quantities \mathbf{C}_{ij}^{01} and \mathbf{C}_{ij}^{10} , which are generally unrelated to one another.
- Particularly with the addition of $\mathbf{\Gamma}_{ij}^{\text{FM}}$, the eigenvalues of $\mathbf{\Gamma}_{ij}$ may be negative. This has the potential to reverse the above criteria, leading to easy axes for ferromagnetically coupled spins rather than easy planes.

Finally, we may comment on the symmetry properties of the above terms. In his seminal paper on anisotropic exchange, Moriya summarized the restrictions on \mathbf{D}_{ij} based on the relative crystallographic symmetries of sites i and j .¹⁵⁰ These restrictions are, specifically:

$$\mathbf{D}_{ij} = \begin{cases} 0 & i \text{ and } j \text{ are related by inversion} \\ \perp \hat{m} & i \text{ and } j \text{ are related by a mirror plane with normal } \hat{m} \\ \parallel \hat{m} & i \text{ and } j \text{ are bisected by a mirror plane with normal } \hat{m} \\ \perp \hat{2} & i \text{ and } j \text{ are related by a two-fold rotation axis along } \hat{2} \\ \parallel \hat{n} & i \text{ and } j \text{ fall on the same } n\text{-fold rotation axis along } \hat{n} \end{cases}$$

Such properties follow from two observations: (1) by definition, $\mathbf{D}_{ij} = -\mathbf{D}_{ji}$, and (2) the DM-vector must transform in the same way as angular momentum i.e. as a pseudo-vector. Such pseudo-vectors have the property that their orientation is unchanged under inversion, but they transform as ordinary vectors under rotation. For example, if sites i and j are related by inversion then the pseudo vector property implies $\mathbf{D}_{ij} = \mathbf{D}_{ji}$, which is consistent with $\mathbf{D}_{ij} = -\mathbf{D}_{ji}$ only if the DM-vector vanishes exactly. These symmetry properties are independent of the nature of the anisotropy, and hold true in the presence of Hund's coupling as may be verified by inspection. In fact, the spin-orbit mediated hopping parameters must transform as pseudo-vectors. Thus, if sites i and j are related by inversion,

$$\mathbf{C}_{ij}^{00} = \mathbf{C}_{ji}^{00} = -\mathbf{C}_{ij}^{00} = 0 \quad i \text{ and } j \text{ are related by inversion} \quad (2.120)$$

For this reason, $\mathbf{\Gamma}_{ij}^{\text{AFM}}$ vanishes under the same conditions as \mathbf{D}_{ij} . It was shown that this condition holds to all orders in perturbation theory in spin-orbit coupling, as $\mathbf{\Gamma}_{ij}^{\text{AFM}} \propto \mathbf{D}_{ij}^{\text{AFM}} \otimes \mathbf{D}_{ij}^{\text{AFM}}$.^{153,154} This same symmetry does not apply to $\mathbf{\Gamma}_{ij}^{\text{FM}}$. To see this, note that:

$$\mathbf{C}_{ij}^{01} = \mathbf{C}_{ji}^{01} = -\mathbf{C}_{ij}^{10} \quad i \text{ and } j \text{ are related by inversion} \quad (2.121)$$

While these restrictions indeed imply the vanishing of $\mathbf{D}_{ij}^{\text{FM}}$, they do not place similar restrictions on the form of $\mathbf{\Gamma}_{ij}^{\text{FM}}$. This observation is of vital importance for thinking about the magnetism of high symmetry structures with significant multi-orbital contributions to the magnetic interactions, as it allows anisotropy where Moriya's theory predicts none. In this case, the anomalous additional symmetry $\mathbf{\Gamma}_{ij} \propto \mathbf{D}_{ij} \otimes \mathbf{D}_{ij}$ is broken, but the resulting terms are all consistent with the symmetry of the lattice. An exceptionally clear example of such a material is discussed in section 7.3.4.

2.3 Ab-Initio Methods for Exchange Interactions in Organics

2.3.1 Broken-Symmetry Density Functional Theory

Molecular broken symmetry density functional theory (BS-DFT)^{155–158} is extensively used for estimating isotropic magnetic exchange parameters \mathcal{J}_{ij} organic and organometallic materials.^{159–165} All unique pairs of neighbouring (radical) molecules i, j are identified, and separate calculations are performed on each to determine the relative energy of the lowest energy singlet (E_{SS}) and triplet (E_{TS}) states of the pair. The BS-DFT method is a trick, essentially, aimed at estimating E_{SS} . In terms of such energies, the exchange constant is given by:

$$\mathcal{J} = E_{SS} - E_{TS} \quad (2.122)$$

To see this correspondence, note that the (single-orbital) Hubbard model on two sites (i, j) has six basis states:

$$\begin{aligned} |(i)(j)\rangle &= |\uparrow_i \uparrow_j\rangle, & |(i)\overline{(j)}\rangle &= |\uparrow_i \downarrow_j\rangle, & |\overline{(i)}(j)\rangle &= |\downarrow_i \uparrow_j\rangle, \\ |\overline{(i)}\overline{(j)}\rangle &= |\downarrow_i \downarrow_j\rangle, & |(i)\overline{(i)}\rangle &= |\uparrow_i \uparrow_i\rangle, & |(j)\overline{(j)}\rangle &= |\uparrow_j \uparrow_j\rangle \end{aligned}$$

where (i) signifies a spin orbital localized to site i , with an overline signifying spin-down with respect to the chosen quantization axis. The first four of such states are charge neutral, having one electron localized to each site, while the final two are charge separated, having both electrons occupying the same site. The effect of the on-site repulsion U is to penalize the charge separated states, while hopping mixes such states with the $S = 0$ neutral states. For arbitrary values of the parameters, the eigenstates are as follows:

- The lowest energy singlet state for all parameters, $|\text{SS}_{(-)}^{(0)}\rangle$ is given by:

$$|\text{SS}_{(-)}^{(0)}\rangle = \frac{\gamma}{\sqrt{2}} \left(|(j)\overline{(i)}\rangle + |(i)\overline{(j)}\rangle \right) + \frac{\sqrt{1-\gamma^2}}{\sqrt{2}} \left(|(i)\overline{(i)}\rangle + |(j)\overline{(j)}\rangle \right) \quad (2.123)$$

where γ ranges between $\frac{1}{\sqrt{2}}$ for $U = 0$ and 1 as $U \rightarrow \infty$. The energy of this state is given by:

$$E_{SS} = K_{ij} + \frac{1}{2} \left(U - \sqrt{U^2 + (4t)^2} \right) \quad (2.124)$$

- The highest energy singlet state for all parameters $|\text{SS}_{(+)}^{(0)}\rangle$, given by:

$$|\text{SS}_{(+)}^{(0)}\rangle = \frac{\sqrt{1-\gamma^2}}{\sqrt{2}} \left(|(j)\overline{(i)}\rangle + |(i)\overline{(j)}\rangle \right) - \frac{\gamma}{\sqrt{2}} \left(|(i)\overline{(i)}\rangle + |(j)\overline{(j)}\rangle \right) \quad (2.125)$$

where γ ranges between $\frac{1}{\sqrt{2}}$ for $U = 0$ and 1 as $U \rightarrow \infty$. The energy of this state is given by:

$$E_{SS+} = K_{ij} + \frac{1}{2} \left(U + \sqrt{U^2 + (4t)^2} \right) \quad (2.126)$$

- The purely charge separated $S = 0$ singlet $|\text{CSS}^{(0)}\rangle$, composed entirely of charge separated states in which both electrons occupy the same site:

$$|\text{CSS}^{(0)}\rangle = \frac{1}{\sqrt{2}} \left(|(i)\overline{(i)}\rangle - |(j)\overline{(j)}\rangle \right) \quad , \quad E_{CSS} = U - K_{ij} \quad (2.127)$$

- The degenerate $S = 1$ triplet state manifold denoted $|\text{TS}^{(m_s)}\rangle$, whose $m_s = \{-1, 0, +1\}$ states are composed entirely of charge neutral states:

$$\left. \begin{aligned} |\text{TS}^{(+1)}\rangle &= |(i)(j)\rangle \\ |\text{TS}^{(0)}\rangle &= \frac{1}{\sqrt{2}} \left(|(j)\overline{(i)}\rangle - |(i)\overline{(j)}\rangle \right) \\ |\text{TS}^{(-1)}\rangle &= |\overline{(i)}(j)\rangle \end{aligned} \right\} E_{TS} = -K_{ij} \quad (2.128)$$

For $U/t \gg 1$, double occupation of either site in the two-site model is severely penalized, so that the only states appearing at low energy are the triplet state $\{|\text{TS}^{(m_s)}\rangle$, and lowest energy singlet $|\text{SS}_{(-)}^{(0)}\rangle$, which contains very little mixture of charge separated states:

$$|\text{SS}_{(-)}^{(0)}\rangle \Big|_{U \rightarrow \infty} \approx \frac{1}{\sqrt{2}} \left(|(j)\overline{(i)}\rangle + |(i)\overline{(j)}\rangle \right) \quad , \quad E_{SS} \approx K_{ij} - \frac{4t^2}{U} \quad (2.129)$$

where the antiferromagnetic exchange term $4t^2/U$ comes from expansion of the square root in the energy. The remaining two singlet states $|\text{CSS}^{(0)}\rangle$ and $|\text{SS}_{(+)}^{(0)}\rangle$ are charge separated, and have very large energy of order U . On this basis, we have:

$$\mathcal{J}_{ij} = E_{SS} - E_{TS} = 2K_{ij} - 4t^2/U \quad (2.130)$$

which is of course the expected result. The most inconvenient aspect of density function calculations for direct calculation of exchange interactions is the limitation to single-determinant (product) states inherent to the method. While the energy of the triplet may be obtained from the single determinant state $|\text{TS}^{(+1)}\rangle$, the lowest energy singlet $|\text{SS}_{(-)}^{(0)}\rangle$ is intrinsically multideterminantal. This problem may be circumvented by introduction of an alternate broken symmetry state that is the lowest energy $m_s = 0$ state that can be written as a single determinant over unrestricted spin orbitals. For the large U limit, this state is equivalent to the Néel ordered state on two-sites:

$$|\text{BSS}\rangle|_{U \rightarrow \infty} = \frac{1}{\sqrt{2}} \left(|\text{TS}^{(0)}\rangle + |\text{SS}_{(-)}^{(0)}\rangle \Big|_{U \rightarrow \infty} \right) = |(j)\overline{(i)}\rangle \quad (2.131)$$

$$E_{BSS}|_{U \rightarrow \infty} = \frac{1}{2} (E_{TS} + E_{SS}|_{U \rightarrow \infty}) \quad (2.132)$$

$$\mathcal{J}_{ij}|_{U \rightarrow \infty} = 2 (E_{BSS} - E_{TS}) \quad (2.133)$$

In the opposite limit where $U \rightarrow 0$, the lowest energy singlet and broken symmetry singlet become identical. To see this, note that the lowest energy singlet in this limit is the conventional closed shell bond, and is representable as a single determinant:

$$|\text{SS}_{(-)}^{(0)}\rangle|_{U \rightarrow 0} \approx \frac{1}{2} \left(|(j)\overline{(i)}\rangle + |(i)\overline{(j)}\rangle + |(j)\overline{(j)}\rangle + |(i)\overline{(i)}\rangle \right) = |\phi_+ \overline{\phi_+}\rangle \quad (2.134)$$

where $\phi_+ = \frac{1}{\sqrt{2}} [(i) + (j)]$. Although it is not necessarily sensible to employ spin Hamiltonians to describe such a weak correlation limit, we nonetheless have the relation:

$$|\text{BSS}\rangle|_{U \rightarrow 0} = |\text{SS}_{(-)}^{(0)}\rangle|_{U \rightarrow 0} \quad (2.135)$$

$$\mathcal{J}_{ij}|_{U \rightarrow 0} = (E_{BSS} - E_{TS}) \quad (2.136)$$

At intermediate coupling, it is common to approximate the magnetic exchange constant by the expression:¹⁶⁶⁻¹⁶⁸

$$\mathcal{J}_{ij} \approx -2 \frac{E_{TS} - E_{BSS}}{\langle S^2 \rangle_{TS} - \langle S^2 \rangle_{BSS}} \quad (2.137)$$

which becomes exact in both limits. Here, $\langle S^2 \rangle$ is the expectation value of the square of the spin operator; nominally, $\langle S^2 \rangle_{TS} = S(S+1) = 2$, while $\langle S^2 \rangle_{BSS}$ ranges between 0 and 1 in the limits of weak and strong Coulomb repulsion, respectively.

There are several notable disadvantages of BS-DFT. The first is that only the total \mathcal{J}_{ij} is estimated, which does not allow for discussion of the various components of the magnetic exchange. Often such analysis is of interest to the chemist because it allows one to correlate various chemical modifications to observed properties. The second disadvantage is that we have found this method to be unreliable in cases where multi-orbital ferromagnetic exchange is expected to be important, in which case the true triplet itself takes on multi-determinantal character. The breakdown of BS-DFT in this case can usually be diagnosed by large spin contamination in the triplet $\langle S^2 \rangle_{TS} > 1.2$, and is characterized by an over stabilization of the triplet by $\sim 50 - 200 \text{ cm}^{-1}$, which results from overestimation of \tilde{K}_{ij} .

2.3.2 Failure of Existing SOC Calculations for Organics

In principle, anisotropic exchange parameters for a pair of radicals (i, j) may be calculated by ab-initio methods in analogy with the BS-DFT technique discussed in the previous section. One computes the zero-field splitting (ZFS) tensor \mathbb{D} of the triplet state of a pair of radicals, which corresponds to the Hamiltonian:

$$\mathcal{H}_{ZFS} = \mathbf{S}_T \cdot \mathbb{D} \cdot \mathbf{S}_T \quad (2.138)$$

$$= (\mathbf{S}_i + \mathbf{S}_j) \cdot \mathbb{D} \cdot (\mathbf{S}_i + \mathbf{S}_j) \quad (2.139)$$

$$= 2 \mathbf{S}_i \cdot \mathbb{D} \cdot \mathbf{S}_j + \text{const.} \quad (2.140)$$

where \mathbf{S}_T is the total spin variable of the pair. Terms like $\mathbf{S}_i \cdot \mathbb{D} \cdot \mathbf{S}_i$ evaluate to constant terms for $S = \frac{1}{2}$ operators, and are thus neglected. The matrix \mathbb{D} can then be decomposed into scalar, antisymmetric, and traceless symmetric components:

$$\tilde{\mathcal{J}}_{ij} \equiv \frac{2}{3} \text{Tr } \mathbb{D} \quad (2.141)$$

$$\mathbf{D}_{ij} \equiv (\mathbb{D} - \mathbb{D}^T) \quad (2.142)$$

$$\mathbf{\Gamma}_{ij} \equiv \left(\mathbb{D} + \mathbb{D}^T - \frac{2}{3} \text{Tr } \mathbb{D} \right) \quad (2.143)$$

which provide the conventional anisotropic exchange terms. However, we have found that currently available methods (implemented in ORCA) fail for the weakly interacting pairs of organic radicals of interest in this thesis. These methods can be grouped into two categories: (i) explicitly multiconfigurational methods,¹⁶⁹ and (ii) perturbative DFT-based approaches.¹⁷⁰ Both have seen great success in computing ZFS terms for metal complexes.^{171–174} We provide some suggestions as to why these methods fail for organics below.

In the first of these methods, \mathbb{D} is obtained via comparison of spin state energies after diagonalizing the SOC matrix in a specific space of multiderterminent states.¹⁶⁹ For transition metal complexes, the state space may often be confined to the few orbitals with significant contributions from metal d -orbitals ($\lesssim 10$ orbitals). In contrast, for organic materials, one naively must include all valence molecular orbitals (~ 100 orbitals), which is completely impossible with current methods. Not surprisingly, we have found that truncating the state space to computationally tractable sizes results in ZFS magnitudes an order of magnitude smaller than experimental anisotropic exchange. In contrast, inclusion of all orbitals can be done, in principle, using the coupled-perturbative DFT approach implemented in ORCA.¹⁷⁰ In this case, the ZFS is treated as a response function of a generalized spin-orbital perturbation; \mathbb{D} is obtained by solving coupled equations describing the mixing of various Kohn-Sham spinorbitals in response to the spin-orbit interaction. In the absence of Hartree-Fock exchange, this becomes equivalent to the perturbative approach of Pederson and Khanna.¹⁷⁵ However, as this method relies on the validity of the Kohn-Sham orbital energies, it is likely to fail for weakly interacting radicals where correlation effects are important, and the Kohn-Sham orbitals are not particularly meaningful as a result. Indeed, we have found this method to routinely produce ZFS values an order of magnitude greater than the experimental anisotropic exchange terms in organic radical pairs.

An alternate method, developed as part of this thesis, is similar in spirit to the Pederson-Khanna approach, but the perturbation is carried out within an effective Hubbard Hamiltonian, whose parameters are obtained from ab-initio methods. In this way, the Coulomb interaction can be properly treated *by hand*, and there is no practical limitation to the size of our orbital basis. Our method for building such Hubbard models is discussed in the next section. The successful applications to heavy Se-based organic radicals, and multi-orbital

radicals is presented in chapters 6 and 7, respectively.

2.4 Constructing Effective Hubbard Models

2.4.1 Introduction

Given the detailed expressions for magnetic interactions \mathcal{J}_{ij} , \mathbf{D}_{ij} , and $\mathbf{\Gamma}_{ij}$ presented in sections 2.1 and 2.2, an alternative approach for the discussion of magnetic properties is in terms of computed microscopic Hubbard Hamiltonian parameters (t, U, Q, K) , rather than state energies. This approach has the advantage that such Hubbard parameters are at least two orders of magnitude larger than the spin Hamiltonians terms, and thus in principle may be obtained with less relative error. Moreover, the effect of the variation of any particular microscopic parameter can be more easily considered. Finally, obtaining t, U, Q, K is desirable because they allow for discussion of other properties such as charge transport and optical response. Of these, the Coulomb parameters are essentially properties of isolated sites, and can therefore be estimated from high level multiconfigurational calculations on individual molecules. Hopping integrals, which are solid state properties, require special care, as discussed in the next sections.

2.4.2 Calculation of Hopping Parameters

By far the greatest complication to calculating solid state hopping integrals from single determinant methods such as DFT is that the one-electron eigenstates in these methods are naturally described in terms of delocalized orbitals. Such crystal orbitals may extend over many molecules in the case of discrete clusters, or the entire crystal as in the Bloch states obtained from solid state band structure calculations. In order to obtain hopping parameters in a local basis, which are more useful for describing highly correlated states, one must transform the Hamiltonian, which is complicated by the apparently infinite number of valid choices for such a local basis. To see this note that, while there is only one eigenbasis that diagonalizes the one-electron Hamiltonian, there are an infinite number of

non-eigenbases in which off-diagonal hopping matrix elements remain. Without explicitly including Coulomb repulsion terms such as U , we do not know which local orbitals provide the best description of the insulating state. In this section, we present two general approaches for uniquely defining local orbitals that are quite reasonable choices. The first is to construct the most spatially local orbitals, which in principle minimizes the Coulomb repulsion between any two electrons occupying different orbitals. This approach is implemented in the `wannier90` code,¹⁷⁶ which is available as an add-on to band structure programs such as `PWSCF`.¹⁷⁷ The second was developed as part of this thesis, and recognizes that for organic molecules, the local basis should not be *more local* than a single molecule. This method employs molecular ab-initio codes such as `ORCA` to obtain local molecular orbitals for the solid state that have maximal overlap with those of isolated “gas-phase” molecules.

Maximally Localized Wannier Orbitals (`PWSCF+wannier90`)

In the maximally localized Wannier orbital (MLWO) approach,^{178–181} local orbitals are constructed from Bloch states obtained from solid state band structure calculations, typically calculated using density functional theory (DFT) methods. A particular energy range is chosen, and Bloch states falling within that range are remixed (by unitary transformation) in order to attempt to minimize the spatial spread of the orbitals defined by:

$$\Omega = \sum_{i,\alpha} [\langle i, \alpha | r^2 | i, \alpha \rangle - \langle i, \alpha | \mathbf{r} | i, \alpha \rangle^2] \quad (2.144)$$

where i, α label those orbitals within the chosen energy window. In this sense, the MLWOs are the solid state equivalent to Foster-Boys localized orbitals sometimes employed in molecular ab-initio codes.¹⁸² The hopping integrals associated with such orbitals are obtained by performing the same transformation to the Bloch Hamiltonian, and reading the off-diagonal matrix elements. The technique is implemented in `wannier90` code, which serves as an add-on to the band structure code `PWSCF` (or `Quantum Espresso`, as it is currently known). The general usage flow follows the steps:

1. A band structure calculation is performed using input crystal structure geometry and the `pw.x` component of the `PWSCF` program.

2. Necessary files for MLWO construction are prepared using the pw2wannier90.x component of the PWSCF programs.
3. The local hopping Hamiltonian is constructed by iterative minimization of Ω using the wannier90.x component of the wannier90 code.

For organic systems, when the molecular orbitals of the isolated molecules are well separated in energy, the energy bands in the solid state will tend to be grouped into multiples equal to the number of molecules per primitive unit cell. Experience suggests that restricting the energy window to encompass only one such group will result in a set of MLWOs localized to each individual molecule, and closely resembling the corresponding orbitals obtained from calculations on isolated single molecules. However, when there are multiple orbitals of interest, or multiple overlapping groups of bands included in the energy window, the MLWOs obtained will always be *more local* than the expected molecular orbitals of the isolated molecules. To see this, note that in the limit where every Bloch state is included in the energy window, the MLWOs will closely resemble the atomic orbitals localized at each atom in the unit cell. Such orbitals represent a very poor starting point for describing the properties of organics, where Coulomb repulsion may localize electrons to a particular molecule, but not to a particular atom. The MLWO approach doesn't "know" that there are supposed to be discrete molecules, and indeed is more commonly used to study inorganic materials.

With this in mind, all is not lost. The expected molecular orbitals may often be recovered by performing a manual rotation of the MLWO basis in order to diagonalize the local on-site kinetic energy provided there is a relatively small number of bands in the energy window. When a very large number of bands (> 20) are included, the minimization of the total spread Ω becomes challenging. For example, it is much easier to accidentally fall into a local minimum where the majority of orbitals are sufficiently localized, but a few are hugely delocalized meaningless soup. For this reason, the MLWO approach is not effective for organic systems where a large number of hopping integrals are desired. In order to describe the effects of multiple orbitals, and particularly spin-orbit coupling, such hopping integrals are required. For this reason, we were motivated to develop an alternate approach for constructing local orbitals, one that "knows" about the molecular orbitals of

the isolated molecules, and can more easily treat large numbers of such orbitals.

Maximally Overlapped Molecular Orbitals (computed with ORCA)

An alternate approach for constructing well-defined local orbitals for the solid state is to require their spatial overlap with corresponding orbitals in isolated “gas-phase” molecules to be maximal under the constraint that all one-electron matrix elements between orbitals at the same site vanish. Such orbitals are dubbed “Maximally Overlapping Molecular Orbitals” or MOMOs. This scheme is similar in spirit to an old proposal for constructing Wannier orbitals from atomic orbitals,¹⁸³ and bears some resemblance to recent proposals for parameterization of tight binding models for solid state calculations.¹⁸⁴ In our current implementation, the hopping integrals are constructed using the molecular ab-initio program ORCA by the following scheme:

1. Calculations are performed separately on each pair of molecules between which hopping integrals are required. Molecular geometries for the pair of molecules i, j are obtained from the crystal structure. The molecules are translated so that they (i) are related by a point group symmetry element such as a two-fold rotation, or mirror plane, and (ii) are sufficiently far apart so as to eliminate electronic communication between molecules. A symmetry restricted DFT calculation is then performed at this “far geometry”, resulting in orbitals that are delocalized over both molecules (by nature of the method), but appear in symmetry related degenerate pairs $\phi_{\alpha,-}, \phi_{\alpha,+}$:

$$\begin{aligned} \text{(From Calculation)} \quad \phi_{\alpha,+} &= \frac{1}{\sqrt{2}} (\phi_{i,\alpha} + \phi_{j,\alpha}) \\ \phi_{\alpha,-} &= \frac{1}{\sqrt{2}} (\phi_{i,\alpha} - \phi_{j,\alpha}) \end{aligned} \quad \text{(Isolated Molecules)} \quad (2.145)$$

where $\phi_{i,\alpha}, \phi_{j,\alpha}$ are the local orbitals associated with the isolated molecular sites i, j . By enforcing the orbitals $\phi_{\alpha,+}$ and $\phi_{\alpha,-}$ to transform as a representation of the introduced two-fold or mirror symmetry, it is ensured that they are exactly either the in-phase or out-of-phase combinations of $\phi_{i,\alpha}, \phi_{j,\alpha}$. This holds provided there are no degenerate orbitals $\phi_{i,\alpha}, \phi_{i,\beta}$ at a given molecule, which applies to all the molecules studied in this thesis, whose highest point group symmetry is C_{2v} . The site-local

orbitals are thus obtained by exactly a 45° rotation of each degenerate pair obtained in the calculation:

$$\begin{aligned} \text{(Isolated Molecules)} \quad \phi_{i,\alpha} &= \frac{1}{\sqrt{2}} (\phi_{\alpha,+} + \phi_{\alpha,-}) & \text{(From Calculation)} \\ \phi_{j,\alpha} &= \frac{1}{\sqrt{2}} (\phi_{\alpha,+} - \phi_{\alpha,-}) \end{aligned} \quad (2.146)$$

These serve as the reference orbitals for the isolated molecules. In the DFT calculation, these are represented as a linear combination of atomic orbitals ϕ_A associated with a particular Gaussian basis:

$$\phi_{i,\alpha} = \sum_A c_{i,\alpha,A} \phi_A \quad (2.147)$$

where A labels the atomic basis functions. The coefficients $c_{i,\alpha,A}$ may be stored in a matrix \mathbf{C}_{iso} . The goal is to construct similar orthonormal basis of orbitals $\phi_{i,\alpha'}$ to describe the pair of molecules in their actual crystal geometry that approximately maximizes the total overlap function Π :

$$\Pi = \sum_{i,\alpha} \langle i, \alpha' | i, \alpha \rangle = \text{Tr} [(\mathbf{C}')^T \mathbf{C}_{iso}] \quad (2.148)$$

where \mathbf{C}^T indicates the transpose of the matrix. Applying this restriction allows site-local orbitals to be defined unambiguously.

2. The pair of molecules are translated back to their crystal geometries, and a DFT calculation at the same level of theory is performed at the “close geometry”. From this calculation, we obtain orbital energies stored in a matrix \mathbf{E}^* , in terms of orbitals defined by \mathbf{C}^* , as well as the overlap matrix \mathbf{S}_A in terms of atomic orbital basis functions. The matrix elements of the latter are $S_{AB} = \langle A | B \rangle$. The overlap matrix in the isolated molecular orbital basis $\phi_{i,\alpha}$ but crystal geometry is obtained as:

$$\mathbf{S}_{iso} = (\mathbf{C}_{iso})^T \mathbf{S}_A \mathbf{C}_{iso} \quad (2.149)$$

Inspection of this matrix reveals that the isolated molecular orbitals $\phi_{i,\alpha}$ do not form an orthonormal basis once the molecules are brought back together. This is because the molecular orbitals on adjacent molecules now overlap, so that the matrix elements of \mathbf{S}_{iso} given by $S_{ij}^{\alpha\beta} = \langle i, \alpha | j, \beta \rangle$ are generally nonzero. For this reason, we cannot simply choose $\mathbf{C}' = \mathbf{C}_{iso}$ in order to construct our local orbitals.

3. In order to define an orthonormal basis that maximizes Π , we perform a symmetric (Löwdin) orthogonalization:^{185,186}

$$\mathbf{C}' = (\mathbf{S}_{iso})^{-\frac{1}{2}} \mathbf{C}_{iso} \quad (2.150)$$

and the Fock matrix for this basis is obtained simply by transforming the diagonal energy matrix into the orthogonalized basis:

$$\mathbf{F}' = (\mathbf{S}_{iso})^{-\frac{1}{2}} (\mathbf{C}_{iso})^T [(\mathbf{C}^*)^{-1}]^T \mathbf{E}^* (\mathbf{C}^*)^{-1} \mathbf{C}_{iso} (\mathbf{S}_{iso})^{-\frac{1}{2}} \quad (2.151)$$

The off-diagonal elements of \mathbf{F}' give the desired hopping integrals, while the on-diagonal elements are the isolated molecular orbital energies. These parameters serve as a starting point for constructing an effective extended Hubbard model for the molecular solid. Since the eigenvalues of \mathbf{F}' are identical to those of \mathbf{E}^* this approach is internally consistent. That is, in the limit where Coulomb terms $U \rightarrow 0$, diagonalization of the one-electron part of the Hamiltonian reproduces the Kohn-Sham eigenvalues obtained from the DFT calculation. What remains is estimation of the Coulomb parameters themselves.

4. One slight shortcoming of this method for constructing the Fock matrix is that \mathbf{F}' as written will generally contain small off-diagonal matrix elements between orbitals within the same molecular site. This effect is expected, because when placed in the crystal, the action of the local environment may remix and deform the molecular orbitals of the isolated molecule, slightly perturbing their energies. For ease of interpretation, it is therefore advantageous to perform a partial diagonalization of the Fock matrix by a unitary transformation \mathbf{U} in order to remove the off-diagonal

elements between orbitals at the same site. The new form of the matrix becomes:

$$\mathbf{C}'' = \mathbf{U} \mathbf{C}' \quad (2.152)$$

$$\mathbf{F}'' = \mathbf{U}^{-1} \mathbf{F}' \mathbf{U} \quad (2.153)$$

$$= \left(\begin{array}{cccc|cccc} \epsilon_{i,1} & 0 & \cdots & 0 & t_{ij}^{11} & t_{ij}^{12} & \cdots & t_{ij}^{1n} \\ 0 & \epsilon_{i,2} & \cdots & 0 & t_{ij}^{12} & t_{ij}^{22} & \cdots & t_{ij}^{2n} \\ \vdots & \vdots & \ddots & \vdots & \vdots & \vdots & \ddots & \vdots \\ 0 & 0 & \cdots & \epsilon_{i,n} & t_{ij}^{n1} & t_{ij}^{n2} & \cdots & t_{ij}^{nn} \\ \hline t_{ij}^{11} & t_{ij}^{21} & \cdots & t_{ij}^{n1} & \epsilon_{j,1} & 0 & \cdots & 0 \\ t_{ij}^{12} & t_{ij}^{22} & \cdots & t_{ij}^{n2} & 0 & \epsilon_{j,2} & \cdots & 0 \\ \vdots & \vdots & \ddots & \vdots & \vdots & \vdots & \ddots & \vdots \\ t_{ij}^{1n} & t_{ij}^{2n} & \cdots & t_{ij}^{nn} & 0 & 0 & \cdots & \epsilon_{j,n} \end{array} \right) \quad (2.154)$$

Since the offending off-diagonal elements in \mathbf{F}' are typically small compared to the difference in energy between any two orbitals, the partial diagonalization usually results in minimal alteration of the orbitals, and remaining energies. That is, the crystal environment does not significantly perturb the molecular orbitals. In fact, experience suggests that the combined orthogonalization and diagonalization in steps 3 and 4 results in orbitals for which $\langle i, \alpha'' | i, \alpha \rangle > 0.98$. However, it must be emphasized that the true crystalline environment is not well represented in the calculations described here because only one neighbouring molecule is present. Orbitals appearing very close in energy may be significantly and anomalously altered by partial diagonalization.

An example of this anomalous alteration of orbitals can be seen in the application to **1-23** ($R_1 = \text{Et}$, $R_2 = \text{Cl}$), which is discussed in greater detail in chapter 6. Partial diagonalization results in overlocalization of $\alpha = +1, +2$ orbitals, which is symptomatic of a rare case in which intermolecular hopping integrals t are on the same order as the energetic splitting $\epsilon_{+2} - \epsilon_{+1}$. In this case, the crystal environment can represent a significant perturbation to the orbital density. In the tetragonal $P4_21m$ unit cell of these materials, each molecule is bisected by a mirror plane, so that the $\alpha = +1, +2$ orbitals, which are symmetric and antisymmetric with respect to the mirror, cannot be mixed in the full symmetry of the crystalline environment. However, inspection of the obtained orbitals for the pair of

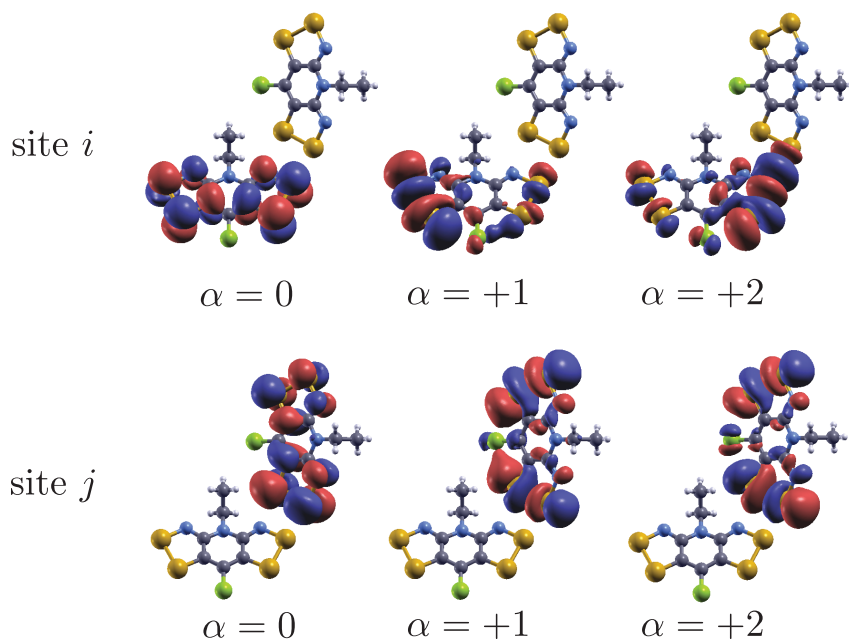


Figure 2.6: MOMOs for **1-23** ($R_1 = \text{Et}$, $R_2 = \text{Cl}$) for a particular pair of radicals showing over localization of the $\alpha = +1, +2$ orbitals at site i .

radicals shown in Fig. 2.6 reveals a significant mixing of such orbitals at site i (although not at site j). It is worth noting, however, that so long as the SOMOs on each site are appropriately reproduced in the MOMO basis, any values of interest appearing at low order in perturbation theory may still be accurately computed even in the over-localized basis provided energy denominators are properly symmetrized. To see this, consider the calculation of a property requiring:

$$A = \frac{(t_{ij}^{01})^2}{D_1} + \frac{(t_{ij}^{02})^2}{D_2} \quad (2.155)$$

for some energy denominator $D_\alpha(\epsilon, U)$. These denominators depend on only single molecule properties, and may be approximated by their single-molecule values, which are guaranteed to respect all appropriate symmetries. However, an error will be incurred whenever the orbital basis for calculation of the hopping integrals significantly differs from that of the isolated molecule. In this case, we may perform an orbital rotation by an arbitrary angle

θ to remix orbitals $\alpha = +1, +2$, providing new hopping integrals. :

$$A(\theta) \sim \frac{\cos^2(\theta)(t_{ij}^{01})^2 + 2 \sin(\theta) \cos(\theta)t_{ij}^{01}t_{ij}^{02} + \sin^2(\theta)(t_{ij}^{02})^2}{D_1} + \frac{\sin^2(\theta)(t_{ij}^{01})^2 - 2 \sin(\theta) \cos(\theta)t_{ij}^{01}t_{ij}^{02} + \cos^2(\theta)(t_{ij}^{02})^2}{D_2} \quad (2.156)$$

The MOMO basis and isolated molecule basis will tend to be largest when the two orbitals in question are close in energy, suggesting that $D_1 \approx D_2$. Setting $D_2 = D_1 + \Delta D$ gives a relative error of:

$$\frac{A(\theta) - A}{A} = \left\{ \frac{2 \cos(\theta)t_{ij}^{01}t_{ij}^{02} + \sin(\theta)[(t_{ij}^{02})^2 - (t_{ij}^{01})^2]}{(t_{ij}^{01})^2 + (t_{ij}^{02})^2} \right\} \frac{\sin(\theta)\Delta D}{D_1} + \mathcal{O}(\Delta D^2) \quad (2.157)$$

which evaluates typically to an error of smaller than 10%. Since all quantities depend on the square of the hopping integrals, in the limit where $\Delta D \rightarrow 0$, the error vanishes because the choice of basis for the two orbitals becomes irrelevant. The error similarly vanishes in the case where $\Delta D \rightarrow \infty$ because no remixing is necessary, and we may set $\theta = 0$. For summations over large numbers of orbitals, in which only a small number are anomalously mixed, this over localization therefore should not be considered a large source of error provided one uses, for the energy denominators, the associated values for the isolated molecules.

There are several major advantages of the MOMO method over the MLWO technique for estimating one-electron terms in the Hamiltonian for organics. The first is that all hopping integrals and orbital energies are obtained, rather than just those within a select energy window. This feature was the main motivation for developing the MOMO method, and allows for calculation of spin-orbit mediated hopping parameters \mathbf{C}_{ij}^{00} , which naively requires summations over all valence molecular orbitals according to eq'n (2.80). The second is that the MOMO method is significantly less computationally expensive in practice, because the construction of MLWOs requires band structures to be computed which becomes very expensive for large unit cells. In some cases, at equivalent levels of theory, all desired hopping integrals can be obtained in 1/100th of the computational time by the MOMO method. This allows more expensive DFT functionals to be employed for MOMO calculations; for example, hybrid functionals like B3LYP or PBE0, which are used extensively in molecular ab-initio calculations, are far too costly for most routine band structure

calculations on single work stations. Finally, since the local orbitals of the MOMO method are built within ORCA and are very similar to those of the isolated molecules by construction, we can reliably employ calculations on isolated molecules in ORCA to estimate other site-local properties for the effective Hubbard model such as Coulomb parameters or spin-orbit matrix elements. This has a huge advantage of allowing us to build an entire effective Hubbard model including all relevant terms but using the same DFT functionals, basis sets, and ab-initio program.

2.5 Chapter Summary

This chapter detailed the origin of various solid-state magnetic interactions, the construction of effective spin Hamiltonians, and ab-initio approaches to compute the parameters of such Hamiltonians. Starting in Sec. 2.1, we introduced a systematic perturbative approach with an accompanying diagrammatic note-keeping device, and derived various isotropic interactions in the large U limit of the Hubbard model. In particular, Section 2.1.4 showed how ferromagnetism may occur via multi-orbital contributions arising from strong Hund's rule coupling between the SOMO and either an empty low-lying LUMO or a filled high lying HOMO. This interaction, we will argue in the following chapters, is relevant to many Oakley-type radicals. Spin-orbit coupling, which also becomes relevant in heavy S-, Se-based radicals, was discussed extensively in section 2.2. Introduction of a pseudospin picture allowed rationalization of Moriya's theory of anisotropic exchange interactions. In the presence of multi-orbital contributions, this picture was shown to be incomplete; we thus derived extensions to Moriya's theory to include such effects, and observed significant qualitative differences. Finally, sections 2.3 and 2.4 detailed ab-initio construction of Hubbard and Spin Hamiltonians. An alternate method for computing hopping integrals was described, and will be used below to address various materials.

Chapter 3

Theoretical Aspects of Electrical Transport

As discussed in the introduction, a significant goal in the research of the Oakley group has been the design of a neutral organic radical displaying a metallic transport properties. It is therefore pertinent that such properties be briefly reviewed. In this chapter, we supplement the theoretical discussion of magnetic properties of the previous chapter with a brief description of theoretical aspects of charge transport in the vicinity of the Mott transition. We also introduce the dynamical mean field approach for the calculation of properties, which is employed in various studies presented in this thesis. In order to introduce the language of Green functions, we refer the reader to Appendix B, which provides a pedagogical introduction to this mathematical technique.

3.1 Conventional Theory of Metals

In the previous chapter, we discussed how the properties of magnetic Mott insulating radicals may be derived perturbatively incorporating the effects of hopping into an effective spin Hamiltonian that acts on pure spin states that become exact eigenstates only in the $U/t \rightarrow \infty$ limit. The validity of this approach was guaranteed for $U > U_c$ by the fact

that the magnetic states at finite hopping were adiabatically connected to the pure spin states. Here U_c is the critical value of Coulomb repulsion above which there is a finite charge gap $\Delta_c \sim U - W$, and electrons are localized at low energy. The conventional theory of metals is predicated on a similar premise, but starts from the opposite $U/t \rightarrow 0$ limit. One assumes that the low energy excitations of an interacting system of electrons at finite $U < U_c$ are adiabatically connected to those of the noninteracting electron gas at $U = 0$.^{187–189} In this non-interacting limit, the electrons form a Fermi sea state $|FS\rangle$ introduced in section 1.2.2, with electrons occupying all one-electron Bloch states $|\phi_{\mathbf{k},0}^\alpha\rangle$ below the chemical potential $\mu = \epsilon_F$ at ($T = 0$).

$$|FS\rangle = \prod_{\epsilon_{\mathbf{k}}^\beta < \epsilon_F} \left(c_{\mathbf{k},\beta,\uparrow}^\dagger c_{\mathbf{k},\beta,\downarrow}^\dagger \right) |\text{Vac}\rangle \quad (3.1)$$

In the momentum state basis, the fully interacting Hamiltonian can be written:

$$\mathcal{H} = \sum_{\alpha,\mathbf{k}} (\epsilon_{\mathbf{k},0}^\alpha - \mu) \mathbf{c}_{\alpha,\mathbf{k}}^{0\dagger} \mathbf{c}_{\alpha,\mathbf{k}}^0 + \sum_{\alpha,\beta,\mathbf{k}_1,\mathbf{k}_2,\mathbf{k}_3} U^{\alpha\beta} \mathbf{c}_{\alpha,\mathbf{k}_1}^{0\dagger} \mathbf{c}_{\alpha,\mathbf{k}_2}^0 \mathbf{c}_{\beta,\mathbf{k}_3}^{0\dagger} \mathbf{c}_{\beta,\mathbf{k}_1+\mathbf{k}_3-\mathbf{k}_2}^0 \quad (3.2)$$

where $\epsilon_{\mathbf{k},0}^\alpha$ gives the Bloch state energies. The characteristic properties of the free electron gas result from excitation of electrons from below to above the Fermi surface at $\epsilon = \epsilon_F$ by the application of an external field. For example, an electric field may shift the occupancies in order to generate a net current $\mathbf{j} = \sum_{\alpha,\mathbf{k}} \nabla_{\mathbf{k}} \epsilon_{\mathbf{k}}^\alpha \mathbf{c}_{\alpha,\mathbf{k}}^\dagger \mathbf{c}_{\alpha,\mathbf{k}}$. As we adiabatically turn up U from zero, the bare electronic excitations will become increasingly mixed and scattered from one another. However, we may describe the resulting physical excitations as free electron-like “quasiparticles” that occupy states in momentum space $|\phi_{\mathbf{k}}^\alpha\rangle$ with a renormalized Hamiltonian given by

$$\mathcal{H}_{eff} = \sum_{\alpha,\mathbf{k}} (\epsilon_{\mathbf{k}}^{\alpha*} - \mu) \mathbf{c}_{\alpha,\mathbf{k}}^\dagger \mathbf{c}_{\alpha,\mathbf{k}} \quad (3.3)$$

where the renormalized single-particle energies are given by:¹⁸⁹

$$\epsilon_{\mathbf{k}}^{\alpha*} = \epsilon_{\mathbf{k},0}^\alpha + \Sigma(\alpha, \mathbf{k}) \quad (3.4)$$

in terms of the complex self-energy function $\Sigma(\alpha, \mathbf{k})$, which completely determines the effect of interactions. The real part of $\Sigma(\alpha, \mathbf{k})$ describes the shifting of quasiparticle energies with

respect to those of the free electrons, which typically results in a narrowing of the bandwidth and relative enhancement of the effective mass $m^* = \partial^2 \epsilon^* / \partial k^2 > m^0 = \partial^2 \epsilon^0 / \partial^2 k$. The imaginary part of $\Sigma(\alpha, \mathbf{k})$ gives the inverse lifetime or scattering rate of the quasiparticles, which measures the time over which the true many body state is well described by a particular configuration of quasiparticle occupancies. That is, residual interactions between quasiparticles cause them to scatter from one another into new Bloch states over a characteristic timescale given by $\tau(\omega) = \hbar / \text{Im}[\Sigma(\omega)]$. Standard solid state DFT band structure calculations provide only $\epsilon_{\mathbf{k}}^\alpha = \text{Re}[\Sigma]$ in principle. However, in the conventional “Fermi liquid” metal $\text{Im}[\Sigma]$ can be nearly neglected as the scattering rate goes as:¹²⁴

$$\frac{\hbar}{\tau} = A\omega^2 + B(k_B T)^2 \quad , \quad A, B \sim \mathcal{O}(1/W^*) \quad (3.5)$$

where ω gives the energy of the quasiparticle state with respect to μ , T is the temperature, and W^* is the renormalized quasiparticle bandwidth. For measurements such as DC conductivity and magnetic susceptibility, which impart little energy to the system, all experimentally relevant excitations are confined to a narrow energy region near ϵ_F (i.e. $\omega \sim 0 \ll W^*$) and typical temperatures satisfy $k_B T \ll W^* \sim 10^4$ K. As a result, the quasiparticle lifetimes are long, and the response of the interacting system is essentially that of a free electron gas with appropriately renormalized $\epsilon_{\mathbf{k}}^\alpha$. The frequency dependence of the electrical conductivity can be expected to follow a Drude form:¹⁹⁰

$$\sigma(\omega) = \frac{\sigma_0}{1 + i\omega\tau(\omega)} \quad , \quad \sigma_0 = \frac{ne^2\tau(0)}{m^*} \quad (3.6)$$

for charge carrier density n , and electron charge e . As n is essentially temperature independent in the Fermi liquid metal, the DC electrical resistivity $\rho_{DC} = 1/\sigma_0$ is dominated by the temperature dependence of τ , which leads e.g. to $\rho_{DC} \propto T^2$ for scattering due to Coulomb interactions. In contrast, in an insulating state, an energy barrier for charge carriers leads to $n \propto e^{-E_A/k_B T}$, which provides the strongest temperature dependence, and $\rho \propto e^{E_A/k_B T}$. For this reason, a resistivity that increases with increasing temperature $d\rho/dT > 0$ is often taken as a sign of a vanishing activation energy, and referred to as “metallic transport”. This observation is, however, not sufficient to indicate a conventional Fermi liquid state with coherent quasiparticle transport. The breakdown of the Fermi liquid with increasing

U can be anticipated by studying the mean free path of quasiparticles, which measures the average distance travelled before a scattering event:

$$\ell = v\tau = \frac{\tau}{\hbar} \frac{\partial \epsilon}{\partial k} \sim \frac{\tau W^*}{\hbar \pi} a \quad (3.7)$$

where a is a lattice spacing associated with the direction of transport. If the scattering rate \hbar/τ exceeds the bandwidth W^* , then the mean-free path will be less than a lattice spacing, which is inconsistent with our ansatz of nearly free quasiparticles with well defined momenta. This threshold value allows us to estimate the minimum conductivity or maximum resistivity consistent with a conventional metal, which was first discussed by Mott, Ioffe and Regel (MIR):^{191–193}

$$\sigma_{MIR} = \frac{ne^2 \pi \hbar}{m^* W} \sim 10^3 - 10^4 \text{ S/cm} \quad , \quad \rho_{MIR} \sim 10^{-3} - 10^{-4} \text{ } \Omega \text{ cm} \quad (3.8)$$

provided $W \sim 1$ eV, $m^* \sim m_e$, and reasonable electron densities in organics. Conventionally, one expects materials approaching ρ_{MIR} to either fall into an insulating state, or exhibit saturation of the resistivity as the scattering rate cannot grow further.^{194,195} It is an important observation that there are many examples of correlated materials, denoted “bad metals”¹ that display metallic transport ($d\rho/dT > 0$) with resistivities exceeding the MIR limit, which cannot be understood in a quasiparticle transport picture.^{19,196} For example, the normal state above the superconducting transition temperature in high- T_c superconductors is often a bad metal at optimal doping.^{197–199} Another example is found in the quasi-1D radical ion Bechgaard salts $(\text{TMTSF})_2\text{X}$, where resistivity along the conducting π -stacks is in the vicinity of the MIR limit, but interstack resistivity is far greater, implying the absence of coherent transport between chains.²⁰⁰ As discussed in chapters 5 and 7 we find bad metal behaviour in radical materials in the vicinity of the Mott transition. In such cases, one clearly needs a different theoretical framework for discussing material properties that incorporates the large $\text{Im}[\Sigma]$ and is thus capable of interpolating between the Mott insulating and Fermi liquid metallic limits. We discuss the use of one such method in the next section.

¹This nomenclature can be traced to Ref. 196, and has survived in the literature despite being poorly descriptive. A more appropriate name might be “non-saturating metals”.

3.2 Dynamical Mean Field Approach

In the Dynamical Mean Field Theory (DMFT) approach,^{17,201–204} the self-energy is approximated as being momentum independent, so that, in Matsubara representation:

$$\Sigma^M(\alpha, \mathbf{k}, \sigma, i\omega_n) \approx \Sigma^M(\alpha, \sigma, i\omega_n) \quad (3.9)$$

which is exact in both the noninteracting limit $U/t \rightarrow 0$, where $\Sigma = 0$, and the strongly interacting Mott insulator $U/t \rightarrow \infty$ where all states are localized and \mathbf{k} is no longer a good quantum number. This approximation is also exact in the limit where the coordination number of the lattice is infinite; for this reason DMFT is often referred to as an infinite dimensional method,¹⁷ as with other mean-field approaches. Since the self-energy is momentum independent by assumption, it may be computed in real space, with respect to the finite temperature Green function at a single site i :

$$\mathcal{G}_i^{\alpha\beta}(\sigma, \tau) = -\frac{i}{\hbar} \left\langle T_\tau (f_{\alpha,\sigma}(\tau), f_{\beta,\sigma}^\dagger(0)) \right\rangle \quad (3.10)$$

where $f_{\alpha,\sigma}^\dagger = c_{i,\alpha,\sigma}^\dagger$ creates an electron at the given site in orbital α . The philosophy of the DMFT approach can be understood in analogy to the more familiar density functional method. The basis of the latter method is that the energy of any interacting system may be written as a universal functional $E = \mathcal{F}[n(\mathbf{r})]$ of the exact electron density $n(\mathbf{r})$.²⁰⁵ In practice, one does not know the exact density functional; different approximations lead to different flavours of DFT. The utility of the method lies in the fact that an approximation of the exact density, denoted $n^*(\mathbf{r})$, may be obtained by self-consistent solution of the auxiliary problem of a noninteracting system (i.e. single determinant state) in the presence of an effective field that depends on $n^*(\mathbf{r})$ through $\mathcal{F}[n^*(\mathbf{r})]$.²⁰⁶ Provided an appropriate functional is chosen, and $n^*(\mathbf{r}) \approx n(\mathbf{r})$, a good approximation for the energy of the interacting system $E \approx E^*$ is obtained without needing to solve the fully interacting problem. In analogy, DMFT may be motivated by noting the existence of a similar universal functional $\Theta[\Sigma]$ which is extremized by the exact single particle self-energy $\Sigma(\mathbf{k}, \alpha, \omega)$.^{207,208} On this basis, we may find approximations to $\Sigma(\mathbf{k}, \alpha, \omega)$ by constructing and solving auxiliary problems designed to extremize $\Theta[\Sigma]$ within a constrained space of possible Σ 's. If one approximates the self-energy to be momentum independent, i.e $\Sigma(\alpha, \omega)$, the appropriate auxiliary problem is that of an interacting impurity embedded in an effective medium whose spectrum

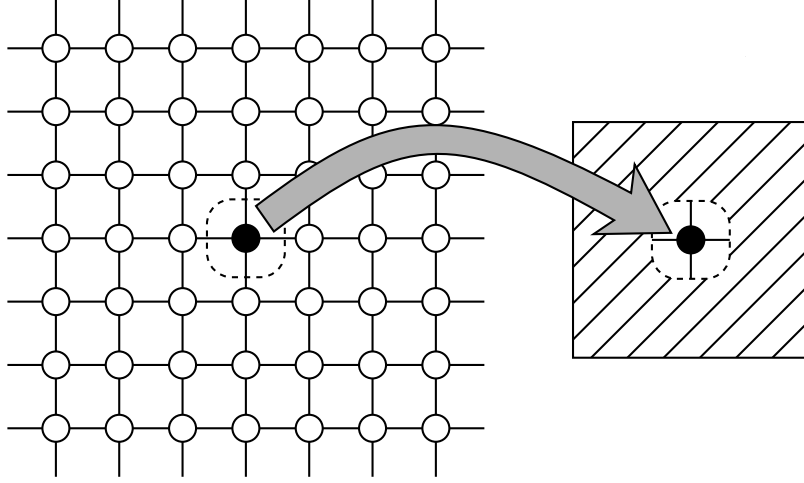


Figure 3.1: Schematic representation of the Dynamical Mean Field Approach. A single site of the interacting lattice is embedded in an effective medium that is self-consistently determined to have the same spectrum self-energy as the “impurity” site.

depends on Σ (Fig. 3.1). Since this problem may be solved self-consistently, properties that depend on the single particle Green function $G(\Sigma)$, such as conductivity, spectral properties, and energy density, may be computed in an approximate, but nonperturbative way. This fact has a significant advantage near the Mott transition, where $U \sim W$, and there is no small perturbative parameter. Different methods of constructing and solving this impurity problem leads to different flavours of DMFT.

To make the above discussion more concrete, consider site i as a single impurity that is embedded in a bath of electrons. The effective Hamiltonian is analogous to an Anderson impurity model, which is given by:

$$\mathcal{H}_{\text{eff}} = \sum_{\alpha,\sigma} \epsilon_{i,\alpha} f_{\alpha,\sigma}^\dagger f_{\alpha,\sigma} + \sum_{\alpha,\beta,\sigma} U_i^{\alpha,\beta} f_{\alpha,\sigma}^\dagger f_{\alpha,\sigma} f_{\beta,\sigma}^\dagger f_{\beta,\sigma} \quad (3.11)$$

$$+ \sum_{\gamma,\sigma} \int_{\mathbf{k}} \left\{ c_{\gamma,\sigma,\mathbf{k}}^\dagger G^{-1}(\alpha, \mathbf{k}, \sigma, i\omega_n) c_{\gamma,\sigma,\mathbf{k}} + V_{\gamma,\mathbf{k}}^\alpha c_{\gamma,\sigma,\mathbf{k}}^\dagger f_{\alpha,\sigma} + (V_{\gamma,\mathbf{k}}^\alpha)^* f_{\alpha,\sigma}^\dagger c_{\gamma,\sigma,\mathbf{k}} \right\}$$

$$V_{\gamma,\mathbf{k}}^\alpha = \sum_j t_{ij}^{\alpha\gamma} e^{i\mathbf{k}\cdot(\mathbf{r}_i - \mathbf{r}_j)} \quad (3.12)$$

where $V_{\gamma,\mathbf{k}}^\alpha$ describes the hopping between the localized impurity states and the states in

the bath representing the rest of the lattice. Since the impurity and the bath are really one and the same, the local Green function $\mathcal{G}_i^{\alpha\beta}(\sigma, \omega)$ must have the same self-energy as the lattice Green function $G^{\alpha\beta}(\mathbf{k}, \sigma, \omega)$.

$$\mathcal{G}_i^{\alpha\beta}(\sigma, i\omega_n) = \frac{1}{i\omega_n + \mu - \epsilon_{i,\alpha}\delta_{\alpha,\beta} - \Sigma^{\alpha\beta}(\sigma, i\omega_n) - \Delta^{\alpha,\beta}(\sigma, i\omega_n)} \quad (3.13)$$

$$\Delta^{\alpha,\beta}(\sigma, i\omega_n) = \sum_{\gamma,\delta} \int_{\mathbf{k}} V_{\gamma,\mathbf{k}}^\alpha (V_{\delta,\mathbf{k}}^\beta)^* G^{\gamma\delta}(\sigma, \mathbf{k}, i\omega_n) \quad (3.14)$$

$$G^{\gamma\delta}(\sigma, \mathbf{k}, i\omega_n) = \frac{1}{i\omega_n + \mu - \epsilon_{\gamma,\mathbf{k}} - \Sigma^{\gamma\delta}(\sigma, \omega)} \quad (3.15)$$

where $\Delta^{\alpha,\beta}(\sigma, i\omega_n)$ is the so-called hybridization function. Together, these equations allow us to determine the self-energy self-consistently by the following cycle:

1. Compute hybridization function(s) $\Delta^{\alpha,\beta}(\sigma, i\omega_n)$ from lattice Green function $G^{\gamma\delta}(\sigma, \mathbf{k}, i\omega_n)$.
2. Solve the impurity problem to find the local Green function $\mathcal{G}_i^{\alpha\beta}(\sigma, i\omega_n)$ given $\Delta^{\alpha,\beta}(\sigma, i\omega_n)$.
3. Compute the self-energy by $\Sigma^{\alpha\beta}(\sigma, i\omega_n) = i\omega_n + \mu - \epsilon_{i,\alpha}\delta_{\alpha,\beta} - \Delta^{\alpha,\beta}(\sigma, i\omega_n) - [\mathcal{G}_i^{\alpha\beta}(\sigma, i\omega_n)]^{-1}$.
4. Compute the lattice Green function $G^{\alpha\beta}(\sigma, \mathbf{k}, i\omega_n)$ from the self-energy $\Sigma^{\alpha\beta}(\sigma, i\omega_n)$.
5. Repeat steps 1-4 until no further changes in $\Sigma^{\alpha\beta}(\sigma, i\omega_n)$.

The most nontrivial step in this procedure is solution of the impurity problem, which despite containing only a single site (coupled to an electron bath), includes all Coulomb interaction terms. Luckily, there are now a variety of options available. The two employed in this thesis will be the simplest methods applicable to multi-orbital problems that have been shown to capture the correct physics:

- Hirsch-Fye Quantum Monte Carlo (HF-QMC) Impurity Solver:^{209–213} In this case, the thermodynamic Green function is computed on discrete points in imaginary time τ_n . On each time slice, the local electron-electron interactions are decoupled via a Hubbard-Stratonich transformation, which allows rewriting of the partition function of the interacting impurity as a noninteracting system coupled to an Ising variable.

The Green function is then sampled with respect to different configurations of the Ising variables using a Monte Carlo algorithm. Since this sampling is somewhat computationally expensive, the method is limited to $n \sim 100$ points on single workstations. This places a limit on the temperatures at which the HF-QMC is applicable, since the Green function must be computed on the imaginary time interval $0 \leq \tau \leq \beta$ that grows with decreasing temperature, reducing the resolution of $\mathcal{G}(\tau)$.

While the HF-QMC method is numerically exact, apart from the discretization error, the most significant disadvantage is that it is formulated in imaginary variables, and thus observables in real frequency can only be obtained after analytic continuation to the real axis $i\omega_n \rightarrow \omega + i\eta$. When $G(i\omega_n)$ is known analytically, operation is rarely a problem, but when it is only known numerically, the analytic continuation is not well posed. Usually it can be done reliably using the Maximum Entropy method (MaxEnt), which yields only the spectral density $A(\omega) = -\text{Im}[G(\omega)]$, or by fitting the imaginary time data with a Padé approximant:

$$P_{m,n}(x) = \frac{\sum_{i=0}^m a_i x^i}{1 + \sum_{j=0}^n b_j x^j} \quad (3.16)$$

for some order (m, n) . The HF-QMC code employed in this thesis is available as an add-on to the PW-SCF band structure software, and is based on the original `lisaqmc` code distributed as part of Ref. 17.

- Iterative Perturbation Theory (IPT):^{214–220} In this method, the impurity problem is not solved exactly to obtain the local self-energy, as above in steps 2 and 3. Rather, it is approximated by a function of its 2nd order value $\Sigma_{(2)}^{\alpha\beta}$ with respect to a perturbation in $U_i^{\alpha\beta}$:

$$\Sigma^{\alpha\beta}(\omega) \approx U_i^{\alpha\beta} n_i^\alpha + \frac{A \Sigma_{(2)}^{\alpha\beta}}{1 + B \Sigma_{(2)}^{\alpha\beta}} \quad (3.17)$$

where A and B depend on the system in question, and are chosen so that the approximate form of $\Sigma^{\alpha\beta}(\omega)$ becomes exact in limits of $U \rightarrow 0$, $U \rightarrow \infty$, and $\omega \rightarrow \infty$. Since this approximation respects both the weak and strong correlation limits, it is expected to give a reasonable description of the intermediate Mott transition,

and benchmarking against more exact methods suggest good qualitative agreement. The two major advantages of the IPT method is that it is very computationally inexpensive, and that the self-energy is calculated analytically, which facilitates or eliminates the need for analytic continuation between real and imaginary frequency. For the purposes of an experimentalist, IPT therefore represents an ideal DMFT method, although one should generally compare the results of different methods. The IPT code employed in this thesis is distributed by LA-SIGMA², and available at <http://www.institute.loni.org/lasigma/package/mo-ipt/>.

3.3 Phenomenology of the Mott Transition

In this section, we briefly review the conventional picture of the Mott transition that has emerged through both DMFT calculations,^{17,203} and a wide variety of experimental studies.^{221–229} In such studies, organic materials have played a particularly prominent role, because they are often well described by a single-orbital Hubbard model, which is easily treated by DMFT calculations. For this reason, correspondence between the calculation and experiments has proven to be excellent.^{230–232} The typical phase diagram with respect to U and T is shown in Fig. 3.2, with data computed for **5-4** via IPT-DMFT calculations (see section 5.3.3).

Starting on the metallic side of the transition at zero temperature, as U is increased, the effective bandwidth W^* of the quasiparticles becomes increasingly narrow, resulting in a strongly renormalized peak in the density of states $A(\omega)$ around the Fermi level. The strongly correlated quasiparticles associated with this peak are nonetheless coherent, and the system behaves, at low energy, as a Fermi liquid. In contrast, the states at the edge of the band, representing high energy excitations, become increasingly localized, as their scattering rate exceeds the coherence limit. As U approaches U_{c1} , spectral weight is transferred from the quasiparticle peak to the localized “Hubbard” bands. At U_{c1} the last of the coherent quasiparticles dies, and a gap of order $\Delta_c = U - W$ opens at the chemical potential, signifying a Mott insulating state. This spectral weight transfer may be observed

²Louisiana Alliance for Simulation-Guided Materials Applications

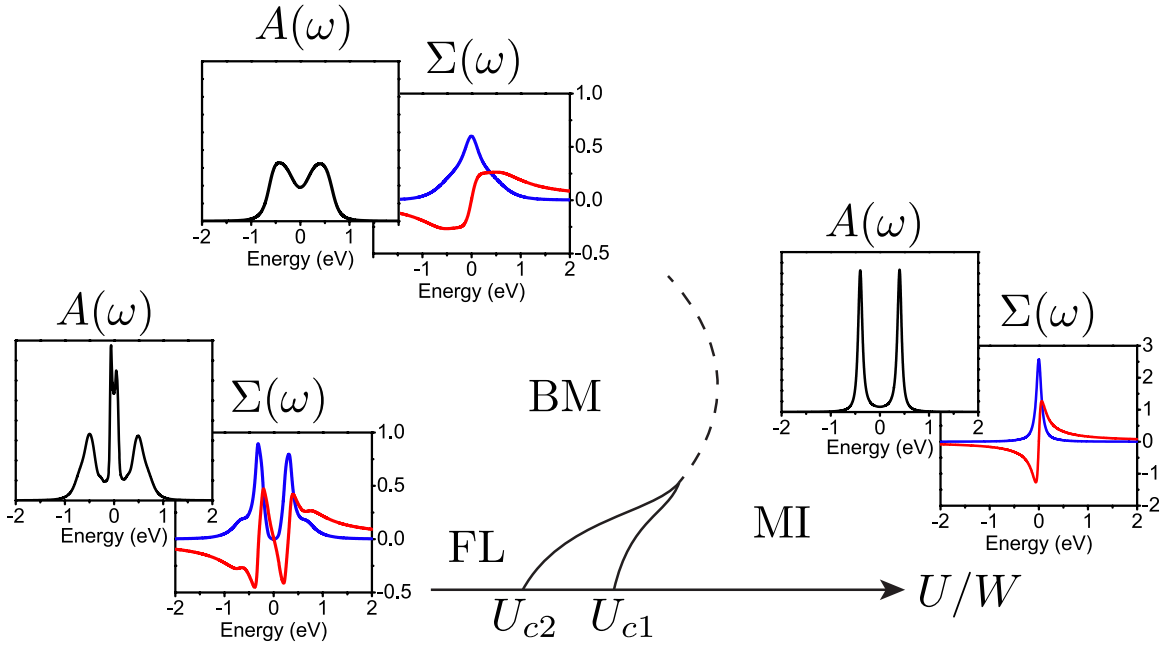


Figure 3.2: Evolution of spectral density $A(\omega)$ and self-energy $\Sigma(\omega)$ as a function of U/W (horizontal axis) and temperature (vertical axis). $\text{Re}[\Sigma]$ is shown in red, and $\text{Im}[\Sigma] \sim 1/\tau$ is shown in blue. At low temperature for $U < U_{c1}$ a renormalized Fermi liquid state (FL) prevails with $1/\tau \propto \omega^2$, but localized Hubbard features at the band edges. For $U > U_{c2}$ a Mott insulator (MI) exists with a diverging scattering rate at low energy, and clear upper and lower Hubbard bands. At high temperature, a smooth crossover occurs between the gapless incoherent bad metal (BM) state and the gapped Mott insulator.

in the frequency dependent conductivity $\sigma(\omega)$ obtained from infrared measurements, as illustrated schematically in Fig. 3.3(b), and discussed in section 7.3.2. At large $U > U_{c1}$, a clear gap is seen in $\text{Re}[\sigma(\omega)]$ at zero energy, signifying a finite Δ_c . At small U , and low temperature, a metallic Drude peak is instead observed at low frequency signifying coherent quasiparticles.^{230,231} In this region, $\rho \propto T^2$ is also observed in organic $[\text{ET}]_2\text{X}$ salts (Fig. 3.3(a)).^{200,232} However, the narrow width of the quasiparticle peak at zero temperature sets an additional temperature scale T^* above which $1/\tau$ exceeds the coherence limit even at the Fermi level, and all charge carriers become nearly localized. Above this temperature, the quasiparticle peak in $A(\omega)$ disappears along with the Drude peak in $\sigma(\omega)$, leaving a finite density of incoherent states in the vicinity of ϵ_F . As a result, the metal and insulator are smoothly connected above T^* , similar to a classical liquid and gas above their critical

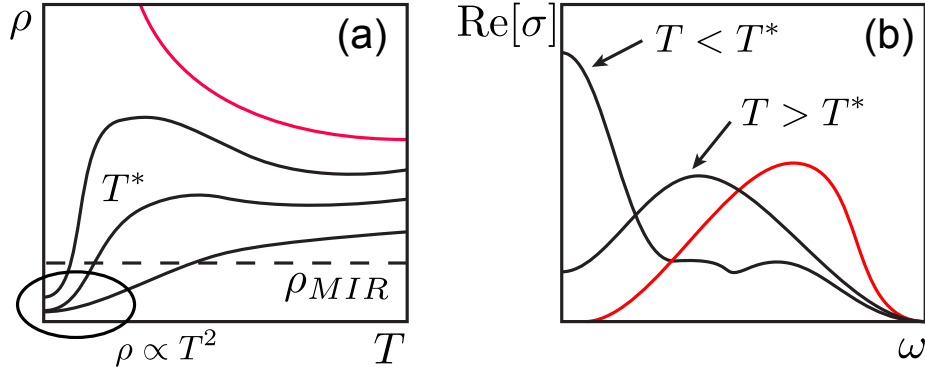


Figure 3.3: (a) Schematic temperature dependence of the DC resistivity in the vicinity of the Mott transition for decreasing U/W from top to bottom. Curves for $U > U_{c1}$ are shown in red, while those for $U < U_{c1}$ are shown in black. In the latter case, $\rho \propto T^2 < \rho_{MIR}$ is observed below the quasiparticle coherence temperature T^* , but metallic transport $d\rho/dT > 0$ may still be observed above this scale. (b) Frequency dependence of $\text{Re}[\sigma(\omega)]$ showing transfer of spectral weight.

temperature and pressure. For this reason, the crossover between the bad metal and Mott insulator is shown as a dashed line in Fig. 3.2. At large U one expects activated behaviour $\sigma \propto e^{-E_A/k_B T}$ at high temperature, while at small U the transport is often found to be metallic $d\rho/dT > 0$, but $\rho > \rho_{MIR}$ signifying a bad metallic state. Finally, starting from the insulating state, and decreasing U , one finds a transition to the metal of similar description, but at a different critical U_{c2} , signifying a small coexistence region consistent with the first order nature of the transition at low temperature.

3.4 Chapter Summary

In this short chapter, we discussed the phenomenology of the Mott transition, and introduced the Dynamical Mean Field approach for treating strongly correlated solid state materials. This method will be used to supplement DFT band structure calculations in order to build a more accurate picture of the Mott physics in the organic radicals discussed below. We also introduced the concept of a minimum metallic conductivity σ_{MIR} , which distinguishes electronic transport via incoherent charge carriers, and coherent quasiparticles. Only when the latter exist do the conventional expectations of Fermi liquid theory

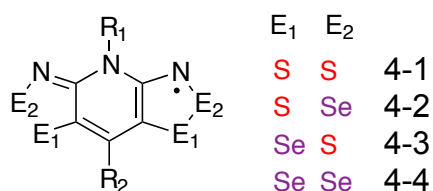
apply. Nonetheless, metallic transport ($d\sigma/dT < 0$) occurs in excess of this limit in strongly correlated materials, which defines a bad metallic state. Elucidating the physics of such states remains an ongoing challenge,¹⁹ motivating study of bad metallic states in neutral radicals presented in chapters 5 and 7.

Chapter 4

Magnetic Properties of Pyridine-Bridged bis-Dithiazolyls and Their Selenium Analogues

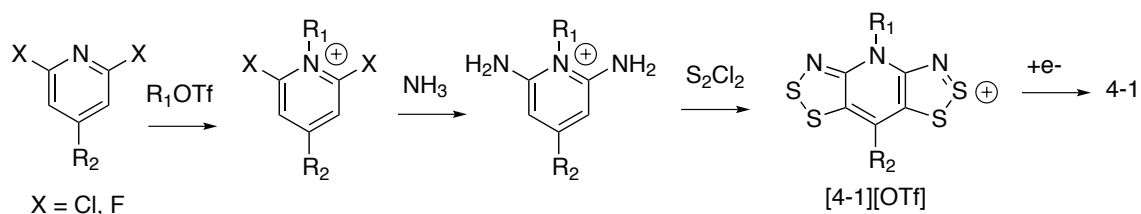
4.1 Synthetic Review

The exploration of the magnetic and electronic properties of pyridine-bridged bis-dithiazolyl radicals **4-1** and their related Se analogues **4-2–4-4** has represented an ongoing project pursued by the Oakley group over the last decade. At the time I joined the group, efficient synthetic pathways to these materials had been developed, and work had begun to focus on the various properties and crystallographic structures obtained by modification of the R_1 , R_2 , E_1 , and E_2 positions.

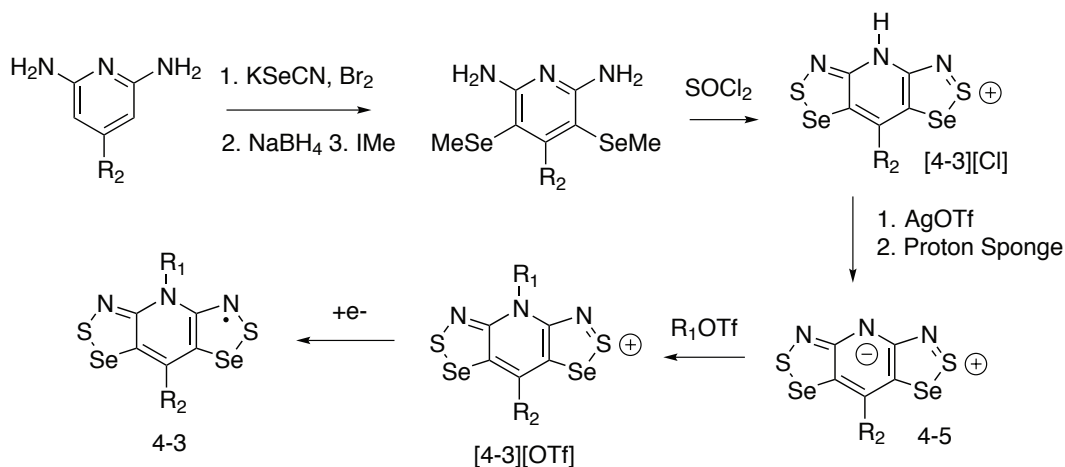


The generic synthesis of the all-sulfur derivative **4-1** begins with reaction of a desired 2,6-dihalopyridine with an alkyl triflate to afford an alkyl pyridinium salt, which is subsequently

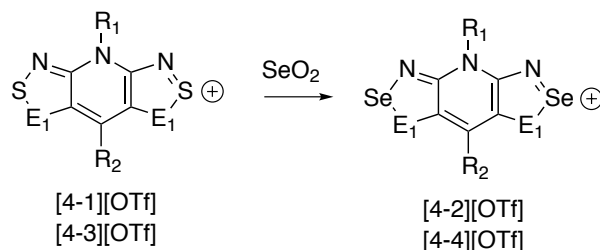
treated with gaseous ammonia to install amino-groups in the 2,6-positions.²³³ The 2,6-diaminopyridinium salt so obtained is then treated with sulfur monochloride resulting in dithiazolyl ring formation via a Herz-type reaction. Finally, one-electron reduction of the cation **[4-1][OTf]**, typically using an appropriate chemical reducing agent such as a octamethyl- or decamethylferrocene produces the desired radical **4-1**.⁶⁷



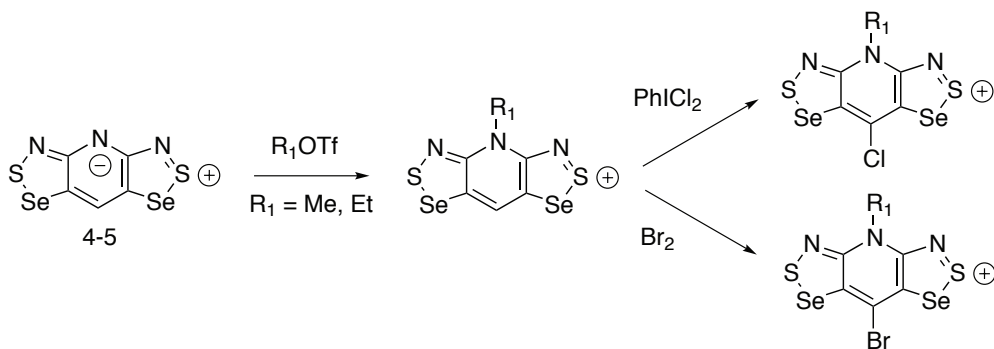
Radicals with selenium in the E₁ position may be obtained by a somewhat more involved synthetic pathway.⁸³ A 2,6-diaminopyridine is treated with KSeCN in the presence of bromine to install -SeCN groups in the 3,5-positions. The selenium is then reduced with NaBH₄, and methylated to afford the -SeMe derivative, which may be reacted with thionyl chloride to generate the **4-3** framework with R₁ = H as a chloride salt. After metathesis to a more soluble triflate salt for example using AgOTf, Proton Sponge may be employed to remove the proton in the R₁ position affording a zwitterionic intermediate **4-5** which when treated with the desired alkyl triflate results in **[4-3][OTf]**. As with **[4-1][OTf]**, a one-electron reduction provides the desired radical.



The remaining radical frameworks **4-2** and **4-4** with Se in the E₂ position may be obtained by treatment of the related triflate salts with SeO₂ typically in acetic acid.



My most significant contributions to the understanding of these materials have been through theoretical analysis of their magnetic and electronic properties, as presented in chapter 5 and the remainder of this chapter. However, during my tenure with the group, I also contributed to the synthesis of several such materials following known procedures and in support of ongoing projects led by other members of the Oakley group. For example, I helped Dr. Leitch to prepare the zwitterionic intermediate **4-5**, R₂ = H, from which various **4-3** and **4-4** derivatives were generated by treatment first with a variety of alkyl triflates, and then halogenating agents such as PhICl₂ or Br₂ to introduce either Cl or Br in the R₂ position.⁸⁹ The magnetic properties of such materials will be discussed in this chapter.



Together with Dr. Legin, we also prepared **4-1**, **4-2** (R₁ = Et, R₂ = F, I). Of particular interest is the F-substituted **4-1**, which crystallizes as a σ -bonded dimer displaying thermal, pressure, and light induced spin-state transitions.⁷⁴⁻⁷⁶

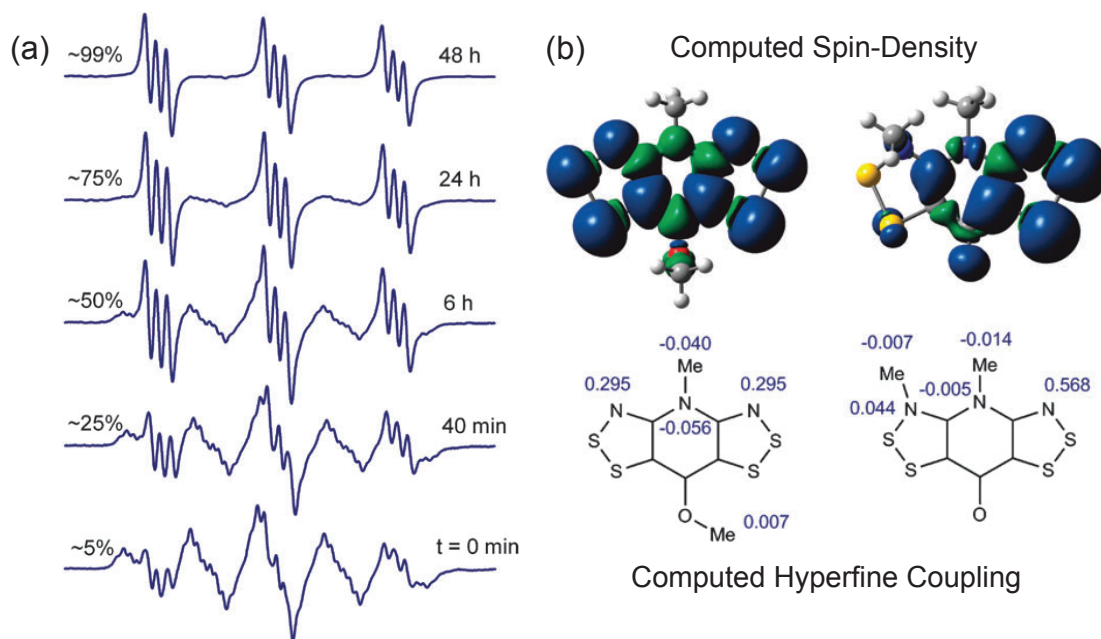
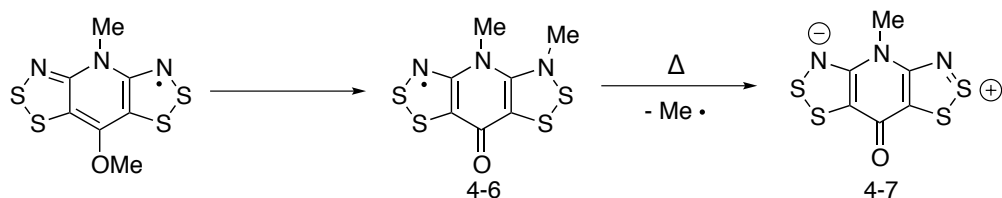


Figure 4.1: (a) Evolution of solution EPR spectrum of **4-1** ($R_1 = \text{Me}$, $R_2 = \text{OMe}$) showing percent conversion to the *N*-Me radical **4-6** as a function of time. In the former, hyperfine coupling to two symmetric wing nitrogens results in a five line pattern. Formation of **4-6** localizes the unpaired electron to one side of the molecule, producing instead a three line EPR pattern due to hyperfine coupling to predominantly a single nitrogen. (b) Computed spin-density and hyperfine coupling constants were found to be consistent with the observed spectra. Figures reproduced from Ref. 234.

While resonance stabilization and heteroatom incorporation allows materials **4-1** – **4-4** to enjoy exceptional chemical and thermal stability compared with previous generations of radicals (chapter 1), it is useful to consider possible decomposition pathways in order to prevent degradation of samples. For this purpose, we have also shown that the appropriate choice of R-groups plays a significant role in the radical stability. For example, I found that **4-1** ($R_1 = \text{Me}$, $R_2 = \text{OMe}$) undergoes a stepwise decomposition in solution, hampering

any efforts to isolate the radical.²³⁴



The first step in this process is believed to involve a shift of the Me group from the basal oxygen to a wing nitrogen presumably through bimolecular reactions, to form the unsymmetrical radical **4-6** in which the unpaired electron is localized to one side of the molecule. This species was identified on the basis of its solution EPR spectrum, which shows hyperfine coupling to primarily a single N and is consistent with computed spectral parameters (Fig. 4.1). However, attempts to purify either **4-1** ($R_1 = \text{Me}$, $R_2 = \text{OMe}$) or **4-6** by recrystallization from hot solution or vacuum sublimation resulted in loss of the Me group to form instead the closed-shell zwitterionic bisdithiazolylpyridone **4-7**. This study suggests avoidance of R-groups with “labile” alkyl components, as such materials are susceptible to rearrangement. As discussed in section 4.3.2, similar rearrangements also occur with shifts of R_1 from the pyridine to wing nitrogen, which must be considered when preparing samples for measurement. Having reviewed the synthetic aspects of pyridine-bridged radicals, we turn to their magnetic structures in the following section.

4.2 Magnetostructural Phase Diagram

4.2.1 Structural Organization

In this section, we consider an organizing principle for classifying the various magnetic phases of pyridine-bridged dithiazolyl radicals **4-1** and their selenium analogues **4-2–4-4**. All such materials crystallize as slipped π -stack arrays (Fig. 4.2), whose particular slippage and relative solid-state packing are determined both by the chalcogen atoms in the wing heterocyclic rings and by the exocyclic R_1 and R_2 groups. In Fig. 4.3, we have organized the crystallographic phases and magnetic response as a function of the approximate size of

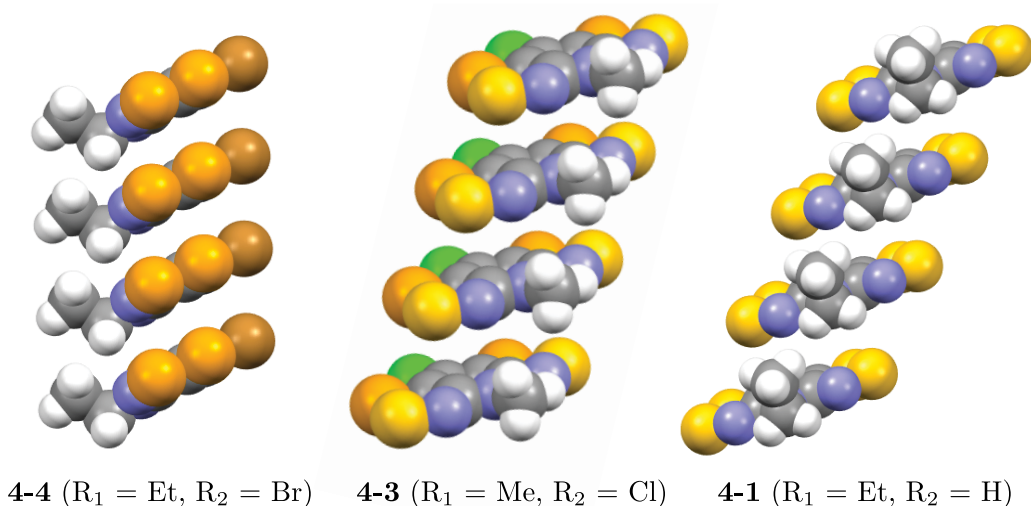


Figure 4.2: Examples of slipped π -stacks.

the R-groups. In Fig. 4.4 we show the relative slippage of adjacent radicals occupying the same π -stack; the increased steric repulsion of larger R-groups tends to increase slippage. For example, when both such R-groups are relatively large, as is the case for $R_1 = \text{Et}$, $R_2 = \text{Cl/Br/Me}$, the radicals tend to crystallize in the tetragonal space group $P\bar{4}2_1m$ with significant slippage along the short axis of the molecules.^{85–87} We refer to this direction as the molecular y -axis. This crystallographic phase displays a range of ordered magnetic states including bulk ferromagnetism and spin-canted antiferromagnetism. Reducing the size of the R_2 group initially yields a band of σ -bonded dimers,^{73,74,235} such as the β -phase of **4-1** ($R_1 = \text{Et}$, $R_2 = \text{F}$), which display light, pressure, and heat induced opening of the dimer in the solid state.^{75,76} Substitution of the R_2 position with even smaller $R_2 = \text{H}$ provides a series of spin-canted antiferromagnets for $R_1 = \text{Et}$ that crystallize in the centric space group $P2_1/c$, and exhibit large slippage primarily along the long-axis of the molecules.⁸⁴ This axis is referred to as the molecular x -direction. Replacement of the R_1 position with a Me group provides a variety of crystallographic packing motifs of reduced slippage. The two $P2_12_12_1$ phases ($R_2 = \text{H}$, and $R_2 = \text{Cl/Br}$) exhibit slippage primarily along the long axis of the molecules, and weak antiferromagnetic response (Weiss constant $-70 \text{ K} < \Theta \lesssim 0 \text{ K}$), although magnetic order has not been convincingly demonstrated in

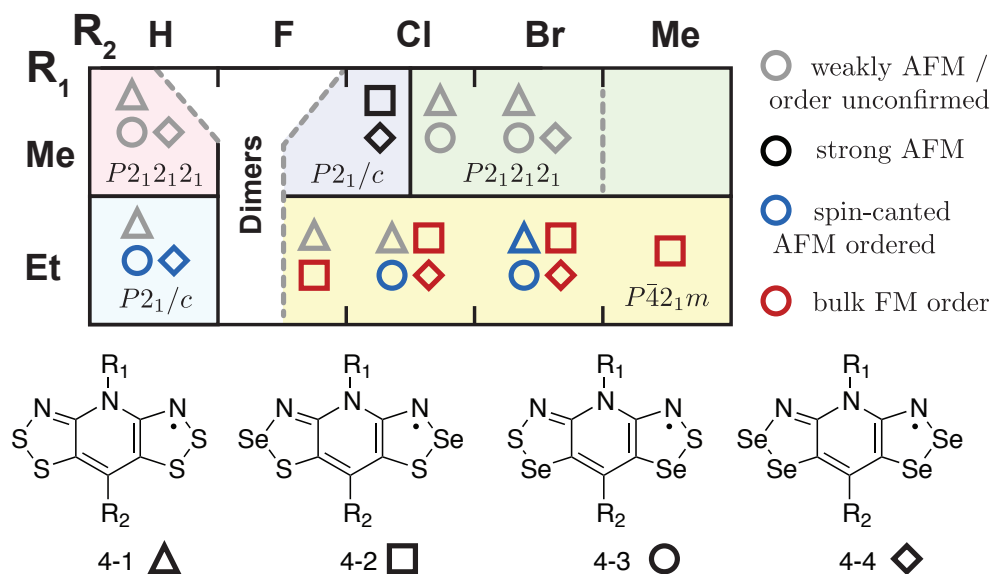


Figure 4.3: A selection of magnetic properties of pyridine-bridged bis-dithiazolyl radicals **5-1** and Se analogues **5-2–5-4**, indicated by a triangle, square, circle, and diamond, respectively. The basic magnetic responses are indicated by the colour of each symbol. Materials are organized by exocyclic R-groups, which are listed roughly in order of increasing size. Radicals with $R_2 = \text{F}$ have a propensity to dimerize in the solid state, and thus only a selection are included.

the majority of cases due to the absence of a canted moment.^{65–67,83,88} For $R_1 = \text{Me}$, $R_2 = \text{Cl}$, half of the S/Se variants crystallize instead in the $P2_1/c$ space group, and display strong antiferromagnetic coupling ($\Theta < -100$ K) associated with slippage along both molecular axes.⁸⁸ Based on broken-symmetry DFT calculations of the unique magnetic exchange constants \mathcal{J}_{ij} , this response has been interpreted in terms of very strong antiferromagnetic interactions between adjacent molecules in the π -stacks. However, magnetic order at high temperatures is unlikely in these materials, due to the relatively one-dimensional nature of their magnetic interactions.

In order to understand the relationship between the observed magnetic phases of the above radicals and their solid state structures we appeal to both symmetry arguments and theoretical exchange calculations. Symmetry considerations provide that such phases may be separated by the sign of the isotropic exchange along the π -stacks. Only a ferromagnetic $\mathcal{J}_{ij}^{(\pi)}$ allows for ordered states with a net moment, both bulk ferromagnets and spin-canted

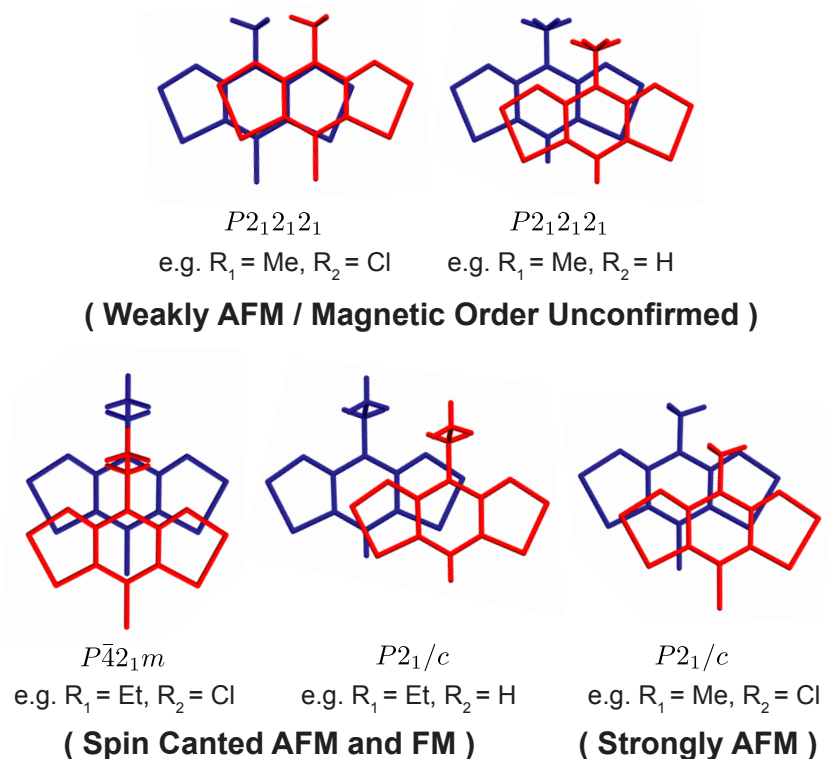


Figure 4.4: Comparing the relative slippage of adjacent radicals in the same π -stack, viewed perpendicular to the molecular planes.

antiferromagnets. Ab-initio calculations of this exchange interaction provide a structure-property map, relating the known crystallographic packing motifs with their magnetic properties.

4.2.2 Symmetry Considerations

There are two types of symmetry to consider when discussing magnetically ordered states: the symmetry group of the underlying Hamiltonian, denoted S_0 , and the symmetry of the physical state of the system, denoted S .²³⁶ In the high temperature, paramagnetic phase, these two groups are equal, $S = S_0$. This property stems from strong thermal fluctuations which ensure that all micro states of the system are occupied according to their Boltzmann

weight. Since any microstates related by symmetry are degenerate, and thus have the same statistical weight, the symmetries of the Hamiltonian are maintained by the macrostate of the system. As the material is cooled through its ordering temperature, a spontaneous breaking of symmetry occurs - the system settles into a local minimum of the free energy, and a large kinetic barrier develops that prevents accessing other degenerate symmetry related states. An obvious example of this effect can be seen in the Heisenberg ferromagnet with isotropic exchange $\mathcal{H} = \mathcal{J}_{ij} \mathbf{S}_i \cdot \mathbf{S}_j$, for which the energy is invariant under a global rotation of all spins by arbitrary angles.¹ When the system orders, it spontaneously breaks this continuous rotational symmetry by choosing a particular direction for the ordered moment.²³⁷ Even though the Hamiltonian has rotational symmetry, the ordered state does not. However, the symmetry group of the state is a subgroup of full Hamiltonian symmetry, $S \subset S_0$. In crystalline systems, the symmetry of the Hamiltonian is determined by the space group and local site symmetry of the magnetic centre, as well as the nature of the magnetic interactions. Ordered magnetic structures can be classified by noting the combination of such symmetries that is broken upon ordering.

A particularly important symmetry element for classifying magnetic symmetries is time-reversal \hat{R} , which acts on spins by flipping their orientation, so that $\hat{R}|\uparrow\rangle = |\downarrow\rangle$.²³⁸ We denote the remaining space-group symmetry elements collectively as $\{\hat{G}\}$. The Hamiltonian commutes with both \hat{R} and $\{\hat{G}\}$, as well as any product of the two, so that $S_0 = \{\hat{G}\} \cup \{\hat{R}\hat{G}\}$. In nonmagnetic or paramagnetic phases, the average spin moment at every site is zero, so that time reversal acts trivially on the state, and it can easily be seen that $S = S_0$ for this case. When magnetic systems order, only certain combinations of \hat{R} and the space group elements are retained as symmetries of the state. These retained symmetries classify the type of magnetic order. In order to demonstrate the utility of classifying various ordered states by symmetry, we make a small diversion to discuss some results from the Landau theory of phase transitions.^{236,239-241} As a function of temperature, we can write the magnetic moment as a function of position as a linear combination of

¹The technical jargon for this symmetry makes reference to the continuous (Lie) groups; one says that the Hamiltonian has SU(2) symmetry.

symmetry adapted functions:

$$\mathbf{m}(\mathbf{r}_i, T) = \sum_p \eta_p(T) \mathbf{n}_p(\mathbf{r}_i) \quad (4.1)$$

where the \mathbf{n}_p basis function belong to the symmetry group S_0 , but have the property that $\hat{R}\mathbf{n}_p = -\mathbf{n}_p$, and are thus antisymmetric with respect to time reversal. Above T_c , the order parameters $\eta_p(T)$ are all precisely zero, so that the average moment at every site is zero. Below T_c one or more of such parameters become nonzero, reducing the symmetry group of the state to S which contains only those elements for which \mathbf{n}_p transforms symmetrically. Very often S is a maximal subgroup of S_0 .²⁴¹ The magnetic part of the free energy may be expanded as a power series in such order parameters as:

$$F(T) = \sum_{p,q,\dots,r,s,\dots} c_{p,q,\dots}^{r,s,\dots}(T) (\eta_p)^r (\eta_q)^s \dots \quad (4.2)$$

but the restriction that F transform as the totally symmetric representation of S_0 places restrictions on the coefficients $c_{p,q,\dots}^{r,s,\dots}$. For example, since all η_p are antisymmetric with respect to \hat{R} , they can only appear in even powers. Moreover, the second order expansion may only contain cross terms $\eta_p\eta_q$ with $p \neq q$ if η_p and η_q transform as the same representation of S_0 . Consider the case where there are two order parameters of the same symmetry, then:

$$F(T) = c_p^2(T) (\eta_p)^2 + c_q^2(T) (\eta_q)^2 + c_{p,q}^{1,1}(T) \eta_p\eta_q + \dots \quad (4.3)$$

At high temperature, all coefficients $c_p^2(T), c_q^2(T)$ are positive, so that the free energy is minimized for all $\eta_p, \eta_q = 0$. At T_c the phase transition occurs typically because one coefficient in the expansion such as c_p^2 becomes negative, so that the free energy is minimized instead for a finite value of the associated order parameter η_p . This critical order parameter defines the emerging magnetic order. However, when small cross terms are present, a finite η_p may prompt the emergence of additional order parameters η_q of the same symmetry. To see this note that:

$$\frac{\partial F}{\partial \eta_q} = 0 \quad \rightarrow \quad \eta_q = -\frac{c_{p,q}^{1,1}}{2c_q^2} \eta_p + \dots \quad (4.4)$$

This effect is ultimately due to some badness in the original choice of basis functions $\mathbf{n}_p(\mathbf{r}_i)$, which can always be remixed within symmetry constraints in order to remove cross terms in the free energy. In essence, η_p and η_q are not independent parameters. In this section, we are mostly concerned with cases where η_p and η_q represent collinear antiferromagnetic and ferromagnetic order parameters, respectively. The simultaneous emergence of both parameters at T_c signifies a spin canted antiferromagnetic state with a weak ferromagnetic moment. Our interest in this case is due to the following observations:

- When two order parameters η_p, η_q emerge simultaneously they must be associated with basis functions $\mathbf{n}_p, \mathbf{n}_q$ of the same symmetry with respect to the grey group S_0 .
- When weak canting is observed in antiferromagnets, it occurs because the dominant critical antiferromagnetic order parameter η_p is coupled to a ferromagnetic order parameter η_q .
- Typically, there are only a select number of representations within S_0 that allow a net ferromagnetic moment, which places similar restrictions on the symmetry of \mathbf{n}_q .
- As a result, when canting is observed in antiferromagnets, the symmetry of the antiferromagnetic basis function can be determined, which often unambiguously defines the pattern of magnetic order. In other words, when canting is observed, symmetry analysis may immediately give the magnetic structure. Conversely, when an antiferromagnet orders, but does not show canting, details of the magnetic structure may also be anticipated.

These assertions rely on some features of organic materials, namely that the magnetic interactions are typically dominated by nearest neighbour isotropic exchange, which plays the most significant role in selecting the critical order parameter. In the absence of magnetic frustration, such interactions prefer simple collinear magnetic structures with at most two magnetic sublattices, justifying our expansion in terms of collinear basis functions. The cross terms coupling such functions arise from weaker spin-orbit effects, which do not directly select the pattern of magnetic order, but may modify the magnetic properties, for example, by promoting spin-canting if allowed by symmetry. It is possible that these weaker

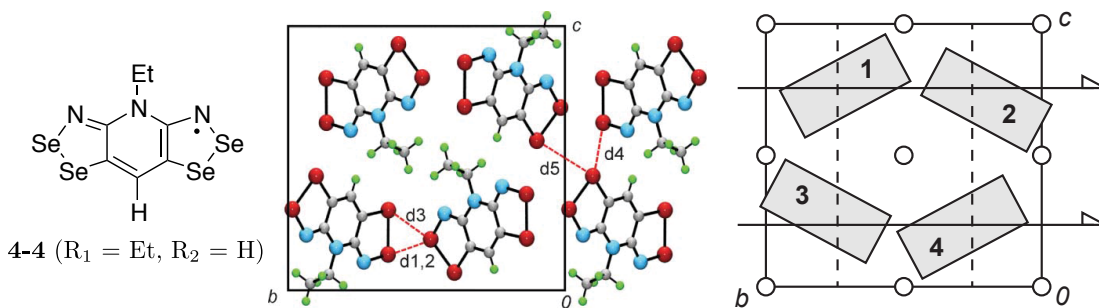


Figure 4.5: Positions of the symmetry elements in the unit cell of **4-4** ($R_1 = \text{Et}$, $R_2 = \text{H}$), as viewed down the π -stacking a -axis. The material orders as a spin-canted antiferromagnet.

interactions result in further symmetry breaking at lower temperatures, as additional order parameters become critical, but the typical energy scale for such transitions should always fall below the experimental range $T > 2$ K.

In order to begin classifying magnetic symmetries of the basis functions \mathbf{n}_p , we first must review the transformation properties of spin functions under the action of the regular point group symmetries. Representing angular momenta, \mathbf{n}_p functions transform locally as pseudovectors which means their orientation is unaltered by spatial inversion, while regular vectors are inverted. Pseudovectors transform in the normal way under rotation. The action of a mirror operation, which can be considered an inversion followed by a two-fold rotation, inverts only the components of the spin in the plane of the mirror.

Example 1: As an example of this symmetry analysis, we consider the case of **4-4** ($R_1 = \text{Et}$, $R_2 = \text{H}$), which crystallizes in the space group $P2_1/c$, and orders as a spin-canted antiferromagnet at $T_N = 27$ K.⁸⁴ The unit cell consists of four radicals, labelled 1–4 in Fig. 4.5, clustered around an inversion centre, which together form the basis for extended radical π -stacks propagating along the a -axis. There are four groups of collinear basis functions that define \mathbf{n}_p within the unit cell, and may be labelled according to the corresponding C_{2h} point group representations. Of these, the first three are totally ferromagnetic states, labelled $\mathbf{f}_x, \mathbf{f}_y, \mathbf{f}_z$, where the magnetic moments of all four sites in the unit cell are oriented along the a, b, c -axes, respectively. In terms of the magnetic moments \mathbf{m}_i at each site, these

Table 4.1: Symmetry classification of basis functions for describing the magnetic structure of **4-4** ($R_1 = \text{Et}$, $R_2 = \text{H}$). Only structures of type AFM1 may cant to produce a net magnetic moment.

State	Basis Function	E	$2_1 \parallel b$	i	c -glide $\perp b$	Point Group	Magnetic Group
						Symmetry in C_{2h}	assuming $\mathbf{k} = [0, 0, 0]$
FM	\mathbf{f}_x	+1	-1	+1	-1	B_g	$P2'_1/c'$
$\uparrow \uparrow$	\mathbf{f}_y	+1	+1	+1	+1	A_g	$P2_1/c$
$\uparrow \uparrow$	\mathbf{f}_z	+1	-1	+1	-1	B_g	$P2'_1/c'$
AFM1	\mathbf{l}_x^1	+1	+1	+1	+1	A_g	$P2_1/c$
$\uparrow \downarrow$	\mathbf{l}_y^1	+1	-1	+1	-1	B_g	$P2'_1/c'$
$\downarrow \uparrow$	\mathbf{l}_z^1	+1	+1	+1	+1	A_g	$P2_1/c$
AFM2	\mathbf{l}_x^2	+1	-1	-1	+1	B_u	$P2'_1/c$
$\uparrow \uparrow$	\mathbf{l}_y^2	+1	+1	-1	-1	A_u	$P2_1/c'$
$\downarrow \downarrow$	\mathbf{l}_z^2	+1	-1	-1	+1	B_u	$P2'_1/c$
AFM3	\mathbf{l}_x^3	+1	+1	-1	-1	A_u	$P2_1/c'$
$\uparrow \downarrow$	\mathbf{l}_y^3	+1	-1	-1	+1	B_u	$P2'_1/c$
$\uparrow \downarrow$	\mathbf{l}_z^3	+1	+1	-1	-1	A_u	$P2_1/c'$

are:

$$\mathbf{f}_\mu = \mathbf{m}_1^\mu + \mathbf{m}_2^\mu + \mathbf{m}_3^\mu + \mathbf{m}_4^\mu \quad (4.5)$$

where $\mu \in \{x, y, z\}$, and the site numbering is defined in Fig. 4.5. The remaining nine basis functions are collinear antiferromagnetic functions:

$$\mathbf{l}_\mu^1 = \mathbf{m}_1^\mu - \mathbf{m}_2^\mu - \mathbf{m}_3^\mu + \mathbf{m}_4^\mu \quad (4.6)$$

$$\mathbf{l}_\mu^2 = \mathbf{m}_1^\mu + \mathbf{m}_2^\mu - \mathbf{m}_3^\mu - \mathbf{m}_4^\mu \quad (4.7)$$

$$\mathbf{l}_\mu^3 = \mathbf{m}_1^\mu - \mathbf{m}_2^\mu + \mathbf{m}_3^\mu - \mathbf{m}_4^\mu \quad (4.8)$$

In order to classify the symmetries of these functions it is necessary only to consider their transformation properties with respect to the crystallographic elements $\{\hat{G}\}$, because the

characters satisfy $\Gamma(\hat{G}) = -\Gamma(\hat{R}\hat{G})$. The characters of these functions are shown in table 4.1. The ferromagnetic basis functions, which display a net moment, transform as either A_g or B_g with respect to the point group symmetry of the cell. The only antiferromagnetic basis functions of these symmetries are of type \mathbf{I}_μ^1 , which can be unambiguously identified with the experimental magnetic structure due to the observation of a canted moment. This finding suggests an important rule:

- In centric space groups, canting may only occur if sites related by inversion belong to the same magnetic sublattice. Otherwise, the symmetry of the antiferromagnetic state will always differ from the totally aligned ferromagnet, and canting is not possible.

So far, we have not considered the relationship between the spins in adjacent unit cells, which are related by translation. The representations of the translation operators can be labelled according to their wave vector \mathbf{k} in the Brillouin zone, with $\hat{T}(\mathbf{r}) \mathbf{n}_p = \text{Re} [e^{i\mathbf{k}\cdot\mathbf{r}}]$. For example, the totally aligned ferromagnetic state for the entire crystal is given by \mathbf{f}_μ , with $\mathbf{k} = [0, 0, 0]$. We may alternately consider a layered antiferromagnetic structure based on the \mathbf{f}_μ function for each unit cell, but with wave vector $\mathbf{k} = [\pi, 0, 0]$, so that spins in adjacent cells along a are required to be oppositely aligned. In the present example, this state breaks inversion symmetry, so canting is forbidden. More generally, however:

- Canting may only occur if all molecules related by translation belong to the same magnetic sublattice. This implies that canting is forbidden for any antiferromagnetic ordering mode for which $\mathbf{k} \neq [0, 0, 0]$, as the symmetry with respect to translation must also match that of the totally aligned ferromagnetic state.

On the basis of these observations, therefore the magnetic structure of **4-4** ($R_1 = \text{Et}$, $R_2 = \text{H}$) must be $\mathbf{I}_\mu^1[0, 0, 0]$ suggesting the isotropic interactions along the π -stacks must be predominantly ferromagnetic, while those between stacks must be antiferromagnetic. The anisotropic interactions will tend to prefer a specific orientation μ of the sublattice moments, but this cannot be determined by symmetry analysis alone in this case.

Example 2: We consider, as a second example, **4-3** ($R_1 = \text{Me}$, $R_2 = \text{Cl}$).⁸⁸ This material crystallizes in the space group $P2_12_12_1$, with pairs of the four molecules per unit

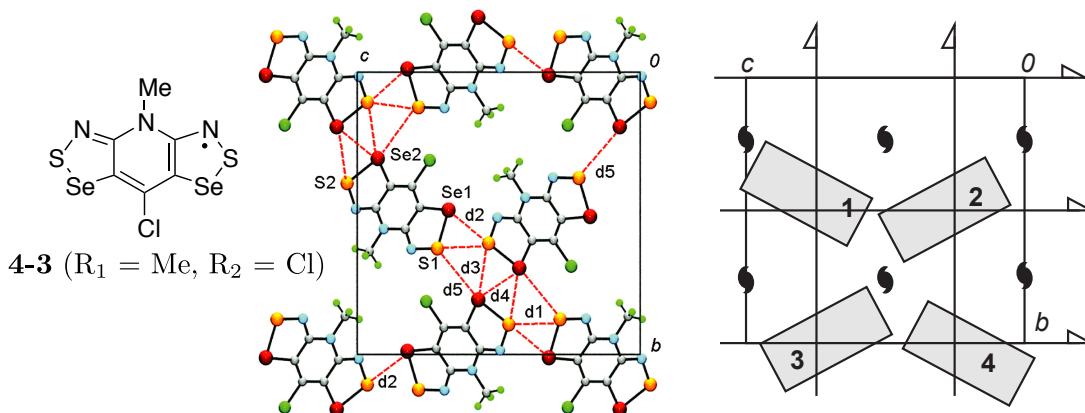


Figure 4.6: Positions of the symmetry elements in the unit cell of **4-3** ($R_1 = \text{Me}$, $R_2 = \text{Cl}$), as viewed down the π -stacking a -axis. The material does not order as a spin-canted antiferromagnet.

cell related by each 2_1 axis. In this case, we may label the basis functions \mathbf{n}_p by their point group symmetry $222 = D_2$. We consider the same basis functions, $\mathbf{f}_\mu, \mathbf{l}_\mu^1, \mathbf{l}_\mu^2, \mathbf{l}_\mu^3$ as in the previous section, with molecules numbered according to Fig. 4.6. While a Weiss constant of $\Theta = -28$ K for this material is indicative of significant antiferromagnetic interactions, canted antiferromagnetic order has not been detected.

In the $P2_12_12_1$ space group, the totally ferromagnetic basis functions \mathbf{f}_μ for the unit cell transform as either B_1 , B_2 , or B_3 depending on the orientation of the local moments with respect to the crystallographic axes (Table 4.2). For all antiferromagnetic arrangements considered, there is at least one orientation of the local moments that matches the above representations, indicating that canting is allowed by symmetry for *any* antiferromagnetic state with $\mathbf{k} = [0, 0, 0]$. In this light, the absence of a canted moment in **4-3** ($R_1 = \text{Me}$, $R_2 = \text{Cl}$) indicates that either the material does not magnetically order, or the magnetic structure is described by $\mathbf{k} \neq [0, 0, 0]$. In the latter case, the most likely ordering vector is $\mathbf{k} = [\pi, 0, 0]$, requiring interactions along the π -stacks to be predominantly antiferromagnetic. In this case, translational symmetry is broken, and canting is forbidden. This finding is in contrast to the previous example of **4-4** ($R_1 = \text{Et}$, $R_2 = \text{H}$), which was found by symmetry to require ferromagnetic interactions along the π -stacks.

Table 4.2: Symmetry classification of basis functions for describing the magnetic structure of **4-3** ($R_1 = \text{Me}$, $R_2 = \text{Cl}$). All antiferromagnetic structures with $\mathbf{k} = [0, 0, 0]$ may exhibit a canted moment, excluding such states from consideration, as the material does not cant.

State	Basis Function	E	$2_1 \parallel c$	$2_1 \parallel b$	$2_1 \parallel a$	Point Group Symmetry in D_2	Magnetic Group assuming $\mathbf{k} = [0, 0, 0]$
FM	\mathbf{f}_x	+1	-1	-1	+1	B_3	$P2'_12'_12_1$
$\uparrow \uparrow$	\mathbf{f}_y	+1	-1	+1	-1	B_2	$P2'_12_12'_1$
$\uparrow \uparrow$	\mathbf{f}_z	+1	+1	-1	-1	B_1	$P2_12'_12'_1$
AFM1	\mathbf{l}_x^1	+1	+1	+1	+1	A	$P2_12_12_1$
$\uparrow \downarrow$	\mathbf{l}_y^1	+1	+1	-1	-1	B_1	$P2_12'_12'_1$
$\downarrow \uparrow$	\mathbf{l}_z^1	+1	-1	+1	-1	B_2	$P2'_12_12'_1$
AFM2	\mathbf{l}_x^2	+1	+1	-1	-1	B_1	$P2_12'_12'_1$
$\uparrow \uparrow$	\mathbf{l}_y^2	+1	+1	+1	+1	A	$P2_12_12_1$
$\downarrow \downarrow$	\mathbf{l}_z^2	+1	-1	-1	+1	B_3	$P2'_12'_12_1$
AFM3	\mathbf{l}_x^3	+1	-1	+1	-1	B_2	$P2'_12_12'_1$
$\uparrow \downarrow$	\mathbf{l}_y^3	+1	-1	-1	+1	B_3	$P2'_12'_12_1$
$\uparrow \downarrow$	\mathbf{l}_z^3	+1	+1	+1	+1	A	$P2_12_12_1$

4.2.3 Organization of Magnetic Phases by $\mathcal{J}_{ij}^{(\pi)}$

In the previous section, it was shown that a net moment, either in bulk ferromagnetic, or canted antiferromagnetic structures can only occur if all molecules related by either translation or inversion belong to the same magnetic sublattice. For radical materials in which molecules within the π -stacks are related by translation, this restriction suggests exchange along the π -stack must be ferromagnetic in order for a net moment to be observed. As discussed in section 2.1.5, the sign of magnetic exchange depends greatly on the relative orientation of molecules, and thus the relative slippage. In order to investigate the specific relationship between slippage and $\mathcal{J}_{ij}^{(\pi)}$, we performed a series of broken-symmetry density

functional calculations² on a model **4-1** radical pair for which $R_1, R_2 = H$.⁸⁸ All calculations were performed at the B3LYP/6-31G(d,p) level. The geometry of each molecule was separately optimized imposing C_{2v} symmetry, and single point exchange energy calculations were performed as a function of slippage. In all cases the separation of the molecular planes was held constant at $\Delta z = 3.5 \text{ \AA}$. Slippage was measured relative to direct eclipse of the molecules, with Δx (Δy) giving the slippage along the long (short) axis of the molecules. Representative slippage coordinates are shown in Table 4.3 for the various crystallographic phases. The results of the exchange energy calculations are summarized in Fig. 4.7, with respect to the Hamiltonian:

$$\mathcal{H} = -2 \sum_{\langle i,j \rangle} \mathcal{J}_{ij} \mathbf{S}_i \cdot \mathbf{S}_j \quad (4.9)$$

so that the exchange constant goes like:

$$\mathcal{J}_{ij} = \tilde{K}_{ij}^{00} - \frac{2(t_{ij}^{00})^2}{U} \quad (4.10)$$

In the model system, positive and negative values of Δx , Δy provide equivalent structures, so we have shown only one quadrant in the above figure. Similar calculations we performed on all S/Se variants **4-2-4-4**, but incorporation of Se serves only to enhance the magnitude of the exchange interactions, while retaining the basic slippage dependence of $\mathcal{J}_{ij}^{(\pi)}$.

When the model molecules are eclipsed at $[\Delta x, \Delta y] = [0.0, 0.0]$, the open-shell broken symmetry singlet state becomes unstable to the closed shell solution, and the resulting $\mathcal{J}_{ij}^{(\pi)}$ is strongly antiferromagnetic. From this position, slippage in either the Δx or Δy direction reaches a narrow ferromagnetic ridge at a distance of roughly 1.75 \AA . Beyond this ridge, a broad antiferromagnetic region appears centred at $[\Delta x, \Delta y] = [2.0, 1.5]$. A second ferromagnetic region appears at extreme slippage along the long axis of the molecule, beyond $\Delta x > 2.5 \text{ \AA}$. This complex topology arises due to variations in the SOMO-SOMO hopping integral along the π -stacks, denoted $t_{ij}^{00,(\pi)}$, which controls the sign of $\mathcal{J}_{ij}^{(\pi)}$ by modulation of the antiferromagnetic kinetic exchange. These hopping integrals were additionally estimated on the basis of Extended Huckel calculations of the dispersion energy of the SOMO band in 1D π -stacks, which follows $\Delta E_k = 4t_{ij}^{00,(\pi)}$. The results, summarized in Fig. 4.8,

²see Section 2.3.1 for description of the BS-DFT method.

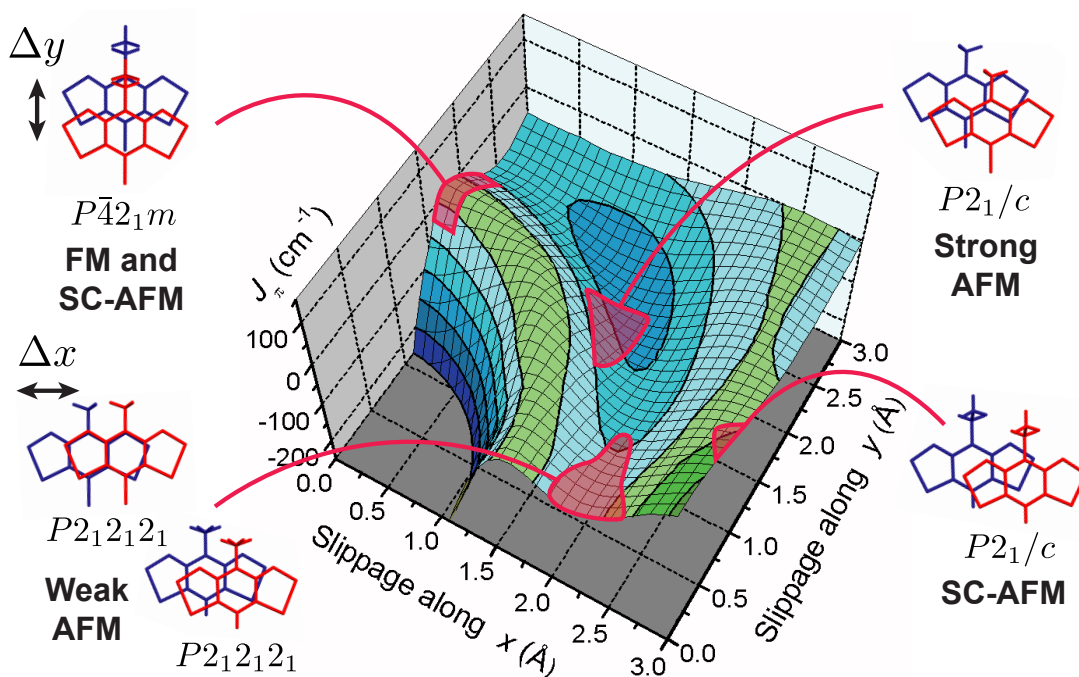


Figure 4.7: Variation of magnetic exchange interactions $\mathcal{J}_{ij}^{(\pi)}$ along the π -stacks as a function of slippage estimated by broken symmetry density functional theory calculations. Slippage along the long (short) axis of the molecule is denoted by Δx (Δy). The locations of various crystallographic phases are indicated.

confirm that the ferromagnetic ridge is associated with a region of vanishing SOMO-SOMO hopping $t_{ij}^{00,(\pi)}$. This orthogonality condition is satisfied along the ridge due to two factors: (1) the electron-rich heteroatom rings are associated with strongly anti-bonding SOMOs with many nodes, and (2) alignment of these nodes with the SOMOs of adjacent radicals results in negligible hopping integrals.

The results of these calculations correlate well with the observed magnetic response of 4-1-4-4 radicals. For example, the tetragonal $P\bar{4}2_1m$ materials for $R_1 = \text{Et}$ all lie very close to the ridge at $[\Delta x, \Delta y] = [0.0, 2.15]$, indicating a ferromagnetic $\mathcal{J}_{ij}^{(\pi)}$ consistent with the observation of ordered ferromagnetic and canted antiferromagnetic states.⁸⁵⁻⁸⁷ The $P2_1/c$ canted antiferromagnets for $R_1 = \text{Et}$, $R_2 = \text{H}$ also fall in a region of ferromagnetic $\mathcal{J}_{ij}^{(\pi)}$, near $[\Delta x, \Delta y] = [3.3, 0.8]$, just beyond the edge of the calculated region.⁸⁴ In contrast,

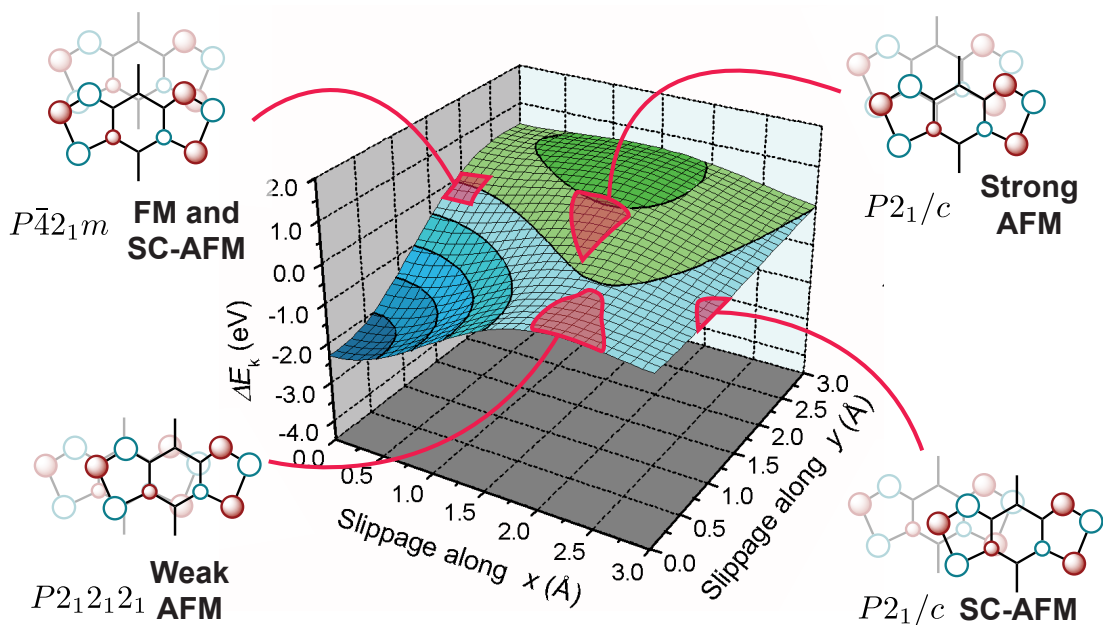


Figure 4.8: Variation of 1D dispersion energy $\Delta E_k = 4t_{ij}^{00,(\pi)}$ with slippage, calculated using Extend Huckel theory. The line of $t_{ij}^{00,(\pi)} = 0$ corresponds well with the position of the ferromagnetic ridge of Fig. 4.7. For each crystallographic phase, the overlap of the SOMOs on adjacent radicals is shown.

the materials that do not display a net moment fall in regions of antiferromagnetic $\mathcal{J}_{ij}^{(\pi)}$. For example, the strongly AFM coupled $R_1 = \text{Me}$, $R_2 = \text{Cl}$ $P2_1/c$ phase lies in the region of slippage near $[\Delta x, \Delta y] = [1.5, 1.6]$, a region predicted to host strong antiferromagnetic interactions.⁸⁸ Not surprisingly, these materials also display enhanced conductivity and the lowest activation energies amongst the pyridine-bridged series, due to large hopping integrals $t_{ij}^{00,(\pi)}$. The two $P2_12_12_1$ phases with weaker AFM coupling are found near $\Delta x = 2.2$, falling between the two ferromagnetic ridges.^{65–67,83,88} In these materials, the antiferromagnetic $\mathcal{J}_{ij}^{(\pi)}$ excludes the possibility of a canted moment, complicating the demonstration of magnetic order from purely magnetic measurements. Ideally, antiferromagnets should display a kink in the magnetic susceptibility at the Néel temperature T_N , as the ordered state (for which $\partial\chi/\partial T > 0$) gives way to the paramagnetic phase (where $\partial\chi/\partial T < 0$).¹²⁴ However, in low-dimensional systems where the magnitude of antiferromagnetic exchange

Table 4.3: Representative slippage coordinates for the various crystallographic phases of pyridine-bridged radicals.

S/Se	R ₁	R ₂	Space Group	Θ	Δx	Δy	Δz
4-2	Me	Cl	<i>P2₁/c</i>	< -100 K	1.60 Å	1.54 Å	3.52 Å
4-4	Me	Cl	<i>P2₁/c</i>	< -100 K	1.49 Å	1.63 Å	3.57 Å
4-3	Me	H	<i>P2₁2₁2₁</i>	-78.3 K	1.94 Å	0.85 Å	3.52 Å
4-4	Me	H	<i>P2₁2₁2₁</i>	-44.3 K	2.04 Å	0.78 Å	3.59 Å
4-1	Me	Cl (<i>T</i> > 93 K)	<i>P2₁2₁2₁</i>	-13 K	2.45 Å	0.07 Å	3.47 Å
4-3	Me	Cl	<i>P2₁2₁2₁</i>	-28 K	2.31 Å	0.11 Å	3.50 Å
4-3	Et	H	<i>P2₁/c</i>	+6.3 K	3.25 Å	0.93 Å	3.66 Å
4-4	Et	H	<i>P2₁/c</i>	-8.0 K	3.30 Å	0.71 Å	3.69 Å
4-2	Et	Cl	<i>P$\bar{4}$₂<i>m</i></i>	+20.3 K	0 Å	2.14 Å	3.52 Å
4-2	Et	Br	<i>P$\bar{4}$₂<i>m</i></i>	+21.0 K	0 Å	2.17 Å	3.52 Å
4-2	Et	Me	<i>P$\bar{4}$₂<i>m</i></i>	+18.4 K	0 Å	2.20 Å	3.51 Å

is very anisotropic, initial singlet formation along directions of strong exchange occurs far above T_N and is associated with a broad maximum in χ , followed by rapid suppression of the susceptibility as T is further lowered. Any susceptibility peaks appearing at T_N may therefore be obscured as the susceptibility is already strongly suppressed in this temperature region. In contrast, a net canted moment appearing at T_N is immediately apparent in magnetic experiments regardless of dimensionality because the spontaneous ordered moment may be directly observed. For this reason, we have only demonstrated antiferromagnetic order in the canted materials. Magnetic order has not been conclusively shown in the majority of $P2_12_12_1$ materials, although further studies will likely shed light on these phases. A notable exception is the well-studied **4-1** ($R_1 = \text{Me}$, $R_2 = \text{H}$), which belongs to the $P2_12_12_1$ phase, and which shows a frequency-independent peak in the AC-susceptibility at $T_N = 5$ K, which we have interpreted in terms of antiferromag-

netic long-range order.⁷⁹ Below this temperature the material exhibits a metamagnetic response, showing a field-induced spin transition to a nearly saturated ferromagnetic state above $H_{ext} = 5$ Tesla. However, ab-initio calculations provided essentially no insight into the magnetic structure, as the computed exchange values are inconsistent with the observed metamagnetic behaviour and absence of a canted moment. As a result, the specific magnetic phases observed in this radical remain an open question.

As a final note, we remark that while the bulk of this chapter has been concerned with magnetic order, the absence of order can be equally interesting from a fundamental perspective. This is true of low-dimensional spin systems with strong magnetic interaction, but which may display unique quantum disordered rather than ordered ground states that are driven by strong quantum fluctuations. An example of such low-dimensional materials will be discussed in the next section.

4.3 Low Dimensional Radical Systems: Ladders

4.3.1 Theoretical Introduction

One-dimensional spin systems have recently attracted interest due to their hosting of quantum disordered spin-liquid states that fail to order due to strong quantum fluctuations. In many cases, such systems can be formally represented as fermionic models through the famous Jordan-Wigner transformation.²⁴² In this representation, spin operators are written as creation and annihilation operators of spinless fermions with the addition of a string operator to ensure correct commutation relations:

$$S_i^+ = c_i^\dagger e^{i\pi \sum_{j<i} c_j^\dagger c_j} \quad (4.11)$$

$$S_i^- = e^{-i\pi \sum_{j<i} c_j^\dagger c_j} c_i \quad (4.12)$$

$$S_i^z = c_i^\dagger c_i - \frac{1}{2} \quad (4.13)$$

The phase associated with each fermion operator depends on the number fermions existing on sites to the “left” of the site in question. In terms of such operators, one-dimensional

spin chains may thus be described in terms of interacting fermions with nearest neighbour repulsion:

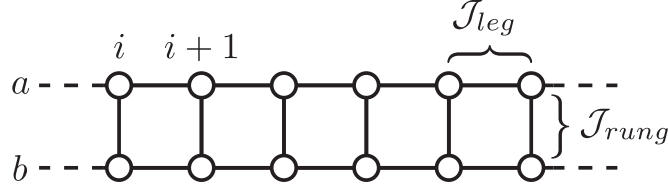
$$\mathcal{J}_{ij} \mathbf{S}_i \cdot \mathbf{S}_j \rightarrow \frac{\mathcal{J}_{ij}}{2} (c_i^\dagger c_j + c_j^\dagger c_i) + \left(n_i - \frac{1}{2}\right) \left(n_j - \frac{1}{2}\right) \quad (4.14)$$

$$HS_i^z \rightarrow H \left(c_i^\dagger c_i - \frac{1}{2}\right) \quad (4.15)$$

The transformation is exact in one dimension due to cancellation of the string phase operators. The interest in this representation of the Hamiltonian is that interacting fermions in one dimension are predicted to form an exotic Tomonaga-Luttinger liquid (TLL) phase with metal-like properties but no sharp Fermi surface, and consequently non-Fermi liquid temperature or field dependence of response functions.^{243,244} Instead, the response functions scale according a single parameter K , where $K > 1$ for attractive interactions, and $K < 1$ for repulsive interactions. Demonstration of such a state in one-dimensional electronic conductors has been met with difficulty for two main reasons i) low-dimensionality often produces instabilities toward insulating phases such as charge or spin-density waves that can only be avoided through higher dimensional interactions, and ii) there is often no convenient method for investigating TLL scaling in a range of properties and over a range of band-fillings.²⁴⁵ In contrast, the density of Jordan-Wigner fermions can also be tuned by an external magnetic field (which plays the role of chemical potential). Moreover, the Green function $\langle c_i^\dagger c_j \rangle \propto \langle S_i^+ S_j^- \rangle$ may be directly measured via electron spin resonance (ESR) and inelastic neutron scattering, thus facilitating investigation. As a result of this experimental convenience, one-dimensional spin chains have been pursued as “quantum simulators” of low-dimensional electronic systems.

Particular interest has been paid to been so-called “spin ladders”, which depart from strictly one-dimension through strong interactions coupling a small number of spin chains. For example, the two-leg spin ladder consists of two coupled chains (labelled a, b), and may be described by the ratio of magnetic exchange along the chain direction, \mathcal{J}_{leg} , to that

between the chains \mathcal{J}_{rung} .



$$\mathcal{H} = \mathcal{J}_{leg} \sum_i \mathbf{S}_{i,a} \cdot \mathbf{S}_{i+1,a} + \mathbf{S}_{i,b} \cdot \mathbf{S}_{i+1,b} + \mathcal{J}_{rung} \sum_i \mathbf{S}_{i,a} \cdot \mathbf{S}_{i,b} + \sum_i h(S_{i,a}^z + S_{i,b}^z) \quad (4.16)$$

In the case where both interactions are antiferromagnetic, it is known that ladders with an even number of legs display an energy gap Δ to all spin excitations for any finite $\mathcal{J}_{rung} > 0$.²⁴⁶ However, the nature of the ground and excited states varies as a function of the ratio $\mathcal{J}_{rung}/\mathcal{J}_{leg}$. The most well-studied case is the strong rung limit $\mathcal{J}_{rung} \gg \mathcal{J}_{leg}$, for which the ground state is a product state of singlets existing on each rung of the ladder.²⁴⁷ Excited states consist of rung-triplons which are dispersive due to the intrachain coupling \mathcal{J}_{leg} . In the presence of a magnetic field $h \sim \Delta$, the $m_s = +1$ branch of the triplons can be brought to sufficiently low energy to allow for a finite triplon density in the ground state. In this case, the low-energy theory can be formulated by projecting out the higher energy triplon branches, and is described in terms of a single chain in which each rung forms a site with a pseudospin variable $\vec{\tau}_i$. This variable describing whether rung is in the singlet $|S_0\rangle$ or triplet $|T_{+1}\rangle$ state, with $\tau_i^z|S_0\rangle = +1/2, \tau_i^z|T_{+1}\rangle = -1/2$. Performing the J-W transformation on these pseudospin variables provides the fermionic model with repulsive interactions ($K < 1$):

$$\mathcal{H}_{J-W} = t \sum_i (c_i^\dagger c_{i+1} + \text{h.c.}) + V \sum_i n_i n_{i+1} - \mu \sum_i n_i \quad (\mathcal{J}_{rung} \gg \mathcal{J}_{leg}) \quad (4.17)$$

$$t = V = \frac{\mathcal{J}_{leg}}{2} \quad , \quad \mu = h - \mathcal{J}_{rung} \quad , \quad \Delta \sim \mathcal{J}_{rung} - \mathcal{J}_{leg} \quad (4.18)$$

For $\mu > -2t \rightarrow h > \mathcal{J}_{rung} - \mathcal{J}_{leg} \sim \Delta$, there is a finite density of J-W fermions, and the model is expected to display a TLL-like phase. This prediction has been investigated experimentally and demonstrated convincingly in the Cu-based ladder materials $(\text{CH}_3)_2\text{CHNH}_3\text{CuCl}_3$ ^{248,249} and $(\text{C}_5\text{H}_{12}\text{N})_2\text{CuBr}_4$.²⁵⁰⁻²⁵⁴

In contrast, the opposite limit strong leg limit $\mathcal{J}_{rung} \gg \mathcal{J}_{leg}$ has been less studied due to the absence of a well-controlled expansion. The standard theoretical approach in this case

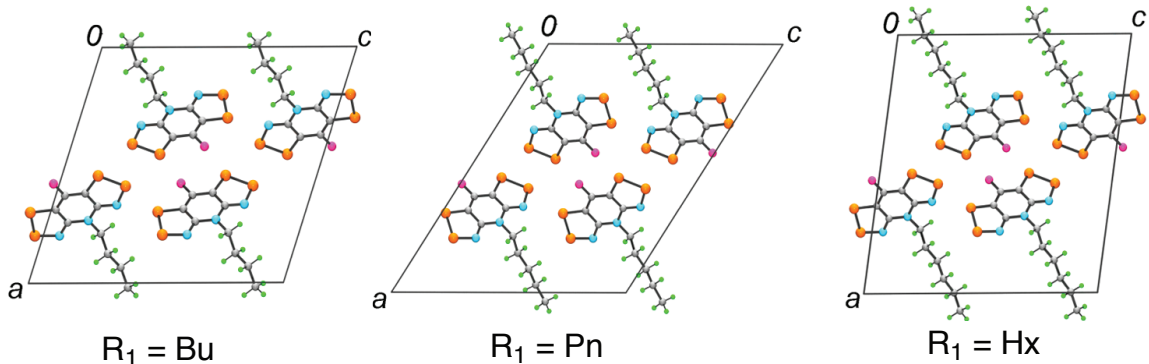


Figure 4.9: Unit cells of spin ladders **4-1** ($R_2 = \text{F}$) viewed parallel to the π -stacking axis.

is to apply the J-W transformation to each chain, providing initially decoupled chains with gapless TLL excitations. The interchain interactions \mathcal{J}_{rung} are then treated perturbatively, and result in an energy gap for spinons. The ground state is thus qualitatively similar to the strong rung case, being a singlet state with triplon excitations. The spin-gap has been estimated by fitting QMC data:²⁵⁵

$$\Delta \sim 0.4030 \mathcal{J}_{rung} + 0.0989 \left(\frac{\mathcal{J}_{rung}}{\mathcal{J}_{leg}} \right)^3 \mathcal{J}_{rung} \quad (\mathcal{J}_{rung} \ll \mathcal{J}_{leg}) \quad (4.19)$$

In the presence of a magnetic field $h \gtrsim \Delta$, projection into the subspace of the lowest singlet and triplon states is thought to result in a 1D fermionic model similar to (4.17), except with attractive interactions ($K > 1$).^{256,257} This regime has been experimentally probed only recently due to the discovery of a long sought after spin ladder compound $(\text{C}_7\text{H}_{10}\text{N})_2\text{CuBr}_4$ with $\mathcal{J}_{rung} < \mathcal{J}_{leg}$.^{258,259} Preparation of materials in the isotropic intermediate coupling regime for which $\mathcal{J}_{rung} \sim \mathcal{J}_{leg}$ and with spin gaps Δ small enough to be reached with laboratory fields has remained an open synthetic challenge.

4.3.2 Studies of Radical Spin Ladders

In this context, we discuss a series of spin-ladder compounds recently discovered by the Oakley group through the synthetic efforts of Dr. Lekin and Ms. Wong (Fig. 4.9, 4.10).²⁶⁰ In order to reduce the dimensionality of magnetic interactions, she incorporated bulky alkyl

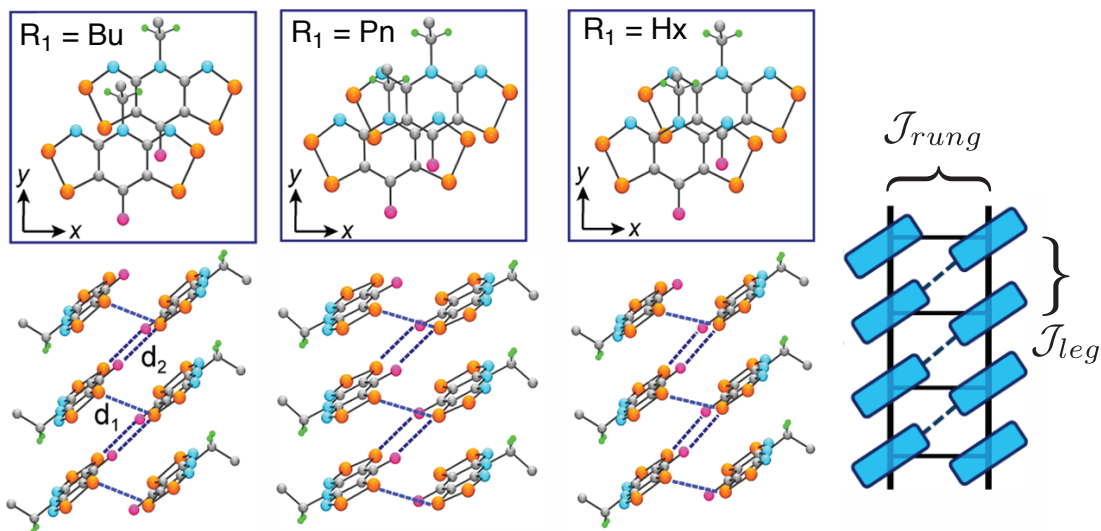


Figure 4.10: Comparison of π -stack slippage of spin ladders **4-1** ($R_2 = F$), which occurs in both the molecular x - and y -directions consistent with strong antiferromagnetic interactions. Electrostatic S-F interactions bind such π -stacks together into ladders as shown below.

groups into the R_1 position of the all-sulfur **4-1**, forming a series of isostructural radicals that crystallize in the $P2_1/c$ space group. These radicals exhibit moderate slippage along both the molecular x - and y -directions, consistent with a region of strong antiferromagnetic exchange \mathcal{J}_{leg} along the π -stacking chain direction. The bulky groups separate the radicals, so that π -stacks are largely isolated. However, adjacent stacks, which are related by inversion, are pinned together into ladders by strong S-F electrostatic interactions afforded by $R_2 = F$, thus forming ladders.

The magnetic topology was investigated through broken symmetry DFT calculations of the values of each pairwise nearest neighbour exchange interactions, which may be divided into five categories by relative proximity. The closest neighbours are adjacent radicals within the same π -stack, with exchange denoted $\mathcal{J}_{(\pi)} = \mathcal{J}_{leg}$. The second closest neighbours are in different legs of the ladders, with $\mathcal{J}_{(1)} = \mathcal{J}_{rung}$. These ladders are held together by close S-F contacts between neighbours labelled (2) with associated exchange constant $\mathcal{J}_{(2)}$. Finally, there are interladder neighbours labelled (3) and (4) as shown in Fig. 4.11. The results of such calculations are summarized in Table 4.4 with reference to the Hamiltonian

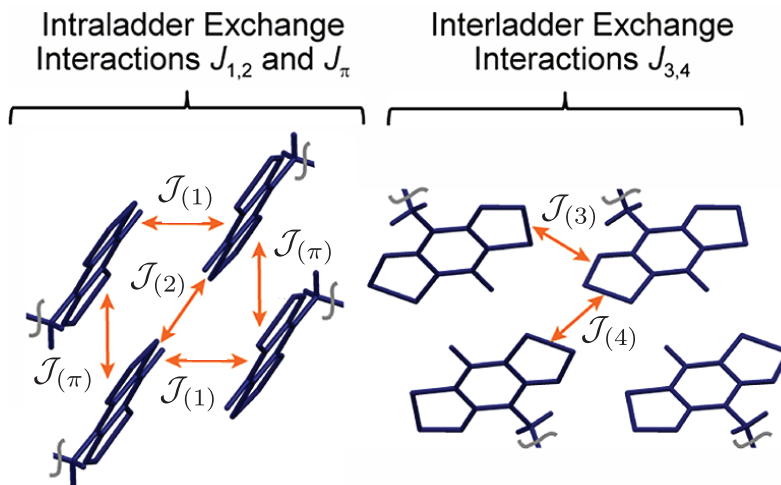


Figure 4.11: Definitions of unique magnetic interactions $\mathcal{J}_{(\pi)}$ and $\mathcal{J}_{(1)-(4)}$.

$\mathcal{H} = \mathcal{J} \mathbf{S}_i \cdot \mathbf{S}_j$. In all three ladder materials, $\mathcal{J}_{(2)}$ and interladder couplings $\mathcal{J}_{(3)}$ and $\mathcal{J}_{(4)}$ were estimated to have magnitudes below 10 K, an order of magnitude smaller than the intraladder couplings $\mathcal{J}_{(1)}$ and $\mathcal{J}_{(2)}$. These results are thus in agreement with the anticipated one-dimensional spin-ladder topology. However, while the calculated exchange constants suggest that all three materials lie within the strong-rung regime ($\mathcal{J}_{(1)} > \mathcal{J}_{(\pi)}$), the experimental magnetic susceptibility is inconsistent with this prediction. We have demonstrated this observation in two ways. First, we fit the observed magnetic susceptibility to functions obtained by Johnston *et al.* from analysis of QMC simulations of spin ladders.²⁵⁵ To these functions, we added a fractional paramagnetic impurity term to account for the observed Curie tail at low temperatures. The results of such fitting are shown in Table 4.4 and Fig. 4.12. In contrast with the computed exchange values, **4-1** ($R_1 = \text{Bu}$, Hx) were found to lie within the strong-leg regime ($\mathcal{J}_{(1)} < \mathcal{J}_{(\pi)}$), while we found $R_1 = \text{Pn}$ to be a nearly isotropic ladder ($\mathcal{J}_{(1)} \sim \mathcal{J}_{(\pi)}$). As a second demonstration of the discrepancy between computed and experimental values, we performed QMC simulations in order to obtain the theoretical susceptibility corresponding to the calculated exchange constants. These latter calculations employed the ALPS program loop, and were performed on 10^4 sites of a single ladder. In all cases, the simulated susceptibilities show suppressed magnitude compared to the experimental data due to an overestimation of the rung exchange.

Table 4.4: Magnetic exchange parameters for spin-ladder compounds **4-1** $R_2 = F$ with reference to the Hamiltonian $\mathcal{H} = \mathcal{J}\mathbf{S}_i \cdot \mathbf{S}_j$. Experimental values were obtained by fitting the magnetic susceptibility as described in the text. For convenience of discussion, the spin gap Δ is presented in magnetic field units Tesla. F% denotes the fraction of paramagnetic impurity.

R_1	BS-DFT Calculations (B3LYP/6-31G(d,p))					Experimental Fitting			
	$\mathcal{J}_{(\pi)}$ (K)	$\mathcal{J}_{(1)}$ (K)	$\mathcal{J}_{(2)}$ (K)	$\mathcal{J}_{(3)}$ (K)	$\mathcal{J}_{(4)}$ (K)	\mathcal{J}_{leg} (K)	\mathcal{J}_{rung} (K)	Δ (T)	F%
Bu	+91.1	+144.9	-1.2	-8.9	-8.7	+190	+49	34.3	2.8
Pn	+26.2	+133.7	-0.2	-2.4	+4.2	+75	+75	56.1	4.2
Hx	+90.2	+189.6	-0.5	-4.1	-5.9	+164	+37.4	22.7	6.1

While all three radical spin-ladder compounds described in this section fall within the desirable strong-leg or isotropic regime, their application for the study of TLL physics is hampered by two main factors. The first is that the spin-gaps Δ are quite large due to the significant magnitude of the exchange interactions, so that accessing the TLL phase will require excessive magnetic field. That being said, for $R_1 = Hx$, the spin-gap is only 22.7 T, which is easily achievable in high field facilities such as the National High Magnetic Field Lab in Tallahassee, Florida. Of particular interest would be to take advantage of the basal F substituent, and measure F^{19} spin-lattice NMR relaxation rate ($1/T_1$), for which theoretical predictions have been made for various ground states of spin-ladders.²⁶¹ This experiment is currently being considered. However, the second factor hampering such work is the existence of a significant fraction of paramagnetic impurities particularly in the Hx sample indicating possible contamination. This contaminant most likely stems from the somewhat atypical method of preparing magnetic samples directly by recrystallization of the radicals from hot solution. The heating process may result in various decomposition products, but many such products will be short lived or not possess an unpaired spin, and thus should not contribute to the paramagnetic signal. In this light, the most likely candidate impurity is the rearranged radical **4-8**, which can be anticipated based on the observed shifting of alkyl groups for **4-1** ($R_1 = Me$, $R_2 = OMe$)²³⁴ discussed in the first

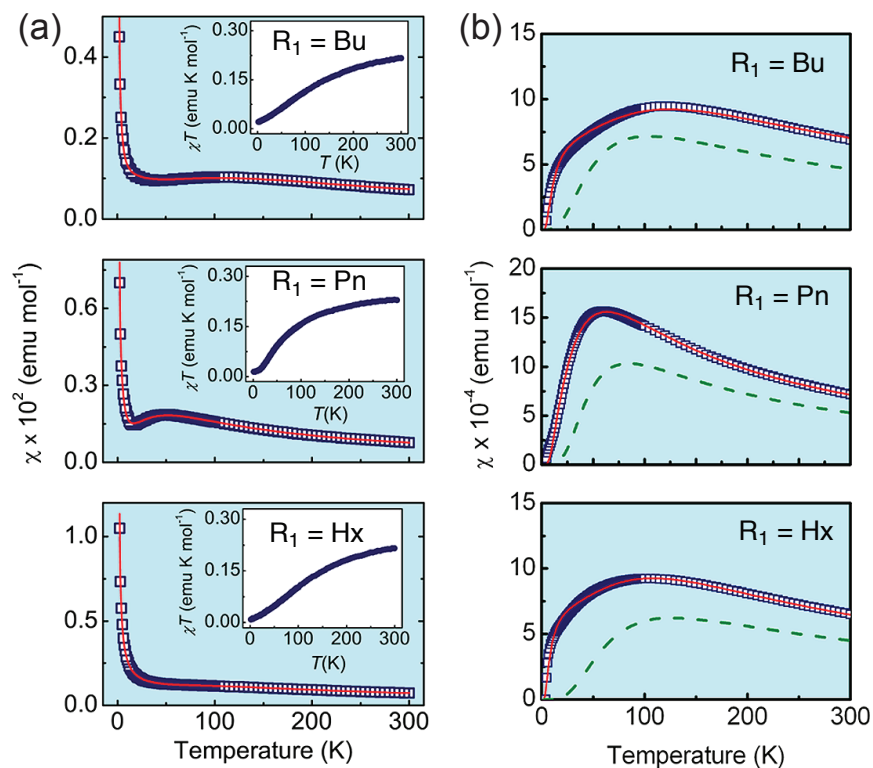
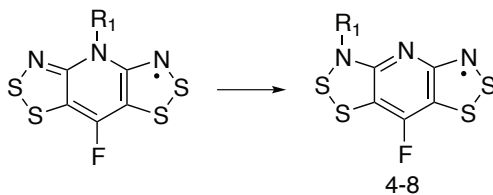


Figure 4.12: (a) Experimental magnetic susceptibility $\chi = M/H$ and inset χT for ladder compounds **4-1** ($R_1 = \text{Bu}, \text{Pn}, \text{Hx}$) (open squares). The results of fitting to the strong-leg ladder function of Johnston *et. al.* is indicated by a red line. (b) Susceptibility after subtraction of fractional impurities (open squares) with the same fits shown with red lines. The results of QMC simulations based on computed exchange parameters is shown by a green dashed line.

section of this chapter.



This rearrangement is also consistent with the EPR spectrum observed after allowing the radicals **4-1** ($R_2 = \text{F}$) to sit in very dilute solutions at room temperature for several days (Fig. 4.13). The unrearranged radicals **4-1** with $R_2 = \text{F}$ display a characteristic seven line

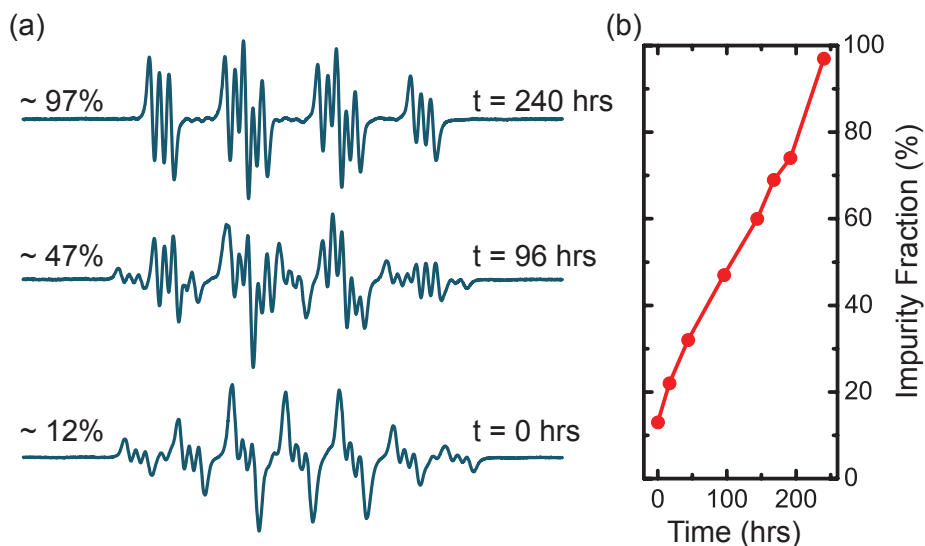


Figure 4.13: (a) Evolution of EPR spectra of dilute solution of **4-1** ($R_1 = \text{Hx}$, $R_2 = \text{F}$) in MeCl as a function of time showing conversion to an asymmetric radical consistent with **4-8**. (b) The fraction of the two radicals as estimated by fitting the spectra as a mixture of products.

pattern in the EPR due to hyperfine coupling primarily to the two wing nitrogens ($I = 1$) and basal F ($I = 1/2$). However, even the initially prepared solutions show some contamination with a single alternate radical whose fraction grows with time. Consistent with **4-8** this contaminant radical shows instead a four line pattern due to coupling to the basal F and only one wing nitrogen. As the conversion may occur as a bimolecular reaction, its rate of formation would be expected to increase significantly with both concentration and heat, suggesting a potential for formation during short heating in concentrated solutions during recrystallization. Indeed, such samples, after initially dissolving them in the EPR cell (in dichloromethane) and degassing already contain a 12% impurity according to the fits of the initial spectrum. Learning to better control this impurity represents an important future area of investigation.

4.4 Chapter Summary

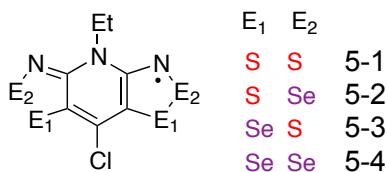
This chapter focussed on the magnetic properties of pyridine-bridged bis-dichalcogenyl radicals. Section 4.1 reviewed the synthetic routes to these materials, all of which were developed prior to my tenure with the Oakley group, but which continued to be employed both by myself and other group members to generate a range of materials. The dominant structural and magnetic phases were discussed in detail in section 4.2. Through symmetry analysis, we suggested that materials **4-1–4-4** could be grouped into two categories based on the sign of $\mathcal{J}_{ij}^{(\pi)}$. Those materials that display ferromagnetic interactions along the π -stacks are allowed to order as bulk ferromagnets and canted antiferromagnets displaying a net moment. In contrast, those that display dominantly antiferromagnetic π -stack interactions are forbidden from possessing a net moment even when ordered. Model BS-DFT calculations of $\mathcal{J}_{ij}^{(\pi)}$ allowed us to correlate the magnetic response with the packing modes of the various structural phases, and explained the clustering of ordered ferromagnets and canted antiferromagnets into the two $P\bar{4}2_1m$ and $P2_1/c$ space groups. Finally, section 4.3 discussed the properties of a new class of radical spin-ladders, for which magnetic order is avoided as a result of strong quantum fluctuations characteristic of one-dimensional magnets. Analysis of their magnetic response suggested these materials are examples of theoretically desirable strong-leg or isotropic ladders. However, their magnetic interactions are likely too strong to allow easy access to the Luttinger liquid regime at high magnetic field. Future work could focus on reducing the strength of interactions, as well as the preparation of samples of higher magnetic purity.

Chapter 5

Isostructural Tetragonal Radical Family $R_1 = \text{Et}$, $R_2 = \text{Cl}$

5.1 Introduction

This chapter focusses on the properties of the isostructural radical family **5-1–5-4** ($R_1 = \text{Et}$, $R_2 = \text{Cl}$), all of which crystallize in the non-centric tetragonal space group $P\bar{4}2_1m$ introduced in the previous chapter (Fig. 5.1):



The fact that the entire family **5-1 – 5-4** are isostructural provides the opportunity to study the effects of Se incorporation on the electronic and magnetic response independent of other structural details. In the first section, we contrast the ambient pressure magnetic structures of the four radical materials. Of key interest is the observation that in the tetragonal $P\bar{4}2_1m$ phase, those radicals with S in the E₂ position tend to order as spin-canted antiferromagnets, while those with Se in this position prefer ferromagnetic order.^{85,86}

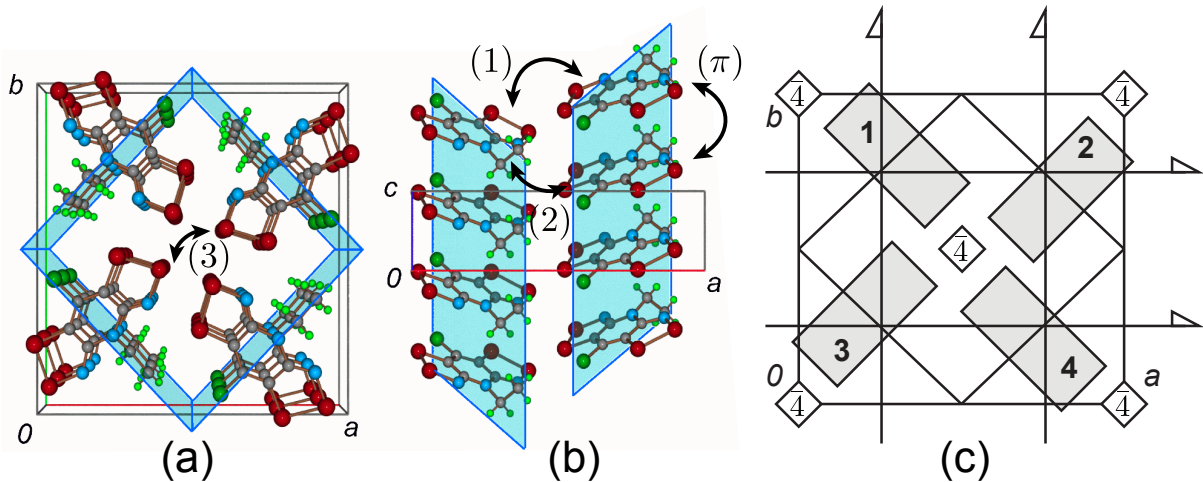


Figure 5.1: Crystal structure of **5-4** viewed (a) parallel to the c -axis, and (b) parallel to the b -axis. All four S/Se variants **5-1**–**5-4** are isostructural. Unique nearest neighbours are labelled (π), and (1) – (3). Crystallographic mirror planes are emphasized. The positions of the remaining symmetry elements are shown in (c).

Indeed, for the specific case of $R_1 = \text{Et}$, $R_2 = \text{Cl}$, **5-2** and **5-4** order ferromagnetically at $T_C = 12.8$ and 17 K, respectively, while **5-3** orders as a canted antiferromagnet at $T_N = 14$ K. Magnetic order in **5-1** has not yet been conclusively demonstrated, but the isostructural material with Br in the R_2 position does indeed show spin-canted order below $T_N \sim 10$ K. In this case, magnetic order is indicated both by a bifurcation in the FC-ZFC susceptibility, and the observation of a spontaneous magnetization that displays hysteresis.

In this chapter, we argue that the dichotomy of magnetic order may be rationalized in terms of multi-orbital contributions to the magnetic exchange between π -stacks. The second section will detail the phase diagram of the all-selenium **5-4** under applied pressure, which prompts not only a loss of ferromagnetic order through enhancement of intermolecular hopping integrals,^{90,91} but also a region of metallic conductivity above 7 GPa.⁸⁹ Finally we address the observation of large magnetic coercivity in the ferromagnets **5-2** and **5-4**, which displays a coercive field H_c orders of magnitude larger than previous organic ferromagnets composed of lighter N, S, O atoms. We demonstrate that this effect is due to spin-orbit effects through studies at both ambient and high pressure.^{262,263}

5.2 Magnetic Structures

The unit cell of **5-1-5-4** consists of four radicals encircling a $\bar{4}$ -point, with each radical being bisected by a mirror plane normal to either the (110) or (1 $\bar{1}$ 0) directions. Adjacent radical stacks are related by 2_1 axes along both the a - and b -directions. Nearest neighbour pairs expected to have significant magnetic interactions may be organized in order of proximity (Fig. 5.1(a),(b)). Those interactions between adjacent radicals in the same π -stack, related by translation along c are labelled (π). The two closest interstack contacts, labelled (1) and (2) occur between radicals related by 2_1 axes in the ab -plane located at $x = 0.0, 0.5$, respectively. Finally, interaction (3) occurs between radicals across the $\bar{4}$ -point, related by $2 = (\bar{4})^2$.

As explained in the previous chapter, the observation of a net moment in the ordered phase of all such materials suggests that $\mathcal{J}_{ij}^{(\pi)}$ must be ferromagnetic for all of **5-1-5-4**. The magnitude of the remaining interactions are expected to satisfy $|\mathcal{J}_{ij}^{(1)}| \sim |\mathcal{J}_{ij}^{(2)}| > |\mathcal{J}_{ij}^{(3)}|$ due to the relative proximity of each radical pair. In order to analyze the possible magnetic structures, we employ a series of collinear basis functions consistent with the D_{2d} point group symmetry of the cell:

$$\mathbf{f}_\mu = \mathbf{m}_1^\mu + \mathbf{m}_2^\mu + \mathbf{m}_3^\mu + \mathbf{m}_4^\mu \quad (5.1)$$

$$\mathbf{l}_\mu^1 = \mathbf{m}_1^\mu - \mathbf{m}_2^\mu - \mathbf{m}_3^\mu + \mathbf{m}_4^\mu \quad (5.2)$$

$$\mathbf{l}_z^2 = \mathbf{m}_1^z + \mathbf{m}_2^z - \mathbf{m}_3^z - \mathbf{m}_4^z \quad (5.3)$$

$$\mathbf{l}_z^3 = \mathbf{m}_1^z - \mathbf{m}_2^z + \mathbf{m}_3^z - \mathbf{m}_4^z \quad (5.4)$$

where $\mu = \{x, y, z\}$. The latter two functions \mathbf{l}_z^2 and \mathbf{l}_z^3 only transform as a representation of D_{2d} for orientation of the moments along the z -direction. For this reason, and for completeness, the basis functions must be supplemented by non-collinear functions with no net moment:

$$\mathbf{nc}^1 = \mathbf{m}_1^{x+y} + \mathbf{m}_2^{x-y} - \mathbf{m}_3^{x-y} - \mathbf{m}_4^{x+y} \quad (5.5)$$

$$\mathbf{nc}^2 = \mathbf{m}_1^{x+y} - \mathbf{m}_2^{x-y} + \mathbf{m}_3^{x-y} - \mathbf{m}_4^{x+y} \quad (5.6)$$

$$\mathbf{nc}^3 = \mathbf{m}_1^{x-y} + \mathbf{m}_2^{x+y} - \mathbf{m}_3^{x+y} - \mathbf{m}_4^{x-y} \quad (5.7)$$

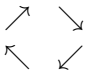
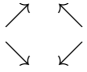
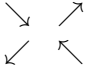
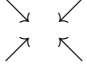
$$\mathbf{nc}^4 = \mathbf{m}_1^{x-y} - \mathbf{m}_2^{x+y} + \mathbf{m}_3^{x+y} - \mathbf{m}_4^{x-y} \quad (5.8)$$

Table 5.1: Symmetry classification of collinear basis functions for describing the magnetic structure of **5-1-5-4**. Only antiferromagnetic structures of E symmetry may give rise to a canted moment.

State	Function	E	$\bar{4}, \bar{4}^3$	2-fold ($\bar{4}^2$)	$2_1 \parallel a, b$	$\sigma \perp x + y, x - y$	Point Group in D_{2d}
$\begin{matrix} \odot & \odot \\ \odot & \odot \end{matrix}$	\mathbf{f}_z	+1	+1	+1	-1	-1	A_2
$\left(\begin{matrix} \uparrow & \uparrow & \rightarrow & \rightarrow \\ \uparrow & \uparrow & \rightarrow & \rightarrow \end{matrix} \right)$	$(\mathbf{f}_x, \mathbf{f}_y)$	+2	0	-2	0	0	E
$\begin{matrix} \odot & \otimes \\ \otimes & \odot \end{matrix}$	\mathbf{l}_z^1	+1	-1	+1	+1	-1	B_1
$\left(\begin{matrix} \uparrow & \downarrow & \rightarrow & \leftarrow \\ \downarrow & \uparrow & \leftarrow & \rightarrow \end{matrix} \right)$	$(\mathbf{l}_x^1, \mathbf{l}_y^1)$	+2	0	-2	0	0	E
$\left(\begin{matrix} \odot & \odot & \odot & \otimes \\ \otimes & \otimes & \odot & \otimes \end{matrix} \right)$	$(\mathbf{l}_z^2, \mathbf{l}_z^3)$	+2	0	-2	0	0	E

Assuming that the isotropic magnetic interactions are dominant, the only antiferromagnetic structures capable of exhibiting a net canted moment must transform as either A_2 or the doubly degenerate E representation, and have a $\mathbf{k} = [0, 0, 0]$ propagation vector (Table 5.1, 5.2). This provides two possible canted antiferromagnetic structures for **5-1** and **5-3** obtained from predominantly either $(\mathbf{l}_x^1, \mathbf{l}_y^1)$ or $(\mathbf{l}_z^2, \mathbf{l}_z^3)$ basis functions, both of E symmetry. In both cases, the corresponding order parameters can be mixed with the ferromagnetic functions $(\mathbf{f}_x, \mathbf{f}_y)$ of E symmetry, resulting in a net canted moment in the ab -plane. Of these, the striped order given by $(\mathbf{l}_z^2, \mathbf{l}_z^3)$ is expected to prevail only for antiferromagnetic $\mathcal{J}_{ij}^{(3)} < 0$, and provided $|\mathcal{J}_{ij}^{(3)}| > |\mathcal{J}_{ij}^{(1)} + \mathcal{J}_{ij}^{(2)}|$. Since this condition is unlikely to be satisfied given the relative proximity of each radical pair, the basis functions $(\mathbf{l}_x^1, \mathbf{l}_y^1)$ should be considered the most likely candidate for the zeroth order magnetic structure. The anticipated order can therefore be described by ferromagnetic 1D π -stacks, coupled antiferromagnet-

Table 5.2: Symmetry classification of noncollinear basis functions for describing the magnetic structure of **5-1-5-4**. Only antiferromagnetic structures of E symmetry may give rise to a canted moment.

State	Function	E	$\bar{4}, \bar{4}^3$	2-fold ($\bar{4}^2$)	$2_1 \parallel a, b$	$\sigma \perp x + y, x - y$	Point Group in D_{2d}
	\mathbf{nc}^1	+1	-1	+1	+1	-1	B_1
	\mathbf{nc}^2	+1	+1	+1	+1	+1	A_1
	\mathbf{nc}^3	+1	-1	+1	-1	+1	B_2
	\mathbf{nc}^4	+1	+1	-1	-1	-1	A_2

ically with their closest neighbours, related by 2_1 axes. On the basis of this discussion, we therefore anticipate that the ferromagnets **5-2** and **5-4** can be distinguished from their canted antiferromagnetic counterparts **5-1** and **5-3** primarily by the sign of $\mathcal{J}_{ij}^{(1)}$ and $\mathcal{J}_{ij}^{(2)}$, which must be antiferromagnetic for the latter materials. In the next section, we discuss how such a dichotomy may arise due to the relative importance of ferromagnetic exchange through empty σ -orbitals.

5.2.1 Molecular Electronic Structure

At each radical site in the crystal, we label molecular orbitals according to their energy relative to the highest, singly occupied molecular orbital (SOMO, $\alpha = 0$). Those orbitals with greater energy are labelled sequentially with $\alpha > 0$, with the lowest unoccupied molecular orbital (LUMO) having $\alpha = +1$. The filled orbitals, at lower energy than the SOMO have $\alpha < 0$. The local point group symmetry of each molecular site is C_s which is sufficiently low to ensure the absence of degenerate orbitals. Nonetheless, the $\alpha = +1$ and $\alpha = +2$ orbitals are nearly degenerate, consisting of A' and A'' combinations of chalcogen-chalcogen σ -antibonding orbitals (Fig. 5.2). Here we suggest that these orbitals play an

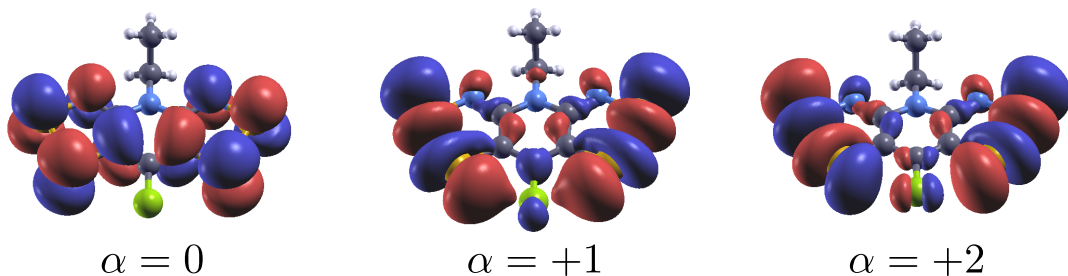


Figure 5.2: Relevant orbitals in three orbital model of the electronic structure of **5-1-5-4**. Plots were generated from B3LYP/6-311G(d,p) calculations on **5-4**.

important role in determining the magnetic structure through small hybridization with the SOMO bands. Within the three orbital manifold we consider a single-site Hamiltonian given by:

$$\begin{aligned} \mathcal{H}_i = & \sum_{\alpha} \epsilon_i^{\alpha} \mathbf{c}_{i,\alpha}^{\dagger} \mathbf{c}_{i,\alpha} + U \sum_{\alpha} n_{i,\alpha,\uparrow} n_{i,\alpha,\downarrow} + V \sum_{\alpha>0} n_{i,0} n_{i,\alpha} + V' n_{i,+1} n_{i,+2} \\ & + \sum_{\substack{\alpha>\beta \\ \sigma,\sigma'}} K_i^{\alpha\beta} \mathbf{c}_{i,\beta,\sigma'}^{\dagger} \mathbf{c}_{i,\alpha,\sigma}^{\dagger} \mathbf{c}_{i,\alpha,\sigma'} \mathbf{c}_{i,\beta,\sigma} \end{aligned} \quad (5.9)$$

where we have explicitly assumed the Coulomb repulsion between electrons in the same orbital $U = U_i^{00} = U_i^{11} = U_i^{22}$ to be orbital-independent, and that $V = V_i^{01} = V_i^{02}$. The former Coulomb term can be estimated from electrochemical measurements to be on the order of $U \sim 0.8$ eV,⁸⁶ while the remaining terms can be estimated on the basis of state energy calculations on the isolated molecular anion. To see this, note that the two-electron, three-orbital system admits 15 states at each radical site. The first 9 can be organized into three sets of triplets of increasing energy with varying occupancy of the three orbitals:

$${}^3|110\rangle \quad , \quad E = \epsilon_i^0 + \epsilon_i^1 - K_i^{12} + V \quad (5.10)$$

$${}^3|101\rangle \quad , \quad E = \epsilon_i^0 + \epsilon_i^2 - K_i^{12} + V \quad (5.11)$$

$${}^3|011\rangle \quad , \quad E = \epsilon_i^1 + \epsilon_i^2 - K_i^{23} + V' \quad (5.12)$$

where the notation ${}^3|110\rangle$ refers to a triplet state (with multiplicity 3), with one electron occupying the SOMO $\alpha = 0$, and one occupying the LUMO $\alpha = +1$. The remaining states

Table 5.3: Single-site Hamiltonian parameters for **5-4** ($R_1 = \text{Et}$, $R_2 = \text{Cl}$) assuming $U \equiv 0.8$ eV.

Method	ϵ_0	ϵ_1	ϵ_2	V	V'	K_i^{01}	K_i^{02}	K_i^{12}
DDCI3	$\equiv 0$	+1.6 eV	+1.9 eV	0.80 eV	0.81 eV	0.11 eV	0.11 eV	0.66 eV
SORCI	$\equiv 0$	+1.5 eV	+1.7 eV	0.87 eV	0.82 eV	0.10 eV	0.10 eV	0.63 eV

are singlets organized in order of increasing energy are given approximately by:

$${}^1|200\rangle, \quad E = 2\epsilon_0 + U \quad (5.13)$$

$${}^1|110\rangle, \quad E = \epsilon_i^0 + \epsilon_i^1 + K_i^{12} + V \quad (5.14)$$

$${}^1|101\rangle, \quad E = \epsilon_i^0 + \epsilon_i^2 + K_i^{12} + V \quad (5.15)$$

$$\left[\frac{1}{\sqrt{2}} {}^1|020\rangle \pm \frac{1}{\sqrt{2}} {}^1|002\rangle \right], \quad E = \epsilon_1 + \epsilon_2 + U \pm \sqrt{(\epsilon_2 - \epsilon_1)^2 + K_i^{23}} \quad (5.16)$$

$${}^1|011\rangle, \quad E = \epsilon_i^1 + \epsilon_i^2 + K_i^{23} + V' \quad (5.17)$$

where the significant mixing of ${}^1|020\rangle$ and ${}^1|002\rangle$ states results from the large repulsion between electrons in the two LUMOs in comparison to the energetic splitting $\epsilon_2 - \epsilon_1$. The energies of the above states have been computed for the all-selenium **5-4** using the relatively inexpensive multiconfigurational methods implemented in ORCA:¹⁴⁸ (i) Difference Dedicated Configuration Interaction with three degrees of freedom (DDCI3)²⁶⁴ and (ii) Spectroscopy Oriented Configuration Interaction (SORCI)²⁶⁵ method. The results should be considered generic for the series **5-1** to **5-4**. Input orbitals we generated from a DFT calculation on the closed shell anion state (${}^1|200\rangle$) at the B3LYP/6-311G(d,p) level, followed by a CASSCF calculation on the CAS(2,3) space with equal energetic weight placed on all above states. The effective Hubbard Hamiltonian parameters were then obtained by fitting the calculated state energies to those in eq'ns (5.10) – (5.17). The results are summarized in table 5.3.

While the energetic splitting of the $\alpha = +1$ and $\alpha = +2$ LUMOs is found to be small in both methods (0.2 – 0.3 eV), both orbitals are well separated from the SOMO, by a large energy of at least 1.5 eV at the molecular level. The value of the Hund's coupling between the SOMO and LUMOs is also small, on the order of 0.1 eV for both K_i^{01} and K_i^{02} ,

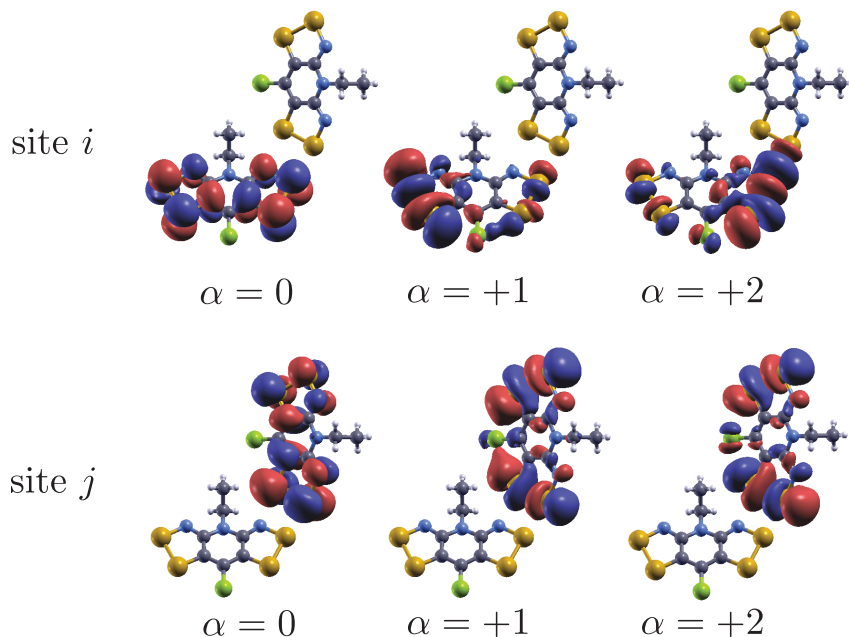


Figure 5.3: MOMOs for **5-4** for interaction (2) showing over localization of the $\alpha = +1, +2$ orbitals at site i .

which follows from the large difference in the spatial density of these orbitals. Given these findings, mixing of the SOMO and LUMO bands in the solid state is expected to be small except in special packing arrangements where the intermolecular hopping integrals between such orbitals t_{ij}^{01}, t_{ij}^{02} becomes large compared to the SOMO-SOMO hopping integrals t_{ij}^{00} . As will be discussed in the following sections, such an arrangement is indeed observed in the present family, so that the empty-orbital contribution to the ferromagnetic exchange may be significant. This possibility is explored in the next section.

5.2.2 Solid State Electronic Structure

In order to investigate the role of multi-orbital exchange in **5-1–5-4**, we have computed hopping integrals for each material using the Maximally Overlapping Wannier Orbital (MOMO) approach detailed in section 2.4.2. In this case, calculations were performed at the B3LYP/6-311G(d,p) level, based on atomic coordinates from room temperature

single crystal x-ray structures. Results for **5-4** are summarized in Table 5.4, and may be compared with the results using the MLWO approach below. Hopping integrals for interaction (3) are not printed because they were found to be small in all cases. The orbital energies agree essentially with those obtained by calculations on single molecules, with $\epsilon_2 - \epsilon_1 \sim 0.3$ eV, although the energetic separation between the SOMO and LUMO is found to be increased to > 2 eV, in comparison with ~ 1.5 eV found in the previous section. For all radicals pairs, hopping integrals between SOMOs were found to be small, on the order of $t_{ij}^{00} \sim 25 - 40$ meV, so that all pairs satisfy the orthogonal overlap requirement for ferromagnetic interactions. In contrast, the hopping integrals between the SOMO and LUMOs on adjacent sites were found to be much larger for interstack interactions (1) and (2), up to $t_{ij}^{10}(2) \sim 350$ meV. Inspection of the obtained MOMOs (Fig. 5.3) reveals an anomalous mixing of the $\alpha = +1, +2$ orbitals in the case of type (1) and (2) interactions, as a result of the small energetic splitting of these orbitals in comparison with the large inter orbital $t_{ij}^{01}(1), t_{ij}^{02}(1), t_{ij}^{10}(2), t_{ij}^{20}(2)$ hopping integrals. As discussed in section 2.4.2, this overlocalization should not be considered a significant source of error for perturbative calculations of pairwise magnetic interactions.

The exceptionally large inter orbital hopping elements for interactions of type (2) stem from the unique packing of radicals, which results in the strong overlap of σ -LUMOs and π -SOMOs on adjacent radicals through orbital density at the E_2 position on both sites. Experimentally, it is also this position that strongly determines the nature of magnetic coupling between such radicals. Recall, for $E_2 = \text{Se}$, ferromagnetic interstack interactions are expected, while for $E_2 = \text{S}$, the anticipated magnetic structure is consistent with antiferromagnetic $\mathcal{J}_{ij}^{(1)}, \mathcal{J}_{ij}^{(2)}$. In order to compare the magnitude of such hopping integrals, and given the observed over localization of the LUMOs, it is useful to discuss values that are independent of orbital rotations. Therefore, we compute the root mean square hopping:

$$t_{rms} = \frac{1}{2} \sqrt{(t_{ij}^{01})^2 + (t_{ij}^{02})^2 + (t_{ij}^{10})^2 + (t_{ij}^{20})^2} \quad (5.18)$$

As can be seen from the values in Table 5.5, the calculated SOMO-SOMO hopping t_{ij}^{00} is not strongly affected by the identities of the chalcogen atoms E_1 and E_2 . In contrast, the magnitude of SOMO-LUMO hopping (characterized by t_{rms}) depends strongly on the chalcogen atom in the E_2 position, particularly for the interstack hopping terms (1) and

Table 5.4: Computed one-electron Hamiltonian parameters for **5-4** using the MOMO method. Calculations were performed at the B3LYP/6-311G(d,p) level. The orbital energies ϵ_i^α represent those of the isolated molecules.

				$t_{ij}^{\alpha\beta}(1)$ (meV)				
				β				
				0	1	2		
				0	1	2		
ϵ_i^α (eV)	$\equiv 0$	+2.39	+2.68	α	0	+13.1	-25.3	+82.1
					1	-6.0	-0.8	+6.0
					2	-9.0	-1.3	+9.1
				$t_{ij}^{\alpha\beta}(2)$ (meV)				
				β				
				0	1	2		
				0	1	2		
$t_{ij}^{\alpha\beta}(\pi)$ (meV)				α	0	+28.8	0	+56.8
					1	0	+23.2	0
					2	-61.6	0	+25.0
				α	0	+1.6	-8.5	+12.7
					1	+112.1	+8.6	-29.0
					2	-351.9	-8.2	+29.3

(2). The magnetic exchange depends on these values approximately as (see section 2.1.4):

$$\mathcal{H} = \sum_{\langle i,j \rangle} \mathcal{J}_{ij} \mathbf{S}_i \cdot \mathbf{S}_j \quad (5.19)$$

$$\mathcal{J}_{ij} \approx \frac{4(t_{ij}^{00})^2}{U} - \frac{8t_{rms}^2 K_i^{01}}{[U + \frac{\epsilon_i^1 + \epsilon_i^2}{2}]^2 - (K_i^{01})^2} \quad (5.20)$$

so that those materials with large t_{rms}/t_{ij}^{00} will display ferromagnetic interstack interactions, while antiferromagnetic coupling will be observed for small t_{rms} . For nearest neighbours (1) and (2), t_{rms} is found to be nearly twice as large for the heavier $E_2 = \text{Se}$ than for $E_2 = \text{S}$ suggesting ferromagnetic interactions four times larger, and a possible explanation for the dichotomy in the magnetic response. However, the SOMO-SOMO hopping is sufficiently small in all of **5-1–5-4** that direct estimation of $\mathcal{J}_{ij}(1), \mathcal{J}_{ij}(2)$ via eq'n (5.20) suggests both interactions should be dominated by multi-orbital exchange and be ferromagnetic for all materials. This computational finding is clearly at odds with the experimental magnetic structures. It may suggest a systematic error in the computational method, or be related to

Table 5.5: Hopping integrals computed by the MOMO method for **5-1–5-4**.

Molecule	E ₁	E ₂	$t_{ij}^{00}(\pi)$	$t_{rms}(\pi)$	$t_{ij}^{00}(1)$	$t_{rms}(1)$	$t_{ij}^{00}(2)$	$t_{rms}(2)$
5-1	S	S	+33.6	29.5	+10.8	22.3	+2.2	135.1
5-2	S	Se	+27.7	57.8	-15.2	84.8	~ 0	269.9
5-3	Se	S	+38.7	34.1	-6.1	25.2	+4.0	104.4
5-4	Se	Se	+28.8	40.2	-13.1	43.3	+1.6	184.8

the fact that all calculated values were based on room temperature structures, and should be expected to shift on cooling.

Taken together, these observations suggest multi-orbital exchange may play a role in the ferromagnetic interactions observed in the tetragonal $P\bar{4}2_1m$ radical phase. However, these interactions are partially mitigated by the relatively large energy gap between the π -SOMO and empty σ -LUMOs. For this same reason, we expect the SOMO band to be essentially electronically isolated despite the fact that its specific dispersion may be affected by small SOMO-LUMO mixing. To emphasize this point, we show in Fig. 5.4 the band structure of **5-4** computed using PW-SCF,¹⁷⁷ and employing ultra-soft PBE pseudo-potentials, with a plane-wave cutoff of 25 Ry and integration mesh of 250 Ry. Self-consistent field (SCF) calculations were performed on a $4 \times 4 \times 4$ Monkhorst-Pack k -point mesh. At no point in the Brillouin zone does the SOMO and LUMO bands intersect, so that the low-energy transport physics should be completely describable within the context of the single SOMO band. At the DFT level of theory, **5-4** is predicted to be a metal, with the Fermi level crossing the half-filled, and isolated SOMO band. However, the bandwidth of $W < 0.3$ eV is far too small to overcome the estimated on-site Coulomb repulsion $U \sim 0.8$ eV at ambient pressure. In the next section, we will consider the evolution of the electronic structure under pressure including correlation effects. The obtained band structure was further analyzed using wannier90.x¹⁷⁶ to construct maximally localized Wannier orbitals, which may be compared with those computed with the MOMO method. These MLWO hopping integrals are shown in Table 5.6, and show excellent qualitative agreement with the corresponding MOMO parameters, although the latter are slightly larger in magnitude

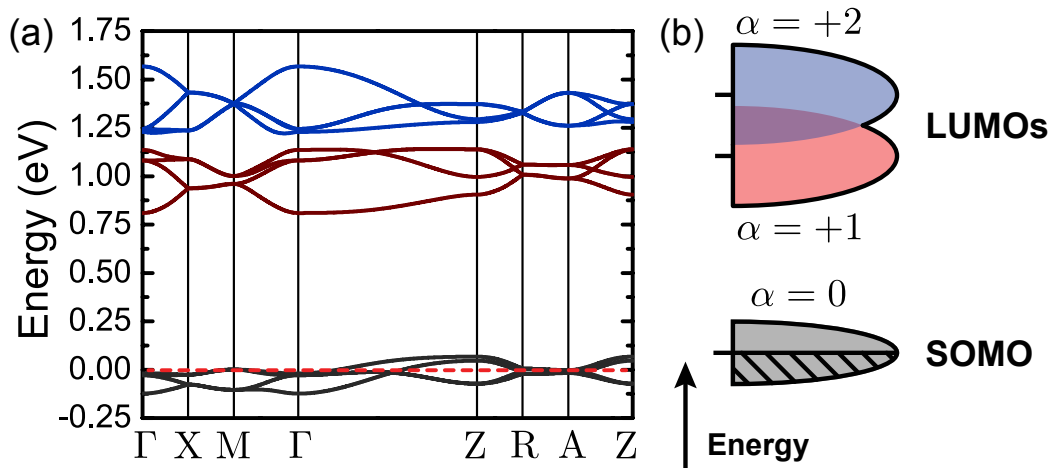


Figure 5.4: (a) Band structure of **5-4** computed with PW-SCF as described in the text. The large energetic spacing between the SOMO and LUMO bands in the solid state suggests that while SOMO-LUMO hopping may alter the dispersion of the bands, the energy levels never overlap. (b) Cartoon of the electronic structure in the absence of correlation.

on average.

5.2.3 Summary / Conclusions

Within the tetragonal $P\bar{4}2_1m$ structural phase, those radicals with Se in the E_2 position tend to order as ferromagnets, while those with S in this position tend to order antiferromagnetically, and display a canted moment. Symmetry analysis suggested that these two magnetic phases must result from a difference in the sign of the magnetic interactions between π -stacks. This dichotomy was argued to arise from an enhancement hopping between the π -SOMO and empty σ -LUMOs on adjacent radicals in the solid state through incorporation of Se into the critical E_2 position. As this hopping sets the magnitude of multi-orbital ferromagnetic exchange, the bulk ferromagnets **5-2** and **5-4** are expected to have more ferromagnetic interstack interactions than the antiferromagnetic **5-1** and **5-3** materials. However, we suggested that the mixing of the SOMO and LUMOs should not significantly alter the charge transport properties, which can be considered within the context of a single band.

Table 5.6: Computed one-electron Hamiltonian parameters for **5-4** using the MLWO method followed by manual site-diagonalization. Calculations were performed as described in the text.

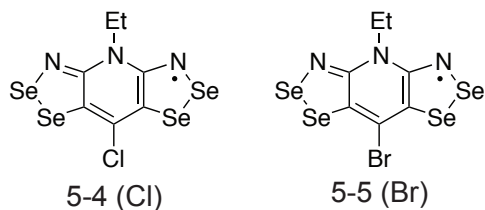
				β			
				$t_{ij}^{\alpha\beta}(1)$ (meV)	0	1	2
				0	+12.3	+41.6	+41.6
				1	-4.0	-0.8	~ 0
				2	-1.6	-2.5	-2.4
				β			
				$t_{ij}^{\alpha\beta}(2)$ (meV)	0	1	2
				0	+5.8	-9.6	+11.8
				1	-141.1	-26.0	-25.6
				2	-143.0	-22.4	-21.5

				α			
				0	1	2	
				$\equiv 0$	+0.94	+1.23	

				β			
				0	1	2	
				+16.4	0	+3.0	
				0	~ 0	0	
				-66.04	0	~ 0	

5.3 Response to Physical Pressure

The previous sections have focussed on the variation of magnetic response with chemical modifications and the corresponding solid state structural changes. In contrast to this *chemical* pressure approach, one can also study the response of these materials to *physical* pressure. The following sections will consider the pressure evolution of the magnetic and electronic properties of **5-4** and the related isostructural material, denoted **5-5**, in which the basal Cl is substituted for a Br.



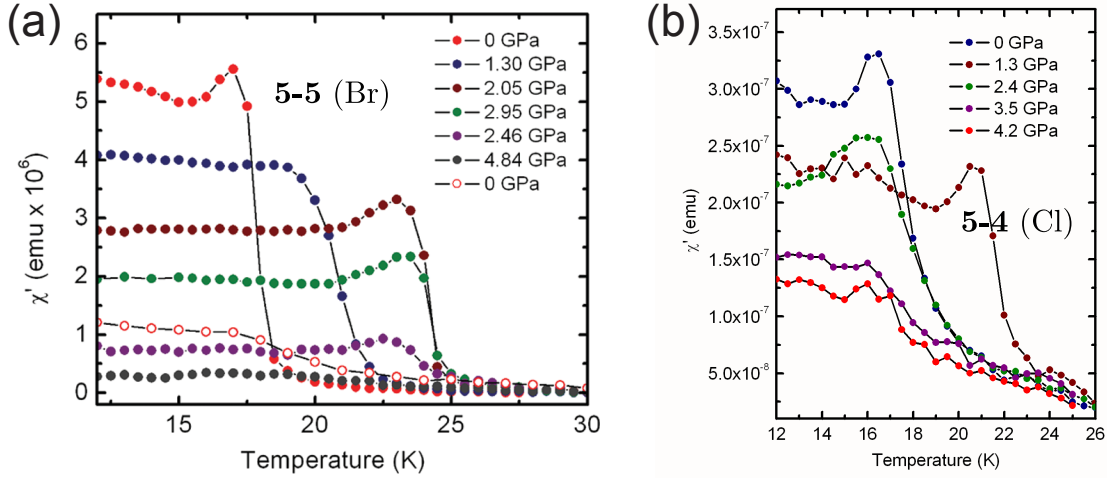


Figure 5.5: AC-susceptibility χ' as a function of pressure for (a) **5-5** and (b) **5-4**. Above Above 4.8 and 3.0 GPa, respectively, the sharp peak in χ' is smeared out, and strongly suppressed, indicating a possible magnetic phase transition to an antiferromagnetic or disordered state.

5.3.1 Magnetic Response

In Ref. 91, we reported the evolution of the crystal structure and magnetic properties of **5-4** (Cl) under pressure. Magnetic susceptibility χ' (1 Hz) measurements were performed on several (microcrystalline) powder samples. Upon initial compression, such measurements showed an enhancement of T_C from 16 K at ambient pressure to 21 K at 1 GPa (Fig. 5.5). However, above this pressure T_C began to retreat with increasing pressure, falling to 16 K at 2.4 GPa (Fig. 5.6). At these higher pressures, the characteristic jump in χ' at T_C was also observed to become increasingly smeared out, with the magnitude of χ' significantly suppressed, so that no clear ordering transition was observed above 2.4 GPa. As discussed in the next section, the electrical transport is still activated in this pressure region, suggesting a Mott insulating state survives at least until 7 GPa. Therefore, the apparent absence of ferromagnetic order above 2.4 GPa signifies either an experimental complication, or a genuine magnetic phase transition to an antiferromagnetic or magnetically disordered state. In support of the latter explanation is the fact that nonhydrostaticity of the pressure may generate a distribution of ordering temperatures within the sample, smearing out

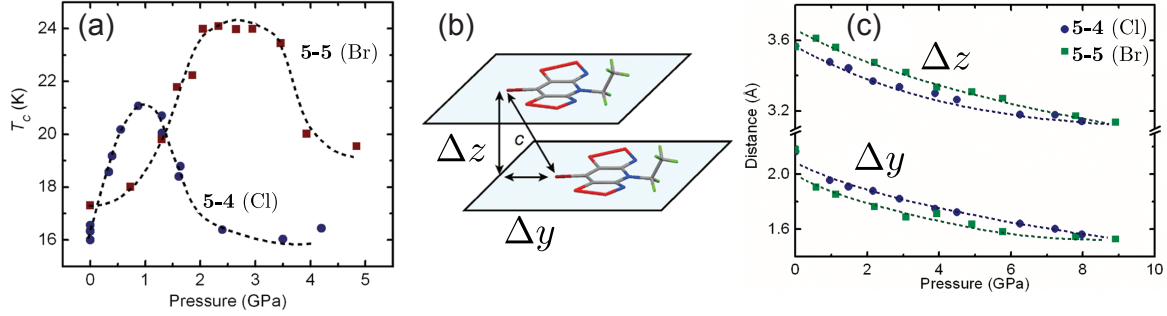


Figure 5.6: (a) Pressure dependence of ferromagnetic ordering temperature for **5-4** and **5-5**. (b) Definition of slippage coordinate Δy and plate-to-plate separation Δz . (c) Pressure dependence of slippage coordinates.

otherwise sharp phase transitions. Support for a magnetic phase transition in the vicinity of 3 GPa can be taken from the theoretical pressure dependence of the magnetic exchange parameters, discussed below.

At ambient pressure, a π -stack slippage of $[\Delta x, \Delta y] = [0.0 \text{ \AA}, 2.14 \text{ \AA}]$ place **5-4** (Cl) on the edge of a narrow region of ferromagnetic $\mathcal{J}_{ij}^{(\pi)}$ predicted to occur around $\Delta y \approx 1.75 \text{ \AA}$. This ferromagnetic “ridge” was described previously in section 4.2.3, and corresponds to vanishing dispersion along the π -stacks $t_{ij}^{00}(\pi) \sim 0$ that separates regions of positive $t_{ij}^{00}(\pi) > 0$ at greater Δy from those of negative $t_{ij}^{00}(\pi) < 0$ at smaller slippage. Consistent with this placement of ambient pressure structure of **5-4** (Cl) is the fact that the computed SOMO-SOMO hopping integrals along the π -stacks are found to be small and positive (Sec. 5.2.2). The action of physical pressure, in addition to overall compression of the unit cell, is to reduce the slippage Δy , thus decreasing $t_{ij}^{00}(\pi)$. Upon compression, $t_{ij}^{00,(\pi)}$ initially approaches zero, and then becomes increasingly negative (Fig. 5.7(c)). This effect is most dramatically seen in the pressure dependence of $\mathcal{J}_{ij}^{(\pi)}$, which BS-DFT calculations suggested should exhibit a maximum (at 3 GPa), due to initial suppression of the antiferromagnetic kinetic exchange. These calculations were based on room temperature powder x-ray structural parameters and were performed at the B3LYP/6-311G(d,p) level; the results of these calculations are shown in Fig. 5.7(a) with reference to the Hamiltonian $\mathcal{H} = -2\mathcal{J}_{ij}\mathbf{S}_i \cdot \mathbf{S}_j$. In ref. 91 we argued that this specific pressure dependence of $\mathcal{J}_{ij}^{(\pi)}$ is primarily responsible for the maximum in T_C around 1 GPa. Further compression beyond

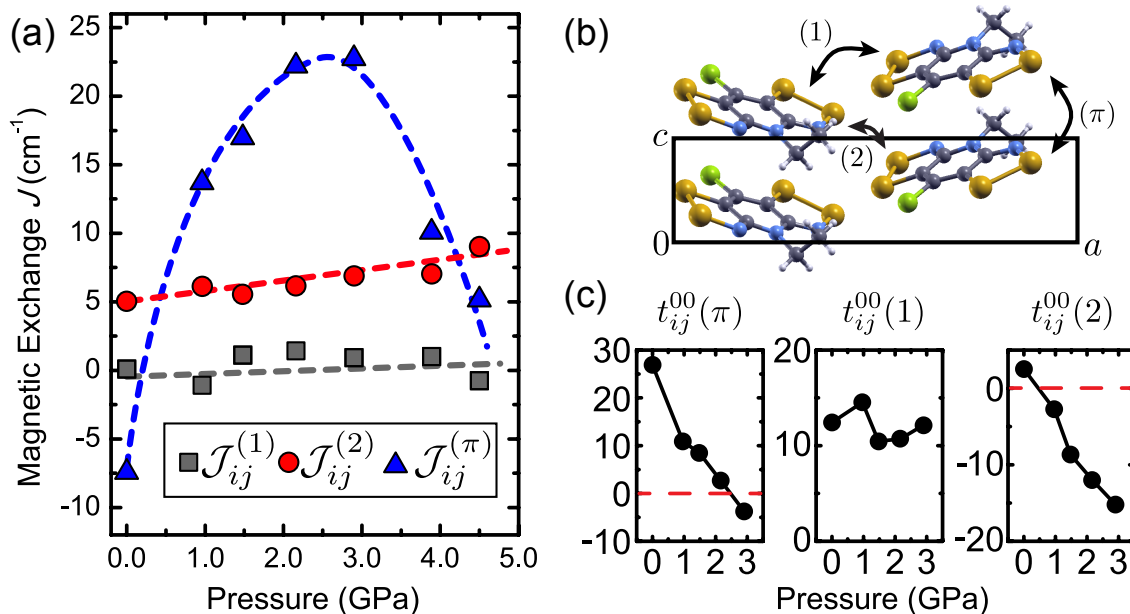


Figure 5.7: (a) Theoretical pressure dependence of magnetic exchange constants for **5-4** (Cl) with reference to the Hamiltonian $\mathcal{H} = -2\mathcal{J}_{ij}\mathbf{S}_i \cdot \mathbf{S}_j$. Values were computed using the BS-DFT method, at the B3LYP/6-311G(d,p) level. (b) Definition of nearest neighbour interactions (π), (1), (2). (c) Pressure dependence of SOMO-SOMO hopping integrals computed using the MOMO method at the same level of theory.

1 GPa is predicted to eventually result in antiferromagnetic $\mathcal{J}_{ij}^{(\pi)}$, as $t_{ij}^{00,(\pi)}$ becomes increasingly negative with reduced slippage. In contrast, the computed pressure dependence of the interstack interactions $\mathcal{J}_{ij}^{(1)}$, $\mathcal{J}_{ij}^{(2)}$ was found to be much milder within BS-DFT, with both interactions remaining ferromagnetic at all pressures. In the latter case, the increasing magnitude of $t_{ij}^{00}(2)$ is offset by similar enhancements of inter orbital hopping, so that multi-orbital ferromagnetic contributions to the exchange dominate at all pressures.

Taken together, the anticipated pressure dependence of the magnetic interactions suggests the possibility of a magnetic phase transition in **5-4** (Cl) at high pressure, brought on by an increasingly antiferromagnetic $\mathcal{J}_{ij}^{(\pi)}$. However, as measurements on **5-4** and **5-5** were performed on powder samples, disorder is expected to be particularly important due to the fact that the pressure gradient is unlikely to be uniform within the sample. The combination of structural disorder and the vicinity of a magnetic phase transition may lead

to a glassy magnetic phase, which may be responsible for the weakening of the magnetic response at high pressures. Measurements of the frequency dependent AC-susceptibility should shed light on this high pressure magnetic phase, and represent a possible avenue of future investigation. At this point, we tentatively classify the low temperature magnetic phase of **5-4** (Cl) appearing between 3.0–7.0 GPa as an antiferromagnetic spin glass.

Since the report of the magnetic response of **5-4** (Cl) to pressure, similar properties were also observed in the isostructural **5-5** (Br).⁸⁹ In this case, the larger Br atom results in slightly larger slippage of $\Delta y = 2.17 \text{ \AA}$ at ambient pressure, and a more sluggish pressure response. In this case, the ambient pressure T_C of 17 K was observed to increase up to 24 K near 3.0 GPa, and a strong suppression of χ' was observed above 4.8 GPa. It is worth noting that this pressure dependence of χ' was also observed to be irreversible, so that only a small fraction of the magnitude returned upon pressure release. This implies the possibility of some sample degradation under pressure and/or a slow response of the lattice to changes in pressure. Both of these are consistent with our suggestion that structural disorder is an important factor to consider when interpreting these results.

5.3.2 Transport Properties and Metallization

With increasing pressure, the enhancement of $t_{ij}^{00}(\pi)$ may be anticipated to eventually become sufficient to induce a metallic state. Indeed, in Ref. 89 we reported transport data on **5-4** (Cl) and **5-5** (Br), which showed a region of metallic response above a critical pressure of $P_c = 7 \text{ GPa}$ and 9 GPa , respectively, as defined by a resistivity that increases with increasing temperature ($d\rho/dT > 0$) above $T = 200 \text{ K}$ (Fig. 5.8). In the same pressure ranges, the resistivity appears to saturate at low temperatures, rather than diverge as would be expected of an insulating state for which all charge carriers eventually become gapped out at low temperature. On this basis, we classified this high pressure state in both materials as a metallic phase, the first observed in neutral radical materials. However, we emphasized the fact that the resistivity of **5-4**, **5-5** in this state above P_c greatly exceeds the Mott-Ioffe-Regal (MIR) limit,^{191–193} of $\rho_{\text{MIR}} \sim 10^{-3} \text{ \Omega cm}$ (see section 3.1). By definition, the high pressure state of **5-4**, **5-5** therefore appears to be a bad metal in the vicinity of room temperature, as $d\rho/dT > 0$. However, at this time, and without single

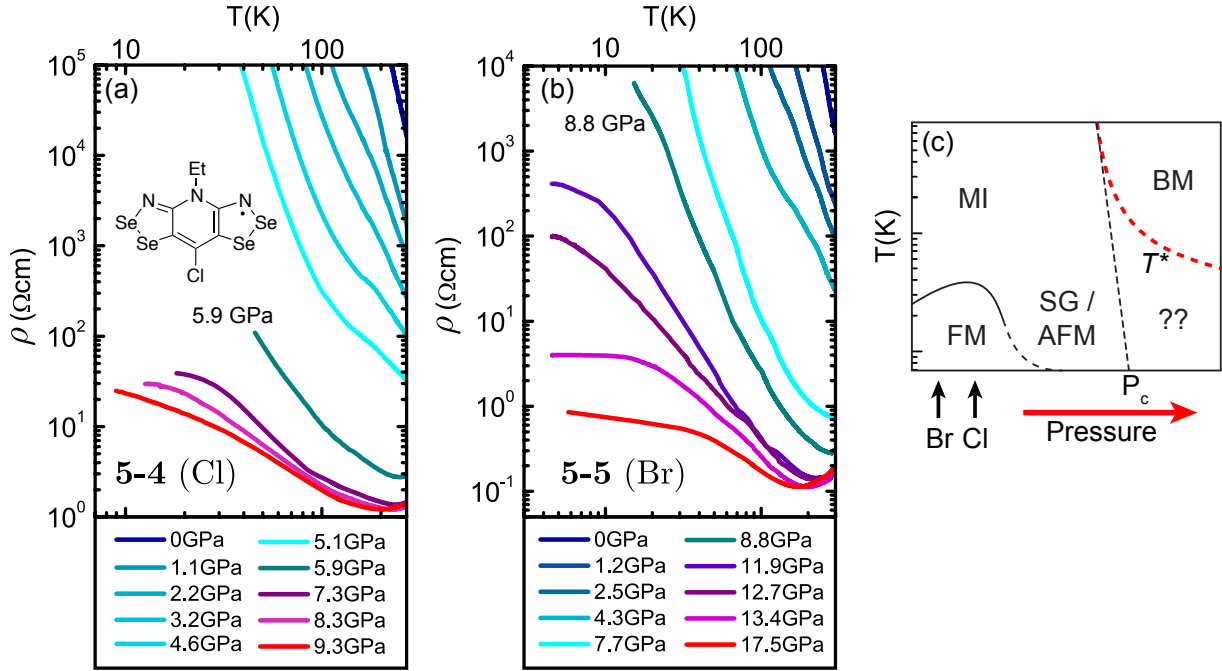


Figure 5.8: (a) Resistivity data measured on pressed pellet samples of **5-4**. Above $P_c \sim 6$ GPa, the resistance becomes a weak function of pressure, and shows a metallic temperature dependence ($d\rho/dT > 0$) above $T = 200$ K. At lower temperatures, the resistivity increases, but saturates, which may be related to disorder or grain boundary scattering. (b) Resistivity data measured on pressed pellet samples of **5-5** showing similar response to **5-4**, but with $P_c \sim 9$ GPa. (c) Putative phase diagram. MI = Mott Insulator, BM = Bad Metal, FM = Ordered Ferromagnet, SG = Spin Glass, AFM = Ordered Antiferromagnet; “??” indicates an unknown phase discussed in the text.

crystal transport measurements, it is very difficult to gain further insight into this observation. What can be said is that the putative metallic state is consistent with theoretical predictions for this material, which we detail in the following section.

5.3.3 Evolution of Electronic Structure

In this section, we focus on the lowest partially filled band in the solid state, which despite being formed from a mixture of molecular SOMO and LUMO density, remains electronically isolated from the other bands at all pressures. We also focus on **5-4**, and take the

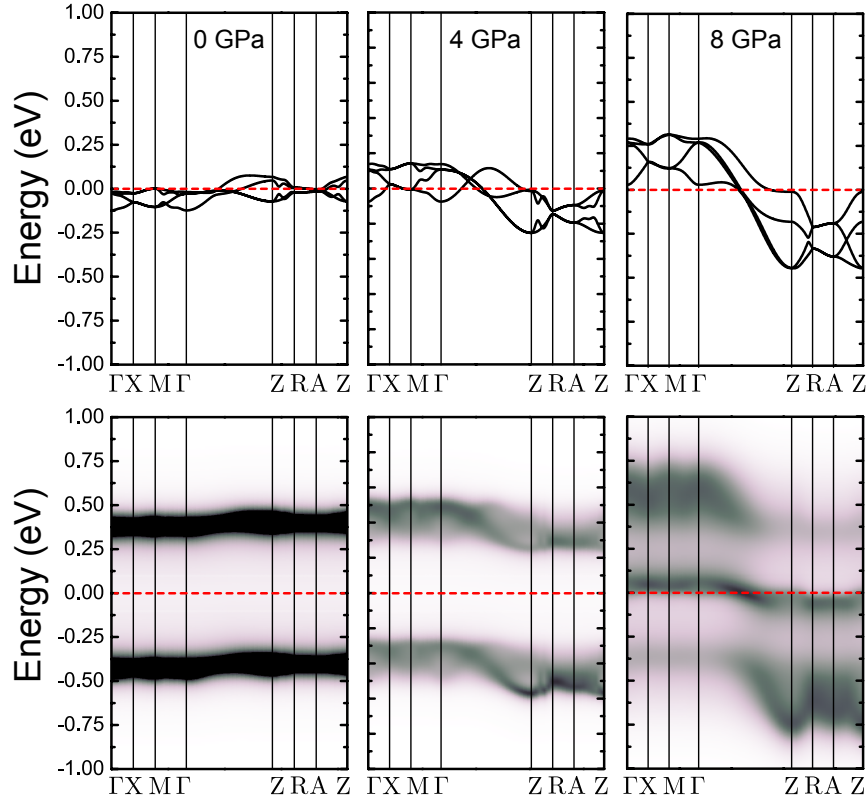


Figure 5.9: Evolution of momentum-resolved spectral density $A(\mathbf{k}, \omega)$ for **5-4** with pressure. (*top*) MLWO-interpolated band structures reveal increasingly 1D character. (*bottom*) Band structures supplemented with IPT DMFT self energy at $T = 300$ K. At 0 GPa and 4 GPa, distinct upper and lower Hubbard bands are observed, but at 8 GPa, dispersion along the π -stacks is sufficient to merge the spectral features providing a narrow band near the Fermi level, and suggesting formation of a putative metallic state

results to be generic for **5-5** as well. Band structures for **5-4** as a function of pressure were computed using PW-SCF using the same methods as detailed in section 5.2.2 employing reported x-ray structures at 0.0, 3.9, and 8.0 GPa.^{89,91} The hopping parameters for the SOMO band alone were extracted by analysis with wannier90.x. The MLWO interpolated band structures are shown in Fig. 5.9 (*top*). Not surprisingly, the SOMO-SOMO hopping integral along the π -stacks $t_{ij}^{00}(\pi)$ is found to have the strongest pressure dependence, decreasing from +16.4 meV at ambient pressure to -51 meV at 3.9 GPa and -120 meV at 8.0 GPa as the molecules are shifted away from orthogonal overlap. This effect can be clearly

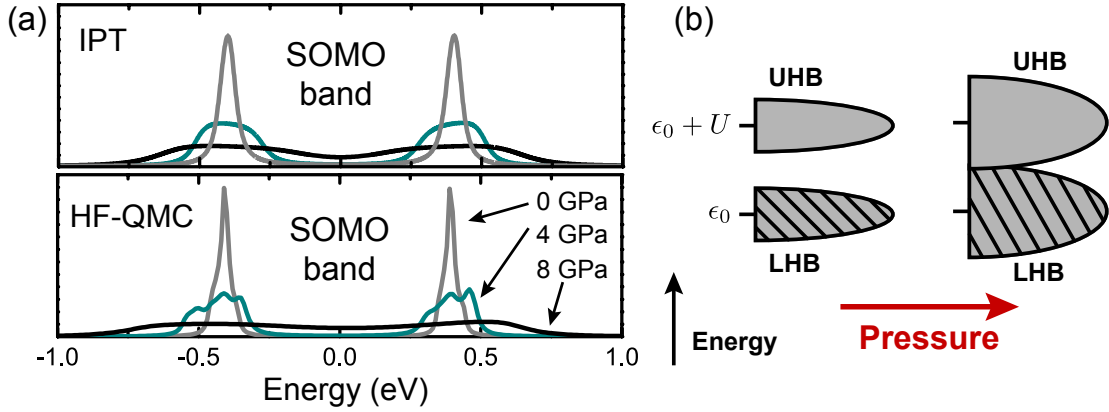


Figure 5.10: (a) Comparison of the momentum-integrated spectral function at $k_B T = 0.1$ eV with correlation (i.e. density of states) obtained from IPT (*top*), and integration of $A(\alpha, \mathbf{k}, \omega)$ obtained from the DFT band structure and analytic continuation of the HF-QMC DMFT self-energy using Padé approximants. The close correspondence validates both methods. (b) Cartoon of the electronic structure showing merging of the upper and lower Hubbard bands with pressure.

seen in the direction and magnitude of the dispersion between the Γ and Z points. In the previous section, we discussed how this enhancement could initially lead to a magnetic phase transition, provided $W < U$ so that the electrons were still sufficiently localized at low temperatures to behave as magnetic spins.

In contrast, at 8 GPa, we find a total SOMO bandwidth of $W = 0.75$ eV, on the same order as the anticipated on-site Coulomb repulsion $U \sim 0.8$ eV, suggesting the possibility of metallization. In order to investigate this possibility, we employed the computed band structures as a starting point for effective one-orbital Iterated Perturbation Theory (IPT)^{214,215} and Hirsch-Fye QMC DMFT^{17,209–213} calculations including an on-site Coulomb repulsion of $U = 0.8$ eV. For the former method, real frequency data is immediately obtained from the calculation, and a variety of temperatures may be studied. For the HF-QMC calculations, we are restricted to a temperature of $k_B T = 0.1$ eV ($T = 1160$ K). In this case, the imaginary frequency DMFT self-energy $\Sigma_{DMFT}(i\omega_n)$ was analytically continued using Padé Approximants. The close correspondence between the density of states $\sum_{\alpha} \int d\mathbf{k} A(\alpha, \mathbf{k}, \omega)$ of both methods at $k_B T = 0.1$ eV (Fig. 5.10(a)) provides validity for the results. On this basis, we have employed the IPT self-energy to compute the

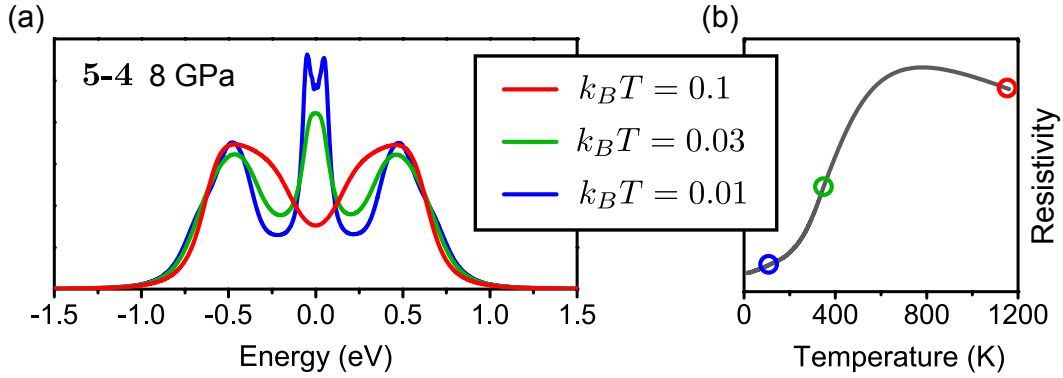


Figure 5.11: (a) Evolution of spectral density $A(\omega)$ predicted from IPT-DMFT calculations with decreasing temperature for **5-4** showing the development of a coherent quasiparticle peak below $\sim 500\text{K}$. (b) Predicted resistivity as a function of temperature, with specific temperatures highlighted. The disagreement between theory and experiment can be attributed to additional scattering mechanisms.

momentum-resolved spectral function at $T = 300$ K according to:

$$A(\alpha, \mathbf{k}, \omega) = \frac{-\text{Im} [\Sigma_{DMFT}(\omega)]}{(\omega + \mu - \epsilon_{\alpha, \mathbf{k}} - \text{Re} [\Sigma_{DMFT}(\omega)])^2 + \text{Im} [\Sigma_{DMFT}(\omega)]^2} \quad (5.21)$$

The results of these calculations are shown in Fig. 5.9 (*bottom*) for $T = 300$ K. The temperature dependence of the density of states at 8 GPa is shown in Fig. 5.11.

At low pressure, the existence of distinct upper and lower Hubbard bands is clearly seen in $A(\mathbf{k}, \omega)$, but at 8.0 GPa, the bandwidth is sufficient to merge these spectral features and generate a finite density of states at the Fermi level. At high temperatures (Fig. 5.10), both the IPT and HF-QMC DMFT calculations suggest a bad metallic state, evidenced by the absence of a quasiparticle peak in $A(\omega)$, appearing in this pressure region, which is roughly consistent with the high temperature metallic phase observed experimentally. The bandwidth of **5-4** at 8.0 GPa should thus be considered theoretically sufficient to produce a metallic state. However, as the temperature is lowered, results from IPT calculations suggest the formation of coherent quasiparticles (Fig. 5.11), which should theoretically be associated with a significant drop in ρ to a value below ρ_{MIR} . Experimentally, while the absence of a diverging resistivity as $T \rightarrow 0$ is characteristic of some gapless charge carriers, the insulating temperature dependence of the resistivity rules against a large density of

coherent quasiparticles expected in DMFT. This observation prompts the consideration of scattering effects that go beyond the paramagnetic single-site DMFT picture. The first possible reason for the suppression of coherent quasiparticles at low temperature is that the antiferromagnetic / spin-glass phase extends to high pressures. In this Slater insulator scenario, such a spin symmetry breaking opens residual energy gap on the order of $T_N \sim \mathcal{J}$ already at the single particle level, resulting in an insulating behaviour.²⁶⁶ The appearance of magnetic order significantly shifts the critical value U_c/W of the Mott transition to lower values, so bandwidth enhancement in **5-4** and **5-5** may not be sufficient to access a Fermi liquid state. This effect could be probed with further studies of the low temperature magnetic phase of these materials. An additional important observation is that, with increasing pressure, the bandwidth enhancement occurs mainly along the π -stacks, resulting in a very one-dimensional (1D) electronic structure. For this reason, the results of a mean field method such as DMFT should be considered with caution.

Indeed, one-dimensional conductors are highly susceptible to a variety of charge and spin density instabilities that ultimately destroy the coherent charge carriers at low temperatures that are not properly captured by DMFT. In the present case, we can rule out the possibility of a commensurate charge density wave (Pierls distortion of the lattice) from powder x-ray analysis which does not reveal any reflections associated with a superlattice at high pressure and low temperature. However, even if insulating charge and spin density states are avoided, the presence of Coulomb interactions ensures that charge transport in strictly one dimension proceeds mainly via the collective sliding motion of bosonic charge density waves, rather than free electron-like excitations.²⁴⁴ In this Luttinger liquid state, the temperature and frequency dependence of the conductivity is not expected to be that of a conventional metal, complicating interpretation.^{243,267} Scattering from impurities or grain boundaries also becomes pronounced in 1D for the intuitive reason that charges confined to travel in straight lines cannot avoid any “bumps” along the way. For this reason, in all but the cleanest 1D conductors, one expects disorder driven (Anderson) localization to set in at low temperatures. This effect ensures a transition to insulating ($d\sigma/dT > 0$) behaviour below some temperature scale set by the energy barrier for tunnelling of charges through the disorder.²⁶⁸ As measurements were performed on pressed pellet samples, inhomogeneous pressure, and grain boundaries would contribute to the disorder scattering.

Inspection of the measured resistance for **5-4** reveals a change in the slope of the resistivity at $T \sim 100$ K, which we attribute to the effects of magnetic and/or disorder scattering on nearly coherent charge carriers. In the Anderson insulator scenario, as temperature is increased, the conductivity is expected to become metallic-like ($d\sigma/dT < 0$) due to sufficient thermal activation across the disorder barriers. In the magnetic symmetry breaking scenario, suppression of the order parameter at high temperatures also results in the appearance of a metallic state. However, given the possibility for a complex interplay between correlation, low-dimensionality, and disorder, it is difficult to make any strong conclusions. Studies on high quality single crystals of both materials, where disorder may be mostly mitigated, represents an important goal of future work.

5.3.4 Summary / Conclusions

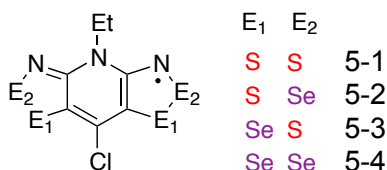
Upon initial pressurization, the ferromagnetic ordering temperature of **5-4** (**5-5**) is enhanced due largely to a suppression of the hopping integrals $t_{ij}^{00,(\pi)}$ along the π -stacks, which reduces the magnitude of antiferromagnetic exchange. Further compression reverses the sign and enhances these integrals, initially suppressing T_C above 1.6 GPa, and then leading to a putative frustrated region in the vicinity of 3.5 GPa (5.0 GPa), which is anticipated to display glassy spin dynamics due to the presence of disorder. At still higher pressures, above 7.0 GPa (9.0 GPa), the radicals display metallic conductivity above 200 K, which does not diverge at low temperatures, and is largely pressure independent. Such a metallic state is anticipated by electronic structure calculations combining DFT and DMFT methods. However, this putative metallic state does not behave as a conventional metal, having a resistivity far above the Mott-Ioffe-Regal limit, and non-metallic transport below a temperature T^* . We have suggested that the explanation of these observations may be related to the combination of disorder, magnetic and grain boundary scattering in a material with an essentially 1D electronic structure, which makes it particularly susceptible to localization of charge carriers. Further studies should be performed on single-crystal samples in order to discern the relative roles of each of these factors.

Chapter 6

Spin-Orbit Effects in Heavy Atom Radicals

6.1 Introduction

In this section, we address the observation of significant magnetic anisotropy in the ordered phases of **5-2**–**5-4**, which we attribute to spin-orbit anisotropic exchange interactions occasioned by incorporation of the heavy Se atoms. For the sake of clarity, we label these radicals according to the scheme in the previous chapter:



In the ferromagnets **5-2** and **5-4**, this manifests most evidently as a large coercive field H_c of 250 Oe and 1370 Oe (at 2 K), respectively.⁸⁶ The antiferromagnet **5-3** displays a small canted moment, with a spontaneous magnetization of $2 \times 10^{-4} \mu_B$, and $H_c = 66$ Oe. To put these values in perspective, recall that prior to their report in 2008, the magnetic properties of the light organic ferromagnets such as nitroxyls,^{35,37,269} thiazyls,^{132,133,270}

and doped fullerenes²⁷¹ had already been the subject of extensive research for over 30 years.^{2,41,272,273} However, none of these materials (neutral or charged) displayed coercive fields (H_c) more than a few tens of oersteds.²⁷⁴ For this reason, the initial report of orders of magnitude larger H_c in **5-2** and **5-4** was met with considerable scepticism. In contrast to $S > 1/2$ metal-based systems, where magnetic anisotropy may be a property of individual ions, Kramers' theorem forbids zero-field anisotropy for single $S = 1/2$ radicals. Instead, the magnetic anisotropy, and therefore coercivity, must result from interactions between radicals. We argue in this chapter that a significantly enhanced magnitude of spin-orbit coupling in the Se-based radicals **5-2–5-4** explains their contrasting magnetic response with previous generations of light-atom materials.

The content below is based, in part, on studies reported in Refs 262 and 263, where we employed single crystal ferromagnetic resonance (FMR) measurements to probe the magnetic anisotropy. Much of the theoretical background for this section was outlined in section 2.2. The main experimental findings, reproduced below, are that conventional dipole-dipole interactions, which represent an alternate source of magnetic anisotropy, are not consistent with all observations, while SOC provides a natural explanation for all the data. These studies are then extended in this chapter in two ways: i) the development of an ab-initio scheme capable of estimating anisotropic exchange terms in organics, and applying this method to understanding the evolution of SOC under pressure in **5-4**, and ii) studying of the antiferromagnet **5-3**, whose resonance properties are consistent not only with the calculated magnetic interactions, but also the anticipated magnetic structure.

6.2 FMR Studies of Tetragonal Ferromagnets

6.2.1 Experimental

In order to probe the magnetic anisotropy of **5-2** and **5-4** we have measured electron spin resonance (ESR) spectra at low temperature, a technique that is sensitive to the bulk magnetic excitations (spin-waves) of the ferromagnetically ordered phase.^{275,276} This technique has been employed in the study of various organic materials including charge-transfer

salts,^{277,278} doped fullerenes,²⁷⁹ and radicals.^{280,281} In a typical single crystal experiment, microwave radiation is applied to a sample at a set frequency, and the energies of magnetic excitations are tuned using an external field \mathbf{H}_{ext} that can be varied in magnitude and direction with respect to the crystal. Whenever the energy of such excitations matches the frequency of applied radiation, resonant absorption is observed. In a semiclassical approach, this resonant frequency is given by the precession frequency of total ordered magnetization \mathbf{M} , which may be determined by solving the Landau-Lifshitz equation of motion:

$$\frac{\partial \mathbf{M}}{\partial t} = \gamma \mathbf{M} \times \nabla_{\mathbf{M}} F \quad (6.1)$$

where $\gamma = g\mu_B/\hbar$ is the gyromagnetic ratio, and F is the free energy density. For tetragonal materials, the latter quantity may be expanded as:²⁸²

$$F = -\mathbf{M} \cdot \mathbf{H}_{ext} - K_2 \cos^2 \theta_M - K_{4\perp} \cos^4 \theta_M - K_{4\parallel} (3 + 4 \cos 4\phi_M) \sin^4 \theta_M - \dots \quad (6.2)$$

where \mathbf{H}_{ext} is the external field, $\{K\}$ are phenomenological anisotropy constants, and θ_M and ϕ_M are the polar and azimuthal angles defining the direction of \mathbf{M} with respect to the crystallographic c -axis. It holds, for the vast majority of microscopic sources of magnetic anisotropy, that the higher order anisotropy constants will diminish in magnitude, so that $|K_2| > |K_{4\perp}| \sim |K_{4\parallel}|$. For this reason, the anisotropy in **5-2** and **5-4** is expected to have primarily uniaxial character; a $K_2 > 0$ denotes easy c -axis anisotropy, while $K_2 < 0$ represents easy ab -plane anisotropy. An alternate view, which allows more transparent relation of the microscopic spin Hamiltonian and the resonant properties, is to consider the excitations of the ordered state as quantized bosonic spin-waves. Since the dimensions of the crystal are much smaller than the wavelength of the applied radiation, only $k = 0$ spin waves are usually excited, which for ferromagnets correspond to uniform precession of \mathbf{M} as above. Consider, for example, a hypothetical 1D ferromagnetic chain described by the Hamiltonian:

$$\mathcal{H} = \sum_{\langle i,j \rangle} \mathcal{J} \mathbf{S}_i \cdot \mathbf{S}_j - \Gamma S_i^z S_j^z - \sum_i g\mu_B \mathbf{H}_{ext} \cdot \mathbf{S}_i \quad (6.3)$$

where the coordinates $\{x, y, z\}$ refer to the crystallographic axes. It is useful to choose, as our quantization axis, the direction of \mathbf{M} , which we label z' . This direction will depend, generally, on both the nature of the anisotropy, and the external field. These new

coordinates are related to the crystallographic ones via:

$$x' = x \cos \theta_M - z \sin \theta_M \quad (6.4)$$

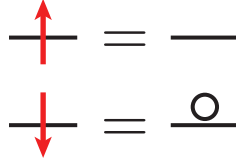
$$y' = y \quad (6.5)$$

$$z' = x \sin \theta_M + z \cos \theta_M \quad (6.6)$$

In terms of such coordinates, we may write the spin-operators in the (Holstein-Primakoff) representation:

$$S_i^{+'} = \left(\sqrt{1 - a_i^\dagger a_i} \right) a_i \quad , \quad S_i^{-'} = a_i^\dagger \left(\sqrt{1 - a_i^\dagger a_i} \right) \quad , \quad S_i^{z'} = \frac{1}{2} - a_i^\dagger a_i \quad (6.7)$$

where a_i^\dagger creates a bosonic magnon at site i . This mapping associates those sites with spin oriented along the positive z' -axis as being empty, while those with spins along the negative z' -axis have exactly one boson, that is $a_i^\dagger a_i = n_i = 1$.



In the ferromagnetic ground state below T_C , we expect only small deviations of the magnetization \mathbf{M} away from the equilibrium orientation along z' , which corresponds to the dilute limit $\langle a_i^\dagger a_i \rangle \ll 1$. It is convenient to work with Fourier transformed operators:

$$a_i = \frac{1}{\sqrt{N}} \sum_k a_k e^{ikr_i} \quad , \quad a_i^\dagger = \frac{1}{\sqrt{N}} \sum_k a_k^\dagger e^{-ikr_i} \quad (6.8)$$

After some manipulations, and retaining only terms quadratic in magnon operators, the Hamiltonian may be written for the $k = 0$ uniform spin precession:

$$\mathcal{H}|_{k=0} = \left\{ \frac{g\mu_B}{|\mathbf{M}|} \mathbf{H}_{ext} \cdot \mathbf{M} + \frac{\Gamma}{2} (3 \cos^2 \theta_M - 1) \right\} a_0^\dagger a_0 - \frac{\Gamma}{2} (a_0^\dagger a_0^\dagger + a_0 a_0) \sin^2 \theta_M \quad (6.9)$$

This equation may be brought into regular form $\mathcal{H}|_{k=0} = \Delta_0 b_0^\dagger b_0$ by a Bogoliubov transformation of the magnon operators:

$$a_0^\dagger = u b_0^\dagger + v b_0 \quad , \quad a_0 = u b_0 + v b_0^\dagger \quad , \quad u^2 - v^2 = 1 \quad (6.10)$$

which for suitable choice of u, v we finally obtain:

$$\hbar\omega_{res} = \Delta_0 = g\mu_B \sqrt{\left\{ H_{ext} \cos(\theta_M - \theta_H) + \frac{H_A}{2}(3 \cos^2 \theta_M - 1) \right\}^2 - \left\{ \frac{H_A}{2} \sin^2 \theta_M \right\}^2} \quad (6.11)$$

which gives the quantized excitation energy of spin-waves, and thus the FMR resonance frequency ω_{res} . Here, we have introduced the anisotropy field:

$$H_A|_{T \rightarrow 0} \equiv \frac{\Gamma}{g\mu_B} \equiv \frac{2K_2}{|\mathbf{M}_{sat}|} \quad (6.12)$$

as well as θ_H , the polar angle between \mathbf{H}_{ext} and the crystallographic c -axis, and the saturation magnetization density $|\mathbf{M}_{sat}|$. It is worth noting that the isotropic exchange constant \mathcal{J} does not contribute to the energy of the $k = 0$ mode, and therefore does not enter into the FMR resonance frequency. Rather, ω_{res} is sensitive only to the (typically) smaller anisotropic interactions, which allows the latter to be studied with great accuracy. Although the coercive field H_c is also related to these anisotropic interactions, experimentally H_c is typically found to vary between 10% and 40% of the more intrinsic quantity H_A .²⁸³ The discrepancy is related to the fact that measured H_c values depend on the dynamics of magnetization reversal, which are affected by e.g. sample morphology and disorder.

In order to probe **5-2** and **5-4** we therefore used single crystal ferromagnetic resonance (FMR) absorption to provide an independent measure of the solid-state magnetic anisotropy. Measurements were performed in collaboration with Professor Hill's group at the National High Magnetic Field Laboratory (NHMFL) in Tallahassee, Florida. Single crystals (dimensions $0.1 \times 0.1 \times 0.2$ mm³) were prepared by known methods.⁸⁶ Orientation- and temperature-dependent studies were performed at multiple frequencies (50–120 GHz) using a superheterodyne-cavity-based spectrometer developed around a Quantum Design PPMS configured with a 7 T split-pair magnet.^{284,285} Measurements below 50 GHz were performed in a homodyne transmission instrument and a commercial X-band (9.7 GHz) spectrometer. Data at 240 GHz were collected using a quasi-optical spectrometer.²⁸⁶ In both materials, the variation of ω_{res} with the orientation of \mathbf{H}_{ext} is consistent with uniaxial easy c -axis anisotropy, $H_A > 0$, and small $K_{4\perp}, K_{4\parallel}$. For this case, when $\mathbf{H}_{ext} \parallel c$, then $\theta_H = \theta_M = 0$ at all values of H_{ext} , and eq'n (6.11) reduces to:

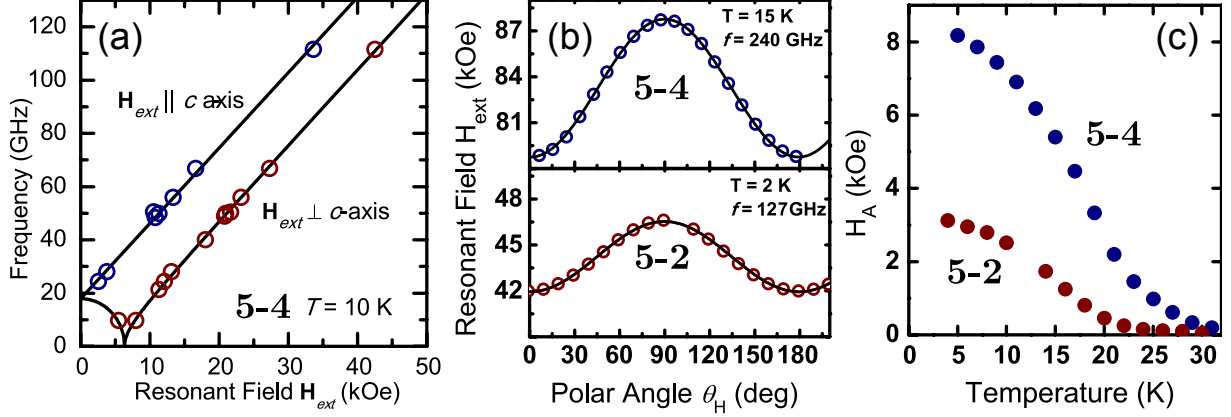


Figure 6.1: (a) Dependence of resonance frequency $f_{res} = \omega_{res}/2\pi$ on magnitude of external field H_{ext} for **5-4** (circles) at $T = 10$ K with fits of eq'n (6.13) and (6.14) shown in black lines. (b) Angular dependence of the resonant field at fixed high frequency of $f = 73, 240$ GHz for **5-2** and **5-4**, respectively. The $\cos^2 \theta_H$ dependence confirms uniaxial anisotropy. (c) Temperature dependence of H_A for **5-2** and **5-4**. The fact that the former is approximately a third of the latter is well explained by spin-orbit effects.

$$\omega_{res} = \gamma(H_{ext} + H_A) \quad (\mathbf{H}_{ext} \parallel c) \quad (6.13)$$

Conversely, when $\mathbf{H}_{ext} \perp c$ ($\theta_H = \pi/2$), the reorientation of \mathbf{M} with increasing field results in a resonant frequency given by:

$$\omega_{res} = \begin{cases} \gamma\sqrt{H_A^2 - H_{ext}^2} & H_{ext} \leq H_A \\ \gamma\sqrt{H_{ext}(H_{ext} - H_A)} & H_{ext} \geq H_A \end{cases} \quad (\mathbf{H}_{ext} \perp c) \quad (6.14)$$

As shown in Fig 6.1(a) for **5-4**, the observed multi-high-frequency resonance positions correspond precisely to these expected relations. Furthermore, at high frequency, such that H_{ext} and $\omega/\gamma \gg H_A$, then $\theta_H = \theta_M$ for all orientations, the approximate angular dependence of the resonance field at fixed frequency can be written:

$$H_{ext}(res) \approx \frac{\omega}{\gamma} - \frac{H_A}{2}(3 \cos^2 \theta_H - 1) \quad (6.15)$$

This relation holds assuming purely uniaxial anisotropy ($K_{4\perp}, K_{4\parallel} = 0$). Such higher-order free energy terms, which are associated with the anisotropy in the ab -plane, introduce higher order $\cos^4 \theta_H$ and $\sin^4 \theta_H$ terms in this high-field limit. Therefore, the finding that

$H_{ext}(res)$ at high frequency for **5-2** and **5-4** conforms to a $\cos^2 \theta_H$ dependence suggests negligible $K_{4\perp}, K_{4\parallel} = 0$ within experimental limits (Fig. 6.1(b)). Taken together, the ferromagnetic resonance response of both materials identify them as uniaxial ferromagnets with an easy c -axis. The temperature dependence of H_A was obtained for **5-2** and **5-4** from fits of eq'n (6.13) to several different frequencies (Fig. 6.1(c)). The results show the onset of anisotropy at temperatures about 10 K above the respective ordering temperatures of the two ferromagnets. As the temperature is decreased, H_A continues to rise, having values of 8.2 kOe (at 5 K) for **5-4** and 3.1 kOe (at 4 K) for **5-2** at the lowest measured temperatures. Not surprisingly, this observed anisotropy field is several orders of magnitude larger than that observed for light atom organic ferromagnets such as TDAE·C₆₀ ($H_A = 0.058$ kOe at 5 K)²⁷⁹ and β - p -NPNN ($H_A = 0.12$ kOe at 0.4 K).²⁸⁰ This trend mirrors the large discrepancy between observed coercive fields.

6.2.2 Sources of Magnetic Anisotropy

In homogeneous magnetic materials, H_A may be viewed in terms of contributions arising from (i) microscopic spin dipole-dipole interactions (H_A^{dip}), (ii) macroscopic demagnetizing fields (H_A^{dem}) (for nonspherical crystals), and (iii) spin-orbit effects (H_A^{SO}):

$$H_A = H_A^{dip} + H_A^{dem} + H_A^{SO} \quad (6.16)$$

Of these, the first two terms arise from the conventional spin dipole-dipole interaction:

$$\mathcal{H}_{dip} = -\frac{g\mu_0\mu_B}{4\pi|\mathbf{r}_{ij}|^3} \left\{ \frac{3}{|\mathbf{r}_{ij}|^2} (\mathbf{S}_i \cdot \mathbf{r}_{ij})(\mathbf{S}_j \cdot \mathbf{r}_{ij}) - \mathbf{S}_i \cdot \mathbf{S}_j \right\} \quad (6.17)$$

where \mathbf{r}_{ij} is the translation vector relating spins i, j . At the microscopic level, this interaction favours alignment of spins along directions of maximum linear spin density, which in the case of **5-2** and **5-4** corresponds to the c -axis. Although the magnitude of this effect can be estimated numerically by using Ewald summation techniques, it should by inspection be on the same order of magnitude as the total anisotropy field H_A measured for spherical samples of β - p -NPNN, for which the demagnetizing and spin-orbit effects are negligible. On this basis, it is reasonable to conclude that H_A^{dip} is ~ 0.1 kOe for **5-2** and

5-4, which represents a very small relative contribution. The second dipolar effect, the shape-dependent demagnetizing field H_A^{dem} , which is often substantial in transition-metal materials, is also small as a result of the low density of spins in **5-2** and **5-4** (and any organic magnet). Indeed, approximating the needlelike crystals as cylinders of infinite length suggests that $H_A^{dem} = \mu_0 |\mathbf{M}_{sat}|/2$, which affords a contribution of only ~ 0.1 kOe. Finally, since **5-2** and **5-4** are isostructural, and have similar crystal morphology, the effects of dipole-dipole interactions should be essentially identical in both materials, and as such cannot explain the observation that H_A for **5-4** is three times greater than that of **5-2**. Therefore, the details of the magnetic anisotropy cannot be explained by dipole contributions H_A^{dip} , H_A^{dem} , which is contrary to what is found for light-element organic magnets.^{287,288} This leaves spin-orbit effects H_A^{SO} as the only plausible cause for the large anisotropy observed.

In order to understand the effects of SOC in **5-2** and **5-4**, recall that for $S = \frac{1}{2}$ radicals, SOC introduces anisotropic exchange interactions between local spin-orbit coupled pseudospin moments (Sec 2.2):

$$\mathcal{H}_{\text{eff}} = \sum_{\langle i,j \rangle} \mathcal{J}_{ij} \tilde{\mathbf{S}}_i \cdot \tilde{\mathbf{S}}_j + \mathbf{D}_{ij} \cdot \tilde{\mathbf{S}}_i \times \tilde{\mathbf{S}}_j + \tilde{\mathbf{S}}_i \cdot \mathbf{\Gamma}_{ij} \cdot \tilde{\mathbf{S}}_j \quad (6.18)$$

Assuming negligible anisotropic contributions from multi-orbital exchange:

$$\mathcal{J}_{ij} = -2\tilde{K}_{ij} + \frac{4}{U} \{ (t_{ij}^{00})^2 - |\mathbf{C}_{ij}^{00} \cdot \mathbf{C}_{ji}^{00}| \} \quad (6.19)$$

$$\mathbf{D}_{ij} = \frac{4i}{U} \{ t_{ij}^{00} \mathbf{C}_{ji}^{00} - \mathbf{C}_{ij}^{00} t_{ji}^{00} \} \quad (6.20)$$

$$\mathbf{\Gamma}_{ij} = \frac{4}{U} \{ \mathbf{C}_{ij}^{00} \otimes \mathbf{C}_{ji}^{00} + \mathbf{C}_{ji}^{00} \otimes \mathbf{C}_{ij}^{00} \} \quad (6.21)$$

where the spin-orbit mediated hopping parameter is:

$$\mathbf{C}_{ij}^{00} = \frac{1}{2} \sum_{\alpha} \left\{ \frac{\tilde{\mathcal{L}}_i^{0\alpha}}{\Delta \epsilon_i^{\alpha}} t_{ij}^{\alpha 0} + t_{ij}^{0\alpha} \frac{\tilde{\mathcal{L}}_j^{\alpha 0}}{\Delta \epsilon_j^{\alpha}} \right\} + \mathcal{O}(\mathcal{L}^2) \quad (6.22)$$

As explained in the previous chapter, the observation of ferromagnetic interactions in **5-2** and **5-4** implies that t_{ij}^{00} is small for all nearest neighbours in the crystal, implying that the Dzyaloshinskii-Moriya interaction, parameterized by \mathbf{D}_{ij} will be very small in these materials. We therefore focus our attention on the pseudo-dipolar interaction, parameterized

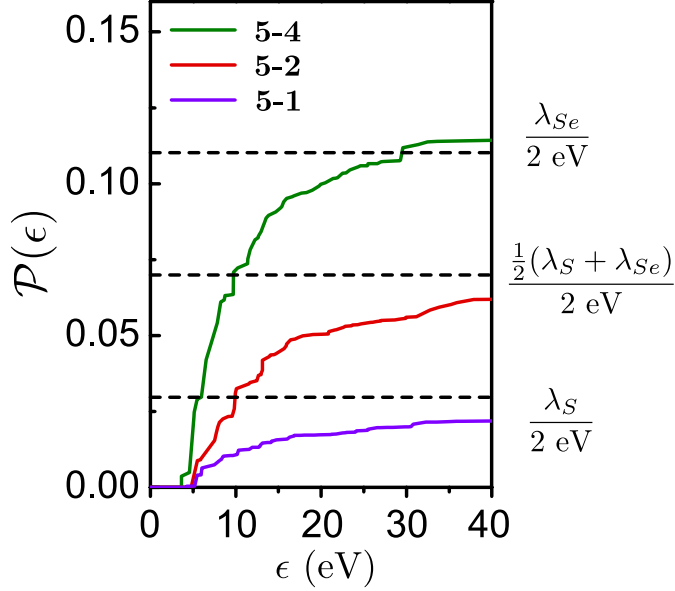


Figure 6.2: Value of weighting function defined in eq'n (6.23) as a function of energy window ϵ . When ϵ becomes large, such that all relevant orbitals are included in the spin-orbit summation, the weighting function approaches a value determined by the average atomic spin-orbit coupling constant of the chalcogen atoms, which are the heaviest atoms in each molecular framework.

by the symmetric tensor $\Gamma_{ij} \propto |\mathbf{C}_{ij}^{00}|^2$. In order to compare the relative magnitude of this interaction in various materials, we introduce the weighting function:

$$\mathcal{P}(\epsilon) = \sum_{\alpha}^{|\Delta\epsilon_i^\alpha| \leq \epsilon} \left| \frac{\vec{\mathcal{L}}_i^{0\alpha}}{\Delta\epsilon_i^\alpha} \right| \quad (6.23)$$

which measures, for a single site, the total weight of orbitals perturbatively mixed with the SOMO that lie within an energy window ϵ . In the limit where ϵ is taken to be large enough to include all relevant orbitals, this dimensionless weighting function generalizes the concept of atomic spin-orbit coupling constants to molecular species, provided a common energy scale for $\Delta\epsilon_i^\alpha$. This weighting function was computed using ORCA at the B3LYP/6-311G(d,p) level based on room temperature crystal geometries for **5-1**, **5-2**, and **5-4**. The magnitudes of the spin-orbit matrix elements $\vec{\mathcal{L}}_i^{0\alpha}$ were computed via the Spin-Orbit Mean Field (SOMF) method, and orbital energies were taken to be the Kohn-Sham orbital

eigenvalues in the absence of SOC. The results, shown in Fig. 6.2, suggest that $\mathcal{P}(\epsilon)$ converges toward a value for each molecule determined essentially by the average atomic spin orbit constant of the chalcogen atoms within the molecular framework. Thus, all other factors assumed equal, the ratio of spin-orbit mediated hopping between **5-2** and **5-4** should follow:

$$\frac{|\mathbf{C}_{ij}^{00}| \text{ (5-2)}}{|\mathbf{C}_{ij}^{00}| \text{ (5-4)}} \sim \frac{\frac{1}{2}(\lambda_S + \lambda_{Se})}{\lambda_{Se}} \sim 0.6 \quad (6.24)$$

and consequently,

$$\frac{H_A \text{ (5-2)}}{H_A \text{ (5-4)}} \sim \frac{|\mathbf{\Gamma}_{ij}| \text{ (5-2)}}{|\mathbf{\Gamma}_{ij}| \text{ (5-4)}} \sim \left\{ \frac{|\mathbf{C}_{ij}^{00}| \text{ (5-2)}}{|\mathbf{C}_{ij}^{00}| \text{ (5-4)}} \right\}^2 \sim 0.3 - 0.4 \quad (6.25)$$

Comparison of H_A for the lowest measured temperatures, 8.2 kOe (at 5 K) for **5-4** and 3.1 kOe (at 4 K) for **5-2**, provides the ratio of anisotropy fields to be in the range of 0.38, which is consistent with the above theoretical predictions. That is, the magnitude of H_A , and therefore the coercive fields H_c in these materials is determined entirely by the relative importance of SOC between the mixed S/Se radical **5-2**, and the heavier all-Se **5-4**.

6.2.3 Analysis of Anisotropic Exchange

Having shown that spin-orbit effects are responsible for the magnetic anisotropy in **5-2** and **5-4**, we now address the microscopic spin Hamiltonian. Inspection of Fig. 6.2 suggests that a large number of molecular orbitals ultimately make significant contributions to the summation in \mathbf{C}_{ij}^{00} , which may be contrasted with the qualitative discussions presented in Sec. 2.2.2. Therefore, in order to facilitate qualitative discussion of such organic systems, it is useful to collect the orbital summation in eq'n (6.22) into a set of orbital-like functions $|\eta_i^\mu\rangle$ defined at each site:

$$|\eta_i^\mu\rangle = \frac{1}{2} \sum_{\alpha \neq 0} |\alpha_i\rangle \frac{\langle \alpha_i | \mathcal{L}_i^\mu | 0_i \rangle}{\epsilon_\alpha - \epsilon_0} \quad (6.26)$$

where $\mu = \{x, y, z\}$. The purely imaginary $|\eta_i^\mu\rangle$ functions are neither normalized nor eigenstates of the Fock operator, and so have no well-defined ϵ , but consideration of their

spatial density and symmetry properties is nonetheless useful. In terms of such functions, the pseudospin creation operator for the SOMO may be written:

$$\tilde{\mathbf{c}}_{i,0}^\dagger = \mathbf{c}_{i,0}^\dagger + \sum_{\mu} \sigma_{\mu} \mathbf{c}_{i,\eta^{\mu}}^\dagger \quad (6.27)$$

and the components of the spin-orbit mediated hopping parameter are simply a sum of hopping integrals:

$$[\mathbf{C}_{ij}]_{\mu} = t_{ij}^{\eta^{\mu}0} + t_{ij}^{0\eta^{\mu}} \quad (6.28)$$

This latter relationship allows us to qualitatively understand the structural dependence of anisotropic exchange terms within the same framework as we discussed the t_{ij}^{00} dependence of the isotropic exchange in section 4.2.3. For this discussion, we define local coordinates for each molecular site i in the $P4_21m$ unit cell: the \hat{x}_i -axis is normal to the crystallographic mirror plane bisecting the molecule, while the \hat{z}_i -axis is oriented along the normal of the molecular plane. The $|\eta_i^{\mu}\rangle$ functions are shown in Fig. 6.3 for **5-4** in terms of such coordinates, as obtained from ORCA using the SOMF method at the B3LYP/6-311G(d,p) level. For this choice of coordinates, the SOMO (Fig. 6.3(a)) is approximately a linear combination of p_z orbitals, so that $|\eta_i^z\rangle \approx 0$, since $\mathcal{L}_i^z|0_i\rangle \sim L^z|p_z\rangle = 0$. The remaining functions $|\eta_i^x\rangle$ and $|\eta_i^y\rangle$ are composed of orbitals within the σ -framework of the molecule, and have density largely confined within the molecular plane, but with significant extension around the periphery of the molecule. Just as we found in the example of section 2.2.2, the action of spin-orbit coupling is to mix the SOMO (of $|p_z\rangle$ character) with orbitals of local $|p_x\rangle$ and $|p_y\rangle$ character.

On the basis of the shapes of the $|\eta_i^{\mu}\rangle$ functions, we may make the following qualitative observations:

- In many radicals, molecules within the same π -stack are related by translation, implying that they share a common set of molecular coordinates, i.e. $\hat{x}_i = \hat{x}_j$, etc. Such molecules are also bisected by a common crystallographic mirror plane in **5-2** and **5-4**, making it useful to discuss the symmetry of the SOMO $|0_i\rangle$ and $|\eta_i^{\mu}\rangle$ functions with respect to the local C_s symmetry. While both $|0_i\rangle$ and $|\eta_i^x\rangle$ are antisymmetric with

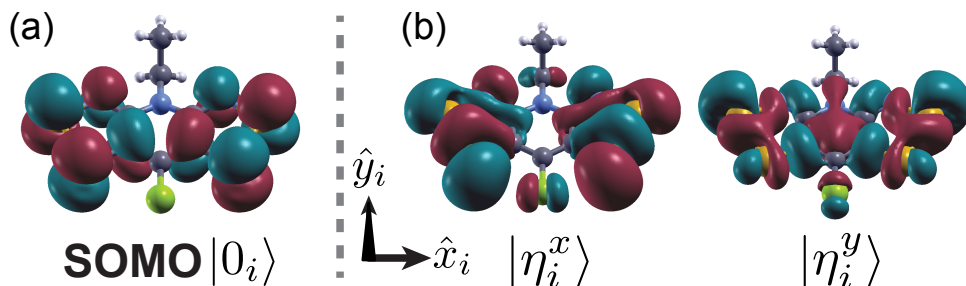


Figure 6.3: (a) Highest occupied orbital (SOMO, $\alpha = 0$) at each radical site i for **5-4** computed that the B3LYP/6-311G(d,p) level. (b) Pseudo-orbital functions defined in eq'n (6.26) to describe SOC hopping parameters \mathbf{C}_{ij} . The shape of $|\eta_i^\mu\rangle$ enhances anisotropic exchange between adjacent π -stacks.

respect to the mirror, and have a representation A'' , the $|\eta_i^y\rangle$ (and $|\eta_i^z\rangle$) functions are symmetric, and transforms as A' . This implies the only non-zero hopping integrals are $t_{ij}^{0\eta^x}$ and $t_{ij}^{\eta^x 0}$, such that $\mathbf{C}_{ij}^{00}(\pi)$ must be oriented in the \hat{x} direction normal to the local mirror plane. This symmetry constraint is already a well known restriction on the orientation of $\mathbf{D}_{ij}(\pi) \propto \mathbf{C}_{ij}^{00}(\pi)$,¹⁵⁰ but emerges naturally in this language.

- The finding that $|\eta_i^z\rangle \approx 0$ holds, in fact, for any planar organic π -system, and suggests that \mathbf{C}_{ij} will tend to be oriented perpendicular to both \hat{z}_i and \hat{z}_j . In **5-2** and **5-4**, this preference ensures that all \mathbf{C}_{ij} lie within, or close to the crystallographic ab -plane. In other materials, it may have more drastic consequences. For example, when the symmetry of sites i, j is such that $\hat{z}_i = \hat{z}_j$, the component of \mathbf{C}_{ij} along this direction will vanish almost exactly. When the two sites are bisected by a common mirror plane, as above, but \hat{z}_i is normal to the mirror, the interactions between the two sites will be entirely isotropic. All components of \mathbf{C}_{ij} will vanish. To see this, note that this orientation ensures the σ -like $|\eta_i^x\rangle$ and $|\eta_i^y\rangle$ functions are precisely orthogonal to the π -SOMO $|0_j\rangle$, so that all hopping integrals $t_{ij}^{\eta^\mu 0}$ and $t_{ij}^{0\eta^\mu}$ are zero. This restriction arises not only due to symmetry constraints, but also the specific π -nature of the SOMO.
- The fact that $|\eta_i^x\rangle$ and $|\eta_i^y\rangle$ are largely confined to the molecular plane, and have a complex arrangements of nodes that differ in placement from the nodes in the SOMO will tend to suppress *interstack* $t_{ij}^{\eta^\mu 0}(\pi)$ and $t_{ij}^{0\eta^\mu}(\pi)$ integrals. At the same time, the

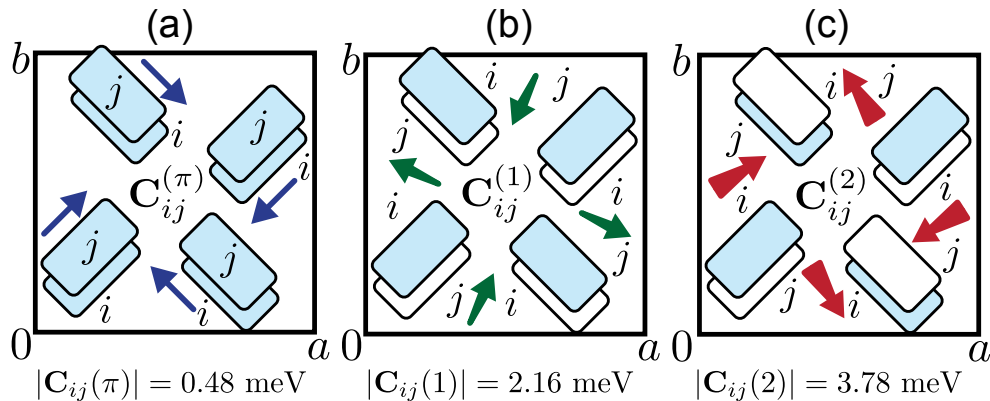


Figure 6.4: (a)-(c): Orientations of the local \mathbf{C}_{ij}^{00} for **5-4**, viewed down the c -axis for interactions (π), (1), and (2), respectively. Molecules are represented by boxes, with shaded boxes indicating interacting molecules (see Fig. 1(a)). For interactions (1) and (2), \mathbf{C}_{ij}^{00} has components in the c -direction, as indicated by tapered arrows.

extension of the pseudo-orbital functions around the molecular periphery enhances interstack $t_{\eta\mu 0}^{ij}$ integrals so that $|\mathbf{C}_{ij}^{00}(1)|, |\mathbf{C}_{ij}^{00}(2)| > |\mathbf{C}_{ij}^{00}(\pi)|$ is expected.

Having these qualitative observations in mind, we estimated \mathbf{C}_{ij}^{00} for **5-4** according to eq'n (6.22) for each nearest neighbour radical pair. An appropriate site-local orbital basis was constructed using the MOMO method in ORCA, which provides the necessary inter orbital hopping integrals. Spin-orbit matrix elements were first computed using the SOMF method on isolated molecules, and then rotated into the final MOMO basis. The results, summarized in Fig. 6.4, conform to the qualitative expectations detailed above. The weakest interactions occur between adjacent radicals in the same π -stack, with $\mathbf{C}_{ij}^{00}(\pi) = i(0.34, 0.34, 0.00)$ meV for the stack closest to the origin of the unit cell. The remaining interstack interactions are greater in magnitude, with $\mathbf{C}_{ij}^{00}(1) = i(1.26, 1.76, 0.67)$ meV and $\mathbf{C}_{ij}^{00}(2) = i(1.91, -2.92, -1.45)$ meV, for the pair of stacks closest to the x -axis of the unit cell. On the basis of these calculated values, the pseudodipolar component of the anisotropic exchange $\mathbf{S}_i \cdot \mathbf{\Gamma}_{ij} \cdot \mathbf{S}_j$ may be computed using eq'n (6.21), assuming $U \sim E_{cell} = 0.8$ eV in related materials (Sec. 1.3.3). For ferromagnetically coupled spins, such interactions prefer alignment of \mathbf{S}_i and \mathbf{S}_j in the plane normal to \mathbf{C}_{ij}^{00} . The finding that the largest magnitude components of \mathbf{C}_{ij}^{00} fall in the ab -plane for all interactions

therefore identifies the crystallographic c -axis as the easy axis of magnetization. Indeed, the anisotropy field may be computed from the zero-field gap in the spin-wave excitations at $k = 0$, which is given for the tetragonal cell by:

$$\Delta_0 \equiv g\mu_B H_A = \frac{1}{2} \sum_j [\mathbf{\Gamma}_{ij}]_{aa} + [\mathbf{\Gamma}_{ij}]_{bb} - 2[\mathbf{\Gamma}_{ij}]_{cc} \quad (6.29)$$

where $\{a, b, c\}$ refer to the crystallographic axes. Here, we have explicitly assumed a collinear magnetic structure, which should prevail given the argued weakness of the DM-interaction. Via this formula, we compute the anisotropy field of **5-4** to be 9.7 kOe, which compares reasonably well in both sign and magnitude with the measured value of 8.8 kOe ($T = 2$ K). Of the total calculated H_A value, roughly 30% is contributed by (1)-type interactions, and 70% by (2)-type interactions, with essentially negligible anisotropy due to (π)-type interactions.

In the previous section, we discussed that the *relative* magnitude of H_A between **5-2** and **5-4** was within the expected relationship given strong anisotropic exchange interactions. In this section, we find that the *absolute* magnitude of H_A also conforms to the predictions from spin-orbit coupling. In calculating H_A we have taken the simplest approach in ignoring both DM-interactions and contributions from multi-orbital anisotropic exchange, discussed in Sec. 2.2.4. The former interaction, characterized by $|\mathbf{D}_{ij}| \propto t_{ij}^{00} |\mathbf{C}_{ij}^{00}|$, makes a contribution to H_A that scales naively as $\sim (1/g\mu_B) |\mathbf{D}_{ij}|^2 / \mathcal{J}_{ij} \sim 0.1 - 0.5$ kOe, and therefore could be included in a more thorough future study. Given the large energetic separation between the SOMO and LUMOs in **5-2** and **5-4**, the contribution due to multi-orbital effects is expect to be smaller by a factor of $K_i^{01} / \Delta\epsilon \sim 0.1$, and thus may also represent a significant correction to the calculated H_A . Nonetheless, we feel the most important contribution to H_A , namely $\mathbf{\Gamma}_{ij}$ has been well addressed using the above computational scheme. Future refinements of this method must address smaller contributions to the anisotropic exchange, as well as extend the studies to a wider range of materials. In the next section, we use this scheme to address the evolution of the magnetic anisotropy of **5-4** under pressure.

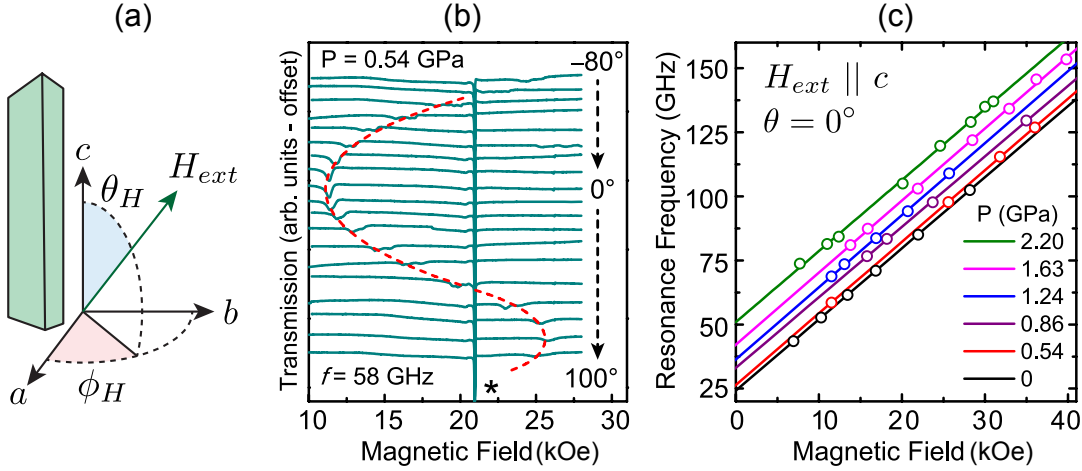


Figure 6.5: (a) Schematic of the **5-4** sample and experimental coordinates. (b) Angle dependent FMR spectra recorded as a function of the polar angle θ_H at $f = 58$ GHz and $T = 2$ K. The angle-dependent dip in transmission (red dash line is a guide to the eye) corresponds to FMR, while the sharp resonance marked by an asterisk (*) corresponds to an impurity signal (see main text). (c) Field dependence of $f_{res} = \omega_{res}/2\pi$ as a function of pressure for $\theta_H = 0^\circ$, i.e. $\mathbf{H}_{ext} \parallel c$.

6.3 FMR Under Pressure

In order to probe experimentally the variation of H_A under pressure for **5-4** and therefore the magnitude of the SOC, we employed recently developed instrumentation at the NHMFL capable of performing high-frequency EPR (or FMR) measurements under quasi-hydrostatic pressure. In this work, high-pressures were obtained by the Hill group using a plastic diamond anvil cell (DAC),²⁸⁹ enabling FMR measurements up to 2.2 GPa. At each pressure, alignment of the sample with respect to the applied field was achieved by performing two-axis crystal rotation studies using a vector magnet by seeking the minimum in the resonant field, which corresponds to $\mathbf{H}_{ext} \parallel c$. The pressure in the DAC was calibrated *in situ* at the measurement temperature by recording the luminescence from a ruby chip via the diamond window and an optical fiber.²⁹⁰ FMR spectra recorded at different polar angles, θ (ϕ undetermined), are shown in Fig. 6.5(b). The FMR signal is seen as a dip in the transmission through the cavity, whose angle-dependence distinguishes it from a strong angle-independent $g = 2$ impurity signal from the diamonds in the DAC. At each pressure,

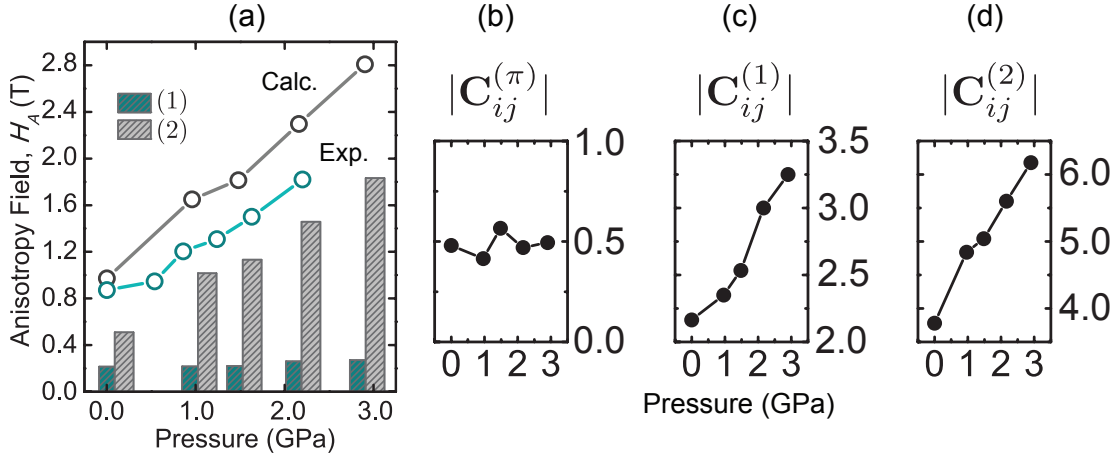


Figure 6.6: (a) Comparison of experimental (for $T = 2$ K) and calculated values of H_A for **5-4** as a function of pressure, with contributions from interactions (1) and (2) indicated by the heights of the bars. The contribution from (π) interactions is negligible on this scale. (b)-(d) Calculated magnitude of C_{ij}^{00} terms as a function of pressure in meV.

the anisotropy field was extracted from linear fits to multifrequency data with $H_{ext} \parallel c$, and was seen to increase monotonically with pressure, as shown in Fig. 6.5(c).

The sensitivity of H_A to structural details is highlighted in its doubling over the pressure range 0–2.2 GPa. In order to probe this result computationally, we performed calculations of C_{ij}^{00} for each interaction as described in the previous section, but employing crystal geometries obtained from powder x-ray diffraction studies under pressure (Fig. 6.6).^{89,91} These same structures served as a starting point for calculations of the isotropic exchange presented in Sec. 5.3.1. The results suggest that while $|C_{ij}^{00}(\pi)|$ remains small at all pressures, the two interstack terms $|C_{ij}^{00}(1)|$ and $|C_{ij}^{00}(2)|$ are significantly enhanced by the compression of the unit cell. The orientation of these (pseudo)vectors remains relatively constant with pressure. Interestingly, the magnitude enhancement is due to the relatively small (2%) compression of a and b from 0 to 3 GPa, which results, for nearest neighbours (2), in an approximately 7% reduction in the E_2-E_2 contact from 3.4 to 3.2 Å.⁹¹ In other words, the structural changes are subtle. Nonetheless, the predicted H_A values derived from the computed C_{ij}^{00} terms track the experiment fairly well, reproducing the monotonic enhancement with pressure. At all pressures, H_A is dominated by contributions from

$\Gamma_{ij}(2)$, which is not surprising given the large values of t_{ij}^{01}, t_{ij}^{02} expected for this nearest neighbour pair. Comparison of the calculated values of t_{ij}^{00} and \mathbf{C}_{ij}^{00} reveals that the pressure dependence of these terms need not be related, which has far reaching consequences for pressure studies of a wide range of spin-orbital coupled materials.

Finally, it is worth noting that, while magnetic measurements on powder samples revealed both a suppression of the T_C and coercive field H_c of **5-4** above 1.6 GPa, that the more intrinsic quantity H_A , measured on single crystal samples, does not show this behaviour. Indeed, the theory and experiment both suggest H_A continues to increase monotonically with pressure even above 1.6 GPa. As H_c may be strongly dependent on sample morphology, this implies the possibility of pressure induced disorder in the powder measurements, which is consistent with our interpretation given in the previous chapter.

6.4 AFMR in Mixed S/Se Antiferromagnet

In this section, we discuss preliminary results on the canted antiferromagnet **5-3**. In this case, spin resonance measurements may also be employed to probe the spin-wave, or antiferromagnetic resonance (AFMR) modes. For this case, the resonance conditions are often more complicated, and depend on the strength of isotropic interactions, as the multiple magnetic sublattices give rise to various precession modes at $k = 0$. In many cases, however, only one such mode appears at low frequency that is able to couple to the microwave field. For example, in the case of an easy *ab*-plane antiferromagnet ($H_A < 0$):²⁷⁶

$$\omega_{res} = \begin{cases} \gamma H_{ext} \sqrt{1 + \frac{|H_A|}{2H_E}} & H_{ext} \perp c \\ \gamma \sqrt{2H_{ext}^2 + 2|H_A|H_E} & H_{ext} \parallel c \end{cases} \quad (6.30)$$

where the exchange field H_E :

$$H_E \equiv \sum_j \frac{\mathcal{J}_{ij}}{4g\mu_B} \quad (6.31)$$

with reference to the Hamiltonian $\mathcal{H} = \mathcal{J}\mathbf{S}_i \cdot \mathbf{S}_j$. This quantity may be estimated by measuring the magnetization versus external field, which saturates for antiferromagnets at

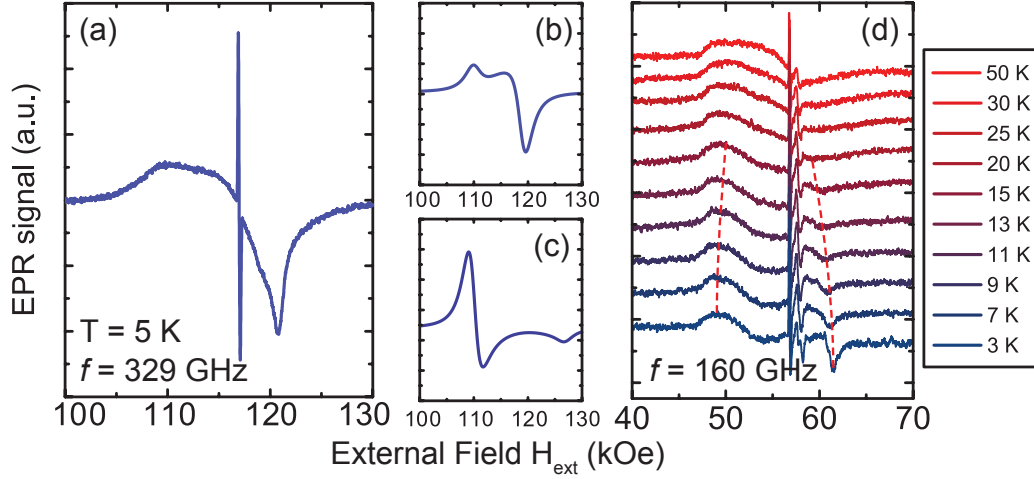


Figure 6.7: (a) Powder AFMR derivative line shape for **5-3** at $T = 5$ K and a frequency of 329 GHz, along with semiclassical simulations for (b) easy-plane anisotropy, and (c) easy-axis anisotropy. The sharp signal in the centre of the resonance is due to $S = 1/2$ impurities. The close correspondence between (a) and (b) identifies **5-3** as an easy-plane antiferromagnet. (d) Temperature dependence of the ESR line shape showing sharpening on AFMR modes below $T_N = 14$ K.

$H_{ext} = 2H_E$. The antiferromagnetic resonance signal intensity is typically much weaker than the FMR signals, and requires large samples and/or high fields to be detected. For this reason, we performed AFMR measurements on powder samples of **5-3**, as sufficiently large single crystals were not attainable. The experimental results are summarized in Fig. 6.7. Modes in the powder spectra corresponding to spin-wave excitations become prominent below $T_N = 14$ K (Fig. 6.7(d)), and may be identified by their narrowing at high fields, as resonances corresponding to the extreme limits at $H_{ext} \perp, \parallel c$ coalesce with one another.

Analysis of both symmetry restrictions and the microscopic anisotropic exchange interactions in **5-3** suggest that it should be an easy *ab*-plane antiferromagnet, with a canted moment also confined to this plane. In order to see this, note that the \mathbf{C}_{ij}^{00} terms in **5-3** are expected to have a similar orientation as found computationally for **5-4** in the previous section. They should similarly be dominated by interstack interactions (1) and (2). When the spins related by such interactions are antiferromagnetically coupled, as suggested for **5-3**, the pseudodipolar interactions $\mathbf{S}_i \cdot \boldsymbol{\Gamma}_{ij} \mathbf{S}_j$ energetically prefer orientation of the sublattice moments *parallel* to the local \mathbf{C}_{ij}^{00} (1) and \mathbf{C}_{ij}^{00} (2). Since these terms have

their largest components in the ab -plane, **5-3** is theoretically predicted to have an easy ab -plane anisotropy. This prediction is entirely consistent with the observed AFMR line shape. While the powder spectra naturally provide less angular information, for tetragonal systems the distribution of spectral density is always dominated by $H_{ext} \perp c$ as this orientation covers the largest solid angle. When this orientation corresponds to an easy direction, the largest and sharpest resonance appears on the high field side, while the converse is true for easy c -axis anisotropy. In order to emphasize this result, we show in Fig. 6.7(b) and (c) semiclassical simulations of the powder AFMR line shape for a simplified model of four magnetic sublattices, with a classical Hamiltonian:

$$\begin{aligned} \mathcal{H} = \mathcal{J} (\mathbf{m}_1 \cdot \mathbf{m}_2 + \mathbf{m}_2 \cdot \mathbf{m}_3 + \mathbf{m}_3 \cdot \mathbf{m}_4 + \mathbf{m}_4 \cdot \mathbf{m}_1) \\ + \Gamma (m_1^x m_2^x + m_2^y m_3^y + m_3^x m_4^x + m_4^y m_1^y) \end{aligned} \quad (6.32)$$

where $\mathcal{J}/g\mu_B = 250$ kOe, and $\Gamma/g\mu_B = \pm 2$ kOe. This model represents a cartoon of the anticipated interactions. For positive Γ , corresponding to easy ab -plane anisotropy (Fig. 6.7(b)), the correspondence between the experimental and simulated line shapes is fair. In contrast, for $\Gamma < 0$ (Fig. 6.7(c)), representing easy c -axis anisotropy, the large spectral density at low field is not consistent with the experimental line shape.

It is interesting to note that while symmetry analysis suggested that the canted moment of **5-3** must lie in the ab -plane, that such canting is not due to the DM-interaction. For example, an ab -plane moment cannot arise due to the DM-interaction between molecules within the same π -stack because the z -component of $\mathbf{D}_{ij}^{(\pi)}$ is restricted by symmetry to be zero. Such a moment also cannot arise as a result of the DM-interaction between pairs (1) or (2), because the z -component of both $\mathbf{D}_{ij}^{(1)}$ and $\mathbf{D}_{ij}^{(2)}$ must have the same sign for all pairs in the unit cell. As such, only spiral structures are promoted, not those with net moments. Canting arises instead due to the much weaker pseudodipolar interaction within the π -stacks $\mathbf{\Gamma}_{ij}^{(\pi)}$, which is associated with local easy-planes for each π -stack that are orthogonal with those of neighbouring stacks. When the sublattice magnetic moments of each stack are confined to the ab -plane, a collinear spin arrangement cannot simultaneously satisfy all (π)-type pseudodipolar interactions. As a result, the moments in neighbouring π -stacks cant with respect to one another not due to interactions between such spins, but rather in an effort to satisfy the local interactions within a given stack. This effect is ultimately

weak, and as a result the canted moment is observed to be small, with a spontaneous magnetization of $2 \times 10^{-4} \mu_B$, despite the expectation of significant anisotropic exchange occasioned by the heavy Se atom. This value may be compared, for example, with the larger value of $5 \times 10^{-3} \mu_B$ reported for the S-based radical *p*-NC-C₆F₄-CNSSN.²⁹¹ In **5-3**, the energy barrier for reversal of the canted moment is also determined essentially by the weak $\Gamma_{ij}^{(\pi)}$ interactions, which explains the observation of a coercive field $H_c = 66$ Oe, which is noticeably smaller than that of **5-2** and **5-4**.

6.5 Discussion of Magnitudes

Research into the understanding and exploitation of spin-orbit coupling has recently attracted much attention due to the discovery of materials with nontrivial band topologies in weakly correlated (band) insulators. In these topological insulating materials, the difference in the nature of band mixing due to SOC at the material surface, and in the bulk, guarantees interesting states living near the edge, with a variety of exotic and desirable properties. In magnetic insulators, anisotropic exchange terms are also implicated in a variety of magnetic phenomena including multiferroicity and topological spin phases. However, the search for materials exhibiting these properties has largely focussed on inorganic solids, drawing particularly from heavy elements with principle quantum number $n \geq 5$ in order to ensure strong spin-orbit coupling. In this light, it is useful to compare the relative strength of spin-orbit effects in the Se-based organics discussed in this chapter. Above, we have introduced a computational scheme for calculating spin-orbit mediated hopping parameters \mathbf{C}_{ij}^{00} , and employed these values to calculate theoretical H_A values. The close agreement between the experimental and theoretical H_A values over the studied pressure range of **5-4** and explanation of the relative H_A in **5-2** validates the magnitude $|\mathbf{C}_{ij}|$ found to be $\sim 1 - 10$ meV for Se-based organics. In comparison, the ordinary hopping parameters for the SOMO band t_{ij}^{00} can be expected to fall in the range $\sim 10 - 100$ meV, suggesting for Se-based organics that $|\mathbf{C}|/t \sim 0.1$ reflects a reasonable estimate. This same ratio of magnitudes has been suggested for low energy theories of topological insulators such as Bi₂Se₃, implying heavy atom organic materials may also fall into the category of strongly spin-orbit coupled materials. This observation follows from

a key feature of organics: due to their molecular nature, all relevant energy scales, such as hopping integrals t , Coulomb repulsion U , and orbital energy splittings $\Delta\epsilon$, may be an order of magnitude smaller than for inorganic materials. Thus SOC can play a significant role in organics despite them being composed of relatively lighter elements (Se, Te vs. Bi). Moreover, SOC must always be considered when it can result in the splitting of otherwise degenerate levels, in which case the only other relevant energy scale is temperature. The materials studied in this section represent an example of the latter case; in **5-2–5-3**, SOC manifests as anisotropic exchange between local moments, opening a gap in the otherwise gapless (anti)ferromagnon spectrum. Such anisotropic exchange terms are also considered important in magnetically ordered sulfur-based organics, such as the spin-canted antiferromagnets (BEDT-TTF)₂Cu[N(CN)₂]Cl,^{292–294} and *p*-NC-C₆F₄-CNSSN.²⁹¹ The possibility of realizing topologically nontrivial phases in organics remains essentially unexplored.²⁹⁵

6.6 Chapter Summary

In this section, we rationalized the magnetic anisotropy observed in the tetragonal Se-based radical magnets **5-2–5-4** in terms of spin-orbit anisotropic exchange. In the two ferromagnets **5-2** and **5-4**, this effect gives rise to a large coercive field arising from pseudo-dipolar interactions. Through ferromagnetic resonance (FMR) measurements, we probed the magnitude and character of the anisotropy, summarized in the magnitude and sign of the anisotropy field H_A . In both cases, uniaxial easy *c*-axis ($H_A > 0$) anisotropy was observed. Both the sign and magnitude of H_A in **5-2** and **5-4** were shown to be consistent with predictions from spin-orbit coupling. In order to do so, we introduced an ab-initio scheme for computing \mathbf{C}_{ij}^{00} in organic materials based on the MOMO method, and allowing spin-orbit coupling to be considered over a large orbital manifold. The computed interactions were also shown to be consistent with preliminary powder AFMR studies of the antiferromagnet **5-3**. Taken together, the large magnitude of such spin-orbit terms identify **5-2–5-4** as strongly spin-orbit coupled materials. The methods and qualitative observations presented in this section will provide a basis for such future exploration of SOC physics in other organics.

Chapter 7

Multi-Orbital Radicals

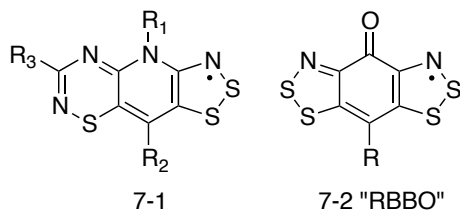
7.1 Introduction

Thus far in this thesis, we have emphasized that the exploration and understanding of strongly correlated electron systems represents a challenging but fruitful subject, which is driven by synthesis of new materials, and the development of new experimental and theoretical avenues of investigation. In this vein, multi-component organic materials such as radical ion salts $(\text{ET})_2\text{X}$ and $(\text{TMTTF})_2\text{X}$,^{296,297} phenylenyl complexes and alkali doped fullerenes^{298,299} X_3C_{60} have played a prominent role, offering unique opportunities for the study of superconductivity,¹¹⁰ Mott criticality,^{200,227,300} and frustrated magnetism.^{301,302} In the introductory chapters it was emphasized that the remarkable properties of many of these materials are related to the presence of local orbital degrees of freedom, which are associated with low Coulomb barriers for charge transport and in some cases ferromagnetic interactions. In comparison, all neutral radicals have displayed Mott insulating behaviour at ambient pressure. In Chapter 5, we discussed a putative 1D metallic state accessed in the Se-based radicals **5-4** and **5-5**, which requires enhancement of solid state bandwidth through both Se-incorporation and the application of high pressures $P \sim 6 - 8$ GPa. The transition to this state was understood in the context of a single electronic band associated with the SOMO at each molecular site. The question addressed in this final chapter is whether a metallic state may be accessed at lower pressures in S-based radicals, thereby

eliminating the need for the synthetically challenging incorporation of Se. To this end, we address radical design strategies for introducing an additional orbital in the vicinity of the Fermi level, and study a new class of such “multi-orbital” radicals. In order to guarantee significant solid-state effects, we consider the following requirements:

- The additional orbital(s) must be sufficiently close in energy ($|\epsilon_\alpha - \epsilon_0| \sim t_{ij}^{\alpha 0}$) to hybridize with the SOMO in the solid state, which requires either a high-lying $\alpha = -1$ HOMO or low-lying $\alpha = +1$ LUMO at the molecular level.
- The additional orbital should be of π -character in order to ensure a wide bandwidth, which will enhance hybridization and dimensionality of interactions.

In the first section of this chapter, we consider the hybrid dithiazolyl/thiadiazinyl radicals **7-1**, which possess the desired π -orbitals for suitable choice of R_3 group. However, we show that these orbitals, both $\alpha = -1, +1$ are not sufficiently close to the SOMO to produce any significant effects on the charge transport. The remainder of the chapter is devoted to the oxobenzene-bridged *bis*-dithiazolyl radicals **7-2** denoted “RBBO”, which possess a very low-lying O-based LUMO, and display remarkable magnetic and transport properties.



7.2 Hybrid Dithiazolyl/Thiadiazinyl Radicals

7.2.1 Synthesis and Structure

As a first approach to the development of multi-orbital radicals, we pursued hybrid dithiazolyl/thiadiazinyl radicals **7-1**, which possess both an $\alpha = +1$ π -LUMO and $\alpha = -1$ π -HOMO for suitable choice of R_3 group, in contrast to previous *bis*-dithiazolyl radicals

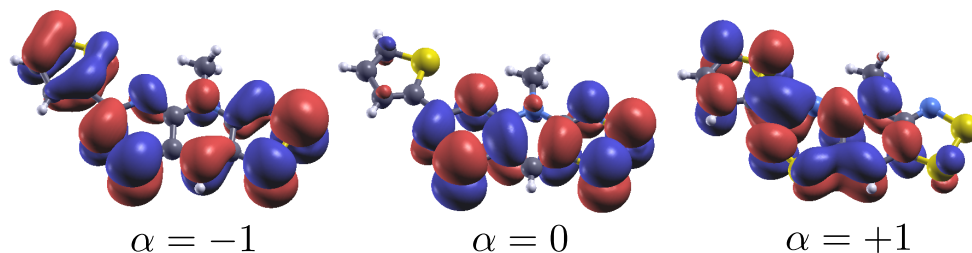
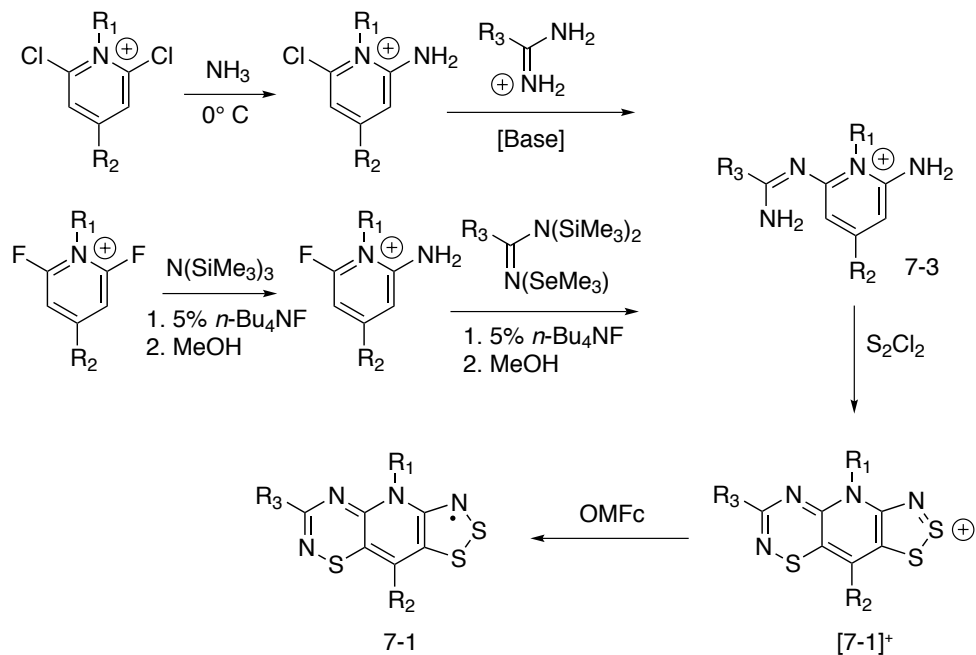


Figure 7.1: Frontier molecular orbitals of hybrid radicals **7-1** ($R_1 = \text{Me}$, $R_2 = \text{H}$, $R_3 = 2\text{-thiophene}$) showing π -character of orbitals in the energetic vicinity of the SOMO.

(e.g. **4-1**) discussed in previous chapters (see Fig. 7.1). As the LUMO is largely localized to the R_3 group, it was believed that its energy relative to the SOMO could be tuned by appropriate chemical modification. As a result, we required a sufficiently generic synthetic route to allow for a variety of R_3 groups to be explored. Such a synthetic route was developed by myself as part of this thesis. In the first series of steps, there are two pathways to generate the intermediate amidine functionalized pyridinium cation **7-3**. The first begins by treatment of an alkylated 2,6-dichloropyridinium salt with gaseous ammonia at low temperature in order to selectively replace one Cl, followed by reaction with a desired amidine under basic conditions. The second route begins with the stoichiometric reaction of an alkylated 2,6-difluoropyridinium salt with nonamethyltrisilazane in the presence of catalytic F^- ion followed by workup in MeOH to remove the remaining *N*-silyl groups.⁹² The amidine functionality can be introduced following a similar reaction with the desired persilylated amidine.^{43,303} The obtained intermediate **7-3** could then be treated with S_2Cl_2 in a variant of the double Herz reaction to produce the desired framework as the cation $[\mathbf{7-1}]^+$, which yields the radical **7-1** after one-electron reduction with octamethylferrocene (OMFc). We have employed this synthetic pathway to provide $[\mathbf{7-1}]^+$ with $R_1 = \text{Me}$, $R_2 = \text{H, F}$, and $R_3 = \text{H, phenyl (Ph), 2-thiophene (2-Th), and 4-pyridine (4-Pyr)}$ in order to investigate the ion energetics as a function of R-groups.



While the prototypal **7-1** radicals with $R_3 = \text{H}$ possess electrochemical cell potentials of $E_{\text{cell}} = 0.83 \text{ V}$, the hybrid radicals with π -substituents such as $R_3 = \text{Ph}$, 2-Th possess lower cell potentials of $E_{\text{cell}} = 0.76 \text{ V}$. This modest reduction in the effective Coulomb repulsion was thought to occur via electronic push-pull effects, which rely on R_3 -based π -orbitals in the vicinity of the Fermi level that are capable of sequestering charge from or furnishing charge to the central radical. In this way, the electron affinity (EA) may be increased in the case of π -accepting substituents, or the ionization potential (IP) reduced for π -donating groups, resulting in a lower $U \sim \Delta H_{\text{disp}} = IP - EA$. Indeed, unlike *bis*-dithiazyl **4-1** radicals, the frontier molecular orbitals of **7-1** are all π -orbitals. However, the range of E_{cell} values observed for **7-1** are the same for **4-1** and *bis*-thiadiazinyl **1-20** radicals, namely 0.76–0.83 V (See Table 1.1), implying this effect is relatively weak. This point is emphasized in the following section where we consider the electronic structure of these radicals.

Inspection of the solid-state structures and magnetic response of the hybrid radicals **7-1** also suggests that intermolecular interactions are relatively weak. For example, **7-1**

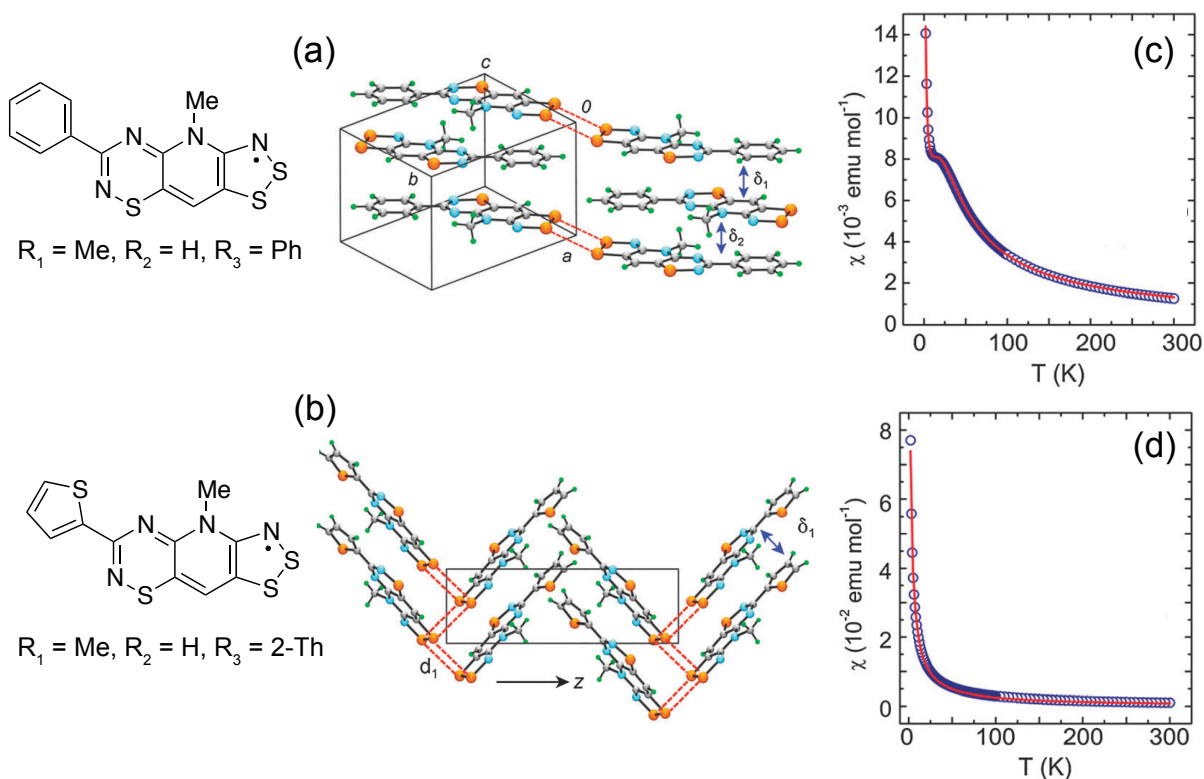


Figure 7.2: (a) Crystal packing of **7-1** ($R_1 = \text{Me}$, $R_2 = \text{H}$, $R_3 = \text{Ph}$) showing ABAB π -stacking. (b) Crystal packing of **7-1** ($R_1 = \text{Me}$, $R_2 = \text{H}$, $R_3 = 2\text{-Th}$) showing close contacts between pairs of π -stacks. (c) Experimental magnetic susceptibility of $R_3 = \text{Ph}$ (open circles) with 1D AFM chain fit shown with a solid line. (d) Experimental magnetic susceptibility of $R_3 = 2\text{-Th}$ (open circles) with Curie-Weiss fit shown with a solid line.

($R_1 = \text{Me}$, $R_2 = \text{H}$, $R_3 = 2\text{-Th}$) crystallizes as slipped π -stack arrays in the $P2_12_12_1$ space group, with short interstack contacts only between pairs of stacks, occurring in a zig-zag fashion (Fig. 7.2(b)).⁹² The presence of the bulky R_3 group prevents any other strong lateral interactions, and the material behaves as a Curie-Weiss paramagnet ($\Theta = -8.4$ K) down to $T = 2$ K (Fig. 7.2(d)). For **7-1** ($R_1 = \text{Me}$, $R_2 = \text{H}$, $R_3 = \text{Ph}$), the π -stacks are composed of an alternating ABAB pattern of radicals, which crystallize in the $P\bar{1}$ space group (Fig. 7.2(a)). This arrangement allows for a somewhat more developed network of magnetic interactions, although the magnetic response is that of a 1D AFM

chain (Fig. 7.2(c)), with $\mathcal{J} = -17$ K along the chain, and weak ferromagnetic interchain $z\mathcal{J} = +6.6$ K.¹ Taken together, these observations imply that intermolecular interactions are weak in these materials, which is not conducive to realization of a metallic state. Indeed, preliminary conductivity measurements indicate room temperature values in the range $\sigma(T = 300 \text{ K}) \sim 10^{-7} - 10^{-5}$ which is the same order as previous pyridine bridged radicals **4-1** and **1-20**.

7.2.2 Electronic Structure

In order to discuss the electronic structure of radicals **7-1**, we consider, at the single site level, an effective three-orbital Hamiltonian that is the sum of orbital energy, Coulomb repulsion, and on-site Hund's rule coupling, respectively:

$$\mathcal{H}_i = \mathcal{E}_i + \mathcal{U}_i + \mathcal{K}_i \quad (7.1)$$

where

$$\mathcal{E}_i = \sum_{\alpha,\sigma} \epsilon_\alpha n_{i,\alpha} \quad (7.2)$$

$$\mathcal{U}_i = U \sum_{\alpha} n_{i,\alpha,\uparrow} n_{i,\alpha,\downarrow} + V^{\alpha\beta} \sum_{\alpha>\beta} n_{i,\alpha} n_{i,\beta} \quad (7.3)$$

$$\mathcal{K}_i = \sum_{\substack{\alpha>\beta \\ \sigma,\sigma'}} K^{\alpha\beta} c_{i,\beta,\sigma'}^\dagger c_{i,\alpha,\sigma}^\dagger c_{i,\alpha,\sigma} c_{i,\beta,\sigma} \quad (7.4)$$

and $\alpha \in \{-1, 0, 1\}$ includes the orbitals in the vicinity of the Fermi level. Parameters of the Hamiltonian can be estimated by state energy calculations on the molecular cation and anion obtained by subtracting or adding an electron from the radical. When mapped into the three-orbital model, the low energy anionic states consist of one triplet in which the SOMO and LUMO are both singly occupied ${}^{2S+1}|n_{i,-1}n_{i,0}n_{i,1}\rangle = {}^3|211\rangle$, and three singlets with varying occupancies $\{{}^1|220\rangle, {}^1|211\rangle, {}^1|202\rangle\}$ (Fig. 7.3). The energies of the eigenstates are:

¹Values with respect to the Hamiltonian $\mathcal{H} = -2\mathcal{J}_{ij}\mathbf{S}_i \cdot \mathbf{S}_j$.

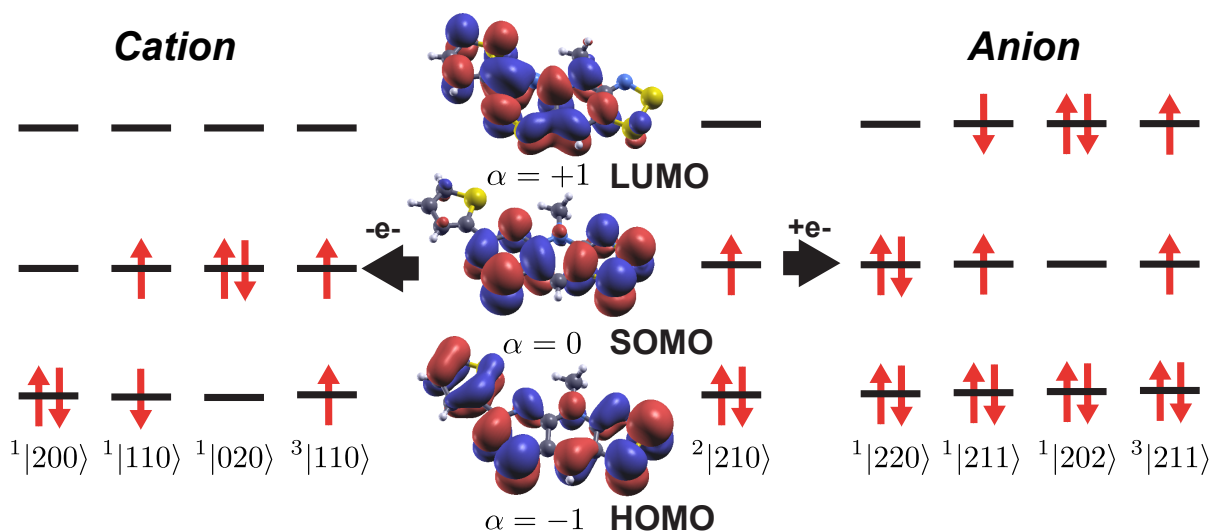


Figure 7.3: Cartoon representation of the electronic states obtained by either removal (left) or addition (right) of an electron to **7-1** ($R_1 = \text{Me}$, $R_2 = \text{H}$, $R_3 = 2\text{-Th}$). Calculation of these state energies allow for estimation of various Hamiltonian parameters.

$$E(^3|211\rangle) = V^{01} + \epsilon_0 + \epsilon_1 - K^{01} \quad (7.5)$$

$$E(^1|220\rangle + \gamma^1|202\rangle) = U + \epsilon_0 + \epsilon_1 - \sqrt{(\epsilon_0 - \epsilon_1)^2 + (K^{01})^2} \quad (7.6)$$

$$E(^1|211\rangle) = V^{01} + \epsilon_0 + \epsilon_1 + K^{01} \quad (7.7)$$

$$E(^1|202\rangle - \gamma^1|220\rangle) = U + \epsilon_0 + \epsilon_1 + \sqrt{(\epsilon_0 - \epsilon_1)^2 + (K^{01})^2} \quad (7.8)$$

From these reference states, the true low energy states may be obtained by explicit inclusion of correlation effects, which mix these configurations not only with one another, but also with those outside the three-orbital active space. It is in this sense that eq'n (7.1) may be considered an effective Hamiltonian, for which $\{K^{01}, U, V^{01}, \Delta\epsilon\}$ are chosen to reproduce the exact low energy spectrum when acting on the unphysical reference space. As an example, the state energies for **7-1** ($R_1 = \text{Me}$, $R_2 = \text{H}$, $R_3 = 2\text{-Th}$) were estimated using the Difference Dedicated Configuration Interaction method^{264,304} with three degrees of freedom (DDCI-3), on the basis of the above CAS(4,3) reference states, as implemented in the ORCA program.¹⁴⁸ Starting orbitals were obtained from a single point B3LYP/def2-VDZ calculation on the closed shell anion using molecular geometry from the ambient pressure crystal structure.

Fitting the obtained state energies to the above expressions yields: $K^{01} = 0.10$ eV, $\epsilon_1 - \epsilon_0 = 1.79$ eV, and the difference of Coulomb repulsion $U - V^{01} = 0.05$ eV. The Coulomb parameters may be estimated by taking U to be the electrochemical cell potential, suggesting $U \sim 0.76$ eV, and $V^{01} \sim 0.71$ eV. Comparison of these values for those obtained in Sec. 5.2.1 suggest that the π -LUMO in **7-1** ($R_1 = \text{Me}$, $R_2 = \text{H}$, $R_3 = 2\text{-Th}$) is no lower lying than the σ -LUMOs in **4-1-4-4**. This is perhaps not surprising, as thiophene is a weak π -donor, so that the empty thiophene-based π -orbitals are expected to be high-lying. When these orbitals mix with those of the central radical framework, the resulting π -LUMO is also high in energy. However, we have also investigated computationally the effects of π -acceptor substituents at the R_3 position, such as $-\text{NO}_2$ and $-\text{CN}$, but find that the LUMO cannot be appreciably lowered by such chemical substitutions.

In this sense, it may be more promising to consider a possible high-lying $\alpha = -1$ filled HOMO level for π -donating substituents. Analogous calculations to those above may be performed on the molecular cation of **7-1** ($R_1 = \text{Me}$, $R_2 = \text{H}$, $R_3 = 2\text{-Th}$), whose low-energy states are:

$$E(^3|110\rangle) = V^{-10} + \epsilon_{-1} + \epsilon_0 - K^{-10} \quad (7.9)$$

$$E(^1|200\rangle + \gamma^1|020\rangle) = U + \epsilon_{-1} + \epsilon_0 - \sqrt{(\epsilon_{-1} - \epsilon_0)^2 + (K^{-10})^2} \quad (7.10)$$

$$E(^1|110\rangle) = V^{-10} + \epsilon_{-1} + \epsilon_0 + K^{-10} \quad (7.11)$$

$$E(^1|020\rangle - \gamma^1|200\rangle) = U + \epsilon_{-1} + \epsilon_0 + \sqrt{(\epsilon_{-1} - \epsilon_0)^2 + (K^{-10})^2} \quad (7.12)$$

DDCI-3 calculations on the molecular cation on the basis of CAS(2,3) reference states yield $K^{-10} = 0.50$ eV, $\epsilon_0 - \epsilon_{-1} = 1.62$ eV, and $V^{-10} \sim 0.57$ eV. The validity of these parameters may be verified by comparing with the solution absorption spectrum of $[\mathbf{7-1}]^+$ ($R_1 = \text{Me}$, $R_2 = \text{H}$, $R_3 = 2\text{-Th}$), which shows singlet \rightarrow singlet transitions of 1.95 eV and 3.87 eV. The above calculations estimate 2.01 eV and 3.38 eV based on state energy differences, which correspond reasonably well with the experiment. Taken together, these values suggest that radicals **7-1** do not offer significant promise for realizing desirable multi-orbital effects, despite the presence of π -orbitals in the energetic vicinity of the SOMO. Such orbitals are simply not sufficiently close to the Fermi level to hybridize with the SOMO in the solid state. Moreover, the bulky R_3 group tends to reduce lateral inter- π -stack interactions in the solid state, which together account for the relatively weak interactions and low conductivity

Table 7.1: Properties of selected oxobenzene bridged radicals **7-2** as a function of exocyclic group R. SC-AFM = Spin canted antiferromagnetic order. “Strong AFM” refers to materials with strong antiferromagnetic coupling that may order but do not display a canted moment. $E_{cell} \sim U$ is the electrochemical cell potential, and $E_A \sim U - W$ is the thermal activation energy for conductivity.

R	Solvent	Space Group	Θ	E_{cell}	E_A	Notes	Ref
F	None	$Cmc2_1$	-18.3 K	0.69 V	0.10 eV	SC-AFM, $T_N = 13$ K	97
H	None	$Fdd2$	+15.6 K	0.56 V	0.10 eV	SC-AFM, $T_N = 4.5$ K	96, 305
Ph	None	$P2_12_12_1$	+32.8 K	0.60 V	0.20 eV	SC-AFM, $T_N = 4.5$ K	93
Cl	MeCN	$Pna2_1$	-61.7 K	0.64 V	0.11 eV	Strong AFM	95
I	EtCN	$Pnma$	+20.9 K	0.66 V	0.15 eV	SC-AFM, $T_N = 34.5$ K	Unpublished
NO ₂	MeCN	$P2_1/c$	-	0.45 V	0.07 eV	Pauli; $\chi = \text{const.}$	Unpublished

of these materials. That being said, the synthetic variability possible at the R₃ position may allow other applications of radicals **7-1**, for example, as polydentate radical ligands for metal complexes with suitable choice of exocyclic R₃ group. This application has yet to be explored. In the remainder of this chapter, we focus instead on an alternate class of radical developed by the Oakley group, in which a strong π -acceptor in the form of a C=O group is built directly into the main radical framework, resulting in much stronger modifications to the electronic structure.

7.3 oxobenzene Bridged Radicals

7.3.1 Introduction

Concurrent with the study of the hybrid dithiazolyl/thiadiazinyl radicals **7-1**, an alternate class of oxobenzene bridged radicals **7-2** were also developed by the Oakley group, which differ from the pyridine bridged framework **4-1** via an isoelectronic substitution of N-R₁ for C=O. Properties of selected radicals is shown in Table 7.1. The initial motivation for this substitution was to reduce steric bulk associated with the exocyclic R-group of the

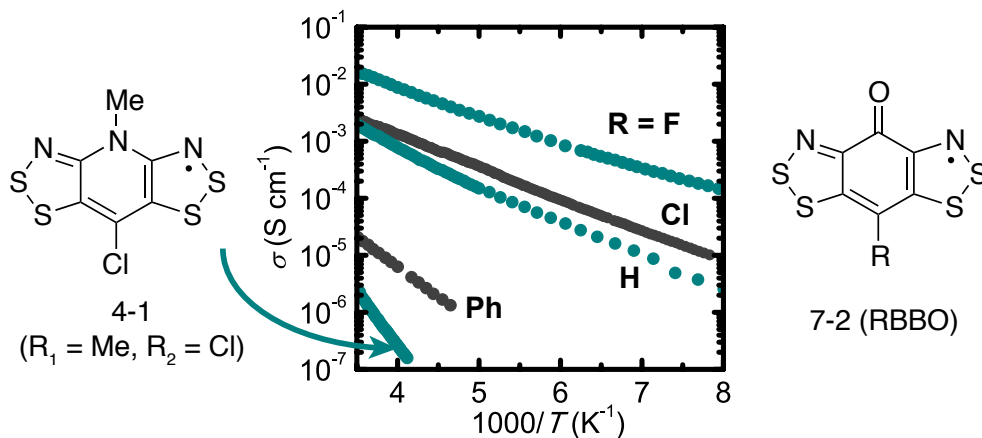


Figure 7.4: Arrhenius plots of conductivity $\sigma = 1/\rho$ in order to compare the response of pyridine **4-1** ($R_1 = \text{Me}$, $R_2 = \text{Cl}$) and oxobenzene bridged **7-2** ($R = \text{F}$, Cl , H , Ph) radicals. Data for $R = \text{Cl}$ represents the MeCN solvate. The oxobenzene bridged materials display orders of magnitude enhanced conductivity and lower thermal activation energies.

former materials, which is partially responsible for the one-dimensional slipped π -stacked packing of **4-1**–**4-4**.^{93–95} As demonstrated via pressure studies in Sec. 5.3.2, increasing the dimensionality of the interactions and reducing the slippage both represent viable strategies for enhancing solid state bandwidth, and thus breaking out of the Mott insulating state. However, introducing the strong π -accepting $\text{C}=\text{O}$ into the central framework also has drastic effects on the electronic structure of **7-2**, generating a very low-lying LUMO capable of hybridizing with the SOMO in the solid state.^{96,306} We discuss this effect in great detail below. The consequences of this additional orbital can be immediately observed in the electrical conductivity, which remains activated, but is several orders of magnitude larger in RBBO radicals **7-2** in comparison with the pyridine-bridged **4-1** (Fig. 7.4). The thermal activation energy is also significantly reduced in the former, falling from 0.4 – 0.5 eV for **4-1** radicals to 0.1 – 0.2 eV for **7-2**. This enhanced conductivity is related to a decrease in the effective Coulomb repulsion, indicated by exceptionally low cell potentials $E_{\text{cell}} = 0.45 - 0.69$ V for **7-2**. Interestingly, these radicals also show a propensity for spin-canted antiferromagnetic order at ambient pressure, which we suggest below provides important clues in regard to their electronic structure. Given the potential for realizing highly conductive states in RBBO radicals **7-2**, research in the Oakley group quickly shifted

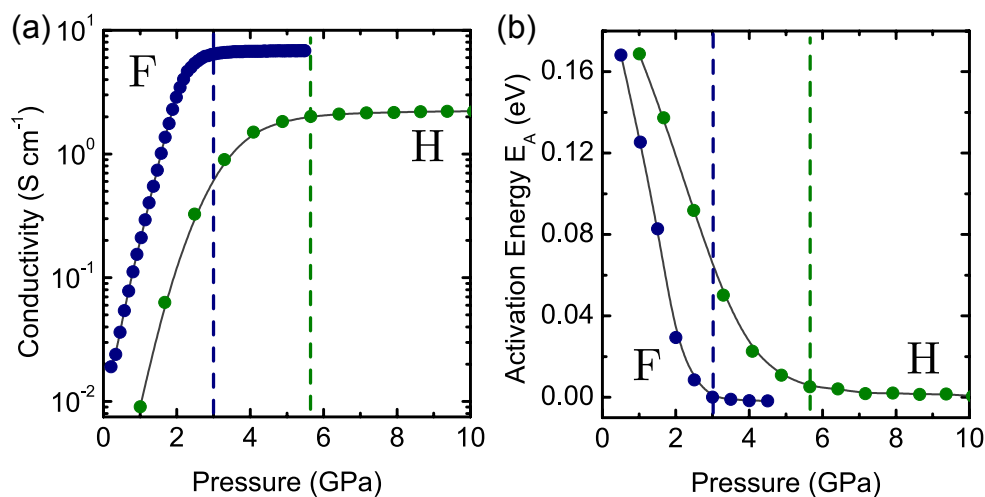


Figure 7.5: (a) Evolution of room temperature electrical conductivity of HBBO and FBBO under pressure, showing saturation above 3 GPa and 5.5 GPa, respectively. (b) Activation energy obtained from Arrhenius fits to $\sigma(T)$ measured from 25–95 °C indicating metallic transport $d\sigma/dT \lesssim 0$ at high pressures. The approximate metallization pressure is indicated for each material by a dashed line.

to focus on these multi-orbital systems, with synthetic contributions led by Dr. Mailman, Ms. Wong and Ms. Yu. Pressure induced metallization ($d\rho/dT > 0$) has now been observed for R = F under applied pressure of $P \sim 3$ GPa,⁹⁷ and for R = H with $P \sim 5$ GPa⁹⁶ in the vicinity of room temperature (Fig. 7.5). My part in this work was performing optical studies on these materials, and developing a model to understand the consequences of the low-lying LUMO, which will be the focus of the remainder of this chapter. We begin by studying the FBBO (i.e. **7-2** R = F), which represents the most well characterized member of the family. We then go on to discuss more recent results on modification of the properties through introduction of a strong π -accepting R-group (NO₂), and a heavy iodine substituent.

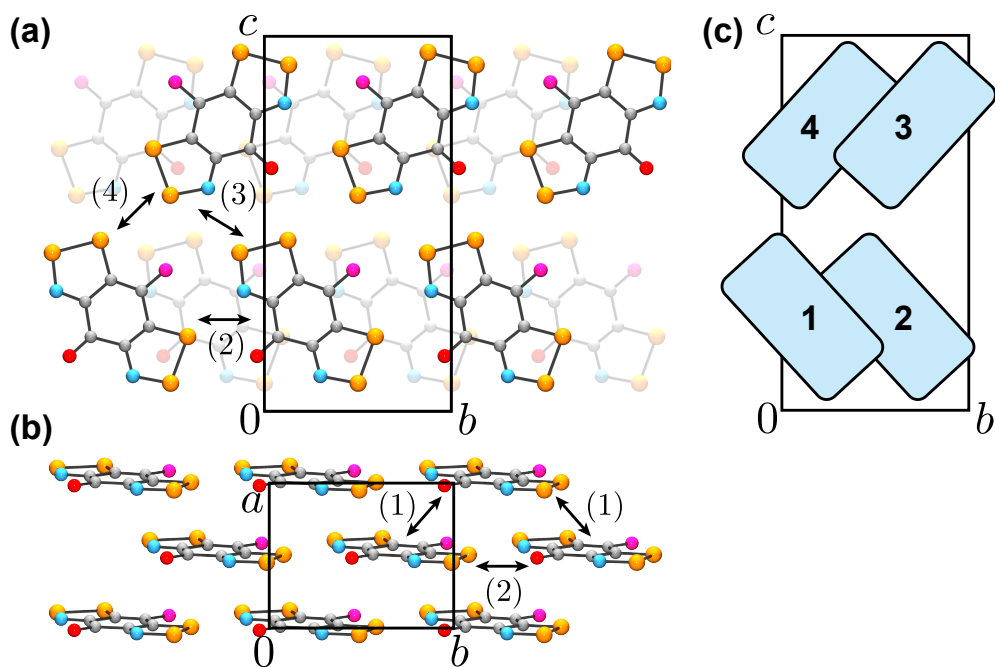


Figure 7.6: (a) Unit cell of FBBO viewed parallel to a . Molecules at $x = \frac{1}{2}$ are shaded to indicate depth. (b) Unit cell of FBBO viewed parallel to c . In both cases, n th nearest neighbour contacts are labelled (1)-(4), with corresponding magnetic interactions shown in Fig. 7.8. (c) Simplified view of the unit cell defining molecular numbering employed in symmetry analysis of magnetic structures.

7.3.2 Fluorine Substituted Radical FBBO

Magnetic Response at Low Pressure

The contents of this section draw from Refs 97 and 306. FBBO (**7-2**, $R = F$) crystallizes in the high symmetry orthorhombic space group $Cmc2_1$, with first and second nearest neighbour pairs, labelled (1) and (2), providing the basis for π -stacked layers in the ab -plane (Fig. 7.6). In both cases these neighbouring molecules are related by translation, either by C -centering, or translation along b . The ab -plane layers are bound together by electrostatic interactions through close S–N, S–O, and S–F contacts with third (3) and fourth (4) nearest neighbours in adjacent layers, which are related by 2_1 axes. At ambient pressure, FBBO orders as a spin-canted antiferromagnet, displaying a bifurcation in the

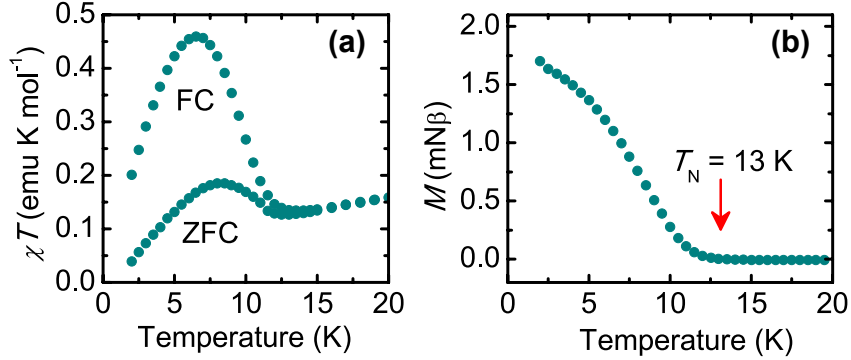


Figure 7.7: (a) Field-Cooled (FC) and Zero-Field-Cooled (ZFC) susceptibility for FBBO showing a bifurcation at $T_N = 13$ K as a result of spin-canting. (b) The spontaneous magnetization due to the small canted moment. Data taken from Ref. 97.

field cooled (FC) and zero-field cooled (ZFC) magnetic susceptibility at $T_N = 13$ K, (Fig. 7.7). Below this temperature, a spontaneous moment saturating at $1.8 \times 10^{-3} \mu_B$ per molecule is observed. Fits of the Curie-Weiss law to the high temperature data (50 – 300 K) give an antiferromagnetic Weiss constant of $\Theta = -18.3$ K.

As discussed extensively in Sec. 4.2.2, for two-sublattice antiferromagnets a net moment may only be induced by weak anisotropic interactions provided the ordered structure retains all the translational symmetry of the underlying lattice. In order to analyze the symmetry of possible magnetic structures of FBBO, we therefore employ the basis functions:

$$\mathbf{f}_\mu = \mathbf{m}_1^\mu + \mathbf{m}_2^\mu + \mathbf{m}_3^\mu + \mathbf{m}_4^\mu \quad (7.13)$$

$$\mathbf{l}_\mu = \mathbf{m}_1^z + \mathbf{m}_2^z - \mathbf{m}_3^z - \mathbf{m}_4^z \quad (7.14)$$

where $\mu = \{x, y, z\}$ refers to the orientation of (sub)lattice moments with respect to the crystallographic directions. Numbering of radicals in the unit cell is shown in Fig. 7.6(c). First nearest neighbours (i.e **1/2** and **3/4**) are related by C -centering translation, requiring such sites to belong to the same magnetic sublattice in any structure able to exhibit a canted moment. For this reason, the antiferromagnetic basis function \mathbf{l}_μ corresponds with the only two-sublattice AFM structure consistent with the magnetic response. As shown in Table 7.2, when sublattice moments are oriented in the bc -plane, corresponding to basis

Table 7.2: Symmetry classification of basis functions for describing the magnetic structure of FBBO (**7-2**, R = F).

State	Basis Function	E	$2_1 \parallel b$	c -glide $\perp b$	$m \perp a$	Point Group Symmetry in C_{2v}	Magnetic Group assuming $\mathbf{k} = [0, 0, 0]$
FM	\mathbf{f}_x	+1	-1	-1	+1	B_2	$Cmc'2'_1$
$\uparrow \uparrow$	\mathbf{f}_y	+1	-1	+1	-1	B_1	$Cm'c'2'_1$
$\uparrow \uparrow$	\mathbf{f}_z	+1	+1	-1	-1	A_2	$Cm'c'2'_1$
AFM	\mathbf{l}_x	+1	+1	+1	+1	A_1	$Cmc2_1$
$\uparrow \uparrow$	\mathbf{l}_y	+1	+1	-1	-1	A_2	$Cm'c'2_1$
$\downarrow \downarrow$	\mathbf{l}_z	+1	-1	+1	-1	B_1	$Cm'c'2'_1$

functions \mathbf{l}_y (A_2), and \mathbf{l}_z (B_1), symmetry allows a canted moment also confined to the bc -plane, through mixing with \mathbf{f}_z (A_2), and \mathbf{f}_y (B_1). The only structure consistent with canting therefore requires a net ferromagnetic \mathcal{J}_1 and \mathcal{J}_2 , in order to ensure alignment of spins within each ab -plane layer, as shown in Fig. 7.8. As shown below, the proximal metallic state in FBBO, which is accessed above 3 GPa, is predicted to have a strongly 2D electronic structure, with maximal dispersion within the ab -layers. Thus ferromagnetic interactions within these layers cannot be understood without the influence of multiple orbitals in proximity to the Fermi level. That is, in single-band Hubbard models, highly conductive states are associated with large t_{ij}^{00} , and as such are characterized by strong antiferromagnetic interactions.

In order to investigate the stability of the layered antiferromagnetic state under pressure, field-cooled susceptibility at 100 Oe was measured by the group of Masaki Mito (Kyushu, Japan) using a piston cylinder cell, installed into the commercial SQUID magnetometer, in the range 0.0 to 1.2 GPa (Fig. 7.9(a)). At low pressures < 0.2 GPa, a surge in χT is observed in the field-cooled susceptibility at $T_N = 13$ K, signalling the transition to the spin-canted ordered state described in the previous section. However, above 0.2 GPa, this surge is reversibly suppressed, indicating either the absence of magnetic order,

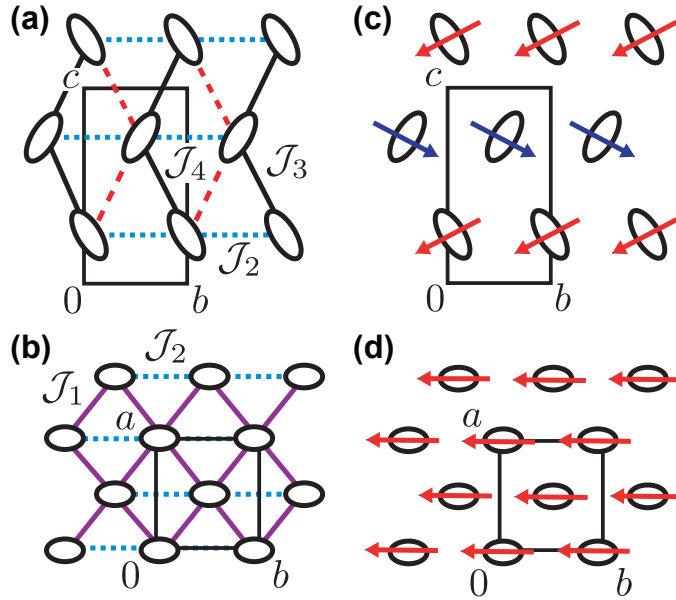


Figure 7.8: Unique nearest neighbour magnetic interactions $\mathcal{J}_1 - \mathcal{J}_4$ for FBBO, as viewed along the a -direction (a), and c -direction (b) showing triangular lattice architectures. The number assigned to each interaction corresponds to the contacts defined in Fig. 7.6. The suggested ambient pressure magnetic structure is also shown, viewed along the a -direction (c), and c -direction (d). Canting to produce a net moment in the bc -plane is emphasized.

or a new magnetic order with no net canted moment. Upon further compression, > 0.6 GPa, χT is further reduced, and shows only weak temperature dependence below 20 K. This high pressure response is roughly consistent with a Curie-like paramagnetic state, but with significantly reduced moment of $\sim 0.2 \mu_B$ compared to the expected $1.0 \mu_B$ for an $S = \frac{1}{2}$ material. Given the previous observation of room temperature metallic conductivity in FBBO for pressures exceeding 3.0 GPa, it is tempting to associate the changes in low temperature magnetic response with the onset of a conducting state. However, evidence against such an electronic phase transition can be seen in the temperature dependence of the resistivity, which was measured in the pressure range 0.0 to 2.0 GPa on pressed pellet samples (Fig. 7.9(b)). Throughout the entire pressure range, FBBO displays activated (insulating) behaviour down to the lowest measured temperatures ~ 10 K. This observation suggests the pressure induced changes in magnetic response between 0.2 and 0.6 GPa are

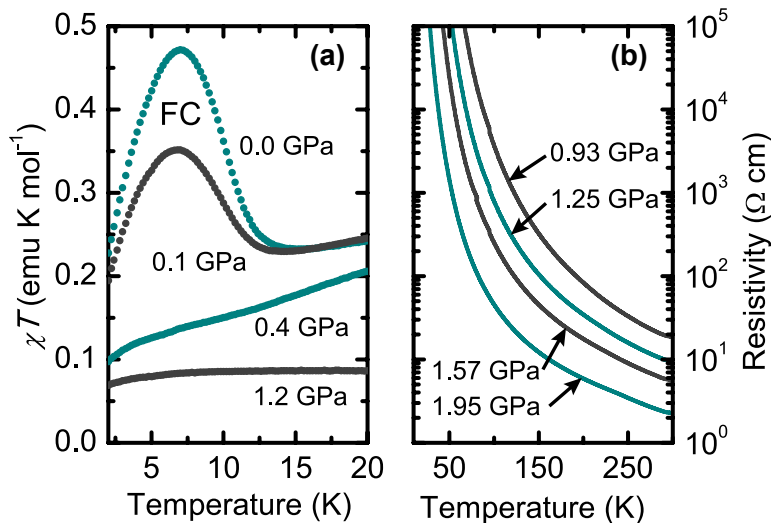


Figure 7.9: (a) Field-Cooled (FC) susceptibility of FBBO under pressure. The increase in χT at low temperatures is suppressed by pressure, indicating a magnetic phase transition. (b) High pressure resistivity. Insulating behaviour under pressure indicates the absence of an electronic phase transition below 2.0 GPa.

related to a genuine magnetic phase transition, rather than the onset of a metallic state. Below, we study the electronic structure of this material, and suggest a possible identity for this high pressure magnetic phase.

Molecular Electronic Structure

A particular feature common to oxobenzene bridged bis-dithiazolyl radicals is the π -accepting character of the carbonyl group ensures the lowest unoccupied molecular orbital (LUMO, $\alpha = +1$) is low-lying, and of π -character, as shown in Fig. 7.10. As described below, explicit consideration of this empty orbital is of key importance not only in the character of the magnetic interactions, but also charge transport properties. Accordingly, at the single site level, we consider an effective two-orbital Hamiltonian that is the sum of orbital energy, Coulomb repulsion, and on-site Hund's rule coupling, as in the case of the hybrid **7-1** radicals:

$$\mathcal{H}_i = \mathcal{E}_i + \mathcal{U}_i + \mathcal{K}_i \quad (7.15)$$

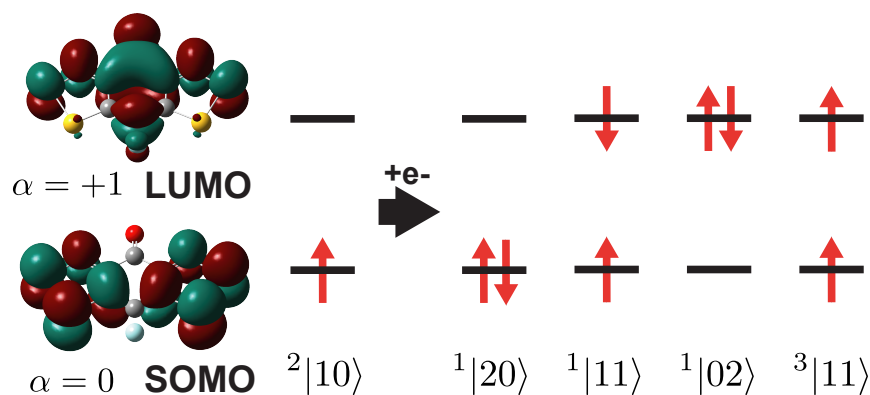


Figure 7.10: Cartoon representation of the states of the anion of FBBO. Comparison of calculated state energies allows estimation of various molecular parameters. The molecular SOMO and LUMO are shown, as computed at the B3LYP/6-31G(d,p) level.

Parameters of the Hamiltonian were estimated by DDCI-3 state energy calculations on the molecular anion obtained by adding an electron to FBBO. Starting orbitals were obtained from a single point B3LYP/6-31G(d,p) calculation on the closed shell anion using molecular geometry from the ambient pressure crystal structure. Relative to the lowest singlet, $^1|20\rangle$, the energies were found to be $E(^3|11\rangle) = +0.174$ eV, $E(^1|11\rangle) = +0.581$ eV, and $E(^1|02\rangle) = +1.234$ eV. This suggests $K^{01} = 0.20$ eV, $\Delta U = U - V = 0.24$ eV, and $\Delta\epsilon = \epsilon_1 - \epsilon_0 = 0.58$ eV. As these values may be significantly influenced by the solid state environment, they should be considered only an approximate starting point for further analysis. It is worth mentioning that the results also depend greatly on the level of theory; Broken Symmetry DFT calculations, for example, suggest triplet ground states for RBBO anions.⁹⁶ Isolation of such an anion of RBBO materials, in order to further characterize its electronic state represents an important goal in order to verify this picture. Finally, we note that while explicit calculation of the solid state Coulomb potential U is not possible by this method, an experimental estimate can be obtained from electrochemical measurements. Given the known $E_{cell} = 0.69$ V for FBBO, we therefore estimate $U \sim 0.69$ eV, and $V \sim 0.45$ eV.

Table 7.3: Tight-binding parameters for FBBO for maximally localized orbitals shown in Fig. 7.12; in this basis, ϕ_- and ϕ_+ orbitals are nearly degenerate and \mathcal{T} is not diagonal at a given site, indicated by $t_{ii}^{-+} \neq 0$. The number in parenthesis beside each label $t_{ij}^{\alpha\beta}$ indicates the associated contact defined in Fig. 7.6.

$t_{ij}^{\alpha\beta}(1)$ (meV)		β		$t_{ij}^{\alpha\beta}(3)$ (meV)		β	
		-	+			-	+
α	-	-125.0	+48.7	α	-	+5.3	+6.1
	+	-98.3	+34.9		+	+40.4	-7.0
$t_{ij}^{\alpha\beta}(2)$ (meV)		β		$t_{ij}^{\alpha\beta}(4)$ (meV)		β	
		-	+			-	+
α	-	-19.1	+18.2	α	-	-17.0	-1.6
	+	-58.3	+38.5		+	+28.5	~ 0

Solid State Electronic Structure

In the solid state, the single-site Hamiltonian of eq'n (7.15) must be supplemented by an intermolecular hopping term:

$$\mathcal{H} = \mathcal{T} + \sum_i \mathcal{H}_i \quad (7.16)$$

where

$$\mathcal{T} = \sum_{\substack{\alpha,\beta,\sigma \\ i,j}} t_{ij}^{\alpha\beta} \left(c_{i,\alpha,\sigma}^\dagger c_{j,\beta,\sigma} + \text{h.c.} \right) \quad (7.17)$$

In order to determine appropriate hopping integrals $t_{ij}^{\alpha\beta}$ for FBBO, band structures were first computed at the DFT level with the PWSCF package¹⁷⁷ using ultrasoft PBE pseudopotentials and a plane-wave cutoff of 25 Ry and a 250 Ry integration mesh. Self-consistent field calculations employed a $4 \times 4 \times 4$ Monkhorst-Pack k-point mesh and the molecular geometry was taken from the ambient pressure crystal structure. At first glance,

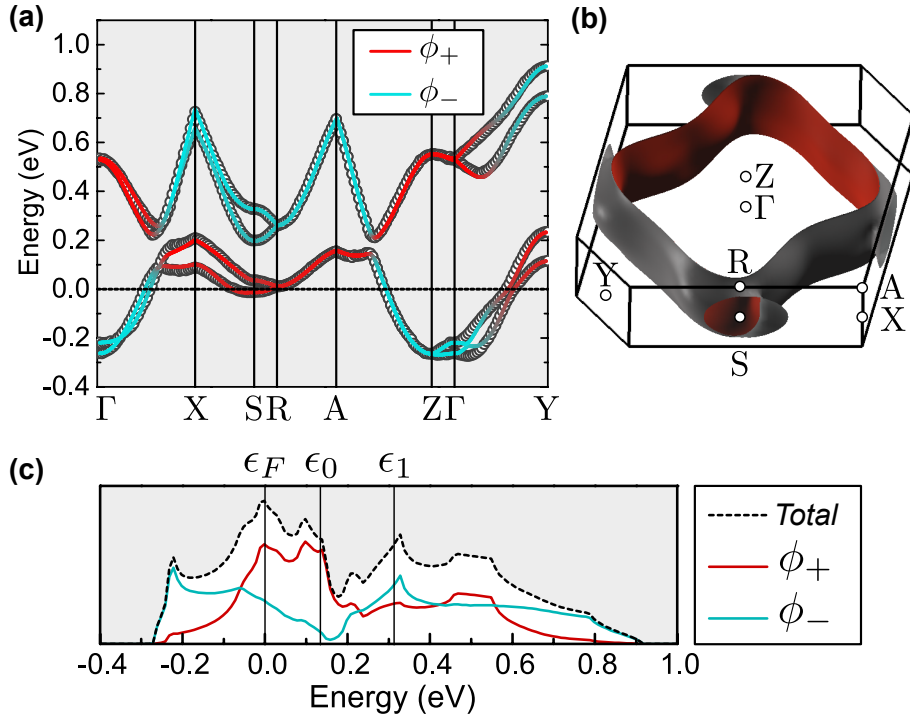


Figure 7.11: (a) Computed DFT band structure of FBBO (open circles). Tight-binding bands obtained by Wannier interpolation are shown with solid lines, the colour of which indicated the contribution of MLWOs. (b) Tight-binding Fermi surfaces shown in the first Brillouin zone. The two bands associated with each of the ab -layers in the unit cell are colored grey and red. Labelling follows the convention in Ref. 307. (c) Density of states obtained from MLWO interpolation. The Fermi level is indicated by ϵ_F , while the energies of the SOMO and LUMO in the rotated basis are indicated by ϵ_0 and ϵ_1 , respectively.

the resulting band structure (Fig. 7.11(a), open circles) is quite simple. In the first Brillouin zone, there are a pair of bands associated with each of the SOMO and LUMO, arising from the two ab -layers of radicals in the unit cell (a total of four bands). Each pair of bands is only very weakly split, due to little interaction between layers, and consequently only weak dispersion along the z -direction. The Fermi level resides in the lower band, and the resulting Fermi surfaces are open (Fig. 7.11(b)), resembling roughly that of an isotropic square lattice near half-filling. However, this relatively simple electronic structure hides a more complicated orbital picture. We have employed the wannier90 code^{176,179} to generate maximally localized Wannier orbitals (MLWOs) $\{\phi_+, \phi_-\}$ for each ab -layer (pictured in Fig.

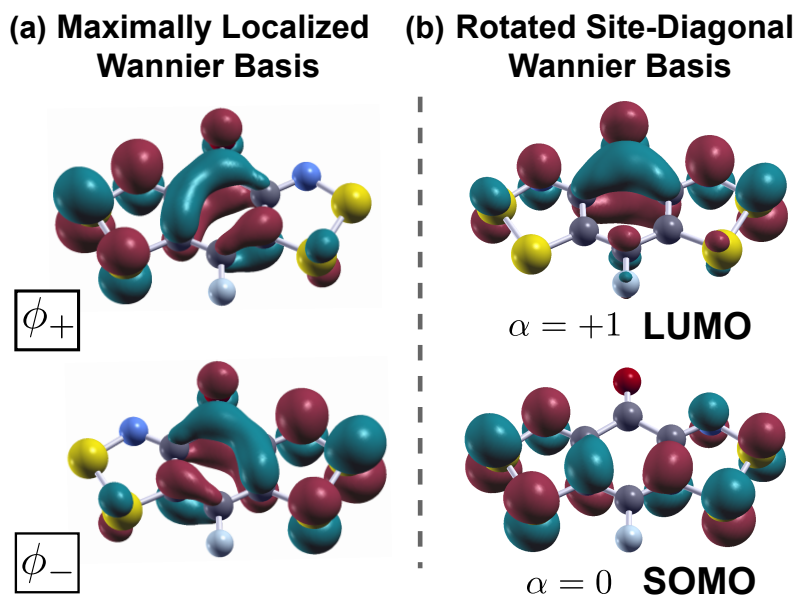


Figure 7.12: Comparison of the Maximally Localized Wannier Orbital (MLWO) basis, and rotated SOMO/LUMO basis orbitals from solid state calculations. The latter may be compared with the orbitals obtained from single molecule calculations in Fig. 7.10.

7.12).² The Wannier interpolated band structure is shown in Fig. 7.11(a) by a solid line, the colour of which indicates the parentage of the crystal orbitals in terms of the derived MLWOs at each k -point. Excellent agreement is observed between the interpolated and DFT bands, validating the fitting procedure. Derived tight-binding hopping integrals for this MLWO basis are shown in Table 7.3.

Visual inspection of the MLWOs ϕ_+ and ϕ_- suggests they are overly localized with respect to the expected molecular orbitals. That is, the MLWOs are in- and out-of-phase combinations of the molecular SOMO and LUMO. They are nearly degenerate each with orbital energy $\sim (\epsilon_0 + \epsilon_1)/2$, which exceeds that of the molecular SOMO by $\Delta\epsilon/2$. However, this local hybridization energy cost for introducing LUMO character into the occupied states is offset by minimization of the *intermolecular* kinetic energy (hopping) so that, over a large region of k -space, the computed crystal orbitals are well described as arising from *purely* ϕ_+ or ϕ_- . Inspection of the hopping integrals in Table I suggest that, within

²Images generated using XCrysden software; code available from <http://www.xcrysden.org/>.³⁰⁸

Table 7.4: Tight-binding parameters for FBBO obtained from a rotation of maximally localized orbitals to ensure a site-diagonal ($t_{ii}^{01} = 0$) hopping Hamiltonian, as described in the text. The number in parenthesis beside each label $t_{ij}^{\alpha\beta}$ indicates the associated contact defined in Fig. 7.6.

$t_{ij}^{\alpha\beta}(1)$ (meV)		β		$t_{ij}^{\alpha\beta}(3)$ (meV)		β	
		0	1			0	1
α	0	+1.2	-3.7	α	0	-24.9	+17.8
	1	+143.3	-91.3		1	-16.6	-23.2
$t_{ij}^{\alpha\beta}(2)$ (meV)		β		$t_{ij}^{\alpha\beta}(4)$ (meV)		β	
		0	1			0	1
α	0	+37.0	-16.2	α	0	-19.1	+27.0
	1	+60.3	-17.6		1	-3.2	-2.0

the ab -plane, the bands arising from ϕ_- and ϕ_+ are described in terms of nearly isotropic square and triangular lattices, respectively. The signs of the hopping integrals are opposite, so that the two bands are well separated over a large region of k -space. Where they meet, interband hopping leads to avoided crossings, ultimately producing discrete lower (half-filled) and upper (empty) bands. Integration of the partial density of filled states (Fig. 7.11(c)) for each orbital, reveals the occupancy to be 0.6 and 0.4 electrons in each of the ϕ_- and ϕ_+ orbitals, respectively. As this picture of the solid state electronic structure inherently neglects correlation effects, it represents a zeroth order description of the metallic state found at high pressure. For this reason, we suggest that the high pressure phase of FBBO is best described as being pseudo quarter-filled with one electron per site on average, occupying one of two degenerate hybrid orbitals.

In contrast, in the Mott insulating state, intermolecular kinetic energy is suppressed by the large Coulomb repulsion barrier, thus eliminating the impetus for local hybridization. For this reason, the hybrid MLWO basis is inappropriate for describing the electronic structure of the low-pressure insulator. In the MLWO basis, hybridization of the SOMO and LUMO results in a kinetic energy \mathcal{T} that is not site-diagonal (i.e. $t_{ii}^{-+} \neq 0$). Diagonalizing

Table 7.5: Ambient pressure magnetic exchange parameters for FBBO up to second order in hopping c.f eq'n (7.19) using hopping integrals from Table 7.4, $K^{01} = 0.20$ eV, $\Delta\epsilon = 0.62$ eV, $V = 0.45$ eV, $U = 0.69$ eV obtained in section III.

Label	Location of Site		Value (K)	
	i	j		
\mathcal{J}_1	(x, y, z)	$(\frac{1}{2} + x, \frac{1}{2} + y, z)$	+86.9	(FM)
\mathcal{J}_2	(x, y, z)	$(x, 1 + y, z)$	-74.3	(AFM)
\mathcal{J}_3	(x, y, z)	$(1 + x, 1 + y, z)$	-38.6	(AFM)
\mathcal{J}_4	(x, y, z)	$(1 + x, 1 + y, z)$	-21.1	(AFM)

the on-site kinetic energy by orbital rotation undoes the hybridization resulting in a more appropriate basis for describing the Mott insulator. Inspection of these rotated orbitals (Fig. 7.12) reveals that they correspond well with the molecular SOMO and LUMO, apart from slight asymmetry due to the local crystal field. Interestingly, $\Delta\epsilon$ is predicted to be only ~ 0.18 eV by this method, which is much reduced from the 0.62 eV predicted by molecular CI calculations in the previous section. In the rotated (SOMO/LUMO) basis, hopping between ab -planes is enhanced, due the more even distribution of electron densities across the molecule. Thus, the 2D electronic structure of the metallic state arises directly from SOMO-LUMO mixing; in the insulating state interactions are significantly more 3D. For molecules in the same ab -plane, the largest hopping integrals are found to occur *between* the SOMO and LUMO on different sites ($t_{ij}^{01}(1), t_{ij}^{10}(1)$). This fact not only drives orbital hybridization in the metallic state, but also has important consequences on the magnetic interactions in the insulator. In the next section, we consider such interactions arising from the multiple orbitals together with strong Hund's rule coupling.

Magnetic Model

As a consequence of a low-lying $\alpha = +1$ LUMO, and strong Hund's Rule coupling, molecular calculations suggested a low-lying triplet state $^3|11\rangle$ in the molecular anion. In the Mott insulator, the importance of this observation can be seen from the fact that magnetic interactions arise from virtual hopping of electrons between sites, which mixes such higher

energy “charged” states into the low energy manifold (composed of “neutral” states with equal electron distribution amongst sites). As described in Sec. 2.1.4, in the present two band case, hopping *between* bands allows access to excited high-spin states, which results in a ferromagnetic interaction. For the two-band model, at second order in hopping, one obtains the familiar Heisenberg Hamiltonian:

$$\mathcal{H}_{\text{spin}} = - \sum_{\langle i,j \rangle} \mathcal{J}_{ij} \mathbf{S}_i \cdot \mathbf{S}_j \quad (7.18)$$

with exchange constant given by contributions from the usual antiferromagnetic kinetic exchange, and ferromagnetic empty-orbital exchange, respectively:

$$\mathcal{J}_{ij} = -\frac{4(t_{ij}^{00})^2}{U} + \frac{2K^{01} [(t_{ij}^{01})^2 + (t_{ij}^{10})^2]}{(V + \Delta\epsilon)^2 - (K^{01})^2} \quad (7.19)$$

In cases where K^{01} and/or t_{ij}^{01}, t_{ij}^{10} are large, one expects the ferromagnetic term to dominate, providing a signature of multi-band character in the magnetic structure. Using eq’n 7.19, together with the hopping integrals for site-diagonal basis from Table 7.4, and the molecular parameters described in section III, we have estimated the exchange parameters for the Mott insulating state of FBBO. Results are shown in Table 7.5. We have also computed corrections up to fourth order in hopping (not shown), and confirm little qualitative difference, justifying use the SOMO/LUMO basis to describe the Mott insulating state.

The computed exchange interactions are in complete agreement with the experimental ambient pressure magnetic structure for FBBO (Fig. 7.8). Within the *ab*-planes, there are two competing terms \mathcal{J}_1 and \mathcal{J}_2 . As a result of the dominant interband hopping integral $t_{ij}^{10}(1) = +143.3$ meV between molecules related by *C*-centering, \mathcal{J}_1 is found to be the strongest magnetic interaction and is ferromagnetic, a fact that agrees with the experimental alignment of spins in the *ab*-planes. This ferromagnetic interaction is partially frustrated by the antiferromagnetic \mathcal{J}_2 term, so that every triangular plaquette contains two ferromagnetic and one antiferromagnetic interaction. While the frustration may reduce both the ordering temperature, and the observed Weiss constant, even for the fully frustrated case where $\mathcal{J}_1 = \mathcal{J}_2$, a quantum disordered (spin-liquid) state is not expected. This is because quantum fluctuations are likely suppressed by interlayer couplings \mathcal{J}_3 and

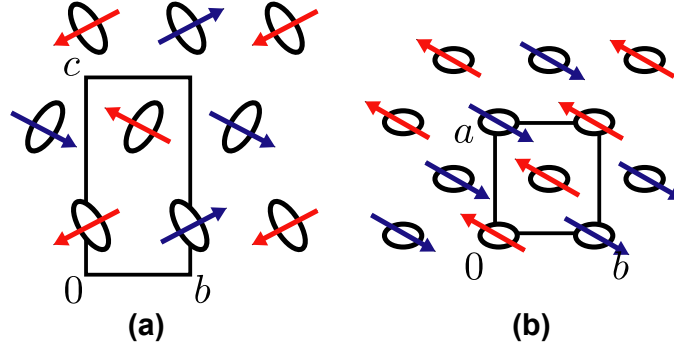


Figure 7.13: Possible magnetic structure of FBBO for pressures above 0.2 GPa viewed down the a -axis (a) and c -axis (b). The stripe pattern emerges as a compromise between ferromagnetic \mathcal{J}_1 and antiferromagnetic \mathcal{J}_2 interactions.

\mathcal{J}_4 . These antiferromagnetic interactions between planes stabilize the experimentally observed layered antiferromagnetic structure. A possible cause of the magnetic transition under pressure may be seen by studying the computed exchange terms. In the ambient pressure magnetic structure, the \mathcal{J}_2 interaction is the only term not minimized energetically. As \mathcal{J}_2 is increased, we suggest stabilization of a new striped ordered phase with wave vector $(\pi, \pi, 2\pi)$ or $(\pi, -\pi, 2\pi)$ as shown in Fig. 7.13. This phase arises as a compromise in which all of the \mathcal{J}_2 interactions, but only half of the \mathcal{J}_1 interactions are satisfied, and should occur around $|\mathcal{J}_2/\mathcal{J}_1| \gtrsim 1$. Based on the above estimates, the ambient pressure structure has $|\mathcal{J}_2/\mathcal{J}_1| = 0.85$, already on the verge of this transition. As this striped structure breaks translational symmetry, no canted moment can be observed, in agreement with experiment. However, further studies (in particular high pressure AFMR) will be required to shed further light on this phase.

Optical Response Under Pressure

In order to probe the evolution of the electronic structure of FBBO with pressure, we have obtained the real part of the optical conductivity $\sigma_1(\omega)$ from analysis of normal incidence reflectivity measurements. The former is related to the complex dielectric function $\epsilon(\omega)$

via: 190,309

$$\sigma(\omega) = \sigma_1(\omega) + i\sigma_2(\omega) = \frac{\omega}{4\pi i}\epsilon(\omega) \quad (7.20)$$

in terms of which the reflectivity $R(\omega)$ is given by the Fresnel formula:

$$R(\omega) = \left| \frac{1 - \sqrt{\epsilon(\omega)}}{1 + \sqrt{\epsilon(\omega)}} \right| \quad (7.21)$$

It is possible to reconstruct both the real and imaginary parts of the complex dielectric function from the real reflectivity because causality requires they are related by the Kramers-Kronig relations, namely:

$$\epsilon(\omega) = \epsilon_1(\omega) + i\epsilon_2(\omega) \quad (7.22)$$

$$\epsilon_1(\omega) = 1 + \frac{2}{\pi} \mathcal{P} \int_0^\infty d\nu \frac{\nu \epsilon_2(\nu)}{\nu^2 - \omega^2} \quad (7.23)$$

$$\epsilon_2(\omega) = -\frac{2}{\pi} \mathcal{P} \int_0^\infty d\nu \frac{\nu \epsilon_1(\nu)}{\nu^2 - \omega^2} \quad (7.24)$$

where \mathcal{P} denotes the principle value of the integral. For this reason, $\epsilon_1(\omega)$ and $\epsilon_2(\omega)$ are not independent functions. However, as the relation between the two is given by an integral over all frequencies, $\epsilon(\omega)$ may only be determined exactly from knowledge of $R(\omega)$ at all ω . In practice, however, the reflectivity is known over a finite frequency range, so analysis is performed by fitting $R(\omega)$ with a variational trial $\epsilon(\omega)$ that is constrained to satisfy the Kramers-Kronig relations. For frequencies outside the known data range, the dielectric function is typically approximated via a simple q -component Drude-Lorentz form:

$$\epsilon(\omega) = \epsilon(\infty) + \sum_q \frac{\omega_{p,q}^2}{\omega_{0,q}^2 - \omega^2 - i\gamma_q\omega} \quad (7.25)$$

where $\omega_{p,q}$, $\omega_{0,q}$ and γ_q are the plasma frequency, resonant frequency, and scattering rate for component q . For the contribution to ϵ by charge carrying excitations, these are often written:

$$\omega_{p,q} = \sqrt{\frac{4\pi n_q e^2}{m_q^*}} \quad (7.26)$$

$$\gamma_q = \frac{1}{\tau_q} \quad (7.27)$$

where e is the elementary charge, and n_q , m_q^* and τ_q are the charge carrier density, effective mass, and scattering time associated with charge carrier flavour q . In this case, the conductivity is simply:

$$\sigma(\omega) = \sum_q \frac{n_q e^2 \tau_q}{m_q^*} \frac{\omega}{\omega + i\tau_q(\omega^2 - \omega_{0,q}^2)} \quad (7.28)$$

with $\omega_0 \rightarrow 0$ representing the Drude limit. In all cases presented in this chapter, fitting of the reflectivity was performed using the REFFIT program³¹⁰ by performing an initial background fitting using a small number of Drude-Lorentz terms (typically $q = 2$), followed by detail-fitting using a Kramers-Kronig constrained local function associated with every data point in the experimental $R(\omega)$.

Ambient pressure, single crystal reflectivity was measured at room temperature with a commercial Nicolet Continuum μm FT-IR microscope with an MCT detector. The light was polarized in the plane of the plate-like crystals, which corresponds to the [111] face. The resulting optical conductivity shows a significant absence of spectral weight at low frequencies, as expected for the Mott insulating state. In this case, for a single band model, $\sigma_1(\omega)$ is expected to display a broad feature centred at $\hbar\omega = U$, and with width $2W$ corresponding to excitations from the lower to upper Hubbard band. The case of the multi-band model is discussed below with reference to results from DMFT calculations. It is worth noting that in the present case, the Hubbard feature is centred at the solution electrochemical cell potential of FBBO $E_{\text{cell}} = 0.69$ V, which validates the latter as a measure of the effective Coulomb potential. The width of the feature is also on the order of twice the Coulomb repulsion, so that some spectral weight extends down to 0.1 eV, which represents the limit of the experimental spectral window, and the thermal activation energy.

The optical conductivity was also obtained under pressure based on reflectivity measurements conducted at the U2A beamline sidestation of the NSLS³. Infrared spectra were collected using a Bruker Vertex 80v FTIR spectrometer and a Hyperion 2000 IR microscope attached with an MCT detector on pressed powder samples in a diamond anvil cell with KBr as a pressure transfer medium. In this case, reflectance from the sample

³National Synchrotron Light Source, Brookhaven National Laboratory, New York, USA

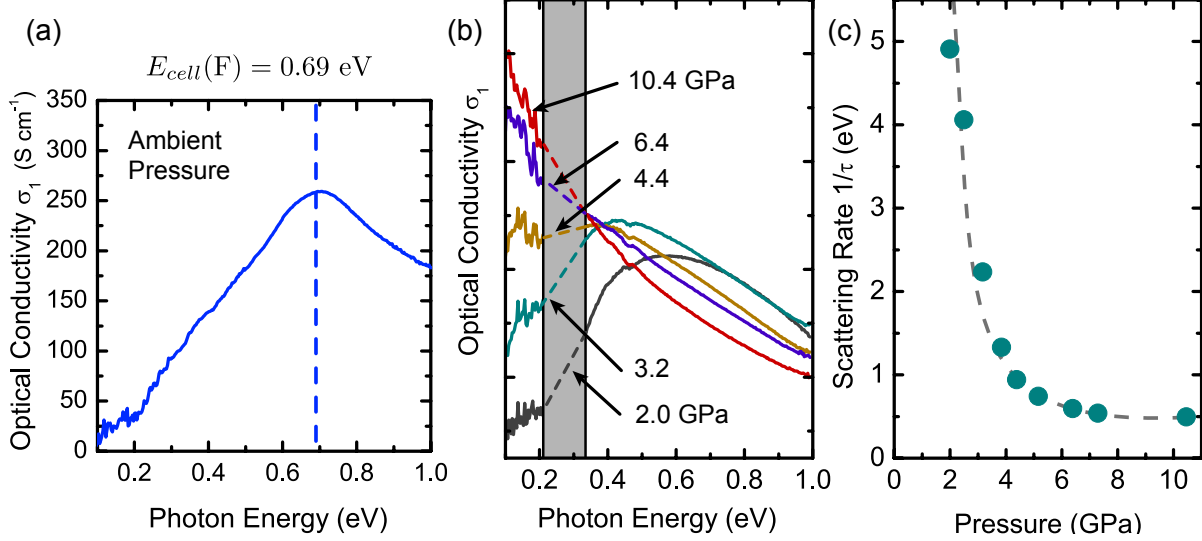


Figure 7.14: (a) Ambient pressure single crystal optical conductivity of FBBO for light polarized in the [111] face. (b) Optical conductivity under pressure. The grey bar denotes an area of the spectrum dominated by phonon modes of the diamond anvil pressure cell. (c) Pressure dependence of the scattering rate obtained from extended Drude analysis as described in the text.

occurs directly at the diamond interface, so that experimental data corresponds to:

$$R(\omega) = \left| \frac{\sqrt{\epsilon_D} - \sqrt{\epsilon(\omega)}}{\sqrt{\epsilon_D} + \sqrt{\epsilon(\omega)}} \right| \quad (7.29)$$

where $\epsilon_D = 5.84$ is the dielectric function of the diamond, which we assume to be real and constant over the frequency range. As an additional complication, the diamond is associated with very strong phonon modes in the spectra range $1700\text{--}2700\text{ cm}^{-1}$, or roughly $0.2\text{--}0.35\text{ eV}$, which obscure the sample reflectance. For this reason, reliable optical conductivity cannot be obtained in this region (shown as a grey bar in Fig. 7.14(b)).

With increasing pressure, there is significant transfer of spectral weight to lower frequencies, resulting in a shift of the peak in $\sigma_1(\omega)$. In the vicinity of 3 GPa, a Hubbard-like feature is still observed at high frequency, indicating a significant influence of correlation effects at this pressure. By 6.4 GPa, the high frequency Hubbard features are nearly absent, and the response is essentially Drude-like. The results can be further analyzed in an extended Drude formalism^{309,311,312} in order to extract the effective quasiparticle scattering

rate at zero frequency:

$$\frac{1}{\tau} \equiv \lim_{\omega \rightarrow 0} -\frac{\omega_p^2}{\omega} \text{Im} \left[\frac{1}{\epsilon(\omega) - \epsilon(\infty)} \right] \quad (7.30)$$

where the plasma frequency is approximated via:

$$\int_0^\Lambda \sigma_1(\omega) d\omega = \frac{\omega_p^2}{8} \quad (7.31)$$

for some suitably large cutoff Λ . As discussed in section 3.1, when $1/\tau > W$, the strength of scattering exceeds the natural energy scale for the quasiparticle kinetic energy, and the mean free path is much smaller than a lattice spacing $\ell < a$, implying that coherent quasiparticles cannot exist.^{191–193,195} Analysis of the obtained optical conductivity suggests that the scattering rate $1/\tau$ decreases by an order of magnitude over the pressure range 2–10 GPa, saturating above 4 GPa at a value of 0.5 eV $\sim W$ (Fig. 7.14(c)). This result is consistent with the observed order of magnitude enhancement and saturation of the DC conductivity $\sigma(\omega = 0) \propto \tau$ over the same pressure range (Fig. 7.5). However, the large value of the scattering rate suggests a bad metallic state at room temperature. Indeed, the room temperature resistivity at high pressure, which saturates near 0.1 Ω cm, exceeds the Mott-Ioffe Regel limit of $\sim 10^{-3}$ Ω cm by several orders of magnitude.

Taken together, these optical conductivity results presented in this section provide strong evidence for a Mott insulator to metal transition in FBBO in the vicinity of 3 GPa, as evidenced by significant shifts in spectral weight to low frequencies, and suppression of the effective quasiparticle scattering rate. Future studies of the temperature dependence of these quantities, and extensions to lower frequency, could provide greater insight into the evolution of the electronic structure of FBBO through this transition. For example, the appearance of Drude-like features has been observed in many strongly correlated systems at low temperature ($T < T^* \sim 40$ K for organics) and frequency ($\omega < 0.05$ eV for organics) associated with quasiparticles that become coherent only below a strongly renormalized effective Fermi temperature T^* , as discussed in Section 3.3.^{200,309,313} Preliminary diamond anvil cell measurements of $\rho(T)$ obtained by the Julian group at the University of Toronto on a pressed pellet of FBBO show a similar response in FBBO (Fig. 7.15). At 2.7 GPa, a downturn of the resistivity and metallic conductivity ($d\rho/dT > 0$) is observed below

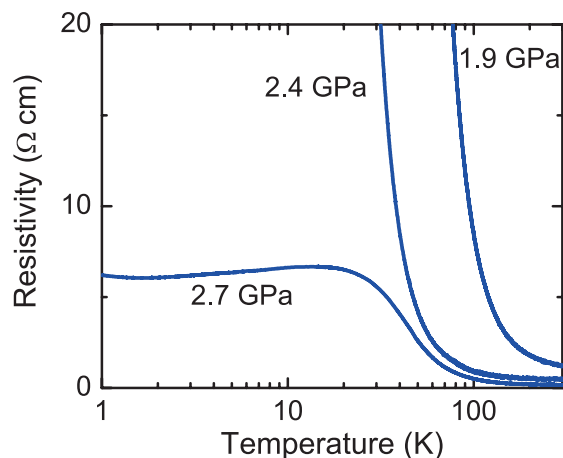


Figure 7.15: Preliminary high pressure resistivity measurements on FBBO showing a region of metallic conductivity at 2.7 GPa and below 20 K.

20 K, while activated behaviour is observed at lower pressures and higher temperatures. However, we find no region of $\rho < \rho_{MIR}$ below this downturn, in contrast with more widely studied radical-ion salts.^{200,228,229} Continued studies of FBBO would help to map out the phase diagram of this material as well as elucidate the reason for this dichotomy. In the next section, we discuss the qualitative picture of the Mott transition in FBBO within the context of the suggested multi-band model.

Description of the Multi-Orbital Mott Transition

In this section, we consider the nature of the insulator to metal transition observed in FBBO around 3.0 GPa, in reference to the described electronic structure. In the insulator, the half-filled SOMO is split into lower and upper Hubbard bands (LHB and UHB, respectively), with a relatively wide LUMO band and small V implying overlap of the LUMO band and UHB. Under applied pressure, a Mott transition in the SOMO band alone is unlikely, due to small t_{ij}^{00} 's and large U . For this reason, we have suggested that this transition proceeds mainly through orbital rehybridization of the molecular SOMO and LUMO to produce a degenerate set of orbitals resembling the MLWOs. Concomitant with this transition is the reduction in the chemical potential, due to LUMO states being drawn to lower energy. The

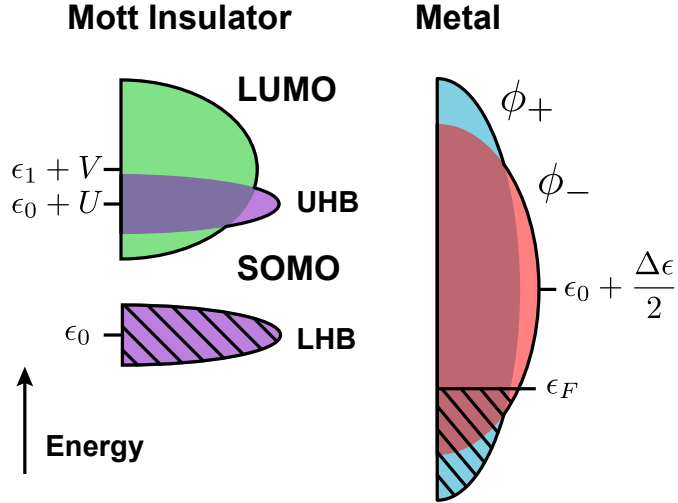


Figure 7.16: Cartoon of the electronic structure of FBBO in the insulating and metallic states. Occupied one-electron states are indicated by diagonal hatching. In the insulator, the SOMO is split into a filled lower Hubbard band (LHB), and empty upper Hubbard band (UHB), which overlaps with the empty LUMO band. In the metal, the SOMO and LUMO hybridize to overlapping ϕ_- and ϕ_+ bands, with roughly equal occupation.

resulting MLWO bands are wide and nearly equally occupied in the metallic state, so that the transition is expected to occur directly between the half-filled insulator and quarter-filled metal, as represented in Fig. 7.16. This scenario is in agreement with previous studies, which suggest a direct transition in the case where the splitting of the MLWOs $\Delta\epsilon' \sim 0$, but such studies considered only weak orbital hybridization ($t_{ij}^{--}, t_{ij}^{++} \gg t_{ij}^{-+}$).³¹⁴ Proximity to this metallic state is also related with the observation of ferromagnetic interactions in the insulator; in the same limit of negligible hybridization, the quarter-filled two-orbital model is known to display ferromagnetically ordered insulating states.³¹⁵

In section III, approximate Coulomb parameters were computed in the SOMO/LUMO

basis; these can be transformed into the MLWO basis:

$$U' = \frac{U + V}{2} + K^{01} \sim 0.77 \text{ eV} \quad (7.32)$$

$$V' = \frac{U + V}{2} - K^{01} \sim 0.37 \text{ eV} \quad (7.33)$$

$$K^{-+} = \frac{U - V}{2} \sim 0.12 \text{ eV} \quad (7.34)$$

$$\Delta\epsilon' \sim 0 \text{ eV} \quad (7.35)$$

As expected, localizing the MOs has the effect of increasing the Coulomb repulsion between electrons in the same orbital, while decreasing the repulsion between electrons in different orbitals. On the basis of these values, the potential energy cost for formation of a metallic state can be estimated in a mean field sense from the expectation value of the Coulomb operator:

$$\langle \mathcal{U}_i \rangle = \frac{U'}{4} (\langle n_{i,-} \rangle^2 + \langle n_{i,+} \rangle^2) + V' \langle n_{i,-} \rangle \langle n_{i,+} \rangle \quad (7.36)$$

which reduces to $\langle \mathcal{U}_i \rangle \sim 0.13 U' + 0.24 V' \sim +0.19 \text{ eV}$ using $\langle n_{i,-} \rangle \sim 0.6$ and $\langle n_{i,+} \rangle \sim 0.4$. For comparison, the reduction in kinetic energy upon formation of the metallic state (including the cost of orbital hybridization) can be estimated by:

$$\Delta E_k = \frac{\int_{-\infty}^{\epsilon_F} (\epsilon_0 - \omega) D(\omega) d\omega}{\int_{-\infty}^{\epsilon_F} D(\omega) d\omega} \quad (7.37)$$

where $D(\omega)$ is the total density of states for the two bands as shown in Fig. 7.11(c), and ϵ_0 is the orbital energy of the unhybridized SOMO. We find $\Delta E_k \sim -0.25 \text{ eV}$ per electron at ambient pressure, which is the same order as the potential cost of 0.19 eV above, consistent with proximity to the Mott transition. However, as $|\Delta E_k| > \langle \mathcal{U}_i \rangle$, a metallic state is anticipated even at ambient pressure, in contrast with experimental findings. Indeed, we show below that DMFT calculations come to the same conclusion. This discrepancy is most likely due to an underestimation of the SOMO-LUMO splitting $\Delta\epsilon \sim 0.18 \text{ eV}$ in the solid state calculations, resulting in a slight overestimation of ΔE_k . It is worth noting that Extended Hückel calculations on isolated molecules incorrectly predict a reversal in the ordering of the SOMO and LUMO, giving negative $\Delta\epsilon$ values. In this sense, $\Delta\epsilon$ is sensitive

to the theoretical method employed, and may not be properly estimated by the solid state DFT technique.

The role of Hund’s rule coupling in stabilizing the metallic state of RBBO materials has been previously discussed, but is revisited here in the context of the above picture of orbital rehybridization. In multiorbital models with no orbital mixing, the effects of Hund coupling, K , has been demonstrated to have a strong filling dependence. In particular, for multiple electrons/holes per site, a large K reduces both the charge gap in the insulating state, and the quasiparticle coherence in the metal, ultimately promoting bad-metallic states over a wide range of t/U .^{316,317} In contrast, for the case with only one electron per site on average, the latter effect is diminished, so that a normal metallic state is always stabilized for large K . For the present picture of orbital mixing in RBBO materials, this discussion is complicated by the state dependency of the Hund coupling magnitude (i.e., $K^{01} \neq K^{-+}$). We therefore restrict the discussion to the influence of K^{01} . On the insulating side, increasing K^{01} reduces the charge gap, thus promoting a metallic state. On the metallic side, the only effect of increasing K^{01} is to increase repulsion between electrons in the same MLWO (U'), while reducing the repulsion between electrons in different orbitals (V'). This combination should stabilize the metal, as the large value of U' is expected to have little impact on the quarter-filled metallic state.^{315,318} That being said, further theoretical investigations into the interplay of orbital hybridization and Hund’s rule coupling are of great interest.

In order to further explore the evolution of the electronic structure through the metalization, we have employed Hirsch-Fye QMC DMFT^{17,209–213} calculations, which are particularly suitable for studying multi-orbital strongly correlated problems.^{319–321} For these calculations, we focus on a single *ab*-plane layer, ignoring all hopping to nearest neighbours (3) and (4). The Coulomb parameters are taken to be $K^{01} = 0.2$ eV, $V = U - 0.2$ eV, and we adjust U in order to tune the Mott transition. In order to ensure convergence of the discrete time Green function $G(\tau)$, we employ a large temperature $T = 0.1$ eV/ $k_b = 1160$ K. At each stage, the Green function is made site-diagonal, so that the two orbitals in the DMFT calculation smoothly commute between the MLWO $\{\phi_+, \phi_-\}$ and SOMO/LUMO $\{\phi_0, \phi_1\}$ basis. For this reason, we label the majority and minority occupied orbital ϕ_a and ϕ_b , respectively. In the absence of correlation ($U = V = K^{01} = 0$), the fractional

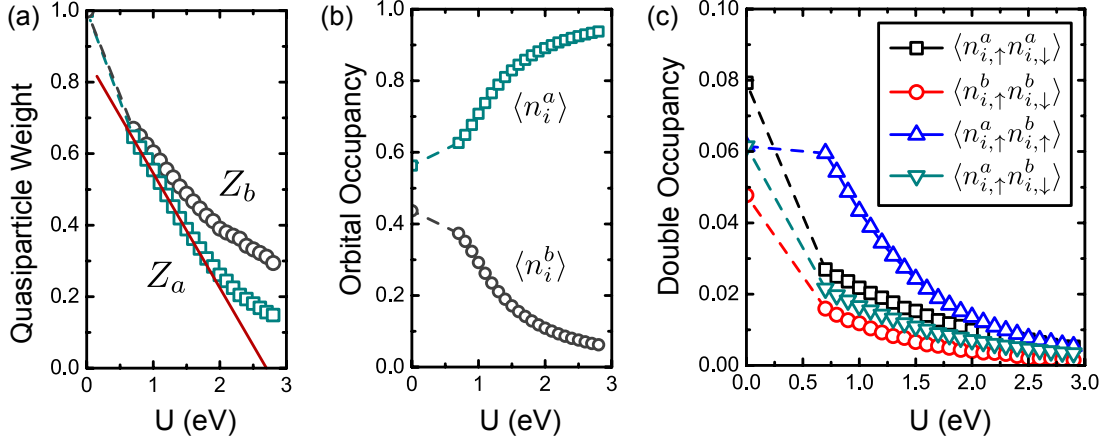


Figure 7.17: Evolution of (a) quasiparticle weight, (b) orbital occupancy, and (c) double occupancy for FBBO as a function of U . The point labelled $U = 0$ corresponds to $V = 0, K^{01} = 0$, while all other points have $V = U - 0.2$ eV and $K^{01} = 0.2$ eV. The metallic states at weak correlation consist of partially occupied SOMO and LUMO bands, in which the effective Coulomb barrier is reduced to $V - K^{01}$, and double occupancy is dominated by $\langle n_{i,\uparrow}^a n_{i,\uparrow}^b \rangle$. Extrapolation of Z_a to zero suggests an insulating state above $U_c \sim 2.6$ eV.

occupancy of these two orbitals is found to be ~ 0.6 and ~ 0.4 , consistent a quarter filled metallic state with $\phi_a = \phi_-$ and $\phi_b = \phi_+$. Setting $U = 0.7$ eV, which corresponds with the parameters estimated above, we still find a metallic solution. This can be seen by estimating quasiparticle weight Z from the value of the self energy at the lowest Matsubara frequency:²⁰⁹

$$Z_\alpha = \frac{m}{m^*} = \frac{1}{1 - \frac{\partial}{\partial \omega} \text{Re} \Sigma(\alpha, \omega)|_{\omega \rightarrow 0^-}} \approx \frac{1}{1 - \frac{1}{\pi T} \text{Im} \Sigma(\alpha, i\omega_n)|_{n=1}} \quad (7.38)$$

which measures the overlap of the states close to the Fermi energy with their uncorrelated counterparts at $U = V = K^{01} = 0$. An insulating state is characterized by the divergence of $\text{Re} \Sigma(\omega)$ at $\omega = 0$, implying a quasiparticle weight of exactly zero. Estimate of Z from the self-energy at discrete Matsubara frequencies via eq'n (7.38) always provides a finite value for Z . Nonetheless, extrapolation Z_a to zero suggests an insulating state appearing above an unrealistically large $U_c \sim 2.6$ eV (Fig. 7.17(a)). For $U = 0.7$ eV, the quasiparticle weight in both bands is found to be in the range 0.6–0.7, suggesting a metallic solution. At this U , the fractional occupancy of each orbital is also altered very little from the

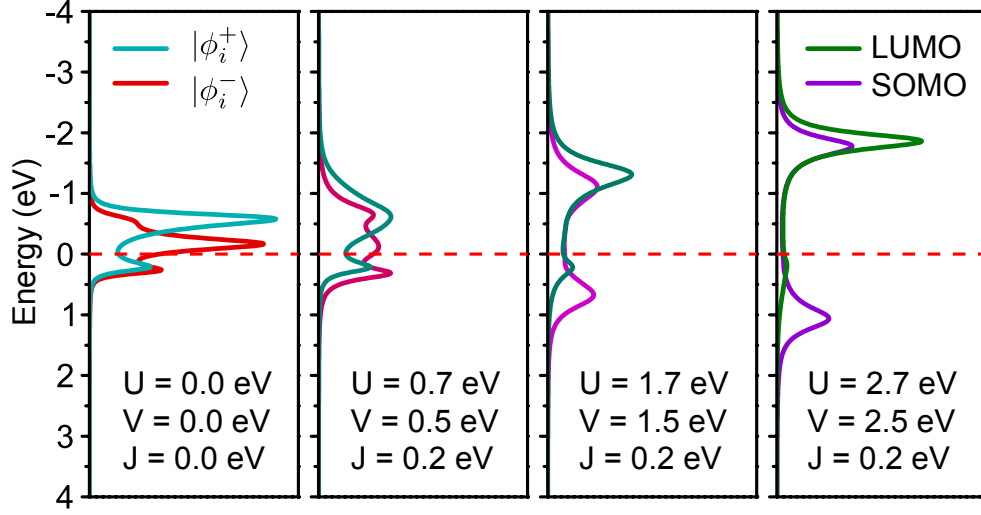


Figure 7.18: Evolution of the integrated spectral weight (i.e. density of states) for FBBO with increasing correlation computed using HF-QMC DFT. As U is increased, the SOMO and LUMO are decoupled, while the LUMO density is pushed to high energy.

uncorrelated values, and inspection of the imaginary time Green functions $G(\tau = 1/2T) \sim \pi A(\omega = 0)$ suggests finite density at the Fermi level. Even at low U , however, statistics of the HF-QMC simulations show that the double occupancy of both minority $\langle n_{i,\uparrow}^a n_{i,\downarrow}^a \rangle$ and majority $\langle n_{i,\uparrow}^b n_{i,\downarrow}^b \rangle$ orbitals is strongly suppressed from their uncorrelated values (Fig. 7.17(c)). In contrast, the occupancy of both orbitals by electrons of the same spin $\langle n_{i,\uparrow}^a n_{i,\uparrow}^b \rangle$ remains essentially unaltered. The strong Hund's coupling ensures the majority of Coulomb repulsion at low U for can be offset by ferromagnetic alignment and occupation of different orbitals by electrons at the same site. With increasing correlation, the occupancy of ϕ_i^b is suppressed, falling to $\langle n_i^b \rangle < 0.1$ in the vicinity of the estimated metal-to-insulator crossover near $U_c \sim 2.6$ eV. In this same region, $\langle n_{i,\uparrow}^a n_{i,\downarrow}^a \rangle \approx \langle n_{i,\uparrow}^a n_{i,\uparrow}^b \rangle$, and the HF-QMC solver shows signatures of instability to strong spin polarization, suggesting the possibility of magnetic order at the mean-field level. We suggest, in this strong correlation limit, that $\phi_i^a \approx \phi_i^0$, and $\phi_i^b \approx \phi_i^1$. The changes in the electronic structure can be tracked by following the evolution of the approximate integrated spectral density of each orbital, obtained by analytic continuation of the self-energy via Padé fitting (Fig. 7.18). As U is increased, the ϕ_b density is shifted to higher energies along with incoherent excitations of the upper

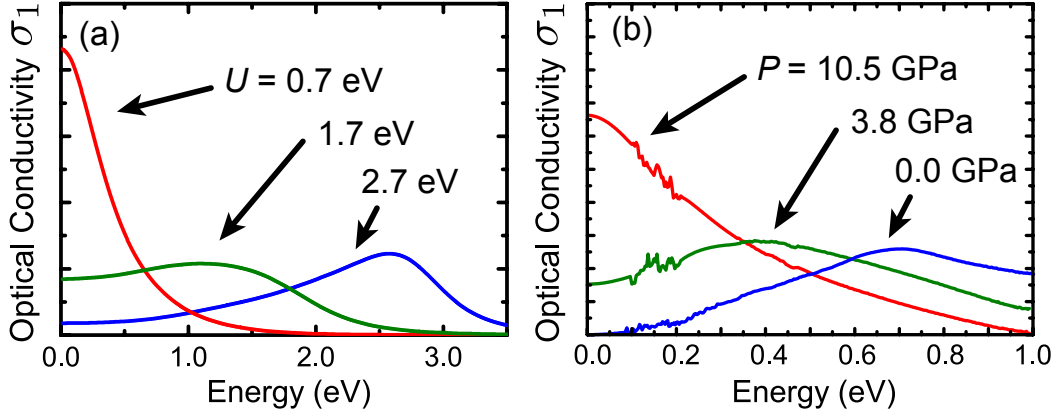


Figure 7.19: (a) Computed real part of the optical conductivity $\sigma_1(\omega)$ within the DMFT approximation for different values of U , with $V = U - 0.2$ eV and $K^{01} = 0.2$ eV for FBBO. (b) Extrapolated experimental optical conductivity based on KK-analysis of normal incidence reflectivity (arb. offset). At weak correlation, a dominant Drude peak is found at low energies. At strong correlation, a single amalgamated feature is found to be peaked near $\omega = U$, corresponding to excitations from the lower Hubbard band to a combination of the upper Hubbard band and the empty LUMO band.

Hubbard band, while the occupied states become increasingly of pure ϕ_a character. The results of these DMFT calculations are therefore consistent with our assertion that the metallic state relies crucially on overlap of SOMO and LUMO spectral density to form a pseudo-quarter-filled system. As U is increased, the LUMO and SOMO are decoupled with the spectral density of the LUMO pushed to higher energies. However, the large value of U_c is alarming; although these calculations provide a compelling cartoon of the metal to insulator transition in FBBO, a more thorough investigation will be required to provide quantitative comparison with experiment.

An important qualitative prediction of DMFT is the strong overlap of the upper Hubbard band and empty LUMO in the insulating state, which has consequences for the optical conductivity, which may be estimated $\sigma(\omega)$ within the DMFT approximation via:^{322–325}

$$\sigma(\omega) = \sigma_0 \sum_{\alpha} \int_{\nu} \int_{\epsilon} A_0^{\alpha}(\epsilon) A^{\alpha}(\epsilon, \nu) A^{\alpha}(\epsilon, \nu + \omega) \frac{f(\nu) - f(\nu + \omega)}{\omega} \quad (7.39)$$

where $A_0^\alpha(\epsilon)$ is the non-interacting momentum integrated spectral function for the α orbital:

$$A_0^\alpha(\epsilon) = \int_{\mathbf{k}} \text{Im} \left[\frac{1}{\epsilon - \epsilon_{\alpha,\mathbf{k}} + i\eta} \right] \quad (7.40)$$

and $A^\alpha(\epsilon, \nu)$ is the DMFT impurity spectral function:

$$A^\alpha(\epsilon, \nu) = \text{Im} \left[\frac{1}{\nu - \epsilon - \Sigma(\alpha, \nu) + i\eta} \right] \quad (7.41)$$

The equation is, strictly speaking, only appropriate for bands where $\epsilon_{\alpha,\mathbf{k}}$ is an injective (1:1) function of momentum and orbital index, as it overcounts the Drude component of the optical conductivity otherwise. However, we can still obtain qualitatively meaningful data provided the computed conductivity is normalized according to the optical f -sum rule: $\int_{\omega} \sigma(\omega) = \text{const.}$ Results of these calculations are shown in Fig. 7.19. At strong correlation, the overlapping of the LUMO spectral density with that of the upper Hubbard band results in a single feature in the optical conductivity centred around $\omega = U$. Thus, only one Hubbard feature is expected, despite contributions from multiple orbitals. Comparison with the experimental optical conductivity (Fig. 7.19(b)) shows good qualitative agreement with the calculations, although the experimental energy scale of interactions is much smaller as noted above. However, the experimental Mott transition is driven by pressure, it is expected to proceed mainly by enhancement of the bandwidth, rather than tuning of the Coulomb repulsion. For this reason, the apparent shifting of the peak in $\sigma_1(\omega)$ should be considered a sign of large particle-hole asymmetry, although further studies will be required to determine the origin and validity of this observation.

Summary and Conclusion

In this section, we studied the charge transport properties and magnetic response of the F-substituted oxobenzene bridged radical (**7-2**, R = F) denoted FBBO. On the basis of the observation of spin canting at ambient pressure, the magnetic structure of FBBO was established to have ferromagnetic interactions within the *ab*-plane layers. This observation was explained on the basis of both molecular and solid state calculations, which implicate a combination of Hund's rule coupling, and a low-lying π LUMO, both of which necessitate

a two-orbital model for the electronic structure. As both of these properties are molecular in origin, they are expected to be common to the entire family of RBBO materials **7-2**. It is therefore satisfying that ferromagnetic interactions are indicated by ferromagnetic Weiss constants $\Theta > 0$ in a large number of RBBO materials, despite variations in solid state packing. For example, substitution of the exocyclic fluorine by a phenyl group to produce PhBBO (**7-2**, R = Ph) provides to one-dimensional chains with large ferromagnetic intrachain coupling $\mathcal{J}_{\parallel} = +84.9$ K,⁴ (interchain $zJ_{\perp} = -7.2$ K) and positive Weiss constant of $\Theta = +32.8$ K.⁹³ Evidence for ferromagnetism has also been observed in HBBO ($\Theta = +15.6$ K), although in this latter case, the complexity of the crystal structure has hindered analysis of the antiferromagnetic order appearing at $T_N = 4.5$ K.³⁰⁵ Analysis of the optical conductivity of HBBO under pressure, reported in Ref. 96, suggests a similar picture of the Mott transition in both FBBO and HBBO. Given these similarities, the essential details discussed in this section for FBBO are expected to be common to the entire radical family.

The enhancement of the conductivity in RBBO radicals in comparison with previous generations of pyridine-bridged radicals can therefore be understood to arise directly from the presence of the low-lying π LUMO. In this section, we have suggested that this LUMO hybridizes with the SOMO in the solid state, which significantly enhances the scale of the electron kinetic energy, promoting delocalization. We considered the evolution of the properties of FBBO under pressure. However, given that the existence of the low-lying LUMO is essentially a molecular property, it is possible to consider how *chemical* modifications to the radical framework might also alter the magnetic and electronic properties. Preliminary studies of such effects are considered in the remaining sections of this chapter.

7.3.3 Nitro Substituted Radical NO₂BBO

Molecular Electronic Structure

Having described the electronic structure of RBBO materials, we now consider how chemical modification may enhance charge transport properties by lowering the SOMO-LUMO gap $\delta\epsilon = \epsilon_1 - \epsilon_0$. In oxobenzene bridged RBBO radicals, the SOMO possesses a nodal plane

⁴With respect to the Hamiltonian $\mathcal{H} = -\mathcal{J}_{ij}\mathbf{S}_i \cdot \mathbf{S}_j$.

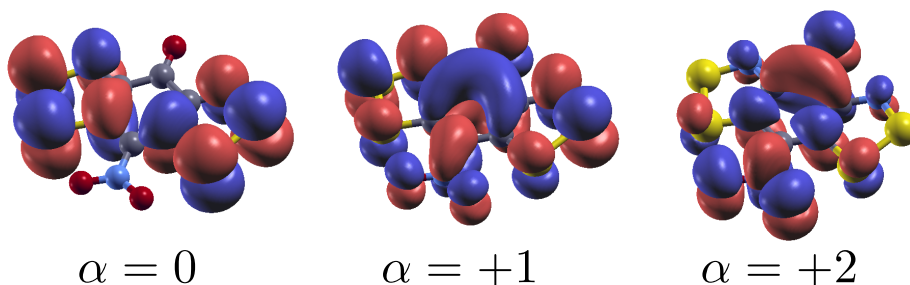


Figure 7.20: Frontier molecular orbitals relevant to the electronic structure of NO_2BBO obtained from DFT calculations at the B3LYP/6-31G(d,p) level.

along the central axis of the molecule, and therefore has little density on the exocyclic R-groups. In contrast, the low-lying LUMO of RBBO radicals has significant density along this axis, and as a result may be tuned via substitution at the R-position. The combination of a strong π -acceptor ($\text{C}=\text{O}$) and weak π -donor ($\text{R} = \text{F}, \text{Cl}, \text{etc.}$) results in an estimated SOMO-LUMO gap of $\Delta\epsilon \sim 0.6$ eV, and electrochemical cell potential of $E_{\text{cell}} = 0.6\text{--}0.7$ V. Introducing a non- π substituent in the form of $\text{R} = \text{H}$ results in a modest reduction to $E_{\text{cell}} = 0.56$ V. It was therefore suggested, and pursued by Dr. Mailman, that substitution with a strong π -acceptor $\text{R} = \text{NO}_2$ would result in significant reduction in the Coulomb gap. Indeed, NO_2BBO exhibits an $E_{\text{cell}} = 0.45$ V, which is lower than that of FBBO by a factor of $1/3$. At the molecular level, the NO_2 group provides an additional low-lying empty π orbital, which may hybridize with the LUMO to produce an exceedingly low-lying $\alpha = +1$ and moderately low-lying $\alpha = +2$ orbital (Fig. 7.20).

In this section, we focus our attention on the just the $\alpha = 0, +1$ orbitals, in order to treat NO_2BBO on the same footing as FBBO. State energy calculations at the DDCI3 level based on a CAS(2,2) reference space on the molecular anion of NO_2BBO suggest an open shell ground state with triplet and lowest singlet energies essentially degenerate. This result may be anticipated from the following Lewis structures, which suggest that localization of

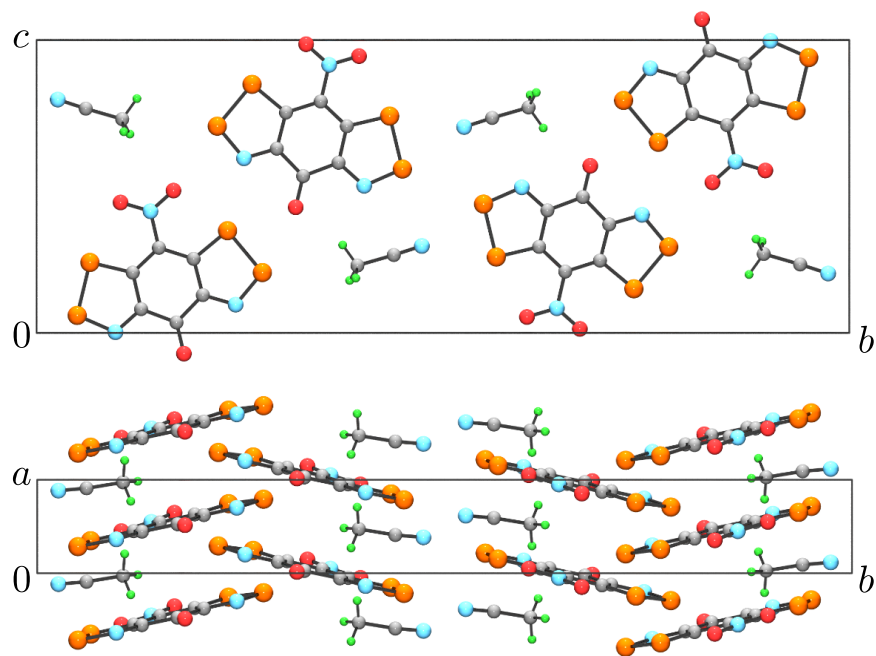
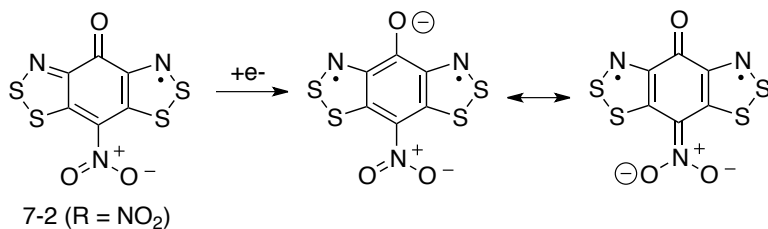


Figure 7.21: Crystal structure of MeCN solvate of NO₂BBO, viewed (a) down the *a*-axis, and (b) down the *c*-axis. The presence of the solvent molecules buffers interactions between π -stacks, resulting in a one-dimensional electronic structure with strong interactions only along the π -stacking *a*-axis.

the negative charge to the C=O and NO₂ moieties naturally gives a diradical structure:



Relative to lowest singlet and triplet the remaining singlets have energies $E(^1|11\rangle) = +1.042$ eV, and $E(^1|02\rangle - \gamma^1|20\rangle) = +1.190$ eV. Based on these values, we therefore estimate $\Delta\epsilon = 0.29$ eV, $K^{01} = 0.52$ eV, $V^{01} = 0.37$ eV, with $U = 0.45$ eV. The reduction in $\Delta\epsilon$ results from the significant mixing of the empty π -orbitals associated with the NO₂ group with only the LUMO, as these orbitals are not of correct energy or symmetry to mix with the

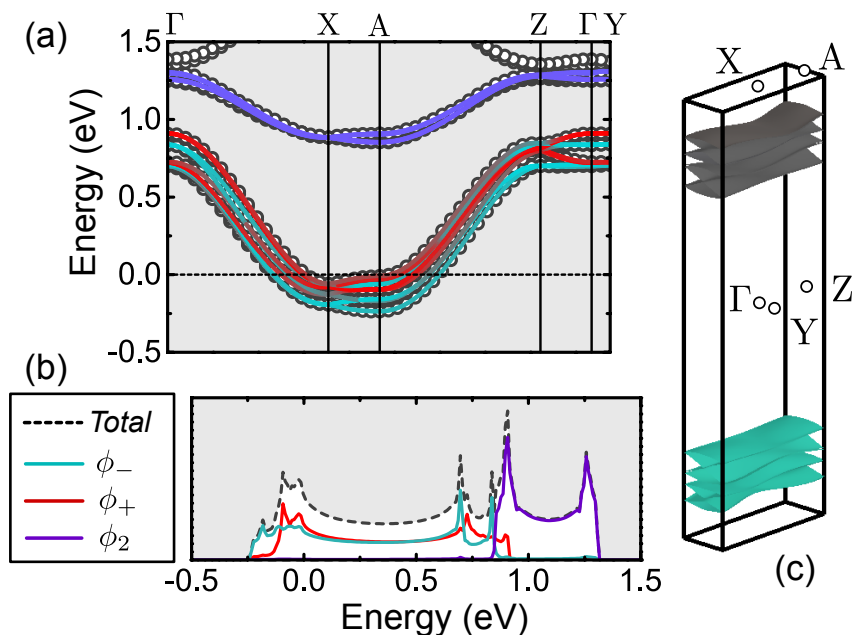


Figure 7.22: Electronic structure of NO₂BBO at the DFT level. (a) Computed band structure (open circles) with Wannier interpolated tight-binding band structure shown with solid lines, the colour of which indicates the contribution from the three MLWOs ϕ_i^- , ϕ_i^+ , ϕ_i^2 . (b) Density of states obtained by MLWO interpolation. (c) Predicted Fermi surfaces corresponding to the eight ϕ_i^- , ϕ_i^+ bands in the Brillouin zone showing 1D character.

SOMO. This mixing also draws LUMO density away from the C=O group in comparison with the LUMO of FBBO, which enhances the overlap density between the SOMO and LUMO. This effect explains the predicted increase of the Hund's coupling K^{01} relative to FBBO by more than a factor of two. Taken together, the predicted suppression of $\Delta\epsilon$ and enhancement of K^{01} should place NO₂BBO in closer proximity to a metallic state.

Solid State Electronic Structure

To date, several crystallographic phases have been found for this material; in this section we focus on the best characterized phase, in which NO₂BBO crystallizes together with MeCN solvent (Fig. 7.21). In this case, the radicals adopt a $P2_1/c$ space group, with solvent molecules separating uniform π -stacks, each with small slippage along the long

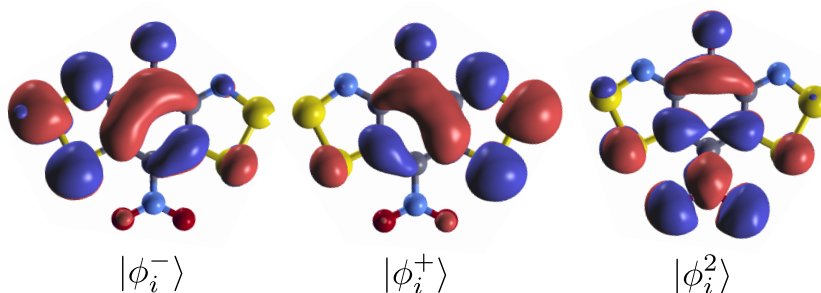


Figure 7.23: Site diagonal orbitals for NO_2BBO . The mixing of the SOMO and LUMO to produce $|\phi_i^+\rangle$ and $|\phi_i^-\rangle$ is reflective of the near degeneracy of the orbitals at this level of theory.

axis of the molecules. Preliminary 4-probe conductivity measurements on pressed pellets of this material suggest a small thermal activation energy of 0.07 eV, which is the lowest observed at ambient pressure in any radical material. However, given the relatively one-dimensional structure, single crystal measurements are desirable. In order to explore the electric structure of this phase, we performed band structure calculations at the DFT level with the PWSCF package¹⁷⁷ using ultrasoft PBE pseudopotentials and a plane-wave cutoff of 25 Ry and a 250 Ry integration mesh. Self-consistent field calculations employed a $2 \times 2 \times 2$ Monkhorst-Pack k -point mesh and the molecular geometry was taken from the preliminary crystal structure, with solvent omitted. At this level of theory, all bands associated with the admixed SOMO and LUMO are found to be essentially degenerate, producing a cluster of eight bands (two from each molecule) intersecting the Fermi energy (Fig. 7.22). These bands show strong dispersion only along the π -stacking a -axis as interstack interactions are buffered by the presence of solvent molecules in the crystal structure. The Fermi energy resides at quarter filling of the combined band cluster, which has a large bandwidth of nearly 1.5 eV, and thus overlaps slightly with the $\alpha = +2$ band appearing 1 eV above ϵ_F .

In order to further analyze the orbital structure, we have employed wannier90 to obtain hopping integrals in the MLWO basis. In contrast with the results on FBBO, the site-diagonalization of the resulting tight binding Hamiltonian does not recover the molecular SOMO and LUMO; as these orbitals are found to be essentially degenerate in these solid state calculations, there is no hybridization cost for their mixing. The MLWOs, shown

Table 7.6: Computed hopping integrals for NO₂BBO **7-2** R=NO₂ obtained via MLWO interpolation.

	$t_{ij}^{\alpha\beta}(\pi)$ (meV)	β		
		-	+	2
α	-	+230.5	-33.3	+8.9
	+	+22.7	+221.4	~ 0
	2	+12.6	-9.5	+100.2

in Fig. 7.23, are already nearly site-diagonal, and may represent an appropriate basis for describing the insulating state. If this result is correct, it implies that even the insulating state of NO₂BBO must be considered in a quarter-filled context, and that the extra orbital degree of freedom afforded by the low-lying LUMO no longer represents only a perturbative effect. Indeed, we find the three MLWOs, denoted ϕ_i^- and ϕ_i^+ , ϕ_i^2 , given by:

$$|\phi_i^-\rangle \approx \frac{1}{\sqrt{2}} (|0_i\rangle - |1_i\rangle) \quad \epsilon_i^- \equiv 0 \text{ eV} \quad (7.42)$$

$$|\phi_i^+\rangle \approx \frac{1}{\sqrt{2}} (|0_i\rangle + |1_i\rangle) \quad \epsilon_i^+ = 0.06 \text{ eV} \quad (7.43)$$

$$|\phi_i^2\rangle \approx |2_i\rangle \quad \epsilon_i^2 = 0.72 \text{ eV} \quad (7.44)$$

Hopping integrals between nearest neighbours in the π -stacks are given in Table 7.6. As a result of the small slippage of the π -stacks, the largest integrals occur between like orbitals, with the wide ϕ^-/ϕ^+ bands characterized by $t_{ij}^{\alpha\beta} > 200$ meV. In contrast, all interstack hopping integrals (not shown) are at least an order of magnitude smaller.

Optical and Magnetic Response

The measured ambient pressure single crystal reflectivity shows marked anisotropy, exhibiting negligible response to light polarized perpendicular to the π -stacking a -axis, and a nearly metallic response, although with $R \sim 0.25$, for light polarized parallel to this axis (Fig. 7.24). This anisotropy is not surprising, given the one dimensional electronic structure suggested in the previous section, and is similar to previous results on quarter

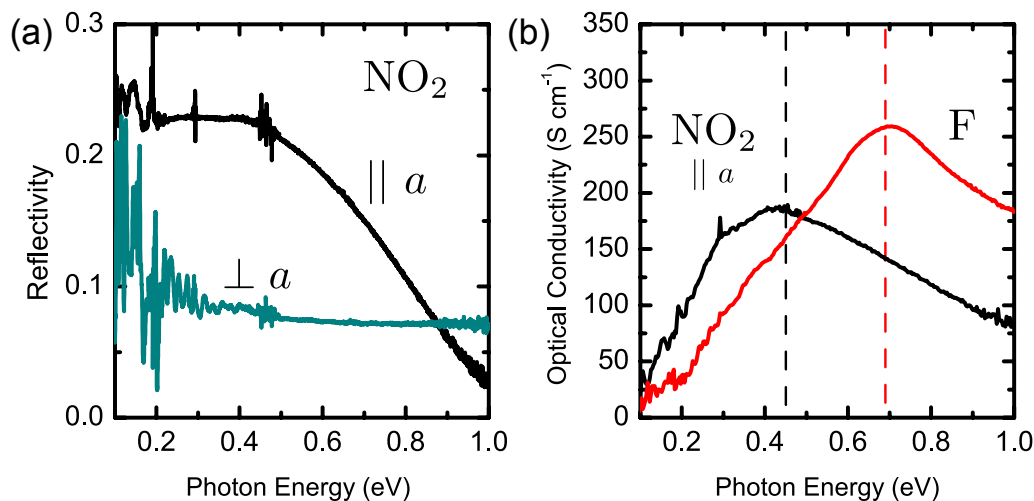


Figure 7.24: (a) Polarized single crystal reflectivity of NO_2BBO at ambient pressure and room temperature. The strong anisotropy is characteristic of the 1D electronic structure, which permits conduction only along π -stacking a -axis. (b) Comparison of the optical conductivity $\sigma_1(\omega)$ obtained by Kramers-Kronig analysis for NO_2BBO and FBBO . The dashed lines indicate the solution electrochemical cell potential values, which correspond with a peak in σ_1 resulting from excitations across the Coulomb gap.

filled organic salts such as $[\text{TMTSF}]_2[\text{X}]$.^{326–328} The optical conductivity for the conductive direction, derived from Kramers-Kronig analysis, shows a broad Hubbard feature centred around the solution electrochemical cell potential $E_{\text{cell}} = 0.45$ V. As a result, there is significantly more spectral weight at low energies compared with FBBO , which is consistent with the suggestion that NO_2BBO is closer to the Mott transition at ambient pressure. The magnetic response is also consistent with this picture, as the magnetic susceptibility follows $\chi T \propto T$, i.e. χ is temperature independent, as one might expect for a metallic conductor (Fig. 7.25).¹²⁴ The measured value of 6×10^{-4} emu mol⁻¹ is enhanced compared with the Pauli susceptibility $\sim 10^{-6}$ emu mol⁻¹ typically found for monovalent metals such as Na, although this is not surprising given the order of magnitude smaller bandwidth in NO_2BBO , and expected influence of correlations. Indeed, susceptibility of this order has been seen in previous metallic organic conductors.^{107,329–331} Reconciling this temperature independent paramagnetic response with the apparent insulating behaviour at ambient pressure represents an important question for future investigation. At this stage, the fact that the electronic structure may be directly tuned via modification of the radical build-

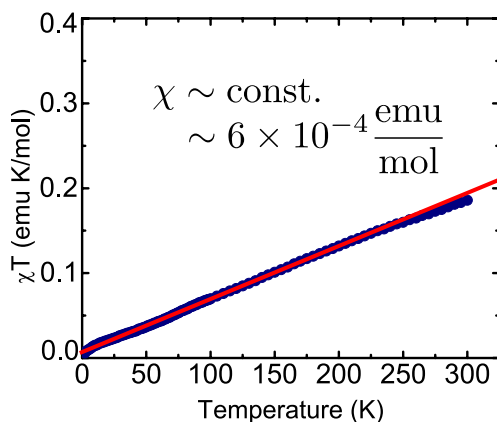


Figure 7.25: Ambient pressure magnetic susceptibility of NO₂BBO showing linear χT , i.e. a temperature independent susceptibility. Such a response might be anticipated for a metallic conductor, indicating proximity to the Mott transition.

ing block offers promise for exploration of strong correlation physics in this new class of multi-band organic radicals.

7.3.4 Iodine Substituted Radical IBBO

Introduction

As the final topic of this chapter, we explore the magnetic properties of **7-2**, R = I, denoted IBBO. As with NO₂BBO, this radical crystallizes in several structural phases; here we focus on the EtCN solvate, which adopts a *Pnma* space group. In this structure, the IBBO radicals form alternating ABAB π -stacks running along the crystallographic *b*-direction, with adjacent radicals in the same stack related by a crystallographic inversion centre. Such pairs of radicals are labelled (π) in Fig. 7.26. Each radical falls on a crystallographic mirror plane normal to *b*, and is linked to adjacent stacks by an *a*-glide (or 2_1), which is the generator of extended ribbons of radicals propagating along the *a*-axis. Nearest neighbours within these ribbons are labelled (1). The presence of the solvent molecules, which also form ribbons along the *a*-axis, separates the radicals such that nearest neighbour interactions (π) and (1) represent the only large symmetry non-equivalent terms. Given

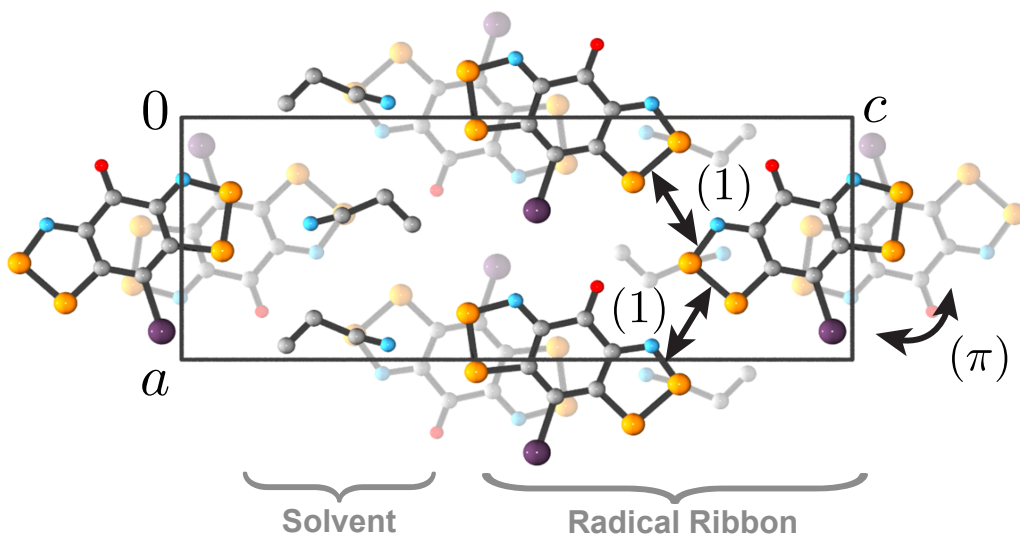


Figure 7.26: Crystal structure of EtCN solvate of IBBO showing definition of nearest neighbour interactions (π) and (1). Hydrogens are omitted from the solvent molecules for clarity.

this relative simplicity, the magnetic response of IBBO is quite compelling.

At ambient pressure, IBBO·EtCN orders as a spin-canted antiferromagnet at $T_N = 34.5$ K, as evidenced by a bifurcation in the field cooled and zero field cooled susceptibility, and the appearance of a spontaneous moment $\sim 1.2 \times 10^{-3} \mu_B$ that displays a relatively large coercive field of 1150 Oe (Fig. 7.27). Given this large magnetic anisotropy, we suspect that spin-orbit effects play an appreciable role in this material. In this light, it is important to note that while SOMO has little density on the heavy I substituent, that the LUMO does contain significant density at this position. For this reason, the R-group may directly influence the scale of spin-orbit coupling corrections to the LUMO, which enter into the multi-orbital anisotropic exchange introduced in section 2.2.4. As the atomic spin-orbit constant of neutral I is $\lambda_I = 0.63$ eV, three times larger than that of Se, even small density on iodine may strongly influence the magnetic anisotropy. We investigate this possibility in this section.

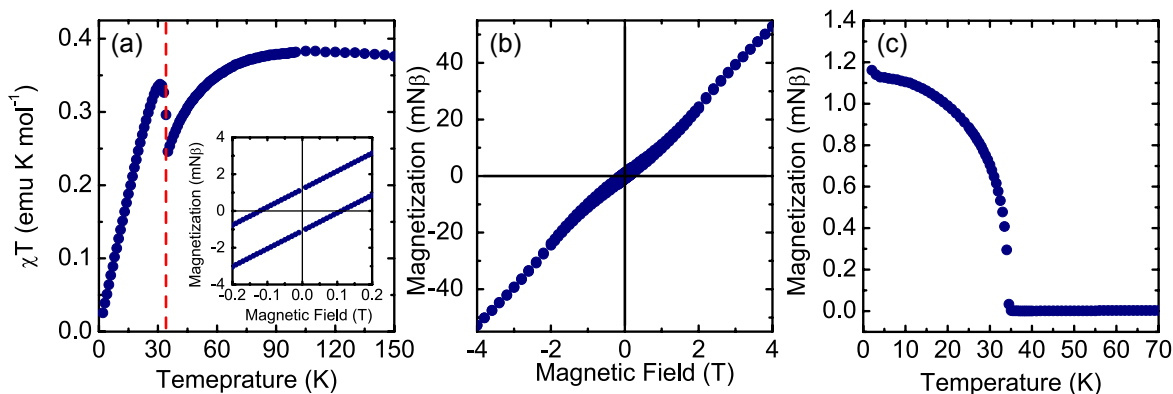


Figure 7.27: Magnetic data on IBBO. (a) Field cooled magnetic susceptibility as a function of temperature showing a surge at the ordering transition $T_N = 34.5$ K. Inset: Magnetization as a function of temperature at low field showing hysteresis of the canted moment. (b) Magnetization over a broader field range. (c) Spontaneous magnetization as a function of temperature.

Isotropic Magnetic Interactions

As with FBBO, the observation of a canted moment in IBBO allows for unambiguous identification of its ordered magnetic structure. In this case, symmetry requires all molecules related by either inversion or translation to belong to the same magnetic sublattice, which implies that adjacent molecules along the π -stack must be ferromagnetically aligned. In contrast, nearest neighbours within the radical ribbons, related by the a -glide must be antiferromagnetically coupled. Given the simplicity of the interactions, this requires $\mathcal{J}_{ij}(\pi) > 0$ and $\mathcal{J}_{ij}(1) < 0$ with reference to the Hamiltonian $\mathcal{H} = -\mathcal{J}_{ij}\mathbf{S}_i \cdot \mathbf{S}_j$. In order to analyze the magnetic interactions, we have estimated hopping integrals via the MOMO method, employing the single crystal structure at 100 K, at the B3LYP/6-311G(d,p) level. The results, shown in Table 7.7, reveal large SOMO-LUMO hopping integrals $t_{ij}^{01}(\pi) = t_{ij}^{10}(\pi)$ between adjacent molecules in the same π -stack. In contrast, interactions along the ribbons are characterized by more evenly distributed magnitudes of all integrals. On the basis of these hopping parameters, and using the Coulomb parameters of FBBO, we estimate the

Table 7.7: Tight-binding parameters for IBBO obtained from a rotation of maximally localized orbitals to ensure a site-diagonal ($t_{ii}^{01} = 0$) hopping Hamiltonian, as described in the text. The number in parenthesis beside each label $t_{ij}^{\alpha\beta}$ indicates the associated contact defined in Fig. 7.26.

	$t_{ij}^{\alpha\beta}(\pi)$ (meV)	β			$t_{ij}^{\alpha\beta}(1)$ (meV)	β	
		0	1			0	1
α	0	+7.7	+182.1	α	0	+29.8	+52.2
	1	+182.1	+127.9		1	+25.2	+35.3

exchange terms to be:

$$\mathcal{J}_{ij}(\pi) = +297.3 \text{ K (FM)} \quad (7.45)$$

$$\mathcal{J}_{ij}(1) = -39.4 \text{ K (AFM)} \quad (7.46)$$

The signs of these terms agree with the anticipated magnetic structure, although the magnitude of $\mathcal{J}_{ij}(\pi)$ is likely overestimated. Nonetheless, the experimental observation of a large positive Weiss constant of $\Theta = +20.9 \text{ K}$ does suggest dominant ferromagnetic interactions.

Anisotropic Magnetic Interactions

The observed anisotropy and spin-canting arise from a combination of long-range magnetic dipolar and spin-orbit anisotropic exchange interactions. For the simple example of a two-sublattice antiferromagnet, the former interaction prefers orientation of a particular local moment along directions of maximum spin density associated with the same sublattice. For the suggested magnetic structure, dipolar interactions can therefore be anticipated to provide an easy b -axis, corresponding to orientation of moments along the π -stacks. Such an orientation, however, is unlikely to lead to a canted moment. As in the case of FBBO, the second order terms in the free energy are restricted by the presence of the mirror plane, which admits only the invariants $\mathbf{l}_x \mathbf{f}_z$ and $\mathbf{l}_z \mathbf{f}_x$. That is, the sublattice magnetization and canted moment must lie in the ac -plane. Indeed, we have explicitly estimated the magnitude of the dipolar interactions, assuming the calculated spin density

of each atom is localized to the atomic position, and find a small dipolar contribution to the anisotropy on the order of ~ 70 Oe. Given that this does not account for the observed anisotropy, we have also estimated the effects of anisotropic exchange interactions in IBBO via the DFT methods. Recall that the anisotropic exchange may be described by the Hamiltonian:¹⁵⁰

$$\mathcal{H}_{anis} = \sum_{i,j} \mathbf{D}_{ij} \cdot \mathbf{S}_i \times \mathbf{S}_j + \mathbf{S}_i \cdot \mathbf{\Gamma}_{ij} \cdot \mathbf{S}_j \quad (7.47)$$

where \mathbf{D}_{ij} is the Dzyaloshinskii-Moriya vector, and $\mathbf{\Gamma}_{ij}$ describes the pseudo-dipolar component of the anisotropic exchange. Due to the presence of the low-lying LUMO with density on the heavy iodine, the multi-orbital FM components of these expressions is expected to produce a significant contribution, and as such must be considered. Accordingly, the anisotropic terms may be decomposed into parts arising from antiferromagnetic interactions between pseudospin moments, described by Moriya's equations,¹⁵⁰ and those arising from ferromagnetic interactions:

$$\mathbf{D}_{ij} = \mathbf{D}_{ij}^{\text{AFM}} + \mathbf{D}_{ij}^{\text{FM}} \quad (7.48)$$

$$\mathbf{D}_{ij}^{\text{AFM}} = \frac{4i}{U} \{t_{ij}^{00} \mathbf{C}_{ji}^{00} - \mathbf{C}_{ij}^{00} t_{ji}^{00}\} \quad (7.49)$$

$$\mathbf{D}_{ij}^{\text{FM}} = -2i \left\{ \mathbf{C}_{ij}^{01} t_{ji}^{10} \frac{Q_j^{01}}{(U + \Delta\epsilon_j^1)^2 - (Q_j^{01})^2} - t_{ij}^{10} \mathbf{C}_{ji}^{01} \frac{Q_i^{01}}{(U + \Delta\epsilon_i^1)^2 - (Q_i^{01})^2} \right\} \quad (7.50)$$

$$\mathbf{\Gamma}_{ij} = \mathbf{\Gamma}_{ij}^{\text{AFM}} + \mathbf{\Gamma}_{ij}^{\text{FM}} \quad (7.51)$$

$$\mathbf{\Gamma}_{ij}^{\text{AFM}} = \frac{4}{U} \{ \mathbf{C}_{ij}^{00} \otimes \mathbf{C}_{ji}^{00} + \mathbf{C}_{ji}^{00} \otimes \mathbf{C}_{ij}^{00} \} \quad (7.52)$$

$$\mathbf{\Gamma}_{ij}^{\text{FM}} = -2 \left\{ \mathbf{C}_{ij}^{01} \otimes \mathbf{C}_{ji}^{10} \frac{Q_j^{01}}{(U + \Delta\epsilon_j^1)^2 - (Q_j^{01})^2} + \mathbf{C}_{ji}^{01} \otimes \mathbf{C}_{ij}^{10} \frac{Q_i^{01}}{(U + \Delta\epsilon_i^1)^2 - (Q_i^{01})^2} \right\} \quad (7.53)$$

The local crystallographic symmetry of each IBBO radical pair places severe restrictions on the form of these interactions. Specifically,

- Due to the fact that nearest neighbours in the same π -stack are related by inversion, $\mathbf{D}_{ij}(\pi) = \mathbf{D}_{ij}^{\text{FM}}(\pi) = \mathbf{D}_{ij}^{\text{AFM}}(\pi) = 0$. To see this, note that the DM-vector transforms

as a pseudo-vector, and is therefore left invariant under inversion, while the sites i, j are interchanged, so that $[\mathcal{H}, \hat{i}] = 0 = 2 \hat{i} \mathbf{D}_{ij} \mathbf{S}_i \times \mathbf{S}_j$ implies $\mathbf{D}_{ij} = 0$, where \hat{i} is the inversion operator.

- Since $\mathbf{\Gamma}_{ij}^{\text{AFM}}(\pi) \propto \mathbf{D}_{ij}^{\text{AFM}}(\pi) = 0$, the AFM contribution to the pseudodipolar interaction also vanishes along the π -stacks.
- For nearest neighbours labelled (1), both molecules lie on the same crystallographic mirror plane, which restricts \mathbf{C}_{ij}^{00} , \mathbf{C}_{ij}^{01} , and \mathbf{C}_{ij}^{10} to be oriented normal to the molecular plane. However, since both $|0_i\rangle$ and $|1_i\rangle$ are π -orbitals, the normal component of all these \mathbf{C}_{ij} terms is required to vanish. As a result, *all* anisotropic interactions $\mathbf{D}_{ij}(1)$ and $\mathbf{\Gamma}_{ij}(1)$ are essentially zero.

In order to emphasize this last point, and in analogy with the discussion of section 6.2.3, we introduce the pseudo-orbital functions $|\eta_i^\mu\rangle$ and $|\kappa_i^\mu\rangle$ associated with the spin-orbit mixing of the SOMO and LUMO, respectively:

$$|\eta_i^\mu\rangle = \frac{1}{2} \sum_{\alpha \neq 0,1} |\alpha_i\rangle \frac{\langle \alpha_i | \mathcal{L}_i^\mu | 0_i \rangle}{\epsilon_\alpha - \epsilon_0} \quad (7.54)$$

$$|\kappa_i^\mu\rangle = \frac{1}{2} \sum_{\alpha \neq 0,1} |\alpha_i\rangle \frac{\langle \alpha_i | \mathcal{L}_i^\mu | 1_i \rangle}{\epsilon_\alpha - \epsilon_0 + U} \quad (7.55)$$

in terms of which, the spin-orbit mediated hopping parameters may be written:

$$[\mathbf{C}_{ij}^{00}]_\mu \equiv t_{ij}^{\eta^{\mu 0}} + t_{ij}^{0\eta^\mu} \quad (7.56)$$

$$[\mathbf{C}_{ij}^{01}]_\mu \equiv t_{ij}^{\eta^{\mu 1}} + t_{ij}^{0\kappa^\mu} \quad (7.57)$$

We introduce the following molecular coordinate system: \hat{z}_i is chosen to be normal to the molecular plane at site i , which in the $Pnma$ cell of IBBO also corresponds with the crystallographic b -axis; the \hat{x}_i and \hat{y}_i directions are along the long and short axis of the molecule, respectively. The pseudo-orbital functions $|\eta_i^\mu\rangle$ and $|\kappa_i^\mu\rangle$ with respect to this coordinate system are shown in Fig. 7.28, as computed at the B3LYP/6-311G(d,p) level. For $\mu = z$, these functions nearly vanish, as explained in section 6.2.3. The SOMO $|0_i\rangle$ and LUMO $|1_i\rangle$ are both π -orbitals, and are antisymmetric with respect to the local mirror

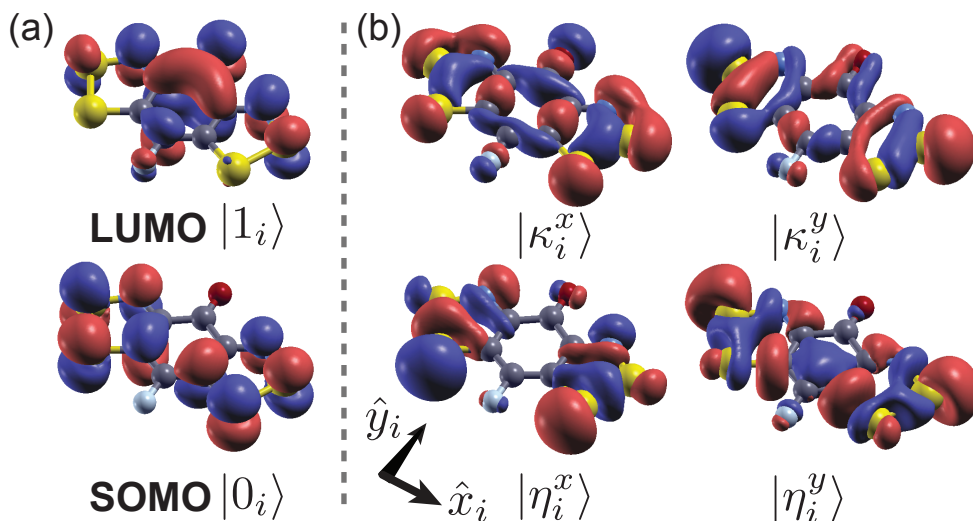


Figure 7.28: (a) SOMO ($\alpha = 0$) and LUMO ($\alpha = +1$) at each radical site i for IBBO computed at the B3LYP/6-311G(d,p) level. (b) Pseudo-orbital functions defined in eq'n (7.54) and eq'n (7.55) to describe SOC hopping parameters \mathbf{C}_{ij} .

plane, while $|\eta_i^\mu\rangle$ and $|\kappa_i^\mu\rangle$ ($\mu = x, y$) are composed of linear combinations of σ -orbitals, and are symmetric with respect to the mirror. For this reason, both \mathbf{C}_{ij}^{00} and \mathbf{C}_{ij}^{01} vanish for pairs of IBBO radicals bisected by the same mirror plane, since $t_{ij}^{0\eta^\mu} = t_{ij}^{1\eta^\mu} = t_{ij}^{0\kappa^\mu} = 0$.

Given the above discussion, and provided the crystallographic symmetry is maintained through the ordering transition, it is clear that the *only* anisotropic exchange interaction allowed by symmetry is the multi-orbital contribution to the pseudodipolar term $\mathbf{\Gamma}_{ij}^{\text{FM}}(\pi)$. We have employed the MOMO method at the B3LYP/6-311G(d,p) level to construct hopping integrals necessary for computing $\mathbf{\Gamma}_{ij}^{\text{FM}}(\pi)$, as discussed in section 2.4.2. The Coulomb parameters were assumed to be those of FBBO. The results indicate that such interactions provide an easy axis for each π -stack that lies in the ac -plane nearly along the short axes of the molecules, making an angle of 16° with the a -axis. The magnitude of this effect is estimated to be $|H_A| \equiv |\text{Tr } \mathbf{\Gamma}_{ij}^{\text{FM}}(\pi)/g\mu_B| = 528$ Oe. In this picture, a canted moment along the c -axis arises due to the misalignment of the local easy axis of the two magnetic sublattices (Fig. 7.29). On the basis of this interaction, and the previously computed isotropic interactions, minimization of the magnetic energy allows us to estimate a canted moment

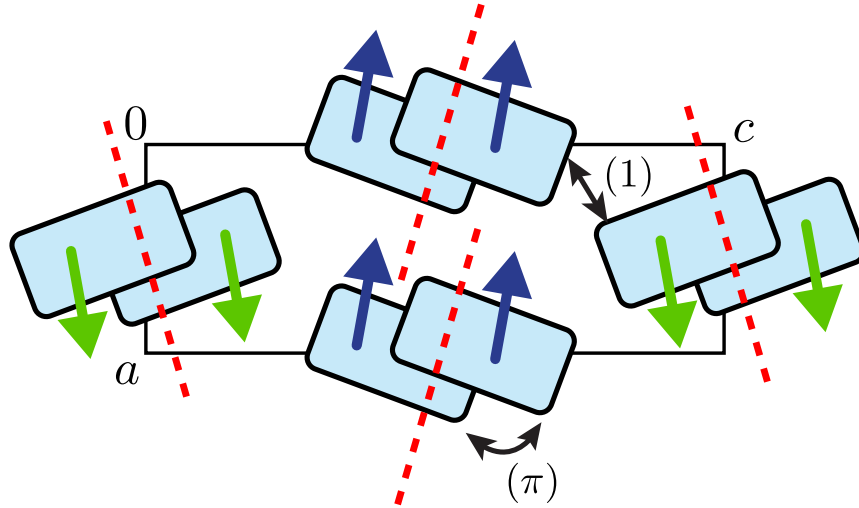


Figure 7.29: Magnetic structure predicted for IBBO-EtCN, emphasizing canting of spins to produce a net moment along the c -direction. Dashed lines indicate the orientation of the local easy-axis associated with each π -stack arising from $\Gamma_{ij}(\pi)$. Canting arises due to the noncollinearity of these local easy axes.

of $0.5 \times 10^{-3} \mu_B$, which is about half of the observed moment. Given the sensitivity of the canting to the orientation of $\Gamma_{ij}(\pi)$, and relative magnitude of $\Gamma_{ij}(\pi)$ and $\mathcal{J}_{ij}(1)$, this agreement between experiment and theory is satisfying. From linear extrapolation of the magnetization as a function of field, we can approximate the exchange field for IBBO to be $H_E = 38$ T, suggesting a spin-flop field of $H_{sf} = \sqrt{2H_E|H_A|} = 2.0$ T,²⁷⁶ based on the computed H_A . Evidence for such a spin-flop can be seen in the derivative of the powder magnetization versus field, which displays a marked peak near $H = 2.1$ T, in complete agreement with the predicted H_{sf} (Fig. 7.30).

On the basis of the above findings, we suggest that multi-orbital anisotropic exchange provides a natural and consistent explanation for the observed anisotropy in IBBO. This is remarkable, because these interactions are not included in Moriya's conventional theory of anisotropic exchange, which serves as the basis for the vast majority of analysis in the literature. Additionally, they rely on the presence of a low-lying LUMO, with strong Hund's coupling to the SOMO, which validates our picture of the electronic structure of these RBBO materials.

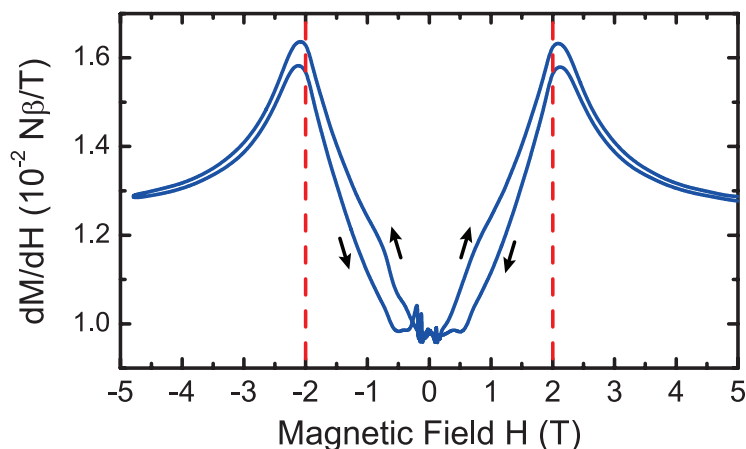


Figure 7.30: dM/dH curves over one hysteresis loop for IBBO showing evidence for a spin-flop transition near 2.1 Tesla. Dashed lines indicate the theoretically predicted spin-flop field $H_{sf} = 2.0$ T.

7.4 Chapter Summary

This final chapter focussed on the recent developments by the Oakley group toward the design of radicals incorporating multiple orbitals in the vicinity of the Fermi energy. The first section focused on our attempts to tune the electronic structure of pyridine-bridged radicals in order to ensure either a low-lying empty LUMO or high-lying filled HOMO. We introduced the asymmetrical hybrid radical family **7-1**, in which variation of the exocyclic R_3 group in principle would allow for modification of the frontier molecular orbital energies. However, evidence from both experiment and state energy calculations suggest that these radicals cannot be tuned to the favourable $\Delta\epsilon \sim t_{ij}^{0\alpha}$ regime. In contrast, the semiquinone bridged radicals **7-2** “RBBO” were shown to have a very low-lying LUMO by virtue of the π -accepting C=O group. This orbital has important consequences for the electronic and magnetic properties of these radicals in the solid state, promoting both ferromagnetic interactions, and charge delocalization. For the case of $R = F$ (FBBO), this last effect allows for a metallic state to be accessed under relatively mild pressure of $P \sim 3$ GPa, which represents the first observation of such a state in S-based neutral radicals. The mechanism for the insulator to metal transition was argued to involve orbital rehybridization, with decreasing effects of correlation introducing more LUMO character into the occupied states.

As this hybridization drives down the kinetic energy of occupied states, it represents an additional effect promoting formation of a metallic state. Charge delocalization is also promoted by strong Hund's coupling between orbitals, which permits double occupation of a given radical site provided triplet polarization of spins. In this way, the presence of the low-lying LUMO is vital for realization of metallic properties in these radicals. Given this understanding, we then described preliminary work on the chemical modification of these radicals through judicious choice of R-group. For the case of the strong π -acceptor $R = \text{NO}_2$, the LUMO is lowered further in energy, and Hund's coupling enhanced, resulting in a highly conductive material with Pauli-like susceptibility, despite crystallization with MeCN solvent, which reduces the dimensionality of the electronic structure. With introduction of the heavy iodine substituent into the R-position, the strength of spin-orbit coupling could also be tuned, bringing together many of the themes of this thesis. For the EtCN solvate of IBBO, we discussed how the magnetic properties could only be understood in the context of multi-orbital anisotropic exchange interactions, which go beyond Moriya's conventional description. Taken together, these results demonstrate a rich variety of physics in this class of multi-band neutral radical materials, which spans from magnetic to metallic states. Given that the RBBO materials were first reported only three years before the writing of this thesis, and represent a small fraction of potential multi-band radicals, much of this physics remains to be explored.

APPENDICES

Appendix A

Mathematical Details

A.1 Details for BW Perturbation Section

A.1.1 Operator Perturbation Theory

Renormalization to produce \mathcal{H}_{eff} may be systematically accomplished through the use of Brillouin-Wigner (B-W) perturbation theory. Following the notation of the previous section, the “Green operator” which is the resolvent operator for the full Hamiltonian $\mathcal{H} = \mathcal{H}_0 + \lambda\mathcal{H}_1$ is defined as¹:

$$\mathcal{G}^\lambda(\omega) = (\omega - \mathcal{H})^{-1} = \sum_n \frac{|\Phi_n^\lambda\rangle\langle\Phi_n^\lambda|}{\omega - E_n^\lambda} \quad (\text{A.1})$$

Following the adiabatic concept, we relabel the states according to the associated states at $\lambda = 0$. The desired effective Hamiltonian $\mathcal{H}_{\text{eff}}^\lambda$ also has a Green operator, which satisfies the equation:

$$\mathcal{G}_{\text{eff}}^\lambda(\omega) = (\omega - \mathcal{H}_{\text{eff}}^\lambda)^{-1} = \sum_{n < \Lambda} \frac{|\Phi_n^0\rangle\langle\Phi_n^0|}{\omega - E_n^\lambda} = \mathbb{P}_L^0 \mathcal{G}^\lambda(\omega) \mathbb{P}_L^0 \quad (\text{A.2})$$

¹Note that the Green operator may be expanded in any complete basis of states for \mathcal{H} , so that $\mathcal{G}(\omega) = \sum_{n,m} |\phi_n\rangle\langle\phi_n|(\omega - \mathcal{H})^{-1}|\phi_m\rangle\langle\phi_m|$. A particularly useful choice is to expand in the eigenstates, for which of course $\langle\Phi_n|\mathcal{H}|\Phi_m\rangle = E_n\delta_{n,m}$.

Note that the exact energies E_n^λ appear in the denominator, but the numerator contains the zeroth order states. We introduce the projection operator into the upper high energy subspace:

$$\mathbb{P}_U^0 = 1 - \mathbb{P}_L^0 = \begin{cases} 0 & \text{if state is in lower Hilbert space} \\ 1 & \text{otherwise} \end{cases} \quad (\text{A.3})$$

In terms of this projection operator, the full Hamiltonian may be recast in matrix form:³³²

$$\omega - \mathcal{H} = \left(\begin{array}{c|c} \mathbb{P}_L^0(\omega - \mathcal{H})\mathbb{P}_L^0 & -\mathbb{P}_L^0\mathcal{H}\mathbb{P}_U^0 \\ \hline -\mathbb{P}_U^0\mathcal{H}\mathbb{P}_L^0 & \mathbb{P}_U^0(\omega - \mathcal{H})\mathbb{P}_U^0 \end{array} \right) \equiv \left(\begin{array}{c|c} \mathbf{A} & \mathbf{B} \\ \hline \mathbf{C} & \mathbf{D} \end{array} \right) \quad (\text{A.4})$$

with each entry in the matrix representing a block that acts only on states in either the lower or upper Hilbert space. On this basis, it is easy to see that the full Green operator in matrix form is given by the general equation for the block inverse of a matrix:

$$\mathcal{G}^\lambda(\omega) = (\omega - \mathcal{H})^{-1} = \left(\begin{array}{c|c} (\mathbf{A} - \mathbf{B}\mathbf{D}^{-1}\mathbf{C})^{-1} & -\mathbf{A}^{-1}\mathbf{B}(\mathbf{D} - \mathbf{C}\mathbf{A}^{-1}\mathbf{B})^{-1} \\ \hline -\mathbf{D}^{-1}\mathbf{C}(\mathbf{A} - \mathbf{B}\mathbf{D}^{-1}\mathbf{C})^{-1} & (\mathbf{D} - \mathbf{C}\mathbf{A}^{-1}\mathbf{B})^{-1} \end{array} \right) \quad (\text{A.5})$$

So that $\mathcal{G}_{\text{eff}}^\lambda(\omega)$ is given by the upper left quadrant, which reads:

$$\omega - \mathcal{H}_{\text{eff}}^\lambda = \mathbf{A} - \mathbf{B}\mathbf{D}^{-1}\mathbf{C} \quad (\text{A.6})$$

which after some algebra yields:

$$\boxed{\mathcal{H}_{\text{eff}}(\omega) = \mathbb{P}_L^0 \mathcal{H}_0 \mathbb{P}_L^0 + \sum_{n=0}^{\infty} \mathbb{P}_L^0 \mathcal{H}_1 [\mathbb{P}_U^0 (\omega - \mathcal{H}_0)^{-1} \mathbb{P}_U^0 \mathcal{H}_1]^n \mathbb{P}_L^0} \quad (\text{A.7})$$

Finally, it is worthwhile to note that eq'n (A.7) may be written in terms of the zeroth order Green operator for the higher energy subspace, denoted $\mathcal{G}_U^0(\omega)$:

$$\mathcal{H}_{\text{eff}}(\omega) = \mathbb{P}_L^0 \left\{ \mathcal{H}_0 + \sum_{n=0}^{\infty} \mathcal{H}_1 [\mathcal{G}_U^0(\omega) \mathcal{H}_1]^n \right\} \mathbb{P}_L^0 \quad (\text{A.8})$$

which proves to be a useful form for later discussions.

A.1.2 Representations of Spin Operators

Recall the use of spinor electron operators:

$$\mathbf{c}_{i,\alpha}^\dagger = \begin{pmatrix} c_{i,\alpha,\uparrow}^\dagger & c_{i,\alpha,\downarrow}^\dagger \end{pmatrix}, \quad \mathbf{c}_{i,\alpha} = \begin{pmatrix} c_{i,\alpha,\uparrow} \\ c_{i,\alpha,\downarrow} \end{pmatrix} \quad (\text{A.9})$$

A significant advantage of such operators is that spin operators in this notation are represented in terms of the Pauli matrices:

$$\boxed{2 \mathbf{S}_{i,\alpha} = \mathbf{c}_{i,\alpha}^\dagger \vec{\sigma} \mathbf{c}_{i,\alpha}} \quad (\text{A.10})$$

where $\vec{\sigma} = \sigma_x \hat{i} + \sigma_y \hat{j} + \sigma_z \hat{k}$ is the Pauli vector. For example, the z-component of the spin at site j , in orbital α is given by:

$$S_{j,\alpha}^z = \frac{1}{2} \mathbf{c}_{j,\alpha}^\dagger \sigma_z \mathbf{c}_{j,\alpha} = \frac{1}{2} \begin{pmatrix} c_{j,\alpha,\uparrow}^\dagger & c_{j,\alpha,\downarrow}^\dagger \end{pmatrix} \begin{pmatrix} 1 & 0 \\ 0 & -1 \end{pmatrix} \begin{pmatrix} c_{j,\alpha,\uparrow} \\ c_{j,\alpha,\downarrow} \end{pmatrix} = \frac{1}{2} (n_{j,\alpha,\uparrow} - n_{j,\alpha,\downarrow}) \quad (\text{A.11})$$

A.1.3 Properties of Pauli Matrices

Along with the 2×2 identity matrix, \mathbb{I} , the Pauli matrices form a complete basis for 2×2 matrices. These matrices are given by:

$$\mathbb{I} = \begin{pmatrix} 1 & 0 \\ 0 & 1 \end{pmatrix} \quad \sigma_x = \begin{pmatrix} 0 & 1 \\ 1 & 0 \end{pmatrix} \quad \sigma_y = \begin{pmatrix} 0 & -i \\ i & 0 \end{pmatrix} \quad \sigma_z = \begin{pmatrix} 1 & 0 \\ 0 & -1 \end{pmatrix} \quad (\text{A.12})$$

The product rule for the Pauli matrices is:

$$\sigma_a \sigma_b = \delta_{ab} \cdot \mathbb{I} + i \sum_c \epsilon_{abc} \sigma_c \quad (\text{A.13})$$

where ϵ_{abc} is the Levi-Civita symbol, which has the definition:

$$\epsilon_{abc} = \begin{cases} +1 & \text{if } (a, b, c) = \{(x, y, z), (y, z, x), (z, x, y)\} \\ -1 & \text{if } (a, b, c) = \{(x, z, y), (y, x, z), (z, y, x)\} \\ 0 & \text{if } a = b \text{ or } b = c \text{ or } a = c \end{cases} \quad (\text{A.14})$$

Some particularly particularly useful identities that follow from these properties relates the dot product of Pauli matrices to a cross product:

$$(\mathbf{A} \cdot \vec{\sigma})(\mathbf{B} \cdot \vec{\sigma}) = \mathbf{A} \cdot \mathbf{B} + i(\mathbf{A} \times \mathbf{B}) \cdot \vec{\sigma} \quad (\text{A.15})$$

$$\begin{aligned} (\mathbf{A} \cdot \vec{\sigma})(\mathbf{B} \cdot \vec{\sigma})(\mathbf{C} \cdot \vec{\sigma}) &= (\mathbf{A} \cdot \mathbf{B})(\mathbf{C} \cdot \vec{\sigma}) + (\mathbf{B} \cdot \mathbf{C})(\mathbf{A} \cdot \vec{\sigma}) \\ &\quad - (\mathbf{A} \cdot \mathbf{C})(\mathbf{B} \cdot \vec{\sigma}) + i(\mathbf{A} \times \mathbf{B}) \cdot \mathbf{C} \end{aligned} \quad (\text{A.16})$$

These can be exploited in order to simplify resulting spin Hamiltonians.

A.1.4 Expansion of Operator Products

Since the Pauli matrices and identity matrix form a complete basis, they may also be used for expansion of operator products such as $\mathbf{c}\mathbf{c}^\dagger$, which can be written as a 2×2 matrix as follows:

$$\mathbf{c}\mathbf{c}^\dagger = \begin{pmatrix} c_\uparrow \\ c_\downarrow \end{pmatrix} \begin{pmatrix} c_\uparrow^\dagger & c_\downarrow^\dagger \end{pmatrix} = \begin{pmatrix} c_\uparrow c_\uparrow^\dagger & c_\uparrow c_\downarrow^\dagger \\ c_\downarrow c_\uparrow^\dagger & c_\downarrow c_\downarrow^\dagger \end{pmatrix} = \begin{pmatrix} 1 - c_\uparrow^\dagger c_\uparrow & -c_\downarrow^\dagger c_\uparrow \\ -c_\uparrow^\dagger c_\downarrow & 1 - c_\downarrow^\dagger c_\downarrow \end{pmatrix} \quad (\text{A.17})$$

It is straightforward to show that:

$$\boxed{\mathbf{c}_{i,\alpha} \mathbf{c}_{i,\alpha}^\dagger = \left\{ 1 - \frac{1}{2} \mathbf{c}_{i,\alpha}^\dagger \mathbf{c}_{i,\alpha} \right\} \mathbb{I} - \mathbf{S}_{i,\alpha} \cdot \vec{\sigma}} \quad (\text{A.18})$$

Given the above projection operator, this combination evaluates to:

$$\mathbb{P}_L^0 \mathbf{c}_{i,\alpha} \mathbf{c}_{i,\alpha}^\dagger \mathbb{P}_L^0 = \begin{cases} 0 & \alpha < 0 \\ \frac{1}{2} \mathbb{I} - \mathbf{S}_{i,\alpha} \cdot \vec{\sigma} & \alpha = 0 \\ \mathbb{I} & \alpha > 0 \end{cases} \quad (\text{A.19})$$

A.1.5 Commutation Relations in Spinor Form

The following commutation relations will be occasionally useful:

$$\left[\mathbf{c}_1^\dagger \mathbf{c}_2, \mathbf{c}_3 \right] = -\delta_{1,3} \mathbf{c}_2 \quad (\text{A.20})$$

$$\left[\mathbf{c}_1^\dagger, \mathbf{c}_2^\dagger \mathbf{c}_3 \right] = -\delta_{1,3} \mathbf{c}_2^\dagger \quad (\text{A.21})$$

$$\left[\mathbf{c}_1^\dagger \mathbf{c}_2, \mathbf{c}_3^\dagger \mathbf{c}_4 \right] = \delta_{2,3} \mathbf{c}_1^\dagger \mathbf{c}_4 - \delta_{1,4} \mathbf{c}_3^\dagger \mathbf{c}_2 \quad (\text{A.22})$$

Appendix B

Green Functions Review

In this section, we review the Green function method in the context of computing properties of solid state systems. We refer the interested reader to the many adequate texts that treat this subject in greater detail, such as Refs 188, and 189.

B.1 Zero Temperature Correlation Functions

Description of solid state systems is significantly complicated by the presence of many degrees of freedom, making it essentially impossible to obtain the exact wave function for the general case, or even to compute properties given a wave function of $\sim 10^{23}$ coordinates. It is therefore very useful to have techniques that allow for estimation of properties that does not require direct knowledge of the eigenstates of the system. One such technique is the Green function method, which we now briefly review. Consider an experiment in which the sample is perturbed by a weak time dependent external field so that:

$$\mathcal{H}_{\text{tot}} = \mathcal{H} + \mathcal{H}' \tag{B.1}$$

$$\mathcal{H}' = \hat{O}_1(t) f(t) \tag{B.2}$$

where $f(t)$ is a time dependent field, and $\hat{O}_1(t)$ represents an operator acting at time t . An example would be a magnetic experiment, in which an external magnetic field couples to

the system through the Zeeman interaction $\mathcal{H}' = g\mu_B \mathbf{S}(t) \cdot \mathbf{H}(t)$; here \hat{O}_1 is a spin operator and $f(t)$ is the external magnetic field. Now, suppose we make a measurement with respect to a second operator at a later time; the expectation value of this measurement is given in linear response theory by the Kubo formula:

$$\langle \hat{O}_2(t') \rangle = \langle \hat{O}_2(t') \rangle_0 + \int_{-\infty}^{t'} \chi(t' - t) f(t) dt \quad (\text{B.3})$$

$$\chi(t' - t) = -\frac{i}{\hbar} \Theta(t' - t) \left\langle [\hat{O}_2(t'), \hat{O}_1(t)]_{\pm} \right\rangle_0 \quad (\text{B.4})$$

where $\langle \dots \rangle_0$ denotes an average with respect to the ground state of \mathcal{H} . The commutator $[\hat{A}, \hat{B}]_{\pm} = \hat{A}\hat{B} \pm \hat{B}\hat{A}$ takes a “+” sign if \hat{A}, \hat{B} are fermionic operators, and a “−” sign for bosonic operators. The function $\chi(t' - t)$ is a generalized susceptibility or retarded correlation function. More commonly, an experiment will measure the frequency dependence of this quantity, which is obtained by Fourier transform:

$$\chi(\omega) = \int_{-\infty}^{\infty} d(t' - t) e^{-i\omega(t' - t)} \chi(t' - t) \quad (\text{B.5})$$

This quantity may be rewritten in a useful form by noting that the time dependence of an operator in the Heisenberg representation is given by:

$$\hat{O}(t) = e^{i\mathcal{H}t/\hbar} \hat{O} e^{-i\mathcal{H}t/\hbar} \quad (\text{B.6})$$

Identifying the ground state energy as E_0 , the susceptibility may be rewritten:

$$\chi(\omega) = \left\langle \hat{O}_2 \hat{\mathcal{G}}_{>}(\omega) \hat{O}_1 \pm \hat{O}_1 \hat{\mathcal{G}}_{<}(\omega) \hat{O}_2 \right\rangle_0 \quad (\text{B.7})$$

where the Green operators $\hat{\mathcal{G}}_{>}(\omega)$ and $\hat{\mathcal{G}}_{<}(\omega)$ are given by:

$$\hat{\mathcal{G}}_{>}(\omega) = -\frac{i}{\hbar} \int_{-\infty}^{\infty} dt \Theta(t) e^{i(\mathcal{H} - E_0 - \hbar\omega)t/\hbar} = \lim_{\eta \rightarrow 0^+} \frac{1}{\hbar\omega + E_0 - \mathcal{H} + i\eta} \quad (\text{B.8})$$

$$\hat{\mathcal{G}}_{<}(\omega) = -\frac{i}{\hbar} \int_{-\infty}^{\infty} dt \Theta(t) e^{-i(\mathcal{H} - E_0 + \hbar\omega)t/\hbar} = \lim_{\eta \rightarrow 0^+} \frac{1}{\hbar\omega + \mathcal{H} - E_0 + i\eta} \quad (\text{B.9})$$

and the Sokhotski–Plemelj formula has been used to achieve the final result. The first term $\hat{\mathcal{G}}_{>}(\omega)$ resembles the resolvent operator of section A.1.1, and represents absorption

of energy from the field to excite the system into a higher energy state. The second term $\hat{\mathcal{G}}_{<}(\omega)$ represents stimulated relaxation of the system from a high lying state to lower energy. These Green operators satisfy the properties of resolvents discussed in section A.1.1. The utility of the Green operator formulation is that the susceptibility may be obtained if the Green operator is expanded in *any* basis, allowing properties to be computed without knowledge of the actual eigenstates of the system. It is convenient to choose a basis that is both conceptually simple, and for which the operators \hat{O} are trivially evaluated. In the next section, we discuss a particularly useful correlation function, which may be related to many physical observables such as the density of states, and conductivity.

B.2 Two-Point Green Functions and Spectral Theory

Consider the following hypothetical experiment: We drop an electron into our system at a position \mathbf{x} , and ask what is the probability of extracting that electron at another position \mathbf{x}' , at a time t later. This function, we denote:

$$G^R(\mathbf{x}' - \mathbf{x}, \sigma, t) = -\frac{i}{\hbar} \Theta(t) \langle [c_{\mathbf{x}',\sigma}(t), c_{\mathbf{x},\sigma}^\dagger(0)]_+ \rangle_0 \quad (\text{B.10})$$

where $\Theta(t)$ is a step function ensuring the logical constraint $t > 0$. This function already tells us a great deal about the electronic structure of the material; if the added electron is delocalized as in a metal, then its wavefunction will tend to spread out over time, and there will be an increasing probability of finding the electron away from its initial position. For reasons that will become clear, it is convenient to discuss the momentum space equivalent of this function. Consider, then, the following related experiment: we connect the system to a featureless bath of electrons that may exchange an electron of a particular crystal momentum and orbital index with those in the system. This may be accounted for by choosing:

$$\hat{O}_1(\alpha, \mathbf{k}) = c_{\alpha, \mathbf{k}, \sigma}^\dagger \quad , \quad \hat{O}_2(\alpha, \mathbf{k}, \sigma) = c_{\alpha, \mathbf{k}, \sigma} \quad (\text{B.11})$$

where $c_{\alpha, \mathbf{k}, \sigma}^\dagger$ creates an electron with spin σ in the Bloch state defined by:

$$|\alpha, \mathbf{k}\rangle = \sum_i e^{i\mathbf{k}\cdot\mathbf{r}_i} |\alpha, i\rangle \quad (\text{B.12})$$

Such a hypothetical experiment allows us to probe the states of the system obtained by injection or removal of a single electron. The correlation function associated with this experiment is called the two-point or single particle retarded Green function:

$$G^R(\alpha, \mathbf{k}, \sigma, t) = -\frac{i}{\hbar} \Theta(t) \left\langle [c_{\alpha, \mathbf{k}, \sigma}(t), c_{\alpha, \mathbf{k}, \sigma}^\dagger(0)]_+ \right\rangle_0 \quad (\text{B.13})$$

which literally gives the probability that an electron added to $|\alpha, \mathbf{k}\rangle$ with spin σ may be removed from the same state at a time t later. The fourier transform of this function is:

$$G^R(\alpha, \mathbf{k}, \sigma, \omega) = \left\langle c_{\alpha, \mathbf{k}, \sigma} \hat{\mathcal{G}}_>(\omega) c_{\alpha, \mathbf{k}, \sigma}^\dagger + c_{\alpha, \mathbf{k}, \sigma}^\dagger \hat{\mathcal{G}}_<(\omega) c_{\alpha, \mathbf{k}, \sigma} \right\rangle_0 \quad (\text{B.14})$$

$$= \lim_{\eta \rightarrow 0^+} \left\langle c_{\alpha, \mathbf{k}, \sigma} \frac{1}{\hbar\omega + E_0 - \mathcal{H} + i\eta} c_{\alpha, \mathbf{k}, \sigma}^\dagger + c_{\alpha, \mathbf{k}, \sigma}^\dagger \frac{1}{\hbar\omega + \mathcal{H} - E_0 + i\eta} c_{\alpha, \mathbf{k}, \sigma} \right\rangle_0 \quad (\text{B.15})$$

which measures the ‘‘susceptibility’’ for the addition or removal of an electron in a particular Bloch state and a particular energy $\hbar\omega$. Suppose we divide the Hamiltonian of the system $\mathcal{H} = \mathcal{H}_0 + \mathcal{H}_1$ as follows:

$$\mathcal{H}_0 = \mathcal{E} + \mathcal{T} \quad \text{‘‘Kinetic Energy Terms’’} \quad (\text{B.16})$$

$$\mathcal{H}_1 = \mathcal{U} \quad \text{‘‘Coulomb Energy Terms’’} \quad (\text{B.17})$$

In the basis of Bloch states, these can be written:

$$\mathcal{H}_0 = \sum_{\alpha, \sigma} \int_{\mathbf{k}} (\epsilon_{\alpha, \mathbf{k}} - \mu) c_{\alpha, \mathbf{k}, \sigma}^\dagger c_{\alpha, \mathbf{k}, \sigma} \quad (\text{B.18})$$

$$\mathcal{H}_1 = \sum_{\sigma_1, \sigma_2} \sum_{\alpha, \beta} \int_{\mathbf{k}_1, \mathbf{k}_2, \mathbf{k}_3, \mathbf{k}_4} U_{\alpha, \beta} c_{\beta, \mathbf{k}_4, \sigma_1}^\dagger c_{\alpha, \mathbf{k}_3, \sigma_2}^\dagger c_{\alpha, \mathbf{k}_2, \sigma_2} c_{\beta, \mathbf{k}_1, \sigma_1} \delta(\mathbf{k}_1 + \mathbf{k}_2 - \mathbf{k}_3 - \mathbf{k}_4) \quad (\text{B.19})$$

where the dispersion of Bloch states is described by $\epsilon_{\alpha, \mathbf{k}}$, the chemical potential is μ , and $U_{\alpha, \beta}$ gives the repulsion between electrons occupying α, β orbitals. Conventional band theory is recovered by in the absence of Coulomb terms \mathcal{H}_1 , in which case the many-electron eigenstates are single determinants specified the occupancy of the various one-electron Bloch states. The ground state at zero temperature is obtained by filling all such states below the chemical potential, which results in N electrons in the system. Schematically, the n th eigenstate with N electrons in this non-interacting limit are:

$$|\Psi_N^n\rangle_0 = c_{\alpha_1, \mathbf{k}_1, \sigma_1}^\dagger c_{\alpha_2, \mathbf{k}_2, \sigma_2}^\dagger \dots c_{\alpha_N, \mathbf{k}_N, \sigma_N}^\dagger |\text{Vac}\rangle \quad (\text{B.20})$$

where $|\text{Vac}\rangle$ is the vacuum state containing no electrons. The action of the Coulomb terms \mathcal{H}_1 is to scatter pairs of electrons into new Bloch states, so that the exact many-electron wave functions in the presence of Coulomb repulsion are generally not representable as single determinants, and instead are:

$$|\Psi_N^n\rangle = \sum_m a_{n,m} |\Psi_N^m\rangle_0 \quad (\text{B.21})$$

We will discuss two useful representations of the two-point Green function $G^R(\alpha, \mathbf{k}, \sigma, \omega)$, which may be obtained by expanding the Green operator in each of these bases. Consider expansion in the exact eigenstates of the $N + 1$ or $N - 1$ electron system:

$$\begin{aligned} G^R(\alpha, \mathbf{k}, \sigma, \omega) = \lim_{\eta \rightarrow 0^+} \sum_n & \frac{\langle \Psi_N^0 | c_{\alpha, \mathbf{k}, \sigma} | \Psi_{N+1}^n \rangle \langle \Psi_{N+1}^n | c_{\alpha, \mathbf{k}, \sigma}^\dagger | \Psi_N^0 \rangle}{\hbar\omega + E_N^0 - E_{N+1}^n + i\eta} \\ & + \frac{\langle \Psi_N^0 | c_{\alpha, \mathbf{k}, \sigma}^\dagger | \Psi_{N-1}^n \rangle \langle \Psi_{N-1}^n | c_{\alpha, \mathbf{k}, \sigma} | \Psi_N^0 \rangle}{\hbar\omega + E_{N-1}^n - E_N^0 + i\eta} \end{aligned} \quad (\text{B.22})$$

This may be rewritten:

$$G^R(\alpha, \mathbf{k}, \sigma, \omega) = \lim_{\eta \rightarrow 0^+} \frac{1}{2\pi} \int_{-\infty}^{\infty} \frac{A(\alpha, \mathbf{k}, \sigma, \nu)}{\hbar\omega - \hbar\nu + i\eta} d\nu \quad (\text{B.23})$$

where the spectral function is related to the imaginary part of the Green function:

$$A(\alpha, \mathbf{k}, \sigma, \nu) = -\text{Im} [G^R(\alpha, \mathbf{k}, \sigma, \nu)] \quad (\text{B.24})$$

$$\begin{aligned} = 2\pi \sum_n & \left\{ |\langle \Psi_{N+1}^n | c_{\alpha, \mathbf{k}, \sigma}^\dagger | \Psi_N^0 \rangle|^2 \delta(E_N^0 - E_{N+1}^n - \hbar\nu) \right. \\ & \left. + |\langle \Psi_{N-1}^n | c_{\alpha, \mathbf{k}, \sigma} | \Psi_N^0 \rangle|^2 \delta(E_{N-1}^n - E_N^0 - \hbar\nu) \right\} \end{aligned} \quad (\text{B.25})$$

which gives the overlap between the states obtained by injection of an electron or hole into a particular Bloch state with the exact eigenstates of the $N + 1$ or $N - 1$ electron system at a particular energy $\hbar\nu$. To understand the meaning of the spectral function, consider once again the non-interacting case where \mathcal{H}_1 is neglected. If we attempt to inject an electron or hole into the Bloch state $|\alpha, \mathbf{k}\rangle$, the new state with $N + 1$ or $N - 1$ electrons, respectively, will be an exact eigenstate of the system with an energy difference of precisely $\hbar\nu = \epsilon_{\alpha, \mathbf{k}}$.

In this case, the spectral function is a delta function:

$$A_0(\alpha, \mathbf{k}, \sigma, \nu) = 2\pi \delta(\epsilon_{\alpha, \mathbf{k}} + \mu - \hbar\nu) \quad (\text{B.26})$$

$$G_0^R(\alpha, \mathbf{k}, \sigma, \omega) = \lim_{\eta \rightarrow 0^+} \frac{1}{\hbar\omega + \mu - \epsilon_{\alpha, \mathbf{k}} + i\eta} \quad (\text{B.27})$$

Integration of the spectral function over the Brillouin zone in this case gives simply the one-electron density of states:

$$D_0(\alpha, \sigma, \nu) = \int_{\mathbf{k}} A_0(\alpha, \mathbf{k}, \sigma, \nu) \quad (\text{B.28})$$

In the time domain, the Green function is:

$$G_0^R(\alpha, \mathbf{k}, \sigma, t > 0) = e^{i(\epsilon_{\alpha, \mathbf{k}} - \mu)t/\hbar} \quad (\text{B.29})$$

which is just the relative quantum mechanical phase accrued over a time t between the zeroth order ground state $|\Psi_N^0\rangle_0$ and the (typically higher) energy state with an injected electron or hole, $c_{\alpha, \mathbf{k}, \sigma}^\dagger |\Psi_N^0\rangle_0$ or $c_{\alpha, \mathbf{k}, \sigma} |\Psi_N^0\rangle_0$. There is a perfect probability that the injected particle remains in the same Bloch state, indicated by $|G_0^R(t > 0)| = 1$, as there is no scattering mechanism in the absence of Coulomb repulsion. As we turn on the Coulomb terms \mathcal{H}_1 , the states $c_{\alpha, \mathbf{k}, \sigma}^\dagger |\Psi_N^0\rangle$ and $c_{\alpha, \mathbf{k}, \sigma} |\Psi_N^0\rangle$ will generally not be eigenstates, but rather will overlap with multiple eigenstates of differing energies in the $N + 1$ or $N - 1$ subspace. The spectral density will thus not be a delta function, but rather will be spread across these energies. We may still build a picture of $\{|\Psi_{N+1}^n\rangle, |\Psi_{N-1}^n\rangle\}$ in terms of single-particle states by expanding the Green operators $\hat{\mathcal{G}}_>(\omega)$ and $\hat{\mathcal{G}}_<(\omega)$ in the suitably normalized basis states $c_{\alpha, \mathbf{k}, \sigma}^\dagger |\Psi_N^0\rangle$ and $c_{\alpha, \mathbf{k}, \sigma} |\Psi_N^0\rangle$, respectively. However, this basis is incomplete, because it does not allow us to fully represent the states obtained by scattering of the added electron or hole with the other particles in the system. We know from the discussion of section A.1.1 that the Green operator in an incomplete basis may be written:

$$\hat{\mathcal{G}}_I(\omega) = \mathbb{P}_I^0 \frac{1}{[\hat{\mathcal{G}}_I^0(\omega)]^{-1} - \hat{\Sigma}(\omega)} \mathbb{P}_I^0 \quad (\text{B.30})$$

$$\hat{\Sigma}(\omega) = \mathcal{H}_1 \mathbb{P}_O^0 \hat{\mathcal{G}}_O(\omega) \mathbb{P}_O^0 \mathcal{H}_1 \quad (\text{B.31})$$

where subscript I refers to the inner subspace described above, and subscript O refers to the outer subspace that contains all other states that do not differ from $|\Psi_N^0\rangle$ by simple addition of an electron or hole. Defining the retarded self-energy function as:

$$\Sigma^R(\alpha, \mathbf{k}, \sigma, \omega) = \text{Re} \left[\langle \hat{\Sigma}(\omega) \rangle \right] + i \text{sgn}(\hbar\omega - \mu) \text{Im} \left[\langle \hat{\Sigma}(\omega) \rangle \right] \quad (\text{B.32})$$

$$\langle \hat{\Sigma}(\omega) \rangle = \langle \Psi_N^0 | c_{\alpha, \mathbf{k}, \sigma} \hat{\Sigma}(\omega) c_{\alpha, \mathbf{k}, \sigma}^\dagger | \Psi_N^0 \rangle \quad (\text{B.33})$$

The two-point retarded Green function may be written:

$$G^R(\alpha, \mathbf{k}, \sigma, \omega) = \frac{1}{\hbar\omega + \mu - \epsilon_{\alpha, \mathbf{k}} - \Sigma^R(\alpha, \mathbf{k}, \sigma, \omega)} \quad (\text{B.34})$$

The meaning of the self-energy may be seen from considering the Green function in the time domain:

$$G_0^R(\alpha, \mathbf{k}, \sigma, t > 0) = e^{i(\epsilon_{\alpha, \mathbf{k}} + \text{Re}[\Sigma^R(\alpha, \mathbf{k}, \sigma, \nu)] - \mu)t/\hbar} e^{-\text{Im}[\Sigma^R(\alpha, \mathbf{k}, \sigma, \nu)]t/\hbar} \quad (\text{B.35})$$

From this form, one can see that the real part of the self energy $\text{Re}[\Sigma^R(\alpha, \mathbf{k}, \sigma, \nu)]$ describes the shifting of the energies of one-electron states by the Coulomb interactions, and appears only in the relative phase. The probability that the injected particle remains in the Bloch state of choice is no longer unity, but rather exponentially decays $|G_0^R(t > 0)| = e^{-\text{Im}[\Sigma]t/\hbar}$ with a characteristic lifetime related to the imaginary part of the self-energy. The associated spectral function is:

$$A(\alpha, \mathbf{k}, \sigma, \nu) = \frac{-\text{Im}[\Sigma^R(\alpha, \mathbf{k}, \sigma, \nu)]}{(\hbar\nu + \mu - \epsilon_{\alpha, \mathbf{k}} - \text{Re}[\Sigma^R(\alpha, \mathbf{k}, \sigma, \nu)])^2 + \text{Im}[\Sigma^R(\alpha, \mathbf{k}, \sigma, \nu)]^2} \quad (\text{B.36})$$

From which one can obtain the density of states in the $N + 1$ and $N - 1$ electron subspace exactly as in the non-interacting limit:

$$D(\alpha, \sigma, \nu) = \int_{\mathbf{k}} A(\alpha, \mathbf{k}, \sigma, \nu) \quad (\text{B.37})$$

From these expressions, it is easy to see that the spectrum of states in the many-electron case can be obtained with knowledge of the Bloch dispersion $\epsilon_{\alpha, \mathbf{k}}$ which is usually trivially computed, and the self energy $\Sigma^R(\alpha, \mathbf{k}, \sigma, \nu)$, which is generally difficult to compute exactly. There are many approximate perturbative schemes, but these methods are generally

inappropriate for studying materials in the vicinity of the Mott transition, because they rely on expansion in $U/t \sim 1$, and are thus weakly convergent. In this light, it is very useful to have an approximate but *nonperturbative* method for calculation of the self-energy. The method employed in this thesis is the Dynamical Mean Field Approach described in Chapter 3.

B.3 Finite Temperature Formalism

We define the finite temperature Green function to be a thermodynamic average:

$$G^R(\alpha, \mathbf{k}, \sigma, t) = -\frac{i}{\hbar} \Theta(t) \left\langle [c_{\alpha, \mathbf{k}, \sigma}(t), c_{\alpha, \mathbf{k}, \sigma}^\dagger(0)]_+ \right\rangle_\beta \quad (\text{B.38})$$

$$= -\frac{i}{\hbar} \frac{1}{\mathbb{Z}} \text{Tr} \left\{ e^{-\beta \mathcal{H}} [c_{\alpha, \mathbf{k}, \sigma}(t), c_{\alpha, \mathbf{k}, \sigma}^\dagger(0)]_+ \right\} \quad (\text{B.39})$$

where \mathbb{Z} is the partition function. The Fourier transform of this quantity is:

$$G^R(\alpha, \mathbf{k}, \sigma, \omega) = \lim_{\eta \rightarrow 0^+} \sum_{n, m} e^{-\beta E_N^m} \left\{ \frac{\langle \Psi_N^m | c_{\alpha, \mathbf{k}, \sigma} | \Psi_{N+1}^n \rangle \langle \Psi_{N+1}^n | c_{\alpha, \mathbf{k}, \sigma}^\dagger | \Psi_N^m \rangle}{\hbar \omega + E_N^m - E_{N+1}^n + i\eta} \right. \quad (\text{B.40})$$

$$\left. + \frac{\langle \Psi_N^m | c_{\alpha, \mathbf{k}, \sigma}^\dagger | \Psi_{N-1}^n \rangle \langle \Psi_{N-1}^n | c_{\alpha, \mathbf{k}, \sigma} | \Psi_N^m \rangle}{\hbar \omega + E_{N-1}^n - E_N^m + i\eta} \right\}$$

which is particularly inconvenient to directly compute. An alternate approach is the so-called Matsubara imaginary time formalism. We introduce the Matsubara Green function:

$$G^M(\alpha, \mathbf{k}, \sigma, \tau) = \left\langle T_\tau (c_{\alpha, \mathbf{k}, \sigma}(\tau) c_{\alpha, \mathbf{k}, \sigma}^\dagger(0)) \right\rangle_\beta \quad (\text{B.41})$$

where T_τ denotes time ordering with respect to the imaginary time variable $\tau = it$, which is defined over the interval $-\beta < \tau < \beta$. This may be Fourier transformed in terms of discrete frequencies $\omega_n = \pi(2n+1)/\beta$, since only odd frequencies have nonzero Fourier components, due to the antiperiodicity of $G^M(\tau)$ with respect to τ .

$$G^M(\alpha, \mathbf{k}, \sigma, i\omega_n) = \int_0^\beta d\tau e^{i\omega_n \tau} G^M(\alpha, \mathbf{k}, \sigma, \tau) \quad (\text{B.42})$$

We may choose to compute this integral following an alternate contour, by noting that:

$$\int_0^\beta d\tau = -\frac{i}{\hbar} \int_0^\infty dt [(\tau \rightarrow it/\hbar) - (\tau \rightarrow it/\hbar + \beta)] \quad (\text{B.43})$$

since the integral vanishes for $\tau = i\infty$. Thus:

$$G^M(\alpha, \mathbf{k}, \sigma, i\omega_n) = -\frac{i}{\hbar Z} \int_0^\infty dt e^{-\omega_n t/\hbar} \text{Tr} \left\{ e^{-\beta\mathcal{H}} e^{i\mathcal{H}t/\hbar} c_{\alpha, \mathbf{k}, \sigma} e^{-i\mathcal{H}t/\hbar} c_{\alpha, \mathbf{k}, \sigma}^\dagger \right\} \quad (\text{B.44})$$

$$- e^{-\omega_n t/\hbar + i\omega_n \beta} \text{Tr} \left\{ e^{i\mathcal{H}t/\hbar} c_{\alpha, \mathbf{k}, \sigma} e^{-i\mathcal{H}t/\hbar} e^{-\beta\mathcal{H}} c_{\alpha, \mathbf{k}, \sigma}^\dagger \right\}$$

$$= -\frac{i}{\hbar Z} \int_0^\infty dt e^{-\omega_n t/\hbar} \text{Tr} \left\{ e^{-\beta\mathcal{H}} [c_{\alpha, \mathbf{k}, \sigma}(t), c_{\alpha, \mathbf{k}, \sigma}^\dagger(0)]_+ \right\} \quad (\text{B.45})$$

$$= G^R(\alpha, \mathbf{k}, \sigma, \omega) |_{\hbar\omega + i\eta \rightarrow i\omega_n} \quad (\text{B.46})$$

Thus, if the Matsubara Green function is known as a function of the discrete frequencies ω_n , then the retarded Green function may be obtained by replacing all $i\omega_n \rightarrow \hbar\omega + i\eta$.

Appendix C

Letters of Copyright Permission



RightsLink®

Home

Account
Info

Help

ACS Publications
Most Trusted. Most Cited. Most Read.**Title:** Magnetic Anisotropy in a Heavy
Atom Radical FerromagnetLogged in as:
Stephen Winter**Author:** Stephen M. Winter, Saiti Datta,
Stephen Hill, et al

LOGOUT

Publication: Journal of the American
Chemical Society**Publisher:** American Chemical Society**Date:** Jun 1, 2011

Copyright © 2011, American Chemical Society

PERMISSION/LICENSE IS GRANTED FOR YOUR ORDER AT NO CHARGE

This type of permission/license, instead of the standard Terms & Conditions, is sent to you because no fee is being charged for your order. Please note the following:

- Permission is granted for your request in both print and electronic formats, and translations.
- If figures and/or tables were requested, they may be adapted or used in part.
- Please print this page for your records and send a copy of it to your publisher/graduate school.
- Appropriate credit for the requested material should be given as follows: "Reprinted (adapted) with permission from (COMPLETE REFERENCE CITATION). Copyright (YEAR) American Chemical Society." Insert appropriate information in place of the capitalized words.
- One-time permission is granted only for the use specified in your request. No additional uses are granted (such as derivative works or other editions). For any other uses, please submit a new request.

BACK

CLOSE WINDOW

Copyright © 2014 [Copyright Clearance Center, Inc.](#) All Rights Reserved. [Privacy statement.](#)
Comments? We would like to hear from you. E-mail us at customercare@copyright.com



RightsLink®

[Home](#)[Account Info](#)[Help](#)

Title: Bisdithiazolyl Radical Spin Ladders
Author: Kristina Lekin, Joanne W. L. Wong, Stephen M. Winter, et al
Publication: Inorganic Chemistry
Publisher: American Chemical Society
Date: Feb 1, 2013
Copyright © 2013, American Chemical Society

Logged in as:
Stephen Winter

[LOGOUT](#)

PERMISSION/LICENSE IS GRANTED FOR YOUR ORDER AT NO CHARGE

This type of permission/license, instead of the standard Terms & Conditions, is sent to you because no fee is being charged for your order. Please note the following:

- Permission is granted for your request in both print and electronic formats, and translations.
- If figures and/or tables were requested, they may be adapted or used in part.
- Please print this page for your records and send a copy of it to your publisher/graduate school.
- Appropriate credit for the requested material should be given as follows: "Reprinted (adapted) with permission from (COMPLETE REFERENCE CITATION). Copyright (YEAR) American Chemical Society." Insert appropriate information in place of the capitalized words.
- One-time permission is granted only for the use specified in your request. No additional uses are granted (such as derivative works or other editions). For any other uses, please submit a new request.

[BACK](#)[CLOSE WINDOW](#)

Copyright © 2014 [Copyright Clearance Center, Inc.](#) All Rights Reserved. [Privacy statement.](#)
Comments? We would like to hear from you. E-mail us at customercare@copyright.com

**RightsLink**®[Home](#)[Account Info](#)[Help](#)

Title: Crossing the Insulator-to-Metal Barrier with a Thiazyl Radical Conductor

Author: Aaron Mailman, Stephen M. Winter, Xin Yu, et al

Publication: Journal of the American Chemical Society

Publisher: American Chemical Society

Date: Jun 1, 2012

Copyright © 2012, American Chemical Society

Logged in as:
Stephen Winter[LOGOUT](#)**PERMISSION/LICENSE IS GRANTED FOR YOUR ORDER AT NO CHARGE**

This type of permission/license, instead of the standard Terms & Conditions, is sent to you because no fee is being charged for your order. Please note the following:

- Permission is granted for your request in both print and electronic formats, and translations.
- If figures and/or tables were requested, they may be adapted or used in part.
- Please print this page for your records and send a copy of it to your publisher/graduate school.
- Appropriate credit for the requested material should be given as follows: "Reprinted (adapted) with permission from (COMPLETE REFERENCE CITATION). Copyright (YEAR) American Chemical Society." Insert appropriate information in place of the capitalized words.
- One-time permission is granted only for the use specified in your request. No additional uses are granted (such as derivative works or other editions). For any other uses, please submit a new request.

[BACK](#)[CLOSE WINDOW](#)

Copyright © 2014 [Copyright Clearance Center, Inc.](#) All Rights Reserved. [Privacy statement.](#)
Comments? We would like to hear from you. E-mail us at customercare@copyright.com



RightsLink®

[Home](#)[Account Info](#)[Help](#)

Title: From Magnets to Metals: The Response of Tetragonal Bisdiselenazoyl Radicals to Pressure

Author: Alicea A. Leitch, Kristina Lekin, Stephen M. Winter, et al

Publication: Journal of the American Chemical Society

Publisher: American Chemical Society

Date: Apr 1, 2011

Copyright © 2011, American Chemical Society

Logged in as:
Stephen Winter

[LOGOUT](#)

PERMISSION/LICENSE IS GRANTED FOR YOUR ORDER AT NO CHARGE

This type of permission/license, instead of the standard Terms & Conditions, is sent to you because no fee is being charged for your order. Please note the following:

- Permission is granted for your request in both print and electronic formats, and translations.
- If figures and/or tables were requested, they may be adapted or used in part.
- Please print this page for your records and send a copy of it to your publisher/graduate school.
- Appropriate credit for the requested material should be given as follows: "Reprinted (adapted) with permission from (COMPLETE REFERENCE CITATION). Copyright (YEAR) American Chemical Society." Insert appropriate information in place of the capitalized words.
- One-time permission is granted only for the use specified in your request. No additional uses are granted (such as derivative works or other editions). For any other uses, please submit a new request.

[BACK](#)[CLOSE WINDOW](#)

Copyright © 2014 [Copyright Clearance Center, Inc.](#) All Rights Reserved. [Privacy statement.](#)
Comments? We would like to hear from you. E-mail us at customercare@copyright.com



RightsLink®

[Home](#)[Account Info](#)[Help](#)

Title: Structure and Property Correlations in Heavy Atom Radical Conductors

Author: Alicea A. Leitch, Xueyang Yu, Stephen M. Winter, et al

Publication: Journal of the American Chemical Society

Publisher: American Chemical Society

Date: May 1, 2009

Copyright © 2009, American Chemical Society

Logged in as:
Stephen Winter

[LOGOUT](#)

PERMISSION/LICENSE IS GRANTED FOR YOUR ORDER AT NO CHARGE

This type of permission/license, instead of the standard Terms & Conditions, is sent to you because no fee is being charged for your order. Please note the following:

- Permission is granted for your request in both print and electronic formats, and translations.
- If figures and/or tables were requested, they may be adapted or used in part.
- Please print this page for your records and send a copy of it to your publisher/graduate school.
- Appropriate credit for the requested material should be given as follows: "Reprinted (adapted) with permission from (COMPLETE REFERENCE CITATION). Copyright (YEAR) American Chemical Society." Insert appropriate information in place of the capitalized words.
- One-time permission is granted only for the use specified in your request. No additional uses are granted (such as derivative works or other editions). For any other uses, please submit a new request.

[BACK](#)[CLOSE WINDOW](#)

Copyright © 2014 [Copyright Clearance Center, Inc.](#) All Rights Reserved. [Privacy statement.](#)
Comments? We would like to hear from you. E-mail us at customercare@copyright.com

References

- [1] McCoy, N. H.; Moore, W. C. *J. Am. Chem. Soc.* **1991**, *33*, 273.
- [2] Hicks, R. *Stable Radicals: Fundamentals and Applied Aspects of Odd-Electron Compounds*; Wiley, 2011.
- [3] Mott, N. F. *Rev. Mod. Phys.* **1968**, *40*, 677–683.
- [4] Mott, N. F. *Proc. Phys. Soc. London, Sec. A* **1949**, *62*, 416.
- [5] Mott, N. F.; Peierls, R. *Proc. Phys. Soc. London* **1937**, *49*, 72.
- [6] Mott, N. *Metal-Insulator Transitions*; Taylor & Francis, 1990.
- [7] Hubbard, J. *Proc. R. Soc. Lond. A* **1963**, *276*, 238–257.
- [8] Hubbard, J. *Proc. R. Soc. Lond. A* **1964**, *277*, 237–259.
- [9] Hubbard, J. *Proc. R. Soc. Lond. A* **1964**, *281*, 401–419.
- [10] Hubbard, J. *Proc. R. Soc. Lond. A* **1965**, *285*, 542–560.
- [11] Gutzwiller, M. C. *Phys. Rev.* **1965**, *137*, A1726.
- [12] Kanamori, J. *Progr. Theoret. Phys.* **1963**, *30*, 275–289.
- [13] Gebhard, F. *The Mott Metal-Insulator Transition: Models and Methods*; Springer Series in Solid-State Sciences no. 137; Springer, 1997.

- [14] Baeriswyl, D. *The Hubbard Model: Its Physics and Its Mathematical Physics*; NATO ASI series; Springer, 1995.
- [15] Rasetti, M. *The Hubbard Model: Recent Results*; Series on advances in statistical mechanics; World Scientific, 1991.
- [16] Essler, F.; Frahm, H.; Göhmann, F.; Klümper, A.; Korepin, V. *The One-Dimensional Hubbard Model*; Cambridge University Press, 2005.
- [17] Georges, A.; Kotliar, G.; Krauth, W.; Rozenberg, M. J. *Rev. Mod. Phys.* **1996**, *68*, 13–125.
- [18] Imada, M.; Fujimori, A.; Tokura, Y. *Rev. Mod. Phys.* **1998**, *70*, 1039–1263.
- [19] Dobrosavljevic, V.; Trivedi, N.; Valles, J. *Conductor Insulator Quantum Phase Transitions*; OUP Oxford, 2012.
- [20] Bryan, C. D.; Cordes, A. W.; Haddon, R. C.; Hicks, R. G.; Kennepohl, D. K.; MacKinnon, C. D.; Oakley, R. T.; Palstra, T.; Perel, A. S. *J. Am. Chem. Soc.* **1994**, *116*, 1205–1210.
- [21] Bryan, C. D.; Cordes, A. W.; Fleming, R. M.; George, N. A.; Glarum, S. H.; Haddon, R. C.; MacKinnon, C. D.; Oakley, R. T.; Palstra, T. T. M.; Perel, A. S. *J. Am. Chem. Soc.* **1995**, *117*, 6880–6888.
- [22] Gombert, M. *J. Am. Chem. Soc.* **1900**, *22*, 757–771.
- [23] Neumann, W. P.; Uzick, W.; Zarkadis, A. K. *J. Am. Chem. Soc.* **1986**, *108*, 3762–3770.
- [24] Ballester, M.; Riera-Figueras, J.; Castaner, J.; Badfa, C.; Monso, J. M. *J. Am. Chem. Soc.* **1971**, *93*, 2215–2225.
- [25] Ballester, M. *Acc. Chem. Res.* **1985**, *18*, 380–387.
- [26] Reid, D. H. *Quart. Rev.* **1965**, *19*, 274.

- [27] Goto, K.; Kubo, T.; Yamamoto, K.; Nakasuji, K.; Sato, K.; Shiomi, D.; Takui, T.; Kubota, M.; Kobayashi, T.; Yakusi, K.; Ouyang, J. *J. Am. Chem. Soc.* **1999**, *121*, 1619–1620.
- [28] Koutentis, P. A.; Chen, Y.; Cao, Y.; Best, T. P.; Itkis, M. E.; Beer, L.; Oakley, R. T.; Cordes, A. W.; Brock, C. P.; Haddon, R. C. *J. Am. Chem. Soc.* **2001**, *123*, 3864–3871.
- [29] Luo, Y.-R. *Comprehensive Handbook of Chemical Bond Energies*; CRC Press, 2007.
- [30] Coulson, C. A. *Valence, 2nd Ed.*; Oxford University Press: London, 1961.
- [31] *Comprehensive Inorganic Chemistry: From Elements to Applications* **2013**, *1*, 375–411.
- [32] Takeda, K.; Konishi, K.; Nedachi, K.; Mukai, K. *Phys. Rev. Lett.* **1995**, *74*, 1673–1676.
- [33] Mukai, K.; Konishi, K.; Nedachi, K.; Takeda, K. *J. Phys. Chem.* **1996**, *100*, 9658–9663.
- [34] Takahashi, M.; Turek, P.; Nakazawa, Y.; Tamura, M.; Nozawa, K.; Shiomi, D.; Ishikawa, M.; Kinoshita, M. *Phys. Rev. Lett.* **1991**, *67*, 746.
- [35] Tamura, M.; Nakazawa, Y.; Shiomi, D.; Nozawa, K.; Hosokoshi, Y.; Ishikawa, M.; Takahashi, M.; Kinoshita, M. *Chem. Phys. Lett.* **1991**, *186*, 401–404.
- [36] Nakazawa, Y.; Tamura, M.; Shirakawa, N.; Shiomi, D.; Takahashi, M.; Kinoshita, M.; Ishikawa, M. *Phys. Rev. B* **1992**, *46*, 8906.
- [37] Chiarelli, R.; Novak, M. A.; Rassat, A.; Tholence, J. L. *Nature* **1993**, *363*, 147–149.
- [38] Lahti, P. M. In *Carbon Based Magnetism: An Overview of the Magnetism of Metal Free Carbon-based Compounds and Materials*; Makarova, T., Palacio, F., Eds.; Elsevier Science, 2006; Chapter 2.

- [39] Kinoshita, M. In *Pi Electron Magnetism: From Molecules to Magnetic Materials*; Veciana, J., Arcon, D., Eds.; Springer, 2001; Chapter 1.
- [40] Mukai, K. In *Carbon Based Magnetism: An Overview of the Magnetism of Metal Free Carbon-based Compounds and Materials*; Makarova, T., Palacio, F., Eds.; Elsevier Science, 2006; Chapter 4.
- [41] Rawson, J. M.; Alberola, A.; Whalley, A. *J. Mater. Chem.* **2006**, *16*, 2560.
- [42] Vegas, A.; Perez Salazar, A.; Banister, A. J.; Hey, R. G. *J. Chem. Soc., Dalton Trans.* **1980**, 1812.
- [43] Cordes, A. W.; Bryan, C. D.; Davis, W. M.; De Laat, R. H.; Glarum, S. H.; Goddard, J. D.; Haddon, R. C.; Hicks, R. G.; Kennepohl, D. K. *J. Am. Chem. Soc.* **1993**, *115*, 7232–7239.
- [44] Cordes, A. W.; Haddon, R. C.; Hicks, R. G.; Kennepohl, D. K.; Oakley, R. T.; Schneemeyer, L. F.; Waszczak, J. V. *Inorg. Chem.* **1993**, *32*, 1554–1558.
- [45] Barclay, T. M.; Cordes, A. W.; George, N. A.; Haddon, R. C.; Itkis, M. E.; Oakley, R. T. *Chem. Commun.* **1999**, 2269–2270.
- [46] Cordes, A. W.; Haddon, R. C.; Hicks, R. G.; Kennepohl, D. K.; Oakley, R. T.; Palstra, T.; Schneemeyer, L. F.; Scott, S. R.; Waszczak, J. V. *Chem. Mat.* **1993**, *5*, 820–825.
- [47] Cordes, A. W.; Haddon, R. C.; Hicks, R. G.; Oakley, R. T.; Palstra, T. *Inorg. Chem.* **1992**, *31*, 1802–1808.
- [48] Clarke, C. S.; Haynes, D. A.; Rawson, J. M.; Bond, A. D. *Chem. Commun.* **2003**, 2774.
- [49] Wolmershäuser, G.; Kraft, G. *Chemische Berichte* **1990**, *123*, 881–885.
- [50] Brownridge, S.; Du, H.; Fairhurst, S. A.; Haddon, R. C.; Oberhammer, H.; Parsons, S.; Passmore, J.; Schriver, M. J.; Sutcliffe, L. H.; Westwood, N. P. *J. Chem. Soc., Dalton Trans.* **2000**, 3365–3382.

- [51] Awere, E. G.; Burford, N.; Mailer, C.; Passmore, J.; Schriver, M. J.; White, P. S.; Banister, A. J.; Oberhammer, H.; Sutcliffe, L. H. *J. Chem. Soc., Chem. Commun.* **1987**, 66–69.
- [52] Awere, E. G.; Burford, N.; Haddon, R. C.; Parsons, S.; Passmore, J.; Waszczak, J.; White, P. S. *Inorg. Chem.* **1990**, *29*, 4821–4830.
- [53] Barclay, T. M.; Cordes, A. W.; George, N. A.; Haddon, R. C.; Oakley, R. T.; Palstra, T. T.; Patenaude, G. W.; Reed, R. W.; Richardson, J. F.; Zhang, H. *Chem. Commun.* **1997**, 873–874.
- [54] Oakley, R. T.; Reed, R. W.; Robertson, C. M.; Richardson, J. F. *Inorg. Chem.* **2005**, *44*, 1837–1845.
- [55] Barclay, T.; Cordes, A.; Haddon, R.; Itkis, M.; Oakley, R.; Reed, R.; Zhang, H. *J. Am. Chem. Soc.* **1999**, *121*, 969–976.
- [56] Barclay, T. M.; Cordes, A. W.; Beer, L.; Oakley, R. T.; Preuss, K. E.; Taylor, N. J.; Reed, R. W. *Chem. Commun.* **1999**, 531–532.
- [57] Beer, L.; Cordes, A. W.; Haddon, R. C.; Itkis, M. E.; Oakley, R. T.; Reed, R. W.; Robertson, C. M. *Chem. Commun.* **2002**, 1872–1873.
- [58] Boere, R. T.; Oakley, R. T.; Reed, R. W.; Westwood, N. P. *J. Am. Chem. Soc.* **1989**, *111*, 1180–1185.
- [59] Boéré, R. T.; Roemmele, T. L. *Phosphorus, Sulfur, and Silicon* **2004**, *179*, 875–882.
- [60] Boéré, R. T.; Roemmele, T. L.; Yu, X. *Inorg. Chem.* **2011**, *50*, 5123–5136.
- [61] Rawson, J. M.; Palacio, F. In *Pi Electron Magnetism: From Molecules to Magnetic Materials*; Veciana, J., Arcon, D., Eds.; Springer, 2001; Chapter 4.
- [62] Fujita, W.; Awaga, K. *Science* **1999**, *286*, 261–262.
- [63] Barclay, T.; Cordes, A.; George, N.; Haddon, R.; Itkis, M.; Mashuta, M.; Oakley, R.; Patenaude, G.; Reed, R.; Richardson, J. *J. Am. Chem. Soc.* **1998**, *120*, 352–360.

- [64] Brusso, J. L.; Clements, O. P.; Haddon, R. C.; Itkis, M. E.; Leitch, A. A.; Oakley, R. T.; Reed, R. W.; Richardson, J. F. *J. Am. Chem. Soc.* **2004**, *126*, 8256–8265.
- [65] Beer, L.; Britten, J. F.; Brusso, J. L.; Cordes, A. W.; Haddon, R. C.; Itkis, M. E.; MacGregor, D. S.; Oakley, R. T.; Reed, R. W.; Robertson, C. M. *J. Am. Chem. Soc.* **2003**, *125*, 14394–14403.
- [66] Beer, L.; Brusso, J. L.; Cordes, A. W.; Haddon, R. C.; Itkis, M. E.; Kirschbaum, K.; MacGregor, D. S.; Oakley, R. T.; Pinkerton, A. A.; Reed, R. W. *J. Am. Chem. Soc.* **2002**, *124*, 9498–9509.
- [67] Beer, L.; Brusso, J. L.; Cordes, A. W.; Godde, E.; Haddon, R. C.; Itkis, M. E.; Oakley, R. T.; Reed, R. W. *Chem. Commun.* **2002**, 2562–2563.
- [68] Leitch, A. A.; Oakley, R. T.; Reed, R. W.; Thompson, L. K. *Inorg. Chem.* **2007**, *46*, 6261–6270.
- [69] Beer, L.; Haddon, R. C.; Itkis, M. E.; Leitch, A. A.; Oakley, R. T.; Reed, R. W.; Richardson, J. F.; VanderVeer, D. G. *Chem. Commun.* **2005**, 1218–1220.
- [70] Leitch, A. A.; Yu, X.; Robertson, C. M.; Secco, R. A.; Tse, J. S.; Oakley, R. T. *Inorg. Chem.* **2009**, *48*, 9874–9882.
- [71] Beer, L.; Brusso, J. L.; Haddon, R. C.; Itkis, M. E.; Leitch, A. A.; Oakley, R. T.; Reed, R. W.; Richardson, J. F. *Chem. Commun.* **2005**, 1543–1545.
- [72] Beer, L.; Brusso, J. L.; Haddon, R. C.; Itkis, M. E.; Kleinke, H.; Leitch, A. A.; Oakley, R. T.; Reed, R. W.; Richardson, J. F.; Secco, R. A.; Yu, X. *J. Am. Chem. Soc.* **2005**, *127*, 18159–18170.
- [73] Lakin, K.; Leitch, A. A.; Tse, J. S.; Bao, X.; Secco, R. A.; Desgreniers, S.; Ohishi, Y.; Oakley, R. T. *Cryst. Growth Des.* **2012**, *12*, 4676–4684.
- [74] Lakin, K.; Winter, S. M.; Downie, L. E.; Bao, X.; Tse, J. S.; Desgreniers, S.; Secco, R. A.; Dube, P. A.; Oakley, R. T. *J. Am. Chem. Soc.* **2010**, *132*, 16212–16224.

- [75] Phan, H.; Legin, K.; Winter, S. M.; Oakley, R. T.; Shatruk, M. *J. Am. Chem. Soc.* **2013**, *135*, 15674–15677.
- [76] Legin, K.; Phan, H.; Winter, S. M.; Wong, J. W. L.; Leitch, A. A.; Laniel, D.; Yong, W.; Secco, R. A.; Tse, J. S.; Desgreniers, S.; Dube, P. A.; Shatruk, M.; Oakley, R. T. *J. Am. Chem. Soc.* **2014**, *136*, 8050–8062.
- [77] Halcrow, M. *Spin-Crossover Materials: Properties and Applications*; Wiley, 2013.
- [78] Létard, J.-F. *J. Mater. Chem.* **2006**, *16*, 2550–2559.
- [79] Winter, S. M.; Cvrkalj, K.; Dube, P. A.; Robertson, C. M.; Probert, M. R.; Howard, J. A.; Oakley, R. T. *Chem. Commun.* **2009**, 7306–7308.
- [80] Cordes, A. W.; Haddon, R. C.; Oakley, R. T. *Phosphorus, Sulfur, & Silicon & Related Elements* **2004**, *179*, 673–684.
- [81] Beer, L.; Brusso, J. L.; Haddon, R. C.; Itkis, M. E.; Oakley, R. T.; Reed, R. W.; Richardson, J. F.; Secco, R. A.; Yu, X. *Chem. Commun.* **2005**, 5745.
- [82] Brusso, J. L.; Derakhshan, S.; Itkis, M. E.; Kleinke, H.; Haddon, R. C.; Oakley, R. T.; Reed, R. W.; Richardson, J. F.; Robertson, C. M.; Thompson, L. K. *Inorg. Chem.* **2006**, *45*, 10958–10966.
- [83] Brusso, J. L.; Cvrkalj, K.; Leitch, A. A.; Oakley, R. T.; Reed, R. W.; Robertson, C. M. *J. Am. Chem. Soc.* **2006**, *128*, 15080–15081.
- [84] Leitch, A. A.; Brusso, J. L.; Cvrkalj, K.; Reed, R. W.; Robertson, C. M.; Dube, P. A.; Oakley, R. T. *Chem. Commun.* **2007**, 3368.
- [85] Robertson, C. M.; Myles, D. J. T.; Leitch, A. A.; Reed, R. W.; Dooley, D. M.; Frank, N. L.; Dube, P. A.; Thompson, L. K.; Oakley, R. T. *J. Am. Chem. Soc.* **2007**, *129*, 12688.
- [86] Robertson, C. M.; Leitch, A. A.; Cvrkalj, K.; Reed, R. W.; Myles, D. J. T.; Dube, P. A.; Oakley, R. T. *J. Am. Chem. Soc.* **2008**, *130*, 8414–8425.

- [87] Robertson, C. M.; Leitch, A. A.; Cvrkalj, K.; Myles, D. J. T.; Reed, R. W.; Dube, P. A.; Oakley, R. T. *J. Am. Chem. Soc.* **2008**, *130*, 14791–14801.
- [88] Leitch, A. A.; Yu, X.; Winter, S. M.; Secco, R. A.; Dube, P. A.; Oakley, R. T. *J. Am. Chem. Soc.* **2009**, *131*, 7112–7125.
- [89] Leitch, A. A.; Legin, K.; Winter, S. M.; Downie, L. E.; Tsuruda, H.; Tse, J. S.; Mito, M.; Desgreniers, S.; Dube, P. A.; Zhang, S.; Liu, Q.; Jin, C.; Ohishi, Y.; Oakley, R. T. *J. Am. Chem. Soc.* **2011**, *133*, 6051–6060.
- [90] Tsuruda, H.; Mito, M.; Deguchi, H.; Takagi, S.; Leitch, A. A.; Legin, K.; Winter, S. M.; Oakley, R. T. *Polyhedron* **2011**, *30*, 2997–3000.
- [91] Mito, M.; Komorida, Y.; Tsuruda, H.; Tse, J. S.; Desgreniers, S.; Ohishi, Y.; Leitch, A. A.; Cvrkalj, K.; Robertson, C. M.; Oakley, R. T. *J. Am. Chem. Soc.* **2009**, *131*, 16012–16013.
- [92] Winter, S. M.; Balo, A. R.; Roberts, R. J.; Legin, K.; Assoud, A.; Dube, P. A.; Oakley, R. T. *Chem. Commun.* **2013**, *49*, 1603.
- [93] Yu, X.; Mailman, A.; Dube, P. A.; Assoud, A.; Oakley, R. T. *Chem. Commun.* **2011**, *47*, 4655.
- [94] Yu, X.; Mailman, A.; Legin, K.; Assoud, A.; Dube, P. A.; Oakley, R. T. *Cryst. Growth Des.* **2012**, *12*, 2485–2494.
- [95] Yu, X.; Mailman, A.; Legin, K.; Assoud, A.; Robertson, C. M.; Noll, B. C.; Campana, C. F.; Howard, J. A. K.; Dube, P. A.; Oakley, R. T. *J. Am. Chem. Soc.* **2012**, *134*, 2264–2275.
- [96] Wong, J. W. L.; Mailman, A.; Legin, K.; Winter, S. M.; Yong, W.; Zhao, J.; Garimella, S. V.; Tse, J. S.; Secco, R. A.; Desgreniers, S.; Ohishi, Y.; Borondics, F.; Oakley, R. T. *J. Am. Chem. Soc.* **2014**, *136*, 1070–1081.
- [97] Mailman, A.; Winter, S. M.; Yu, X.; Robertson, C. M.; Yong, W.; Tse, J. S.; Secco, R. A.; Liu, Z.; Dube, P. A.; Howard, J. A. *J. Am. Chem. Soc.* **2012**, *134*, 9886–9889.

- [98] Torrance, J. B. *Acc. Chem. Res.* **1979**, *12*, 79–86.
- [99] Ferraris, J.; Cowan, D.; Walatka, V. t.; Perlstein, J. *J. Am. Chem. Soc.* **1973**, *95*, 948–949.
- [100] Chappell, J. S.; Bloch, A. N.; Bryden, W. A.; Maxfield, M.; Poehler, T. O.; Cowan, D. O. *J. Am. Chem. Soc.* **1981**, *103*, 2442–2443.
- [101] Matsuzaki, S.; Kuwata, R.; Toyoda, K. *Solid State Commun.* **1980**, *33*, 403–405.
- [102] Pouget, J. P.; Khanna, S. K.; Denoyer, F.; Comes, R.; Garito, A. F.; Heeger, A. J. *Phys. Rev. Lett.* **1976**, *37*, 437.
- [103] Williams, J. M.; Wang, H. H.; Beno, M. A.; Emge, T. J.; Sowa, L.; Copps, P.; Behroozi, F.; Hall, L.; Carlson, K. D.; Crabtree, G. *Inorg. Chem.* **1984**, *23*, 3839–3841.
- [104] Bechgaard, K.; Carneiro, K.; Rasmussen, F. B.; Olsen, M.; Rindorf, G.; Jacobsen, C. S.; Pedersen, H. J.; Scott, J. C. *J. Am. Chem. Soc.* **1981**, *103*, 2440–2442.
- [105] Bechgaard, K.; Jacobsen, C.; Mortensen, K.; Pedersen, H.; Thorup, N. *Solid State Commun.* **1980**, *33*, 1119–1125.
- [106] Geiser, U.; Schlueter, J. A. *Chem. Rev.* **2004**, *104*, 5203–5242.
- [107] Kobayashi, H.; Cui, H.; Kobayashi, A. *Chem. Rev.* **2004**, *104*, 5265–5288.
- [108] Bechgaard, K.; Jérôme, D. *Phys. Scripta* **1991**, *1991*, 37.
- [109] Jérôme, D.; Schulz, H. J. *Adv. Phys.* **1982**, *31*, 299–490.
- [110] Lebed, A. *The Physics of Organic Superconductors and Conductors*; Springer, 2008.
- [111] Toyota, N.; Lang, M.; Müller, J. *Low-Dimensional Molecular Metals*; Springer Series in Solid-State Sciences; Springer, 2007.
- [112] Pal, S. K.; Itkis, M. E.; Tham, F. S.; Reed, R. W.; Oakley, R. T.; Donnadieu, B.; Haddon, R. C. *J. Am. Chem. Soc.* **2007**, *129*, 7163–7174.

- [113] Chi, X.; Itkis, M. E.; Kirschbaum, K.; Pinkerton, A. A.; Oakley, R. T.; Cordes, A. W.; Haddon, R. C. *J. Am. Chem. Soc.* **2001**, *123*, 4041–4048.
- [114] Chi, X.; Itkis, M. E.; Reed, R. W.; Oakley, R. T.; Cordes, A. W.; Haddon, R. C. *J. Phys. Chem. B* **2002**, *106*, 8278–8287.
- [115] Chi, X.; Itkis, M. E.; Tham, F. S.; Oakley, R. T.; Cordes, A. W.; Haddon, R. C. *Int. J. Quantum Chem.* **2003**, *95*, 853–865.
- [116] Pal, S. K.; Itkis, M. E.; Reed, R. W.; Oakley, R. T.; Cordes, A. W.; Tham, F. S.; Siegrist, T.; Haddon, R. C. *J. Am. Chem. Soc.* **2004**, *126*, 1478–1484.
- [117] Pal, S. K.; Itkis, M. E.; Tham, F. S.; Reed, R. W.; Oakley, R. T.; Haddon, R. C. *Science* **2005**, *309*, 281–284.
- [118] Mandal, S. K.; Samanta, S.; Itkis, M. E.; Jensen, D. W.; Reed, R. W.; Oakley, R. T.; Tham, F. S.; Donnadiou, B.; Haddon, R. C. *J. Am. Chem. Soc.* **2006**, *128*, 1982–1994.
- [119] McKenzie, R. H. *Comments Cond. Matt. Phys.* **1998**, *18*, 309.
- [120] Pal, S. K.; Itkis, M. E.; Tham, F. S.; Reed, R. W.; Oakley, R. T.; Haddon, R. C. *J. Am. Chem. Soc.* **2008**, *130*, 3942–3951.
- [121] Zheng, S.; Thompson, J. D.; Tontcheva, A.; Khan, S. I.; Rubin, Y. *Org. Lett.* **2005**, *7*, 1861–1863.
- [122] Haddon, R. C.; Wudl, F.; Kaplan, M. L.; Marshall, J. H.; Cais, R. E.; Bramwell, F. B. *J. Am. Chem. Soc.* **1978**, *100*, 7629–7633.
- [123] Kubo, T.; Katada, Y.; Shimizu, A.; Hirao, Y.; Sato, K.; Takui, T.; Uruichi, M.; Yakushi, K.; Haddon, R. C. *J. Am. Chem. Soc.* **2011**, *133*, 14240–14243.
- [124] Ashcroft, N.; Mermin, N. *Solid State Physics*; Cengage Learning, 2011.
- [125] Anderson, P. W. *Phys. Rev.* **1959**, *115*, 2.

- [126] Goodenough, J. B. *Magnetism and the Chemical Bond*; John Wiley & Sons Inc., 1963.
- [127] Kahn, O. *Molecular Magnetism*; VCH New York, NY, 1993.
- [128] Kahn, O.; Galy, J.; Journaux, Y.; Jaud, J.; Morgenstern-Badarau, I. *Journal of the American Chemical Society* **1982**, *104*, 2165–2176.
- [129] Auerbach, A. *Fullerene Science and Technology* **1998**, *6*, 1–29.
- [130] Seshadri, R.; Rastogi, A.; Bhat, S. V.; Ramasesha, S.; Rao, C. *Solid State Commun.* **1993**, *85*, 971–974.
- [131] Wolmershäuser, G.; Schnauber, M.; Wilhelm, T.; Sutcliffe, L. H. *Synt. Met.* **1986**, *14*, 239–244.
- [132] Fujita, W.; Awaga, K. *Chem. Phys. Lett.* **2004**, *388*, 186–189.
- [133] Fujita, W.; Awaga, K. *Chem. Phys. Lett.* **2002**, *357*, 385–388.
- [134] Barclay, T. M.; Cordes, A. W.; De Laat, R. H.; Goddard, J. D.; Haddon, R. C.; Jeter, D. Y.; Mawhinney, R. C.; Oakley, R. T.; Palstra, T.; Patenaude, G. W. *J. Am. Chem. Soc.* **1997**, *119*, 2633–2641.
- [135] Mattar, S. M. *Chem. Phys. Lett.* **2006**, *427*, 438–442.
- [136] Williams, K. A.; Nowak, M. J.; Dormann, E.; Wudl, F. *Synt. Met.* **1986**, *14*, 233–238.
- [137] Marian, C. M. In *Reviews in Computational Chemistry. Volume 17*; Lipkowitz, K. B., Boyd., D. B., Eds.; Wiley-VCH, New York, 2002; Chapter 3.
- [138] Richards, W.; Trivedi, H.; Cooper, D. *Spin-Orbit Coupling in Molecules*; International Series of Monographs on Chemistry; Clarendon Press, 1981.
- [139] Barysz, M.; Ishikawa, Y. *Relativistic Methods for Chemists*; Challenges and Advances in Computational Chemistry and Physics; Springer, 2010.

- [140] McQuarrie, D.; Simon, J. *Physical Chemistry: A Molecular Approach*; University Science Books, 1997.
- [141] Softley, T. *Atomic spectra*; Oxford chemistry primers; Oxford University Press, 1994.
- [142] Wittel, K.; Manne, R. *Theor. Chem. Acc.* **1974**, *33*, 347–349.
- [143] Wood, D. R.; Andrew, K. L.; Giacchetti, A.; Cowan, R. D. *J. Opt. Soc. Am.* **1968**, *58*, 830–836.
- [144] Bencini, A.; Gatteschi, D. *EPR of Exchange Coupled Systems*; Dover Books on Chemistry; Dover Publications, 2012.
- [145] Hess, B. A.; Marian, C. M.; Wahlgren, U.; Gropen, O. *Chem. Phys. Lett.* **1996**, *251*, 365–371.
- [146] Hess, B. *Relativistic Effects in Heavy-Element Chemistry and Physics*; Wiley Series in Theoretical Chemistry; Wiley, 2003.
- [147] Neese, F. *J. Chem. Phys.* **2005**, *122*, 034107.
- [148] Neese, F. *WIREs Comput Mol Sci* **2012**, *2*, 73–78.
- [149] Dzyaloshinskii, I. *J. Phys. Chem. Solids* **1958**, *4*, 241–255.
- [150] Moriya, T. *Phys. Rev.* **1960**, *120*, 91–98.
- [151] Yildirim, T.; Harris, AB.; Entin-Wohlman, O.; Aharony, A. *Phys. Rev. Lett.* **1994**, *73*, 2919.
- [152] Yildirim, T.; Harris, A. B.; Aharony, A.; Entin-Wohlman, O. *Phys. Rev. B* **1995**, *52*, 10239–10267.
- [153] Shekhtman, L.; Entin-Wohlman, O.; Aharony, A. *Phys. Rev. Lett.* **1992**, *69*, 836.
- [154] Yildirim, T.; Harris, AB.; Entin-Wohlman, O.; Aharony, A. *Phys. Rev. Lett.* **1994**, *72*, 3710.

- [155] Noodleman, L.; Davidson, E. R. *Chem. Phys.* **1986**, *109*, 131–143.
- [156] Noodleman, L.; Norman Jr, J. G.; Osborne, J. H.; Aizman, A.; Case, D. A. *J. Am. Chem. Soc.* **1985**, *107*, 3418–3426.
- [157] Noodleman, L. *J. Chem. Phys.* **1981**, *74*, 5737.
- [158] Noodleman, L.; Norman, J. G. *J. Chem. Phys.* **1979**, *70*, 4903.
- [159] Decken, A.; Mattar, S. M.; Passmore, J.; Shuvaev, K. V.; Thompson, L. K. *Inorg. Chem.* **2006**, *45*, 3878–3886.
- [160] Luzon, J.; Campo, J.; Palacio, F.; McIntyre, G. J.; Rawson, J. M. *Polyhedron* **2005**, *24*, 2579–2583.
- [161] Novoa, J. J.; Deumal, M.; Jornet-Somoza, J. *Chem. Soc. Rev.* **2011**, *40*, 3182.
- [162] Deumal, M.; LeRoux, S.; Rawson, J. M.; Robb, M. A.; Novoa, J. J. *Polyhedron* **2007**, *26*, 1949–1958.
- [163] Deumal, M.; Robb, M. A.; Novoa, J. J. *Progress in Theoretical Chemistry and Physics* **2007**, *16*, 271–289.
- [164] Hicks, R. G.; Lemaire, M. T.; Öhrström, L.; Richardson, J. F.; Thompson, L. K.; Xu, Z. *J. Am. Chem. Soc.* **2001**, *123*, 7154–7159.
- [165] Pantazis, D. A.; Krewald, V.; Orio, M.; Neese, F. *Dalton Transactions* **2010**, *39*, 4959–4967.
- [166] Yamaguchi, K.; Tsunekawa, T.; Toyoda, Y.; Fueno, T. *Chem. Phys. Lett.* **1988**, *143*, 371–376.
- [167] Yamaguchi, K. *Chem. Phys. Lett.* **1979**, *66*, 395–399.
- [168] Yamaguchi, K. *Chem. Phys. Lett.* **1975**, *33*, 330–335.
- [169] Ganyushin, D.; Neese, F. *J. Chem. Phys.* **2006**, *125*, 024103.

- [170] Neese, F. *J. Chem. Phys.* **2007**, *127*, 164112.
- [171] Kubica, A.; Kowalewski, J.; Kruk, D.; Odelius, M. *J. Chem. Phys.* **2013**, *138*, 064304.
- [172] Zein, S.; Duboc, C.; Lubitz, W.; Neese, F. *Inorg. Chem.* **2008**, *47*, 134–142.
- [173] Duboc, C.; Ganyushin, D.; Sivalingam, K.; Collomb, M.-N.; Neese, F. *J. Phys. Chem. A* **2010**, *114*, 10750–10758.
- [174] Liakos, D. G.; Ganyushin, D.; Neese, F. *Inorg. Chem.* **2009**, *48*, 10572–10580.
- [175] Pederson, M. R.; Khanna, S. N. *Phys. Rev. B* **1999**, *60*, 9566.
- [176] Mostofi, A. A.; Yates, J. R.; Lee, Y.-S.; Souza, I.; Vanderbilt, D.; Marzari, N. *Comput. Phys. Commun.* **2008**, *178*, 685–699.
- [177] Giannozzi, P.; Baroni, S.; Bonini, N.; Calandra, M.; Car, R.; Cavazzoni, C.; Ceresoli, D.; Chiarotti, G. L.; Cococcioni, M.; Dabo, I. *J. Phys.: Condens. Matter* **2009**, *21*, 395502.
- [178] Marzari, N.; Mostofi, A. A.; Yates, J. R.; Souza, I.; Vanderbilt, D. *Rev. Mod. Phys.* **2012**, *84*, 1419–1475.
- [179] Souza, I.; Marzari, N.; Vanderbilt, D. *Phys. Rev. B* **2001**, *65*, 035109.
- [180] Marzari, N.; Vanderbilt, D. *Phys. Rev. B* **1997**, *56*, 12847–12865.
- [181] Berghold, G.; Mundy, C. J.; Romero, A. H.; Hutter, J.; Parrinello, M. *Phys. Rev. B* **2000**, *61*, 10040.
- [182] Marzari, N.; Souza, I.; Vanderbilt, D. *Psi-K newsletter* **2003**, *57*, 129.
- [183] Carlson, B. C.; Keller, J. M. *Phys. Rev.* **1957**, *105*, 102.
- [184] Urban, A.; Reese, M.; Mrovec, M.; Elsässer, C.; Meyer, B. *Phys. Rev. B* **2011**, *84*, 155119.
- [185] Löwdin, P.-O. *Adv. Quantum Chem.* **1970**, *5*, 185–199.

- [186] Löwdin, P.-O. *Adv. Phys.* **1956**, *5*, 1–171.
- [187] Giuliani, G.; Vignale, G. *Quantum Theory of the Electron Liquid*; Cambridge University Press, 2005.
- [188] Abrikosov, A.; Gorkov, L.; Dzyaloshinskii, I.; Silverman, R. *Methods of Quantum Field Theory in Statistical Physics*; Dover Books on Physics; Dover Publications, 2012.
- [189] Mahan, G. *Many-Particle Physics*; Physics of Solids and Liquids; Springer, 2000.
- [190] Dressel, M.; Grüner, G. *Electrodynamics of Solids*; Cambridge University Press, 2002.
- [191] Ioffe, A.; Regel, A. *Prog. Semicond* **1960**, *4*, 237–291.
- [192] Mott, N. F. *Philos. Mag.* **1972**, *26*, 1015–1026.
- [193] Gurvitch, M. *Phys. Rev. B* **1981**, *24*, 7404.
- [194] Gunnarsson, O.; Calandra, M.; Han, J. E. *Rev. Mod. Phys.* **2003**, *75*, 1085.
- [195] Hussey, N. E.; Takenaka, K.; Takagi, H. *Philos. Mag.* **2004**, *84*, 2847–2864.
- [196] Emery, V. J.; Kivelson, S. A. *Phys. Rev. Lett.* **1995**, *74*, 3253.
- [197] Cooper, R. A.; Wang, Y.; Vignolle, B.; Lipscombe, O. J.; Hayden, S. M.; Tanabe, Y.; Adachi, T.; Koike, Y.; Nohara, M.; Takagi, H. *Science* **2009**, *323*, 603–607.
- [198] Tyler, A. W.; Mackenzie, A. P.; NishiZaki, S.; Maeno, Y. *Phys. Rev. B* **1998**, *58*, R10107.
- [199] Fradkin, E.; Kivelson, S. A. *Nature Physics* **2012**, *8*, 864–866.
- [200] Dressel, M. *J. Phys.: Condens. Matter* **2011**, *23*, 293201.
- [201] Georges, A. *arXiv preprint* **2004**, *cond-mat/0403123*.
- [202] Avella, A.; Mancini, F. *Strongly Correlated Systems*; Theoretical Methods; Springer Science & Business Media, 2011.

- [203] Kotliar, G.; Savrasov, S.; Haule, K.; Oudovenko, V.; Parcollet, O.; Marianetti, C. *Rev. Mod. Phys.* **2006**, *78*, 865–951.
- [204] Kotliar, G.; Vollhardt, D. *Phys. Today* **2004**, *57*, 53–60.
- [205] Hohenberg, P.; Kohn, W. *Phys. Rev.* **1964**, *136*, B864.
- [206] Kohn, W.; Sham, L. J. *Phys. Rev.* **1965**, *140*, A1133–A1138.
- [207] Potthoff, M. *Eur. Phys. J. B* **2003**, *36*, 335–348.
- [208] Potthoff, M. *Eur. Phys. J. B* **2003**, *32*, 429–436.
- [209] Koch, E.; Vollhardt, D.; Li, In *The LDA+DMFT approach to strongly correlated materials lecture notes of the Autumn School 2011*; Lichtenstein, A. I., Ed.; Forschungszentrum Jülich, Zentralbibliothek, Verl.: Jülich, 2011.
- [210] Georges, A.; Krauth, W. *Phys. Rev. Lett.* **1992**, *69*, 1240.
- [211] Rozenberg, M. J.; Zhang, X. Y.; Kotliar, G. *Phys. Rev. Lett.* **1992**, *69*, 1236.
- [212] Jarrell, M. *Phys. Rev. Lett.* **1992**, *69*, 168.
- [213] Hirsch, J. E.; Fye, R. M. *Phys. Rev. Lett.* **1986**, *56*, 2521.
- [214] Potthoff, M.; Wegner, T.; Nolting, W. *Phys. Rev. B* **1997**, *55*, 16132.
- [215] Kajueter, H.; Kotliar, G. *Phys. Rev. Lett.* **1996**, *77*, 131.
- [216] Fujiwara, T.; Yamamoto, S.; Ishii, Y. *J. Phys. Soc. Jpn.* **2003**, *72*, 777–780.
- [217] Rozenberg, M. J.; Kotliar, G.; Zhang, X. Y. *Phys. Rev. B* **1994**, *49*, 10181.
- [218] Georges, A.; Krauth, W. *Phys. Rev. B* **1993**, *48*, 7167.
- [219] Yosida, K.; Yamada, K. *Progr. Theoret. Phys. Suppl.* **1970**, *46*, 244–255.
- [220] Barman, H.; Vidhyadhiraja, N. S. *Int. J. Mod Phys B* **2011**, *25*, 2461–2479.

- [221] Limelette, P.; Georges, A.; Jérôme, D.; Wzietek, P.; Metcalf, P.; Honig, J. M. *Science* **2003**, *302*, 89–92.
- [222] Qazilbash, M. M.; Brehm, M.; Chae, B. G.; Ho, P. C.; Andreev, G. O.; Kim, B. J.; Yun, S. J.; Balatsky, A. V.; Maple, M. B.; Keilmann, F.; Kim, H. T.; Basov, D. N. *Science* **2007**, *318*, 1750–1753.
- [223] Kanoda, K.; Kato, R. *Annu. Rev. Condens. Matter Phys.* **2011**, *2*, 167–188.
- [224] Sasaki, T.; Yoneyama, N.; Kobayashi, N. *Phys. Rev. B* **2008**, *77*, 054505.
- [225] Sano, K.; Sasaki, T.; Yoneyama, N.; Kobayashi, N. *Phys. Rev. Lett.* **2010**, *104*, 217003.
- [226] Yasin, S.; Dumm, M.; Salameh, B.; Batail, P.; Mézière, C.; Dressel, M. *Eur. Phys. J. B* **2011**, *79*, 383–390.
- [227] Kagawa, F.; Miyagawa, K.; Kanoda, K. *Nature Physics* **2009**, *5*, 880–884.
- [228] Kurosaki, Y.; Shimizu, Y.; Miyagawa, K.; Kanoda, K.; Saito, G. *Phys. Rev. Lett.* **2005**, *95*, 177001.
- [229] Kanoda, K. *Physica C: Superconductivity* **1997**, *282*, 299–302.
- [230] Dumm, M.; Faltermeier, D.; Drichko, N.; Dressel, M.; Mézière, C.; Batail, P. *Phys. Rev. B* **2009**, *79*, 195106.
- [231] Ferber, J.; Foyevtsova, K.; Jeschke, H. O.; Valenti, R. *Phys. Rev. B* **2014**, *89*, 205106.
- [232] Limelette, P.; Wzietek, P.; Florens, S.; Georges, A.; Costi, T.; Pasquier, C.; Jérôme, D.; Mézière, C.; Batail, P. *Phys. Rev. Lett.* **2003**, *91*, 016401.
- [233] Beer, L.; Britten, J. F.; Clements, O. P.; Haddon, R. C.; Itkis, M. E.; Matkovich, K. M.; Oakley, R. T.; Reed, R. W. *Chem. Mat.* **2004**, *16*, 1564–1572.
- [234] Winter, S. M.; Roberts, R. J.; Mailman, A.; Cvrkalj, K.; Assoud, A.; Oakley, R. T. *Chem. Commun.* **2010**, *46*, 4496.

- [235] Tse, J. S.; Leitch, A. A.; Yu, X.; Bao, X.; Zhang, S.; Liu, Q.; Jin, C.; Secco, R. A.; Desgreniers, S.; Ohishi, Y.; Oakley, R. T. *J. Am. Chem. Soc.* **2010**, *132*, 4876–4886.
- [236] Izyumov, Y. A.; Syromyatnikov, V. N. *Phase Transitions and Crystal Symmetry*; Kluwer Academic Publishers, 1990.
- [237] Goldenfeld, N. *Lectures on Phase Transitions and the Renormalization Group*; Frontiers in physics; Addison-Wesley, Advanced Book Program, 1992.
- [238] Birss, R. *Symmetry and magnetism*; Science Education and Future Human Needs Series; Elsevier, 1965.
- [239] Landau, L. D. *Zh. Eksp. Teor. Fiz.* **1937**, *11*, 19.
- [240] Landau, L. D. *Zh. Eksp. Teor. Fiz.* **1937**, *11*, 627.
- [241] Wadhawan, V. *Introduction to Ferroic Materials*; Taylor & Francis, 2000.
- [242] Tsvetlik, A. *Quantum Field Theory in Condensed Matter Physics*; Cambridge University Press, 2006.
- [243] Giamarchi, T. *Chem. Rev.* **2004**, *104*, 5037–5056.
- [244] Giamarchi, T. *Quantum Physics in One Dimension*; International Series of Monographs on Physics; Clarendon Press, 2003.
- [245] Ward, S.; Bouillot, P.; Ryll, H.; Kiefer, K.; Krämer, K. W.; Rüegg, C.; Kollath, C.; Giamarchi, T. *J. Phys.: Condens. Matter* **2012**, *25*, 014004.
- [246] Dagotto, E.; Rice, T. M. *Science* **1996**, *271*, 618–623.
- [247] Mila, F. *The European Physical Journal B-Condensed Matter and Complex Systems* **1998**, *6*, 201–205.
- [248] Masuda, T.; Zheludev, A.; Manaka, H.; Regnault, L. P.; Chung, J. H.; Qiu, Y. *Phys. Rev. Lett.* **2006**, *96*, 047210.

- [249] Garlea, V.; Zheludev, A.; Masuda, T.; Manaka, H.; Regnault, L. P.; Ressouche, E.; Grenier, B.; Chung, J. H.; Qiu, Y.; Habicht, K.; Kiefer, K.; Boehm, M. *Phys. Rev. Lett.* **2007**, *98*, 167202.
- [250] Lorenz, T.; Heyer, O.; Garst, M.; Anfuso, F.; Rosch, A.; Rüegg, C.; Krämer, K. *Phys. Rev. Lett.* **2008**, *100*, 067208.
- [251] Savici, A.; Granroth, G.; Broholm, C.; Pajeroski, D.; Brown, C.; Talham, D.; Meisel, M.; Schmidt, K.; Uhrig, G.; Nagler, S. *Phys. Rev. B* **2009**, *80*, 094411.
- [252] Thielemann, B.; Rüegg, C.; Rønnow, H.; Läuchli, A.; Caux, J. S.; Normand, B.; Biner, D.; Krämer, K.; Güdel, H. U.; Stahn, J.; Habicht, K.; Kiefer, K.; Boehm, M.; McMorrow, D.; Mesot, J. *Phys. Rev. Lett.* **2009**, *102*, 107204.
- [253] Chaboussant, G.; Fagot-Revurat, Y.; Julien, M.-H.; Hanson, M. E.; Berthier, C.; Horvatić, M.; Lévy, L. P.; Piovesana, O. *Phys. Rev. Lett.* **1998**, *80*, 2713.
- [254] Watson, B.; Kotov, V.; Meisel, M.; Hall, D.; Granroth, G.; Montfrooij, W.; Nagler, S.; Jensen, D.; Backov, R.; Petruska, M.; Fanucci, G.; Talham, D. *Phys. Rev. Lett.* **2001**, *86*, 5168–5171.
- [255] Johnston, D. C.; Troyer, M.; Miyahara, S.; Lidzky, D.; Ueda, K.; Azuma, M.; Hiroi, Z.; Takano, M.; Isobe, M.; Ueda, Y.; Korotin, M. A.; Anisimov, V. I.; Mahajan, A. V.; Miller, L. L. *arXiv preprint* **2000**, *cond-mat/0001147*.
- [256] Schmidiger, D.; Bouillot, P.; Muhlbauer, S.; Gvasaliya, S.; Kollath, C.; Giamarchi, T.; Zheludev, A. *Phys. Rev. Lett.* **2012**, *108*, 167201.
- [257] Giamarchi, T.; Tsvelik, A. M. *Phys. Rev. B* **1999**, *59*, 11398.
- [258] Hong, T.; Kim, Y. H.; Hotta, C.; Takano, Y.; Tremelling, G.; Turnbull, M. M.; Landee, C. P.; Kang, H. J.; Christensen, N. B.; Lefmann, K.; Schmidt, K. P.; Uhrig, G. S.; Broholm, C. *Phys. Rev. Lett.* **2010**, *105*, 137207.
- [259] Jeong, M.; Mayaffre, H.; Berthier, C.; Schmidiger, D.; Zheludev, A.; Horvatić, M. *Phys. Rev. Lett.* **2013**, *111*, 106404.

- [260] Lekin, K.; Wong, J. W. L.; Winter, S. M.; Mailman, A.; Dube, P. A.; Oakley, R. T. *Inorg. Chem.* **2013**, *52*, 2188–2198.
- [261] Chitra, R.; Giamarchi, T. *Phys. Rev. B* **1997**, *55*, 5816.
- [262] Winter, S. M.; Datta, S.; Hill, S.; Oakley, R. T. *J. Am. Chem. Soc.* **2011**, *133*, 8126.
- [263] Winter, S. M.; Oakley, R. T.; Kovalev, A. E.; Hill, S. *Phys. Rev. B* **2012**, *85*, 094430.
- [264] Miralles, J.; Castell, O.; Caballol, R.; Malrieu, J. P. *Chem. Phys.* **1993**, *172*, 33–43.
- [265] Neese, F. *J. Chem. Phys.* **2003**, *119*, 9428.
- [266] Gebhard, F. *The Mott Metal-Insulator Transition: Models and Methods*; Springer-Verlag Berlin Heidelberg, 2000.
- [267] Giamarchi, T. *Phys. Rev. B* **1991**, *44*, 2905.
- [268] Giamarchi, T.; Nattermann, T.; Le Doussal, P. In *Fundamental Problems of Mesoscopic Physics: Interactions and Decoherence*; Lerner, I., Altshuler, B., Gefen, Y., Eds.; Springer, 2004; Chapter 16.
- [269] Kinoshita, M.; Turek, P.; Tamura, M.; Nozawa, K.; Shiomi, D.; Nakazawa, Y.; Ishikawa, M.; Takahashi, M.; Awaga, K.; Inabe, T.; Maruyama, Y. *Chem. Lett.* **1991**, 1225.
- [270] Alberola, A.; Less, R. J.; Pask, C. M.; Rawson, J. M.; Palacio, F.; Oliete, P.; Paulsen, C.; Yamaguchi, A.; Farley, R. D.; Murphy, D. M. *Angew. Chem. Int. Ed.* **2003**, *42*, 4782–4785.
- [271] Allemand, P. M.; Khemani, K. C.; Koch, A.; Wudl, F.; Holczer, K.; Donovan, S.; Gruner, G.; Thompson, J. D. *Science* **1991**, *253*, 301.
- [272] Blundell, S. J. *Contemp. Phys.* **2007**, *48*, 275–290.
- [273] Awaga, K.; Tanaka, T.; Shirai, T.; Umezono, Y.; Fujita, W. *C. R. Chim.* **2007**, *10*, 52–59.

- [274] Day, P. *Nature* **1993**, *363*, 113–114.
- [275] Vonsovskii, S. V. *Ferromagnetic Resonance*; Pergamon Press, 1966.
- [276] Gurevich, A. G.; Melkov, G. A. *Magnetization Oscillations and Waves*; CRC Press, Inc., 1996.
- [277] Coulon, C.; Clerac, R. *Chem. Rev.* **2004**, *104*, 5655–5688.
- [278] Dumm, M.; Loidl, A.; Alavi, B.; Starkey, K. P.; Montgomery, L. K.; Dressel, M. *Phys. Rev. B* **2000**, *62*, 6512–6520.
- [279] Arcon, D.; Cevc, P.; Omerzu, A.; Blinc, R. *Phys. Rev. Lett.* **1998**, *80*, 1529–1532.
- [280] Kambe, T.; Kajiyoshi, K.; Oshima, K.; Tamura, M.; Kinoshita, M. *Polyhedron* **2005**, *24*, 2468 – 2471.
- [281] Rawson, J. M.; Alberola, A.; El-Mkami, H.; Smith, G. M. *J. Phys. Chem. Solids* **2004**, *65*, 727 – 731.
- [282] Farle, M. *Rep. Prog. Phys.* **1998**, *61*, 755.
- [283] Coey, J. *Magnetism and Magnetic Materials*; Magnetism and Magnetic Materials; Cambridge University Press, 2010.
- [284] Mola, M.; Hill, S.; Goy, P.; Gross, M. *Rev. Sci. Instrum.* **2000**, *71*, 186.
- [285] Takahashi, S.; Hill, S. *Rev. Sci. Instrum.* **2005**, *76*, 023114.
- [286] Morley, G. W.; Brunel, L. C.; van Tol, J. *Rev. Sci. Instrum.* **2008**, *79*, 064703.
- [287] Stanger, J.-L.; André, J.-J.; Turek, P.; Hosokoshi, Y.; Tamura, M.; Kinoshita, M.; Rey, P.; Cirujeda, J.; Veciana, J. *Phys. Rev. B* **1997**, *55*, 8398.
- [288] Kobayashi, T.; Takiguchi, M.; Amaya, K.; Sugimoto, H.; Kajiwara, A.; Harada, A.; Kamachi, M. *J. Phys. Soc. Jpn.* **1993**, *62*, 3239–3243.
- [289] Graf, D. E.; Stillwell, R. L.; Purcell, K. M.; Tozer, S. W. *High Pressure Research* **2011**, *31*, 533–543.

- [290] Barnett, J. D.; Block, S.; Piermarini, G. J. *Rev. Sci. Instrum.* **1973**, *44*, 1–9.
- [291] Palacio, F.; Antorrena, G.; Castro, M.; Burriel, R.; Rawson, J.; Smith, J. N. B.; Bricklebank, N.; Novoa, J.; Ritter, C. *Phys. Rev. Lett.* **1997**, *79*, 2336.
- [292] Smith, D. F.; De Soto, S. M.; Slichter, C. P.; Schlueter, J. A.; Kini, A. M.; Daugherty, R. G. *Phys. Rev. B* **2003**, *68*, 024512.
- [293] Smith, D. F.; Slichter, C. P.; Schlueter, J. A.; Kini, A. M.; Daugherty, R. G. *Phys. Rev. Lett.* **2004**, *93*, 167002.
- [294] Lunkenheimer, P.; Müller, J.; Krohns, S.; Schrettle, F.; Loidl, A.; Hartmann, B.; Rommel, R.; de Souza, M.; Hotta, C.; Schlueter, J. A.; Lang, M. *Nat Mater* **2012**, *11*, 755–758.
- [295] Wang, Z. F.; Liu, Z.; Liu, F. *Nat Comms* **2013**, *4*, 1471.
- [296] Jérôme, D. *Chem. Rev.* **2004**, *104*, 5565–5592.
- [297] Saito, G.; Yoshida, Y. *Bull. Chem. Soc. Jpn.* **2007**, *80*, 1–137.
- [298] Haddon, R. C.; Hebard, A. F.; Rosseinsky, M. J.; Murphy, D. W.; Duclos, S. J.; Lyons, K. B.; Miller, B.; Rosamilia, J. M.; Fleming, R. M.; Kortan, A. R. *Nature* **1991**, *350*, 320–322.
- [299] Hebard, A. F.; Rosseinsky, M. J.; C, H. R.; Murphy, D. W.; Glarum, S. H.; Palstra, T. T. M.; Ramirez, A. P.; Kortan, A. R. *Nature* **1991**, *350*, 600.
- [300] Kagawa, F.; Miyagawa, K.; Kanoda, K. *Nature* **2005**, *436*, 534–537.
- [301] Itou, T.; Oyamada, A.; Maegawa, S.; Tamura, M.; Kato, R. *Phys. Rev. B* **2008**, *77*, 104413.
- [302] Shimizu, Y.; Miyagawa, K.; Kanoda, K.; Maesato, M.; Saito, G. *Phys. Rev. Lett.* **2003**, *91*, 107001.
- [303] Boéré, R. T.; Oakley, R. T.; Reed, R. W. *J. Organomet. Chem.* **1987**, *331*, 161–167.

- [304] Miralles, J.; Daudey, J.-P.; Caballol, R. *Chem. Phys. Lett.* **1992**, *198*, 555–562.
- [305] Wong, J. W. L.; Mailman, A.; Winter, S. M.; Robertson, C. M.; Holmberg, R. J.; Murugesu, M.; Dube, P. A.; Oakley, R. T. *Chem. Commun.* **2014**, *50*, 785.
- [306] Winter, S. M.; Mailman, A.; Oakley, R. T.; Thirunavukkuarasu, K.; Hill, S.; Graf, D. E.; Tozer, S. W.; Tse, J. S.; Mito, M.; Yamaguchi, H. *Phys. Rev. B* **2014**, *89*, 214403.
- [307] Setyawan, W.; Curtarolo, S. *Comput. Mater. Sci.* **2010**, *49*, 299–312.
- [308] Kokalj, A. *Computational Materials Science* **2003**, *28*, 155–168.
- [309] Basov, D. N.; Averitt, R. D.; Van Der Marel, D.; Dressel, M.; Haule, K. *Rev. Mod. Phys.* **2011**, *83*, 471.
- [310] Kuzmenko, A. B. *Rev. Sci. Instrum.* **2005**, *76*, 083108.
- [311] Götze, W.; Wölfle, P. *Phys. Rev. B* **1972**, *6*, 1226.
- [312] Allen, J. W.; Mikkelsen, J. C. *Phys. Rev. B* **1977**, *15*, 2952.
- [313] Dressel, M.; Drichko, N. *Chem. Rev.* **2004**, *104*, 5689–5716.
- [314] Poteryaev, A. I.; Ferrero, M.; Georges, A.; Parcollet, O. *Phys. Rev. B* **2008**, *78*, 045115.
- [315] Peters, R.; Pruschke, T. *Phys. Rev. B* **2010**, *81*, 035112.
- [316] de' Medici, L.; Mravlje, J.; Georges, A. *Phys. Rev. Lett.* **2011**, *107*, 256401.
- [317] Georges, A.; Medici, L. d.; Mravlje, J. *Annu. Rev. Cond. Mat. Phys.* **2013**, *4*, 137–178.
- [318] Amaricci, A.; Camjayi, A.; Haule, K.; Kotliar, G.; Tanasković, D.; Dobrosavljević, V. *Phys. Rev. B* **2010**, *82*, 155102.
- [319] Han, J. E.; Jarrell, M.; Cox, D. L. *Phys. Rev. B* **1998**, *58*, R4199.

- [320] Jakobi, E.; Blümer, N.; van Dongen, P. *Phys. Rev. B* **2013**, *87*, 205135.
- [321] Arita, R.; Held, K. *Phys. Rev. B* **2005**, *72*, 201102.
- [322] *Magnetism and Magnetic Materials*.
- [323] Jarrell, M.; Pruschke, T. *Z. Phys. B: Condens. Matter* **1993**, *90*, 187–194.
- [324] Pruschke, T.; Jarrell, M. *Physica B: Condensed Matter* **1994**, *199*, 217–218.
- [325] Pruschke, T.; Cox, D. L.; Jarrell, M. *Phys. Rev. B* **1993**, *47*, 3553.
- [326] Dressel, M.; Grüner, G.; Eldridge, J. E.; Williams, J. M. *Synt. Met.* **1997**, *85*, 1503–1508.
- [327] Dressel, M. *Condens. Matter Phys.* **2012**, *2012*, 1–21.
- [328] Jacobsen, C. S.; Tanner, D. B.; Bechgaard, K. *Phys. Rev. B* **1983**, *28*, 7019.
- [329] Kobayashi, A.; Fujiwara, E.; Kobayashi, H. *Chem. Rev.* **2004**, *104*, 5243–5264.
- [330] Bommeli, F.; Degiorgi, L.; Wachter, P.; Legeza, Ö.; Jánossy, A.; Oszlányi, G.; Chauvet, O.; Forró, L. *Phys. Rev. B* **1995**, *51*, 14794.
- [331] Mori, T.; Kawamoto, T.; Yamaura, J.; Enoki, T.; Misaki, Y.; Yamabe, T.; Mori, H.; Tanaka, S. *Phys. Rev. Lett.* **1997**, *79*, 1702.
- [332] Auerbach, A. *Interacting Electrons and Quantum Magnetism*; Springer, 1998.